A S P E C T S

O F

Z I N C

E L E C T R O C H E M I S T R Y

by

Peter Charles Morgan

Supervisor: Prof. N. A. Hampson

Industrial Supervisor: Dr. D. J. Spiers

A Doctoral Thesis submitted in partial fulfilment of the requirements for the award of Doctor of Philosophy of the Loughborough University of Technology, October 1982.

The work described in this thesis has not been submitted, in full or in part, to this or any other institution for a higher degree

ACKNOWLEDGEMENTS

I would like to express my gratitude to my supervisor, Professor N. A. Hampson, for his guidance, help and continued encouragement throughout the duration of this work.

My thanks also go to Dr. D. J. Spiers for his advice, discussions and encouragement during this project, and I would like to acknowledge the financial support of the Advanced Projects Laboratory, Berec Group Ltd.

I am grateful to Dr. Leek, Dr. Karunathilaka and Dr. McNeil, and to my fellow research students for the helpful discussions and their friendship which has made my time in Loughborough such a happy one.

I would also like to thank Mr. A. Bower, Mr. M. Coupe and Mr. M. Godwin for their technical assistance, and Miss L. Hockey for typing this thesis.

To Roma .....

SUMMARY

The electrochemistry of porous, and planar zinc electrodes has been examined in connection with the application of zinc in electrochemical power sources. Planar, horizontal, upward-facing zinc electrodes have been galvanostatically oxidised in a convection-free system containing KOH under a series of different conditions. A plot of i vs. $\tau^{-\frac{1}{2}}$ (where τ was the time to passivation) followed the Sand's equation. Many additives have been reported to increase τ, but in the convection-free system no significant increase has been observed.

Porous electrodes have been oxidised in the same system. The formation of duplex films has been confirmed optically, and the expansion of an oxidising electrode has been followed using a travelling microscope. A reaction plane parallel to the external surface has been observed penetrating the electrode.

Rotating disc electrode experiments have been used to study the oxidation of zinc in a number of electrolytes. In $NaClO_4$ semi-conducting films were formed. In KOH a solution soluble region was identified. Linear sweep voltammograms were recorded in KOH, KOH containing polymaleic acid, and $NaClO_4/ZnBr_2$ solutions. The techniques have been combined to show that the cathodic peak observed on reversing an anodic sweep in KOH is due to the reduction of soluble species from a Type I film, rather than reduction of a solid state film.

The A.C. impedance of zinc in KOH, and in KOH with a carboxymethylcellulose, has been measured, and a theory proposed to explain the experimental results.

A practical cell has been modelled. The current distribution along the porous zinc electrodes has been measured.

Cadmium ring counter electrodes have been developed of greater recoverable charge capacity, and longer cycle life than the zinc electrode. These have been assembled in a 3-tier stack with separators and zinc electrodes in the central cavity. This complex cell was cycled under electrolyte-starved conditions, and the current passing in each segmental ring has been measured, and the charge recoverable calculated. The differences between oxidative and reductive charge in each cycle was attributed to zinc relocation. An electrode which only partially filled the cavity showed rapid shape-change. Electrodes that filled the cavity showed an expansion above the level of the rings during cycling, and ultimately failed due to oxygen evolution.

The implications of these researches to contemporary porous zinc electrode technology are discussed.

LIST OF SYMBOLS

a	activity of absorbate
A	electrode surface area
b	Tafel slope
C	Total differential capacitance
C_{comp}	differential capacitance of the compact double layer
C_{diff}	differential capacitance of the diffuse double layer
C_{dl}, C_L	double layer capacitance
C_o^b, C_R^b, $C_{o,R}^\infty$	bulk concentration of o and R
C_o^s, C_R^s	surface concentrations of o and R
D_o, D_R	diffusion coefficient of o and R
E	electrode potential on a suitable reference scale
E^o	standard electrode potential
E_p	potential of peak or current density
E_r	reversible electrode potential (at i = o)
E_{rat}	rational potential
$E_{\frac{1}{2}}$	polarographic half wave potential
f	frequency in Hertz
F	Faraday's constant
h	height of nucleus
i	current or current density
i_a, i_c	anodic current density, cathodic current density
i_d, i_L	diffusion controlled current density
i_p	peak current or current density
i_∞	charge transfer limited current
i_o	exchange current density
k_a, k_c	potential dependent rate constants for the anodic and
$\vec{k}$, $\overleftarrow{k}$	cathodic reactions
k_s	specific rate constant at E

k_{sh}	standard heterogeneous rate constant
K^o	apparent standard rate constant
m	metres
M	molar mass
n	number of electrons
N	number of moles of reactant
o	oxidised species
P_f	porosity factor
Q_m	maximum charge
q	charge on electrode, flux of diffusing species
r	radius of nucleus
R	gas constant, reduced species
R_{CT}, R_D	charge transfer resistance
R_Ω	ohmic resistance of electrode
S	electrode surface area
t	time
t_m	time taken to reach maximum current
T	temperature
u	age of the nucleus
V	Volts
W	Warburg impedance
$(\bar{x})$, x	(mean) distance from the electrode
Z	total cell impedance
Z'	real part of electrode impedance
Z''	imaginary part of electrode impedance
Z_W	Warburg impedance
α	charge transfer coefficient
δ, x_{Hy}	diffusion boundary layer thickness
η (η_p)	charge transfer overpotential

θ	phase angle, charge transfer coefficient
ν	kinematic viscosity, potential sweep rate
ν_1, ν_2	rates of reaction
σ	Warburg coefficient
ϕ	potential difference between the electrode and solution
ω	angular velocity, angular frequency
Γ	surface coverage

CONTENTS

CHAPTER 1

INTRODUCTION

Zinc is one of the metals known longest to man, a zinc idol being found in the prehistoric Dacian settlement at Dordosch, Transylvania. Since Volta's[1] early work at the beginning of the 19th century, zinc has been widely employed as an electrode by the battery industry. It is relatively cheap, and dissolves rapidly in aqueous acid, and alkali solutions. Its low density gives rise to a high specific power rating. In alkali, high anodic current regions may produce reaction products that passivate the electrode. Porous structures with large specific surface areas have been developed in an attempt to alleviate the problem.

The application of zinc as a secondary electrode has been hindered by the formation of zinc dendrites on recharging, which may puncture the separator and lead to cell short-circuiting, and by the relocation and densification of the zinc electrode on cycling. If the advantages of the primary electrode can be maintained in a secondary system, then there are good prospects for the development of relatively cheap power sources, and the system's possible use in electric vehicles. The problem has been the subject of a large research effort. The present study investigated the anodic oxidation of zinc in a number of alkali and bromide electrolytes. An experimental system has been constructed to measure the current distribution along an operating porous zinc electrode during oxidation and reduction cycling.

The galvanostatic technique most closely represents the performance of a working electrochemical energy device. The oxidation of planar, and porous zinc electrodes in alkali solutions has been studied using

this method. Linear sweep voltammetry, and rotating disc electrode experiments have been used to examine the mechanisms of some of these reactions.

A more detailed study was made of the oxidation of zinc in alkali of the concentration used in the commercial cells using the a.c. impedance technique.

A model of an R6 size cell was constructed using a segmented cadmium ring electrode. The cavity was filled with a commercial porous zinc gel electrode and the current through each segment was measured.

The results are presented in a manner that the author hopes will lead the reader from an understanding of the basic chemistry under controlled conditions, to the complex reactions in a working cell. It should be recognised that this is not necessarily in chronological order.

CHAPTER 2

THEORETICAL PRINCIPLES

2.1.1. The Electrode-Electrolyte Interphase

An interphase can be considered as the region between two phases in which the properties have not yet reached the bulk of either phase. The electrode-electrolyte interphase is of fundamental importance in determining electrode kinetics, since the reactions occur in this region. Therefore it is essential that any discussion of an electrode process is accompanied by a description of the electrode-electrolyte interphase. When an electrode is placed in an electrolyte, there is a breakdown of electrical neutrality at the phase boundaries, and an electrical double layer exists at the interphase. Two layers of electrical charge and opposite sign are separated by a distance of the order of tenths of nanometers producing a potential difference across the interphase.

The simplest model was proposed by Helmholtz[2] in 1879. He regarded the interphase as consisting of two rigidly held planes of equal charge fixed by electrostatic forces. The ions in solution lined up at a fixed distance from the electrode, with their charges balanced by the electrons at the electrode surface. Three assumptions are necessary:-

i) the separated charges are in electrostatic equilibrium.

ii) no transfer of charge occurs across the interphase with changes in electrode potential.

iii) the charge in solution changes with electrode potential.

These conditions resemble those of a parallel-plate capacitor with a small charge separation ($\sim$ 0.3 nm), and an electrical capacitance (C_{dl}). The field strengths may approach $10^6 Vcm^{-1}$ in the plane of closest

approach. The electrical behaviour of the double layer should be purely capacitive with no ohmic leakage in parallel corresponding to ion discharge. The Helmholtz model is illustrated in Figure 2.1. Electrodes which closely obey these conditions are termed "ideally polarisable", but a mercury electrode between the reversible hydrogen potential and 0.9V (s.h.e.) is the only practical system approaching ideality.

The Helmholtz model of a compact layer of ions in the electrolyte was later modified by Gouy[3] and Chapman[4]. Independently they developed the concept of a diffuse layer in the electrolyte where the distribution of ions was the result of the ordering forces of the electric field, and the disorder due to thermal motion. The model assumed the ions to be point charges which could approach to within infinitely small distances of the electrode surface. The predicted theoretical capacitance is lower than that observed experimentally.

The theory was further developed by Stern[5] who combined the two earlier models, and taking into account the size of the ions. A monolayer of ions are held at a finite distance from the electrode, backed by a diffuse layer extending to the bulk of solution. He assumed that the plane of closest approach was the same for anions and cations, but indicated that this assumption may not be valid. He also postulated that some ions could undergo adsorption by means other than electrostatic attraction.

The Stern model was further modified by Grahame[6] who suggested the interphase consisted of three layers. The Helmholtz plane was divided in two, with the inner Helmholtz plane passing through the centres of the specifically adsorbed anions which are unlikely to be hydrated, and the outer Helmholtz plane passing through the hydrated cation centres at their plane of closest approach. The third layer

Fig. 2.1 Helmholtz Model of the Double Layer.

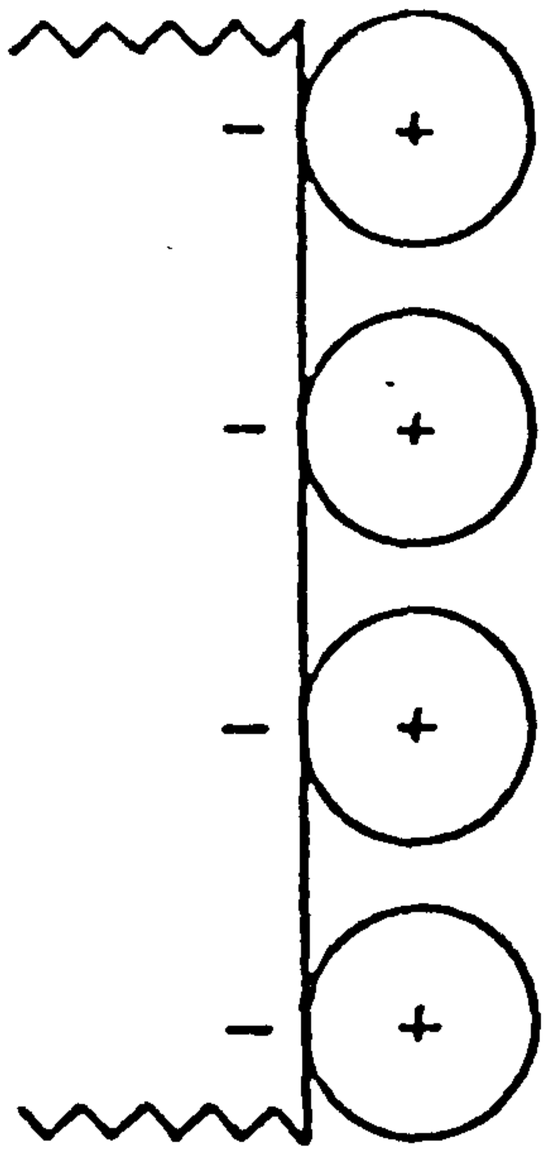

Variation of Potential with Distance through the Interface predicted by the Helmholtz Model.

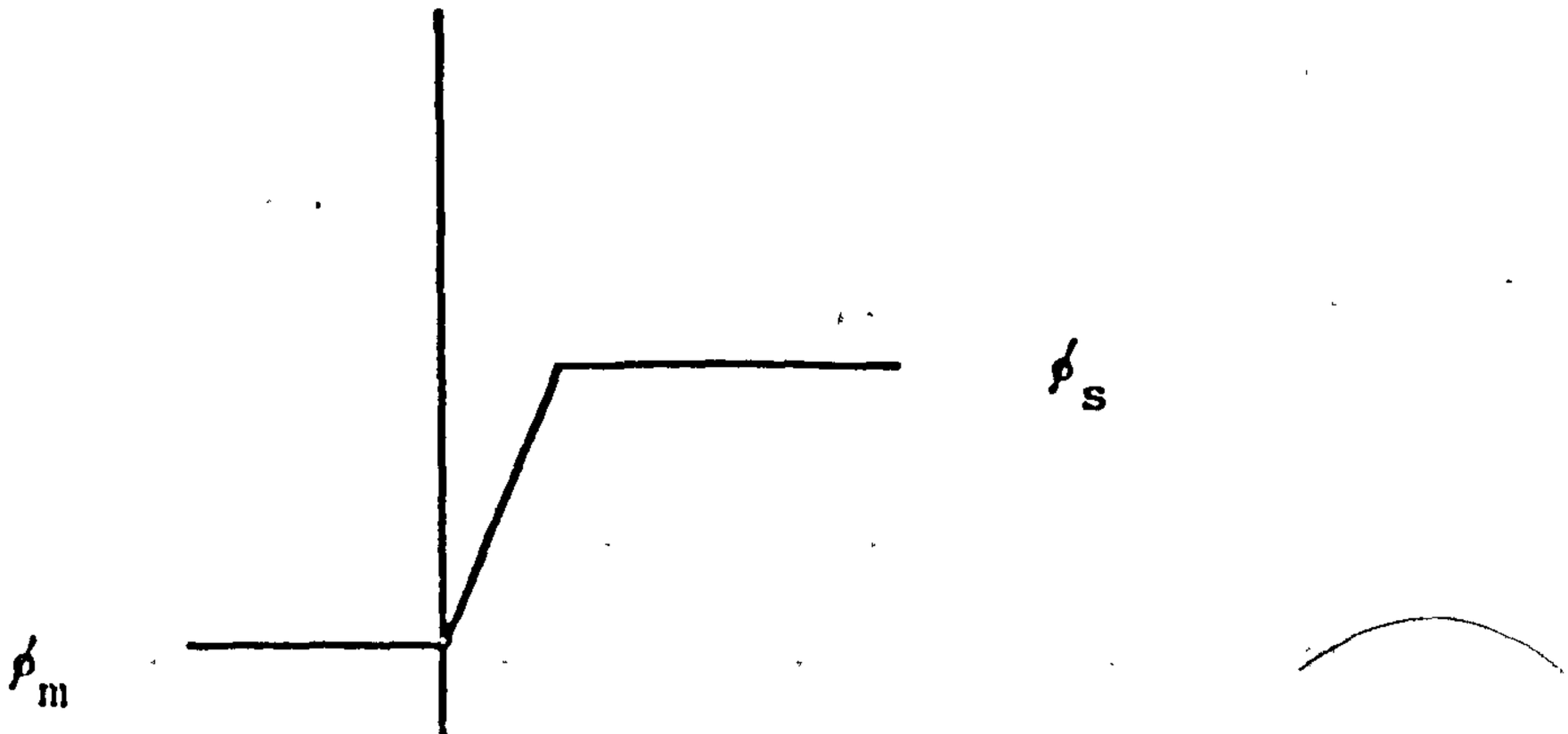

corresponds to the diffuse layer of Gouy - Chapman. A schematic representation is shown in Figure 2.2, along with the variation of potential ϕ, across the interphase. Using this model Grahame showed that the total differential capacitance of the double layer is the result of two capacitors in series, and is given by:-

$$\frac{1}{C_{dl}} = \frac{1}{C_{diff}} + \frac{1}{C_{comp}} \qquad (2.1)$$

where C_{dl} = total differential double layer capacitance

C_{diff} = differential capacitance of the diffuse layer

C_{comp} = differential capacitance of the compact layer.

From the equation (2.1) it can be seen that the smaller capacitance will determine the magnitude of the total capacitance. In dilute solution C_{dl} becomes virtually independent of C_{comp}. At very low concentrations a sharp minimum is obtained on a C_{dl} versus potential plot. This minimum is associated with the point of zero charge (p.z.c.) of the electrode.

A more recent theory for the distribution of ions in the double layer has been proposed by Bockris, Devanathan and Müller[7] taking into account the predominant existance of solvent in the interphase. They suggest that the surface of the electrode is covered with an orientated layer of water molecules, but on certain sites the water molecules are displaced by specifically adsorbed ions which do not carry a hydration shell. The inner Helmholtz plane passes through the centres of the specifically adsorbed ions, the centres of adsorbed metal "adatoms", and in the case of gas electrodes (e.g. s.h.e.), through the centres of adsorbed gas molecules. Grahame had assumed that specific adsorption was the result of covalent bonding, but Bockris et al showed it to be due to a lack of "primary" hydration. The outer Helmholtz plane passes

FIG. 2.2 Grahame Model of the Double Layer.

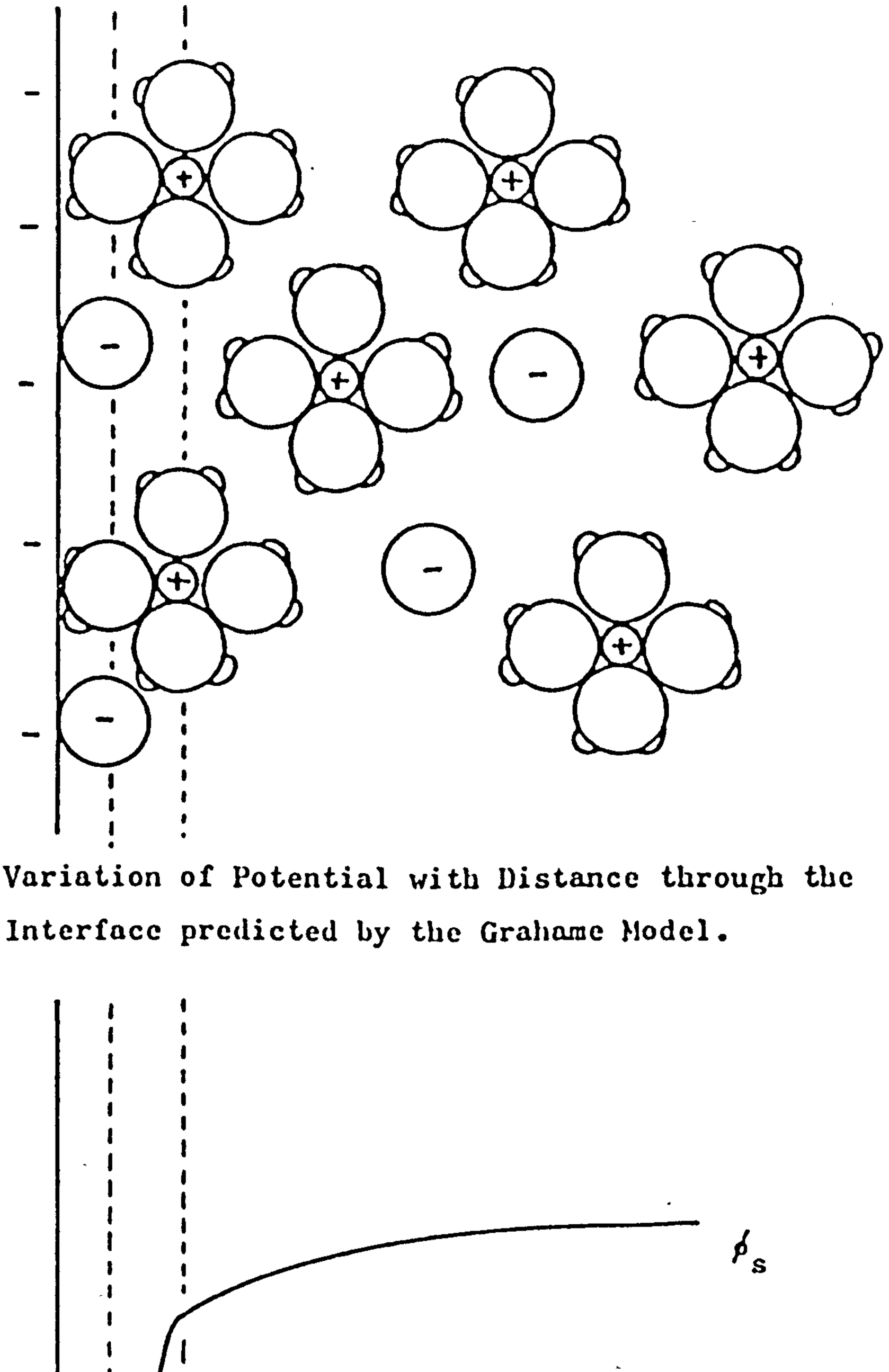

through the centres of the solvated metal ions (Figure 2.3).

Frumkin[8,9] discussed the importance of the p.z.c., and indicated that it is not affected by the introduction of potential-determining ions, and can therefore be used when considering charge adsorption at a polarisable electrode.

Later studies of the structure of the double layer have mainly concentrated on the orientation of water dipoles in the compact layer[10-12]. Cooper and Harrison[13-16] have questioned the conventional sub-division of the double layer. They consider the structure of the interphase to arise specifically from the known differences between the anions and cations in solution, and the net distributed charge acts at a mean distance, $\bar{x}$, from the electrode. The effective dielectric constant will vary directly with $\bar{x}$, and $\bar{x}$ varies inversely with surface charge density, and the electrolyte concentration. The distance $\bar{x}$, is also determined by the different effective sizes of anions and cations in the aqueous solution.

2.1.2. Solid Electrodes

The discussion of the double layer so far has concentrated on that part in solution, and is really only applicable to mercury and other liquid metal electrodes. The distribution of charge on the electrode side of the double layer is in the realms of solid-state physics, and can often be neglected due to high conductivity. It may become important however when a semi-conducting electrode material is used.

The packing of atoms in a crystal results in some crystal planes having a higher packing density, and a higher number of satisfied bonds.

FIG. 2.3 Bockris et al Model of the Double Layer.

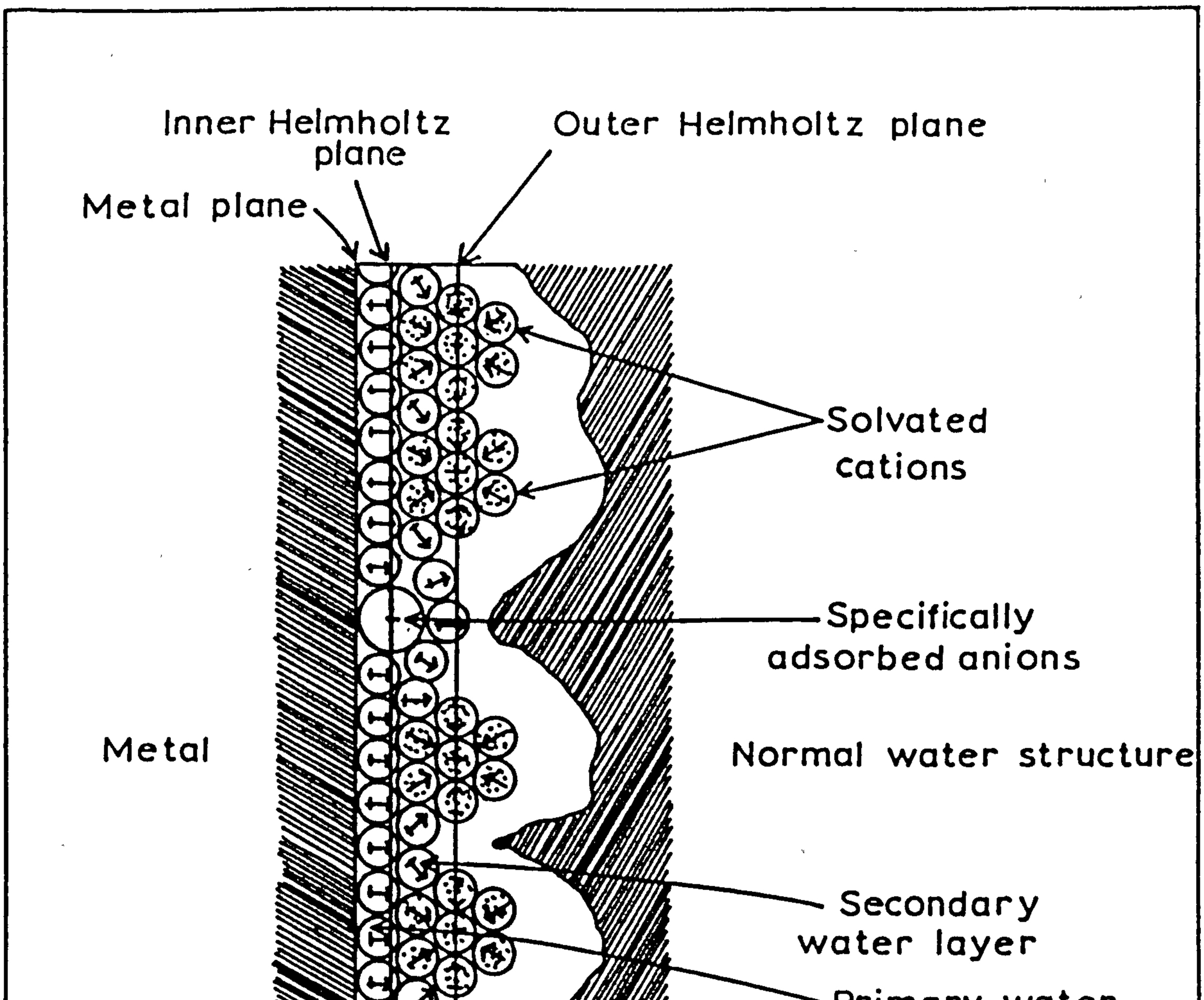

A number of observations[17,18] indicate that in a solid, each component single-crystal face of an electrode surface possesses a characteristic point of zero charge (E_z), and double layer capacitance at a particular potential. The non-uniform double layer capacitance results in a frequency dispersion. Leek and Hampson[19,20] have proposed a Ladder network of resistors and capacitors to model the situation, and their calculations show that surface heterogeneity is an important factor in the development of frequency dispersion. Some experimental testing of these theories is given in Appendix 2.

2.2. The Charge Transfer Process

Electrode processes are heterogeneous reactions that occur at the electrode-electrolyte interphase accompanied by the transfer of charge through the interphasial region. The reaction is therefore a redox-type reaction, and may be represented by the overall equation:-

$$O + ne \underset{k_a}{\overset{k_c}{\rightleftharpoons}} R \qquad (2.2)$$

At the equilibrium potential charge is simultaneously being donated and accepted by the electrode in a dynamic equilibrium. According to the generally accepted theory of Volmer and Erdy-Gruz[21] both cathodic and anodic processes are controlled by potential dependent energy barriers; this has been discussed elsewhere[22].

For the forward reaction the current is given by:

$$i_c = nFk_c C_o^s \qquad (2.3)$$

And for the backward reaction:

$$i_a = nFk_a C_R^s \qquad (2.4)$$

The total overall current (per unit electrode area) flowing at a given potential can be expressed as:-

$$i = nF\,(k_c\,C_o^{\,s} - k_a\,C_R^{\,s}) \qquad (2.5)$$

i.e. the difference between the forward and reverse rates; $C_o^{\,s}$ and $C_R^{\,s}$ are the surface concentrations of species o and R, whilst k_c and k_a are the potential dependent rate constants given by:-

$$k_c = k_c^{\,o}\,\exp\left(\frac{-\alpha\,n\,FE}{RT}\right) \qquad (2.6)$$

$$k_a = k_a^{\,o}\,\exp\left(\frac{(1-\alpha)\,n\,FE}{RT}\right) \qquad (2.7)$$

where α is the charge transfer coefficient

E is the potential of the electrode measured against a convenient reference electrode

$k_c^{\,o}$ is the value of k_c at the reference potential

$k_a^{\,o}$ is the value of k_a at the reference potential

By substitution of equation (2.6) and (2.7) into (2.5) we obtain:-

$$i = nF\left[k_c^{\,o}\,C_o^{\,s}\,\exp\left(\frac{-\alpha nFE}{RT}\right) - k_a^{\,o}\,C_R^{\,s}\,\exp\left(\frac{(1-\alpha)nFE}{RT}\right)\right] \qquad (2.8)$$

At the reversible potential (E_r) the net current is zero and hence:-

$$i_c = i_a = i_o$$

$$i_o = nF\,k_c^{\,o}\,C_o^{\,s}\,\exp\left(\frac{-\alpha nFE_r}{RT}\right)$$

$$= nF\,k_a^{\,o}\,C_R^{\,s}\,\exp\left(\frac{(1-\alpha)nFE_r}{RT}\right) \qquad (2.9)$$

where i_o is the exchange current density.

By solving (2.9) for $nFk_c^{\,o}C_o^{\,s}$ and $nFk_a^{\,o}C_R^{\,s}$ and substituting into (2.8) we obtain:

$$i = i_o \exp\left[\frac{-\alpha nF(E-E_r)}{RT}\right] - \exp\left[\frac{(1-\alpha)nF(E-E_r)}{RT}\right] \qquad (2.10)$$

where $E-E_r$ is defined as the charge transfer (or activation) overpotential (η_D).

For low overpotentials ($\eta_D \ll \frac{RT}{nF}$) the overpotential-current curve is linear with the current corresponding to an electrical resistance, the charge transfer resistance (R_D).

$$R_D = -\left(\partial\eta_D / \partial i\right)_{i \to o} \qquad (2.11)$$

Differentiating equation (2.9) at $\eta_D = 0$ the expression becomes

$$\left(\frac{\partial i}{\partial \eta_D}\right)_{\eta_D = 0} = \frac{-nFi_o}{RT} \qquad (2.12)$$

and

$$R_D = \frac{RT}{nF} \cdot \frac{1}{i_o} \qquad (2.13)$$

Therefore the exchange current density may be obtained from the charge transfer resistance at the reversible potential (E_r, $\eta_D = 0$).

For high overpotentials $|\eta_D| \gg \frac{RT}{\alpha nF}$

or $|\eta_D| \gg \frac{RT}{(1-\alpha)nF}$

one of the exponential terms in (2.9) can be neglected. At high cathodic overpotentials

$$\eta_D = \frac{RT}{\alpha nF} \ln i_o - \frac{RT}{\alpha nF} \ln i \qquad (2.14)$$

At high anodic overpotential

$$\eta_D = \frac{RT}{(1-\alpha)nF} \ln i_o + \frac{RT}{(1-\alpha)nF} \ln i \qquad (2.15)$$

Equations (2.14) and (2.15) are the Tafel[23] relationships and are generally used by converting natural logarithms to $\log_{10}$.

The exchange current density can therefore be obtained from values of the charge transfer resistance at low overpotentials, and by extrapolation of the log i - potential plots back to the equilibrium potential at high overpotentials.

The dependence of the exchange current on the reactant concentration has been established and for the reaction (2.2) it can be shown that[24]

$$i_o = nFk^o a_R^{\alpha} a_o^{(1-\alpha)} \qquad (2.16)$$

a_R and a_o are the activities of the reduced and oxidised species respectively, and are usually replaced by the corresponding concentrations, since the activities are usually unknown. k^o is the apparent standard rate constant.

This theory of charge transfer applies only to the simple electrode reaction in which all the electrons are transferred simultaneously. Losev[25] has considered the case of successive electron transfer with a single rate-determining step, and others with comparable rate constants. Recent workers[26-28] have derived charge transfer equations using a quantum mechanical approach. The reaction does not occur in one smooth step over a single energy barrier, but proceeds in various stages. The reactant must first diffuse to the electrode and then the ionic atmosphere rearranges, and the solvent molecules orientate to form the transition state. Finally, the electron is transferred and only this step has to be treated kinetically. The earlier stages of the reaction are all in equilibrium and can be treated by thermodynamics. Following electron transfer, the ligand bond distances are altered and the solvent dipoles and ion atmosphere reorientate. The electron

transfer step involves no change in energy, and is a central feature of the Marcus and Levich theories. A detailed theory for the process of solvent reorganisation has been worked out by Levich and Dogonadse[29].

2.3.1. Mass Transport Processes

The electrode process represented by equation (2.2) may be considered to be composed of three individual processes

$$O_{bulk} \longrightarrow O_{electrode} \qquad (2.17)$$

$$O_{electrode} + ne \longrightarrow R_{electrode} \qquad (2.18)$$

$$R_{electrode} \longrightarrow R_{bulk} \qquad (2.19)$$

The rate of an electrode reaction can be totally or partially controlled by mass transfer. If (2.17) or (2.19) are the slowest steps the overall reaction is said to be mass transfer controlled. If (2.18) has a slower rate then the process is limited by the rate of electron transfer, and the reaction is charge transfer controlled. In some cases neither of the above processes are as slow as a chemical transformation involving the electroactive species, in which case the chemical transformation is the rate determining process.

Three modes of mass transfer are normally encountered; migration, convection, and diffusion.

2.3.2. Migration

Mass transfer by migration is the result of the forces exerted on the charged particles by an electric field. In the presence of a large excess of support electrolyte the migration of electroactive material is minimised to such an extent that it may be neglected.

2.3.3. Convection

Natural, or free convection will always develop spontaneously in any solution undergoing electrolysis. It arises as a result of density differences near the electrode and may include contributions from thermal and mechanical disturbances.

2.3.4. Diffusion

Whenever concentration differences are established, diffusion will result. Since a concentration gradient develops as soon as electrolysis is initiated, diffusion occurs to some extent in every electrode reaction. Consider the linear diffusion of reacting species to a planar electrode in a static solution, (no migration or convection), with respect to the reaction in equation (2.2). The number of moles (N) of a substance diffusing across a cross-sectional area (A in cm^2) in a time (dt) is proportional to the concentration gradient of the diffusing species.

$$\frac{dN}{dt} = D_o A \frac{\partial C_o}{\partial x} \qquad (2.20)$$

where the proportionality constant D_o is defined as the number of molecules per second crossing unit area under unit concentration gradient, and is called the diffusion coefficient.

Equation (2.20) relates the diffusion rates to concentration, and is known as Ficks first law. Rearranging (2.20) we obtain the "flux" (q) of material, the number of moles through a unit area in a unit time.

$$q = \frac{dN}{Adt} = D_o \frac{\partial C_o}{\partial x} \qquad (2.21)$$

As electrolysis continues C_o and hence $\frac{\partial C_o}{\partial x}$ decrease with time, since "o" is being consumed at the electrode surface. C_o is therefore a

function of distance from the electrode, and time. The change in C_o with time between two planes a distance x and x + dx from the electrode surface (x = o) will be the difference between the number of moles of "o" entering the plane at (x + dx), and the number leaving at the plane x.

Thus:
$$\frac{\partial C_o}{\partial t} = \frac{q\ (x + dx) - q(x)}{dx} \qquad (2.22)$$

but
$$\frac{\partial C_o}{\partial t} = \frac{\partial q}{\partial x} \qquad \text{as } dx \longrightarrow o$$

Therefore
$$\frac{\partial C_o}{dt} = \frac{D_o\ \partial^2 C_o}{\partial x^2} \qquad (2.23)$$

This is Fick's second law and the fundamental equation for linear diffusion. The current density i, at any time t, is proportional to the flux per unit area at the electrode surface

$$i = nF\ A\ q(o,t) = \left(nF\ A\ D_o \frac{\partial C_o}{\partial x}\right)_{o,t} \qquad (2.24)$$

The value of $\left(\frac{\partial C_o}{\partial x}\right)$ can be obtained by solving the differential equation (2.23) applying the appropriate boundary conditions

(i) $C_o^s = o$ at $t > o$

(ii) as $x \longrightarrow \infty$ $C_o^x \longrightarrow C_o^b$

(iii) $t < o$ $C_o^s = C_o^b$

The final expression for the instantaneous current at a planar electrode under diffusion control becomes

$$i = \frac{nF\ A\ D_o^{\frac{1}{2}}\ C_o^b}{\pi^{\frac{1}{2}}\ t^{\frac{1}{2}}} \qquad (2.25)$$

This is sometimes called the Cotterell equation.

CHAPTER 3

THEORIES OF THE RELEVANT ELECTROCHEMICAL TECHNIQUES

3.1. The Rotating Disc Electrode

The Cotterell equation (2.25) holds for an electrode in a stationary solution. At long times a negligable current is predicted, but this is not observed experimentally. Density differences due to species reacting at the electrode start a convective flow, bringing fresh electroactive species to the electrode. A precise mathematical definition of these fluid flow processes is required before the equations from Chapter 2 can be applied. The rotating disc electrode is an example of a convective-diffusion system where a complete solution of the hydrodynamics has been obtained.

Levich[29] has derived the solution for the hydrodynamic equations at a rotating disc electrode. The electrode radius is designed to be small compared with its insulating sheath, and is rotated at a constant measurable angular velocity. At the electrode a layer of solution spins around at the same speed as the electrode, while at some distance away measured in the x direction normal to the electrode, the flow velocity has a value characteristic of the bulk solution unaffected by the solid body. Approaching the electrode along the x direction Levich has shown that the flow velocity is dependent on the rotation speed of the disc. Rotation maintains the bulk concentration until just outside the hydrodynamic boundary layer by forcing convection. The boundary layer is a region near the electrode with a substantial velocity gradient, the thickness of which is given by:-

$$x_{Hy} = 2.7 \left(\frac{\nu}{\omega}\right)^{\frac{1}{2}} \qquad (3.1)$$

where ν is the kinematic viscosity (viscosity/density) in $m^2\ s^{-1}$

ω is the angular velocity in rad s^{-1}.

The range of application is limited to a Reynolds number of $10^2 < R_e < 5.4 \times 10^4$ where

$$R_e = \left(\frac{a^2\ \omega}{\nu}\right) \qquad (3.2)$$

a is the radius of the disc.

This extends in practice from 100 - 10,000 r.p.m. At lower Reynolds numbers natural convection may become the dominant mass transport process while at high Reynolds numbers turbulent flow occurs. Having established the operating conditions Levich has shown that the diffusion boundary layer δ is constant at constant rotation speed, and is given by

$$\delta = 1.62\ D^{1/3}\ \nu^{1/6}\ \omega^{-\frac{1}{2}} \qquad (3.3)$$

or more simply $\delta = B\ \omega^{-\frac{1}{2}}$

D is the diffusion coefficient of electroactive species in units $m^2\ s^{-1}$.

The concentration gradient across δ is given by

$$\frac{dC_o}{dx} = \frac{C_o^{\infty} - C_o^{s}}{\delta}$$

As $\omega \longrightarrow \infty$, $\delta \longrightarrow o$ and $C_o^{s} \longrightarrow C_o^{\infty}$

The total current can be resolved into contributions from the electron transfer step and mass transfer using the rotating disc electrode. It is this property that makes the method such a powerful electrochemical

technique. For the reduction of species o

$$o + ne \xrightarrow{\vec{k}} R$$

$$i = \frac{nF \vec{k} C_o^{\infty}}{1 + 1.61 \vec{k} \omega^{-\frac{1}{2}} \nu^{1/6} D_o^{-2/3}} \qquad (3.5)$$

where $\vec{k}$ is the potential dependent rate constant for the forward reaction, and ω is the rotation speed in radians s^{-1}.

At large overpotentials $\vec{k}$ will be large and the electron transfer is fast compared with mass transport. The electrode process is mass transfer controlled. For large $\vec{k}$ equation (3.5) reduces to

$$i = 0.621 nF D_o^{2/3} \nu^{-1/6} C_o^{\infty} \omega^{\frac{1}{2}} \qquad (3.6)$$

and a plot of i vs $\omega^{\frac{1}{2}}$ will be linear.

Conversely for small values of $\vec{k}$, at low overpotentials, the electron transfer step is slow compared with mass transfer and equation (3.5) becomes

$$i_{\infty} = nF \vec{k} C_o^{\infty} \qquad (3.7)$$

The current will not vary with rotation speed, and kinetic data can be directly calculated.

For intermediate values of $\vec{k}$ mass transfer and electron transfer are of comparable rates and equation (3.5) must be used in full. It is usually rewritten

$$\frac{1}{i} = \frac{1}{nF \vec{k} C_o^{\infty}} + \frac{1.61 \nu^{1/6}}{nF D_o^{2/3} C_o^{\infty}} \cdot \frac{1}{\omega^{\frac{1}{2}}} \qquad (3.8)$$

The reciprocal of the intercept as ($\omega \longrightarrow \infty$, $\omega^{-\frac{1}{2}} = o$) is the current corrected for mass transport (equation 3.7). Therefore $\vec{k}$ can be obtained from the intercept of a $\frac{1}{i}$ vs $\frac{1}{\omega^{\frac{1}{2}}}$ plot. The potential dependence of i_∞ is given by

$$i_\infty = nF\ C_O^\infty\ \vec{k}\ \exp\left[\frac{\alpha\ (E-E^\circ)\ nF}{RT}\right] \qquad (3.9)$$

A plot of log i_∞ versus E is linear with a slope of $\frac{\alpha nF}{2.303\ RT}$ (3.10)

and an intercept

$$\log\left[nF\ C_O^\infty\ \vec{k}^{\theta}\right] \qquad (3.11)$$

The slopes of the lines on the $\frac{1}{i}$ vs $\frac{1}{\omega^{\frac{1}{2}}}$ plots (S) are also potential dependent.

$$S = \frac{d(i^{-1})}{d(\omega^{-\frac{1}{2}})} = 1.61\ \nu^{1/6}\ D^{-2/3} \exp\left[\frac{nF\ (E-E^\circ)}{RT}\right] \qquad (3.12)$$

Taking logs

$$\log |S| = \log\left(\frac{1.61\ \nu^{1/6}\ D^{-2/3}}{nFC_O^\infty}\right) - \frac{nF}{2.303\ RT}\ (E-E^\circ) \qquad (3.13)$$

A plot of log |S| against E is linear with a slope of

$$\frac{nF}{2.303\ RT} \qquad (3.14)$$

from which the number of electrons involved in the charge transfer process can be calculated. If this value is substituted into equation (3.10) the value of the charge transfer coefficient can be obtained, and from equation (3.11) $\vec{k}^{\theta}$. The diffusion coefficient can be determined from the intercept on the log |S| against E plot

$$D^{-2/3} = \frac{s\ nF\ C_O^{\infty}}{1.61\ \nu^{1/6}} \qquad (3.15)$$

When the reaction is reversible the contribution from the backward reaction has to be considered and the current is given by

$$\frac{1}{i} = \frac{1}{nF(\vec{k}\ C_O^{\infty} - \overleftarrow{k}\ C_R^{\infty})} + \frac{1.61\ \nu^{1/6}(\vec{k}\ D_O{}^{1/3} + \overleftarrow{k}\ D_O/D_R{}^{2/3})}{nF\ D_O(\vec{k}\ C_O^{\infty} - \overleftarrow{k}\ C_R^{\infty})\ \omega^{\frac{1}{2}}} \qquad (3.16)$$

A plot of $\frac{1}{i}$ vs $\frac{1}{\omega^{\frac{1}{2}}}$ is again linear. For a reversible reaction the intercept is zero, and all the $\frac{1}{i}$ vs $\frac{1}{\omega^{\frac{1}{2}}}$ plots pass through the origin. In this case a plot of i vs $\omega^{\frac{1}{2}}$ is also linear.

3.2. Linear Potential Sweep/Cyclic Voltammetry

Since the introduction[30] and theoretical analysis by Randles[31] and Sevcik[32] the techniques have proved useful tools in obtaining detailed pictures of charge transfer systems and in examining reaction mechanisms. Cyclic voltammetry has also been useful in studying the formation and reduction of oxide films on metal layers

Potential sweep methods depend on applying a linear potential/time function to an electrode and observing the subsequent current response. If only a single sweep is performed the technique is known as linear sweep voltammetry (L.S.V.). If the sweeps are repetitive the technique is called cyclic voltammetry. The position and shape of the current peaks obtained depends on many factors including solution composition, concentration, electrode material and the sweep rate. Slow sweep rates are used to measure "steady-state" current/voltage curves on the assumption that the surface relaxes sufficiently rapidly, and the system approaches a true steady-state. Very high sweep rates are used to test

the existence of short-lived intermediates. Only the linear potential sweep can give accurate kinetic parameters, as the equations derived only apply if there are no concentration gradients in solution prior to the start of the sweep. Complex concentration gradients near the electrode surface are common with cyclic voltammetry, and it is therefore better suited to the identification of steps in the overall reaction and detecting new species appearing during electrolysis. In spite of its limitations cyclic voltammetry is widely used for qualitative evaluation of intermediates formed in complex reaction processes. The expected results for various reaction schemes have been discussed in a review by Nicholson and Shain[33].

For a simple electron transfer process, increasing the sweep rate (ν) increases the peak current density (i_p) at the corresponding peak potential (E_p). If the electron transfer rate is sufficiently high to maintain Nernstian equilibrium at the electrode surface (the reversible case), then the peak current density for a cathodic sweep follows the relationship

$$i_p = 2.72 \times 10^5 \, n^{3/2} \, D^{1/2} \, C_o^{\infty} \, \nu^{1/2} \qquad (3.17)$$

where n is the number of electrons transferred in the overall electrode process

D is the diffusion coefficient ($cm^2 \, s^{-1}$)

C_o^{∞} is the concentration of oxidised species in the bulk solution (mol cm^{-3})

i_p is measured in Acm^{-2}

ν is the sweep rate (Vs^{-1})

The peak potential is independent of sweep rate and is related to the polarographic half-wave potential by:-

$$E_p = E_{\frac{1}{2}} - 1.109 \frac{RT}{nF} \qquad (3.18)$$

If the reaction is slow compared with the sweep rate Nernstian response cannot be assumed. The peak characteristics change and the following limiting behaviour is approached at high rates under irreversible conditions

$$i_p = 3.01 \times 10^5 \, n \left[\frac{2.3 \, RT}{bF}\right]^{\frac{1}{2}} D^{\frac{1}{2}} C_o^{\infty} \nu^{\frac{1}{2}} \qquad (3.19)$$

where b is the Tafel slope.

The peak potential is given by

$$E_p = E_{\frac{1}{2}} - b(0.52 - \tfrac{1}{2} \log \frac{b}{D} - \log k_s + \tfrac{1}{2} \log \nu) \qquad (3.20)$$

where k_s is the electrochemical specific rate constant at the standard electrode potential E°.

The dependence of E_p on ν indicates the departure of the system from equilibrium. Provided D is known, k_s and b can be calculated from a plot of E_p vs $\log \nu$.

For a given system, as the sweep rate increases to a point at which the Nernstian equilibrium cannot be maintained it will behave irreversibly. It is therefore possible to determine the specific rate constant from the characteristic sweep rate at which the transformation occurs. The above equations apply quantitatively to first order charge transfer reactions with no kinetic or catalytic complications.

3.3. The A.C. Impedance Technique

3.3.1. Introduction

The a.c. impedance characteristics of electrochemical systems are important as their study enables us to measure the kinetic parameters of the cell. These parameters can give indications of the type of reaction, and transport mechanisms. The application of a.c. theory to reproducible liquid-metal electrodes has led to a better understanding of electrode reaction mechanisms. Reproducible values for exchange current densities, and transfer coefficients have been obtained for simple charge transfer processes. The method is also being successfully used in evaluating more complex processes involving specific adsorption of reactants or products, and to chemical reactions preceeding or following the charge transfer process.

Industrial investigations of electrode processes are usually concerned with solid or even porous electrodes, for example, those in fuel cells, batteries, electrochemical synthesis, electrolysis, electroplating, etc. Although the results obtained on liquid electrodes are of limited use for these systems, the theoretical principles have been established for the interpretation of these measurements in terms of structure, exchange current density, double layer capacitance, and surface area. The method is being employed to determine the state of charge of primary, and secondary cells.

When a constant potential difference is maintained between two electrodes in a cell, a direct current flows between them. If an alternating voltage ν of relatively small amplitude is superimposed on the potential difference the current contains an alternating component of amplitude i. When the amplitude of the alternating voltage varies sinusoidally with time t, and frequency f, we may write:-

$$\omega = 2\pi f \qquad (3.21)$$

$$\nu = V_{max} \sin \omega t \qquad (3.22)$$

$$i = I_{max} \sin (\omega t - \phi) \qquad (3.23)$$

and

$$Z = \frac{V_{max}}{I_{max}} \arg \phi$$

$$= |Z| \arg \phi \qquad (3.24)$$

where Z is the impedance of the cell

ϕ is the phase angle between the current and the voltage.

When ϕ is a negative quantity the current leads the voltage. The impedance can be represented by a network of resistors and capacitors. Conversely, when ϕ is positive the current lags behind the voltage and the impedance may be represented by an inductive-resistive circuit. The impedance can be plotted in conventional complex form on an Argand diagram. In electrochemistry the reactances most often encountered are capacitive, giving a negative quantity on the Argand diagram. However it has become standard practice to use the first quadrant of the complex plane for their presentation (Sluyters Plot). The impedance may be resolved into resistive and capacitive components which are plotted against $\omega^{-\frac{1}{2}}$ (Randles Plot). Both methods give detailed information about the electrochemistry.

3.3.2. The Cell Impedance

The faradaic impedance of a cell was first calculated by Warburg[34] but without taking into account the capacitance due to the double layer present at the electrode surface. Randles[35] has established the impedance for fast electrode reactions in a galvanic cell with a simple

one step redox reaction, the rate of which is controlled solely by charge transfer, and diffusional mass transfer processes.

The impedance of an electrolytic cell can be represented by the network[36,37] shown in Fig. 3.1 often described as a Randles Circuit. In this circuit R_Ω is the ohmic resistance of the electrolyte solution between the electrodes, including the resistance of the metal leads to the electrode. C_{dl} is the double layer capacitance which varies with d.c. potential, and is dependent on the concentration and nature of the electrolyte. R_D is the charge transfer resistance, and therefore represents the activation polarisation of the electrode reaction.

The Warburg impedance $W(W = R_W + C_W)$ is the impedance to a.c. current due to the charged species diffusing to and from the electrode. Warburg showed that this part of the current may be thought of as flowing in an impedance Z_W by solution of Fick's second law of diffusion taking into account the appropriate boundary conditions. The impedance consists of a series resistive and capacitive component, the magnitude of each component being inversely proportional to the square root of the frequency:-

$$Z_W = \sigma \omega^{-\frac{1}{2}} - j \sigma \omega^{-\frac{1}{2}} \qquad (3.25)$$

where σ is the Warburg coefficient

ω is the angular frequency of the alternating current

The charge transfer resistance R_D, and the Warburg coefficient σ, at the equilibrium potential are given by:-

$$R_D = \frac{RT}{n^2F^2\, k_o^{\ominus}\, (C_o^{\infty})^{\alpha}\, (C_R^{\infty})^{1-\alpha}} \qquad (3.26)$$

Fig. 3.1 Electrical analogue of the electrode interphase

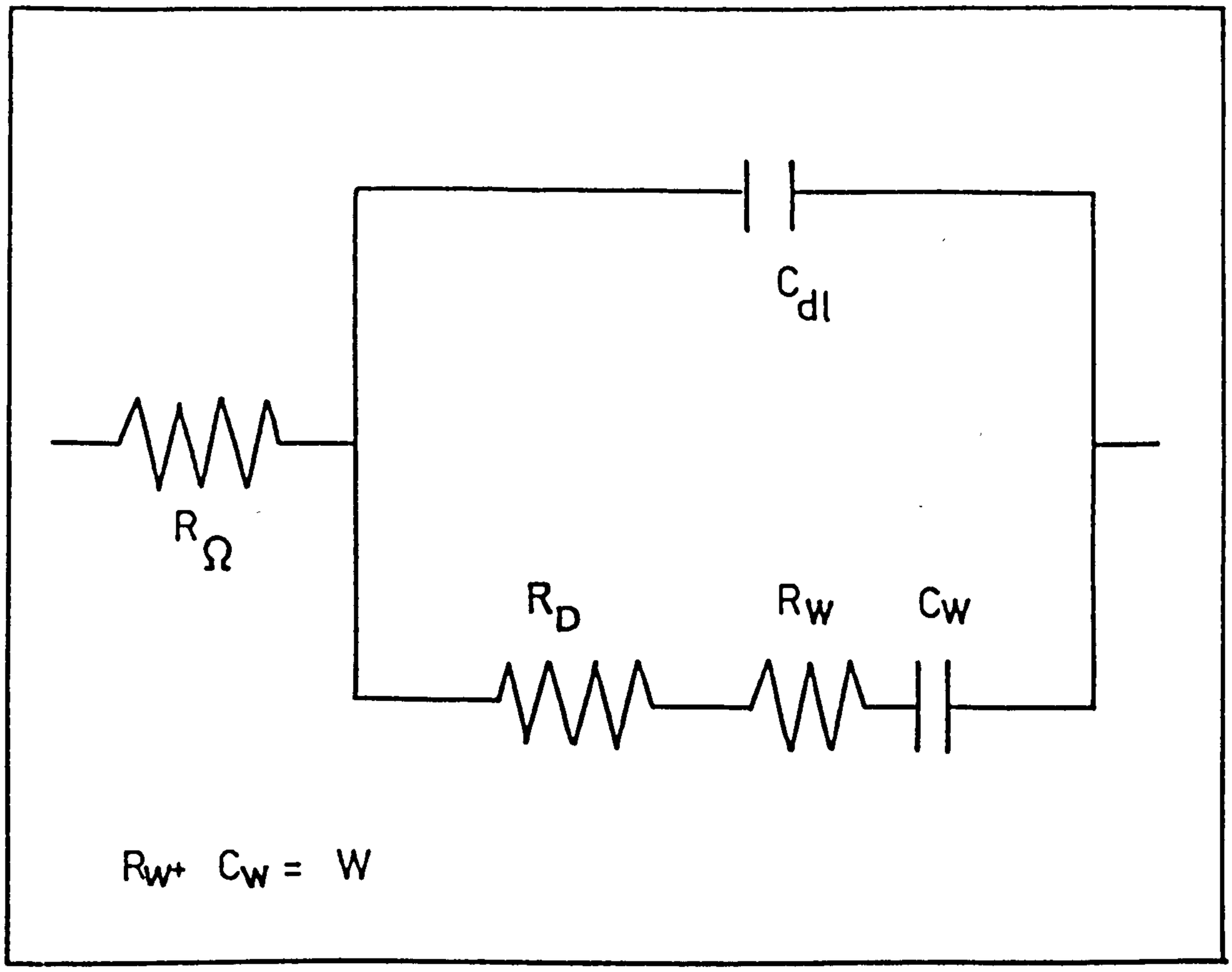

Fig. 3.2 Complex plane display – diffusion control

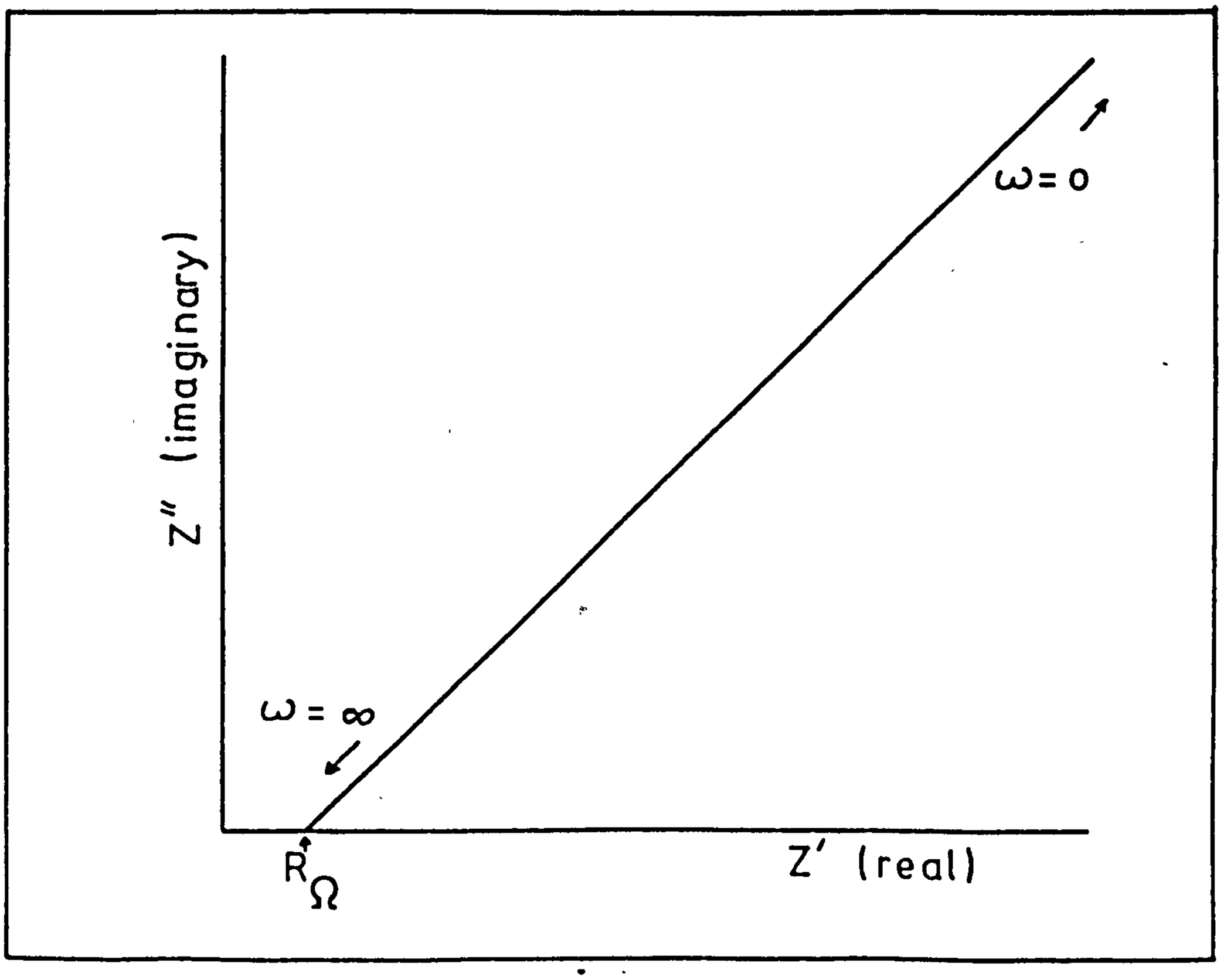

and

$$\sigma = \frac{RT}{n^2F^2\ 2^{\frac{1}{2}}} \left(\frac{1}{C_O^{\infty}\ D^{\frac{1}{2}}} + \frac{1}{C_R^{\infty}\ D_R^{\frac{1}{2}}} \right) \qquad (3.27)$$

At potentials away from this value R_D and σ can be expressed in terms of bulk concentrations providing equation (3.26) and (3.27) are suitably modified[38].

Sluyters[39] and Sluyters-Rehback[40] interpreted the total cell impedance in terms of R_Ω, C_{dl}, R_D, and σ, and represented the frequency dependent impedance of the simple electrode, by plotting the impedance as a vector in the complex plane. The method entails plotting the real component Z', and the imaginary component Z'' of the cell impedance against each other, as a function of some varied parameter, (e.g. frequency, concentration, d.c. potential).

From the Randles circuit (Fig. 3.1) the cell impedance is given by:-

$$Z = R_\Omega + \frac{1}{j\omega C_{dl} + \left(\frac{1}{R_D + \sigma\omega^{-\frac{1}{2}} - j\sigma\omega^{-\frac{1}{2}}} \right)} \qquad (3.28)$$

After separation of the real and imaginary parts of Z we obtain:-

$$Z = Z' - jZ'' \qquad (3.29)$$

where Z' and Z'' are given by:-

$$Z' = \frac{R_\Omega + R_D + \sigma\omega^{-\frac{1}{2}}}{(\sigma\omega^{\frac{1}{2}}C_{dl} + 1)^2 + \omega^2 C_{dl}^2\ (R_D + \sigma\omega^{-\frac{1}{2}})^2} \qquad (3.30)$$

and

$$Z'' = \frac{\omega C_{dl}(R_D + \sigma\omega^{-\frac{1}{2}}) + \sigma\omega^{-\frac{1}{2}}(\sigma\omega^{\frac{1}{2}}C_{dl} + 1)}{(\sigma\omega^{\frac{1}{2}}C_{dl} + 1)^2 + \omega^2 C_{dl}^2 (R_D + \sigma\omega^{-\frac{1}{2}})^2} \qquad (3.31)$$

At low frequencies, when the effects of the double layer capacitance may be neglected, the impedance Z from equation (3.29) reduces to:-

$$Z = R_\Omega + R_D + \sigma\omega^{-\frac{1}{2}} - j(\sigma\omega^{-\frac{1}{2}} + 2\sigma^2 C_{dl}) \qquad (3.32)$$

The impedance tends to Z_w and a plot on the Argand diagram is a straight line of 45° slope (Fig. 3.2).

At higher frequencies, and with a fairly irreversible reaction, the concentration polarization can be neglected, and equation (3.29) reduces to:-

$$Z = R_\Omega + \frac{R_D}{1 + \omega^2 C_{dl}^2 R_D^2} - \frac{j\ \omega\ C_{dl}\ R_D}{1 + \omega^2 C_{dl}^2 R_D^2} \qquad (3.33)$$

Figure 3.3 shows the Sluyters plot. A semicircle is obtained arising from the behaviour of R_D and C_{dl} acting as a parallel resistance and capacitance, and shunted along the real axis from the origin by the ohmic resistance of the electrolyte and test leads (R_Ω). The diagram shows that R_Ω and R_D can be easily obtained from such an experiment. In addition, the double layer capacitance, C_{dl}, can be calculated, even in the presence of a redox system, using the frequency at the top of the semicircle:-

$$\omega = \frac{1}{R_D\ C_{dl}} \qquad (3.34)$$

At lower frequencies the diffusion polarization gives rise to a distortion of the semicircle. Figure 3.4 shows that a 45° slope is obtained at low frequency.

Fig. 3.3 Complex plane display - charge transfer control

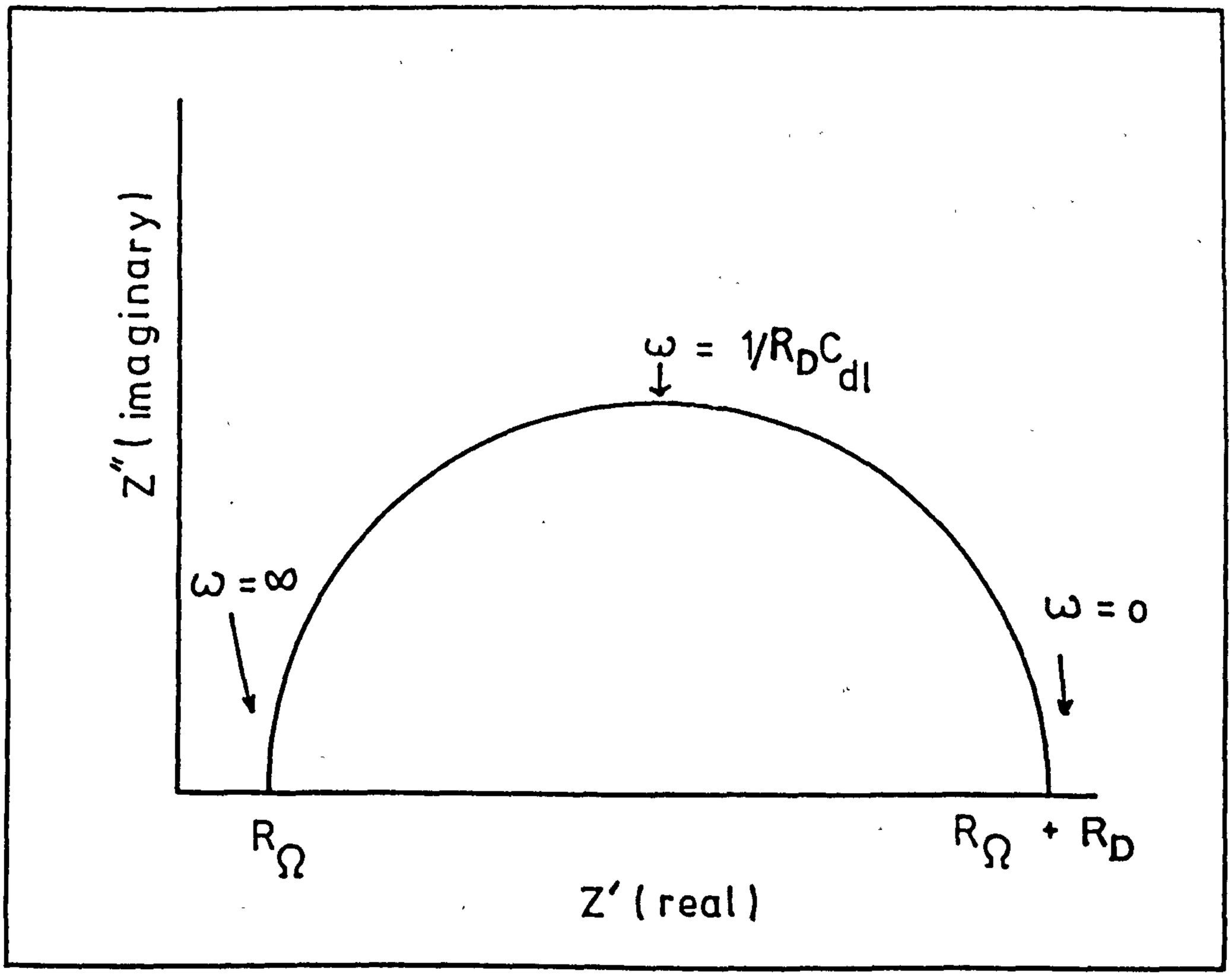

Fig. 3.4 Complex plane display - mixed control

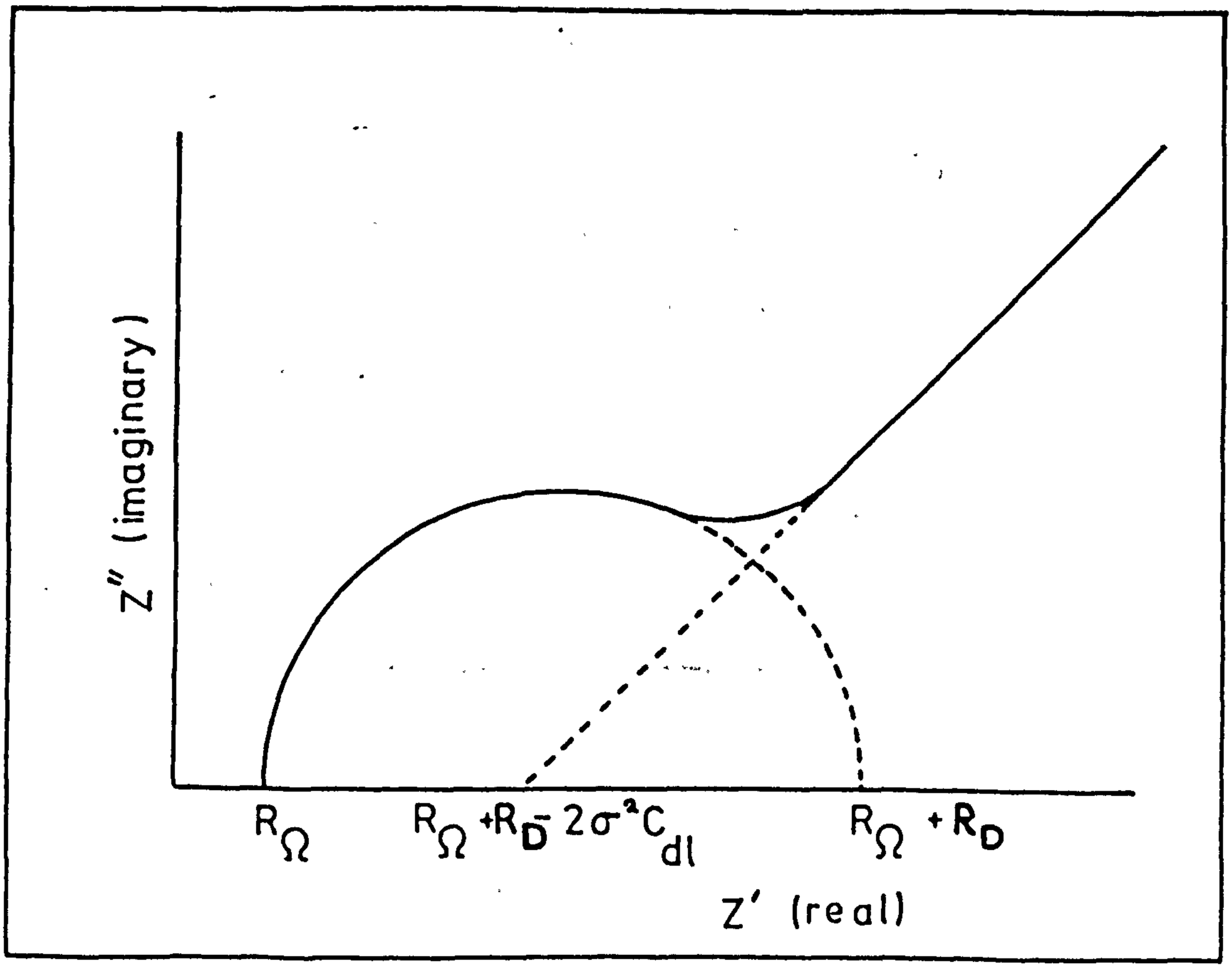

3.3.3. Practical Considerations

Many systems investigated by a.c. impedance techniques have shown deviations in behaviour from that expected from the Randles circuit (Fig. 3.1). The simple process has been extended to incorporate the effects of surface processes by Grahame[41], and more significantly by Sluyters[40]. Thus the adsorption of species is represented by incorporating extra resistances and capacitances in the electrode analogue, in effect shunting the double layer[42].

In a series of papers and reviews by Armstrong and co-workers[43-50] the discussion has been extended to complex reactions with adsorbed, and soluble intermediates, and to reactions with electrode dissolution, deposition and an active-passive transition. The impedance during nucleation and growth has also been considered. A number of impedance loci have been computed in each case, to show the interaction of the charge transfer resistance, double layer capacitance, and relaxation times for the various processes.

Impedance measurements have been made on complete cells[51,52]. The loci show gross changes occurring as cells are discharged. This means that it may well be possible to develop a state of charge test based on a frequency response experiment. Finally, the requirement for high surface area electrodes for storage cells means the modifications to the planar electrode behaviour are gross[18]. An extension of the existing theory would give a better understanding of commercial cells. Difficulties arise from the recognition that, in principle, for a planar electrode, the current lines are perpendicular to the surface, where for a porous electrode they are effectively parallel to it. A consequence of this is that the Warburg impedance for the porous electrode is dependent on terms proportional to $\omega^{-\frac{1}{4}}$ rather than $\omega^{-\frac{1}{2}}$ in equation (3.25). Similarly

the high frequency semicircle which cuts the real axis normally for the planar electrode, comes off at $\pi/4$ in the case of the porous one. A further interesting feature is the inductive behaviour observed at high frequencies for porous electrodes. Darby[53] showed that the inductive impedance arises when mass transfer, and electrochemical reactions can occur simultaneously over a distributed region of the electrode. Gutman[54] ascribed it to geometrical effects of the electrode pores. It was suggested that the inductive part of the frequency spectrum arose due to the time elapsed between the arrival of the signal at the mouth of the electrode pore, and its reaching the bottom.

CHAPTER 4

POROUS ZINC ELECTRODES - A REVIEW

4.1. Introduction

The electrochemistry of zinc has been the subject of a number of earlier reviews[55-60] and the importance of the metal as an electrode material in commercial cells has been emphasized. Zinc has a high exchange current density and a low eletronegativity (high cell voltage), and practical advantages such as low cost, low toxicity, and ease of fabrication. The reactions at solid zinc are complex, and its behaviour as a porous electrode more complex still. A large research effort continues in an attempt to preserve the desirable characteristics of the zinc electrode on oxidation, while producing an electrode that can be efficiently recharged many times. In this review the initial development of porous zinc electrodes is summarized, followed by a classification of the recent literature of the three main areas of investigation. These comprise the application of electrochemical techniques to investigate the primary oxidation process of porous zinc electrodes, the modelling of zinc pores and their behaviour, and finally measurements taken during the repeated oxidation and reduction of a complete porous zinc electrode.

The zinc electrode is most familiar as the (anode) can for the Leclanché cell, where zinc is used in solid form in conjunction with a $NH_4Cl/ZnCl_2$ electrolyte. The zinc readily dissolves anodically forming complex ions. In an alkaline electrolyte the cell performance can be limited, because the sheet zinc electrode has a tendency to passivate. The formation of oxide films results in the complete

concentration polarisation of the electrode during oxidation. Early attempts to solve the problem used finely divided zinc with the intention of reducing the current density at the anode surface, and the zinc powders were amalgamated with mercury, and compacted to form high surface area electrodes.

4.2. Surface Area Measurement

In order to make electrochemical measurements the area of the reacting interface must be known. The standard method for determining the surface area of a porous material uses the B.E.T. technique of nitrogen adsorption. Coates et al[61] compared this technique with that of methylene blue adsorption (M.B.I.). The change in concentration of the dye produced by the addition of a weighed sample of zinc to a known volume of aqueous dye solution was measured colourometrically. The area was calculated assuming monolayer coverage by molecules occupying 8.4 nm^2 (N_2 has a cross-sectional area of 0.162 nm^2). Electrodes with larger surface areas did not give proportionally improved anodic performance. The best correlation of the electrode polarization parameters was with the M.B.I. surface area, although the specific polarization rate associated with the early stages of oxidation was found to correlate better with the B.E.T. surface area. A qualitative explanation was advanced whereby the B.E.T. area was a measure of the true surface area, but this included all the micropores of the surface. The size of the methylene blue molecules did not allow them to penetrate into these micropores. On oxidation these pores were quickly blocked, and the surface area rapidly reduced to a superficial value. The true surface area determined the current-voltage relationship when the diffusion layer was thin, and subsequently the important area was that which was superficially accessible.

Myers and Marchello[62] noted that the double layer capacitance could be measured using an a.c. bridge technique, or by using a galvanostatic pulse current. They utilised the pulse technique to measure the capacitance of planar and porous zinc electrodes, and hence estimate their wet surface area. Measurements were made near the hydrogen evolution potential at -1.76V (S.C.E.) with a cathodic pulse to eliminate errors due to zinc dissolution. Values of roughness defined as the ratio of double layer area to geometric area were in the range 40 - 200 for electroplated porous zinc electrodes. Average pore diameters were calculated to be 0.05 - 0.10 cm. They concluded that the method was not suitable for electrolytes containing zincate ions, because of the faradaic currents resulting from the zinc deposition reaction.

The surface area wetted by electrolyte can be reduced by the inclusion of air bubbles in the porous electrode structure. Commercial electrodes are often vacuum impregnated with electrolyte to overcome this problem. Duperay et al[63] have pointed out that the wetted area may change during oxidation and reduction cycles, or corrosion on standing, due to hydrogen evolution expelling electrolyte from the electrode pores. In the zinc/air system hydrogen peroxide produced on the cathode is reduced on the zinc evolving hydrogen and oxygen. The hydrogen peroxide concentration is kept low by inserting a manganese dioxide membrane at a floating potential between the zinc and the air electrode, or by putting nickel oxide into the carbon cathode lattice.

4.3. Passivation and Primary Oxidation

Electrode passivation occurs when the electrolyte becomes blocked off from the electrode. This can be the result of gas evolution, film formation on the electrode, or precipitation of a non-conducting solid

from the electrolyte. Powers and Breiter[64] investigated the anodic passivation of zinc in alkali, and identified the formation of a duplex film. They described a film that they called Type I which was white, loose, and flocculant, and precipitated from a supersaturated zincate solution near the electrode surface. A coloured, compact Type II film was observed forming directly on the electrode surface rather than by precipitation, and Powers and Breiter held this responsible for passivating the electrode.

Anodic linear potential sweeps on zinc show violent current oscillations in the region of oxide formation. Powers[65] showed that the Type II film could act as a catalyst for hydrogen evolution at these potentials, and correlated the current oscillations with hydrogen bubbles mechanically dislodging parts of the passivating film. Hampson and Marshall[66] showed that passivation occurred at the time when the hydroxide ion concentration was reduced to just twice that of the Zn(II) in the supersaturated solution layers (i.e. when no further $(OH)^-$ is available to form $Zn(OH)_2$). McKubre and Macdonald[67] have made a rotating disc study of the electrode system. Current oscillations were correlated with a reducible concentration wave of soluble zincate in the electrolyte. The initial stages of passivation were postulated as $Zn(OH)_2$ precipitation from supersaturated zincate solution. This corresponds to a Type I film. Dissolution of an oxide film continues until the pH within the porous film is reduced to a value where ZnO is insoluble. The electrode passivates due to the formation of a surface (Type II) film, and the dissolution current decreases. Now the zincate concentration in solution declines and the pH increases redissolving Type I and Type II films. In the absence of a Type I film reactivation results initially in a current limited only by the rate of hydroxide migration, and the next cycle is initiated by $Zn(OH)_2$ precipitation.

This mechanism is consistent with the observations made by Katan et al[68], who reactivated thin layer zinc cells by the addition of small amounts of fresh hydroxide.

Hampson and co-workers[69,70] determined times for the galvanostatic transition between the active and passive states for planar zinc electrodes in vertical, and horizontal upward-facing orientations, and found the transition time for the vertical electrodes was considerably longer. Elsdale et al[71] determined times for similar transitions for porous zinc electrodes. Interrupted polarizations gave shorter transition times. It was concluded that the anodic process produced soluble zincate which slowly decomposed leaving a resistive film in the pores of the electrode making a large ohmic contribution to the total electrode overpotential. It was suggested that this ohmic overpotential was the major factor in determining the useful discharge life of a porous zinc electrode. Vertical and horizontal porous electrodes had similar transition times, and no abrupt transition from active to passive conditions was observed (cf Refs 69 and 70). This is consistent with the electrode reaction being driven deeper into the electrode as the discharging pores become blocked with oxide.

Breiter[72] has studied the anodic dissolution and passivation of vertical porous electrodes in 6M KOH + 0.25M ZnO. Potentiostatic current-voltage curves were recorded at a sweep rate of 1 mVs^{-1}, and the physical structures of the electrodes were examined optically. Comparison of results for smooth and porous zinc indicated that only a small fraction of the porous electrode interior participated in the electrochemical processes. The lowest parts of vertical electrodes of both smooth and porous zinc were found to be much less reactive than other parts of the electrodes. This was related to the hydrodynamic

flow pattern on the thickness of the diffusion layer. Repeated cycling of porous electrodes resulted in reduction of particle size, though this effect was diminished by amalgamation.

In a series of papers Karunathilaka et al[52,73-77] have applied the a.c. impedance technique to commercial cells containing zinc electrodes. The cells were galvanostatically discharged and the impedance spectra were recorded at the open circuit voltage at various states of charge over the frequency range 10 kHz - 1 mHz. Each cell component had its own impedance, but a single component dominated some spectra. An undischarged Leclanché cell gave the impedance spectrum of the zinc can. The impedance spectrum for the zinc can was also observed for partly discharged cells, where manganese dioxide additions had depolarised the carbon electrode[74]. New undischarged cells had a Warburg slope of 45° characteristic of a planar electrode[73], while this slope tended to 22.5° as discharging roughened the electrode[52]. Undischarged cells that had been stored also showed low angle Warburg slopes, and this was attributed to porosity developed by pitting corrosion. The Zn/MnO_2 and Zn/HgO alkaline cells examined also displayed a zinc dependent impedance in the early stages of discharge, and the porous electrodes used in these systems gave a Warburg slope of approximately 45° throughout virtually all states of charge[75]. This was interpreted as a quasiplanar reaction zone that originates at the outer surface of the electrode, and progresses into the porous mass as the reaction proceeds. Liu et al[78] have re-examined the galvanostatic oxidation transition times on planar electrodes. At low current densities a double passivation process has been proposed including a period of restricted hydroxide ion diffusion due to the formation of a porous oxide layer on the electrode. From these considerations it can be seen that planar electrodes can sometimes behave as if they were porous, with Warburg

impedances approaching those described by De Levie[18b] for semi-infinite pores, and porous electrodes may behave as if they were planar.

Nagy and Bockris[79] examined porous zinc electrodes that had been galvanostatically discharged. The current distribution was determined by chemical analysis of microslices of the electrode. The morphology of the reaction products was investigated using scanning electron microscopy, and a carpet-like structure was found suggesting a dissolution-precipitation mechanism. The pattern of current distribution in the porous electrode and its current density was explained on the basis of the duplex film model in which a thin, resistive, compact film formed beneath a porous oxide.

4.4. Pore Models

Katan et al[68] constructed a thin-layer cell (14 μm) to use as an experimental analogue of a single-pore zinc anode and cathode. Constant currents were applied and the progress of the reactions followed by optical microscopy. A thin, tightly adherent layer of oxidation product rapidly advanced over the anode beginning at the edge nearest the cathode. The dissolution-precipitation mode of ZnO formation was the predominant process eventually leading to passivation, with a primary penetration depth of 0.09 cm. Zinc dissolution sites formed with an initial density of 5.8×10^2 cm^{-2} during oxidation, forming pits which grew and merged, though less than 2% of the original surface initially participated in the reaction. S.E.M. examination of the precipitated ZnO showed it to have a needle-like microstructure with about 80% porosity, and a specific surface area of approximately 8×10^4 cm^2 cm^{-3}. Prior to passivation a white precipitate was formed filling the entire pore, with loss of $(OH)^-$ ion and consequent concentration polarization. Cathodic zinc dendrite

growth was found to be related to the presence of hydrogen bubbles producing areas of locally increased current density. The workers note that the applied current densities are rather high in terms of cross-sectional area of the pore, but point out that such conditions may arise at open areas during discharge after adjacent solid portions of the frontal area of a real porous electrode become blocked off by reaction product.

Spzak and Gabriel[80] investigated the dissolution-precipitation mechanism of ZnO formation by galvanostating a similar thin-layer cell pore analogue as used by Katan[68]. Spzak and Gabriel considered the $Zn(OH)_3^-$ ion a more important intermediate than the zincate ion. In excess electrolyte the $Zn(OH)_3^-$ ion readily complexes with a further $(OH)^-$ ion to give the zincate $Zn(OH)_4^{2-}$ ion. As the reaction proceeds the electrolyte becomes depleted of $(OH)^-$ ions, and the $Zn(OH)_3^-$ ion may complex with itself to form a dimer, and may continue to complex to form a macromolecule. Nucleation takes place when a macromolecule attains a critical size dependent on the ambient degree of supersaturation, and surface tension between such a particle and the parent phase. The effect of electric field on mass transport in the diffusion layer was considered negligable at moderate current densities, but may become significant and effect film morphologies at higher current densities.

Spzak, Gabriel and Katan[81] examined another zinc pore analogue during galvanostatic oxidation and reduction cycles. Fragmentation of dendritic clusters was observed on both the anodic and cathodic part of the cycles. On the anodic half-cycle it was suggested that fracturing may result from an anomalous current distribution, or from a non-uniform cross-section of metallic stems. On the cathodic half cycle fracturing requires a current reversal. Fragments of the order of 10^{-3} cm or less

were propelled through the bulk electrolyte. Initially the fragments move as though their surfaces are positively charged, but shortly after fragmentation the movement is in accord with a negatively charged surface. Fragments larger than about 10^{-3} cm are found to exhibit motion principally by displacement, generated by dissolution at one end and deposition at the other. The processes of fragmentation were advanced as a major contributor to zinc electrode shape change.

Yao and co-workers[81,82] constructed a novel porous electrode to measure the reaction distribution along a single pore. A photolithography method was used to produce a number of thin electrode plates (0.01 cm) with the pore pattern etched through each one with nitric acid. The photoresist films were used as insulators, and the electrode assembled by mounting the plates in a frame to align the holes. The current distribution was measured in early experiments by connecting a shunt resistor to each plate, and measuring the potential drop across each resistor. This method was improved in later experiments where operational amplifiers were used in a zero-resistance ammeter circuit, and the current passing through the individual segments was recorded sequentially using a 10-channel scanning-unit. Different current distributions were observed for the oxidation and reduction processes, the reduction current penetrating deeper into the pore than the oxidation current. On oxidation the initial penetration depth was 0.015 cm and decreased to 0.008 cm. Analysis of the high non-uniformity of the current distribution showed it was due to the $(OH)^-$ ion diffusion resistance. A model incorporating a surface blocking mechanism by compact ZnO was not completely satisfactory, and passivation may be due to pore-plugging by catalytic hydrogen evolution.

4.5. Secondary Zinc Electrodes and Shape Change

McBreen[83] has investigated the current and potential distribution over the surface of a square porous zinc electrode during constant current oxidation and reduction cycles. A segmented cadmium counter electrode with series shunts was used to determine the current distribution, while the potential distribution was measured using a number of Hg/HgO reference electrodes with the luggin capillaries spread out in an array over the back of the zinc electrode. Initially the current and potential distribution was relatively even. On reduction the segment currents tended to diverge with time, whereas on oxidation the currents converged. After about 15 cycles the upper portion of the zinc electrode began to polarize on reduction with a simultaneous drop in current. Eventually most of the current was being carried by the central and lower electrode sections. Post-mortem examination showed large areas at the top and peripheries denuded of zinc although the silver screen current collector remained completely intact.

McBreen identified this shape change as the limiting factor in the life of a secondary zinc electrode, and attributed it to the generation of concentration cells that transfer zincate from the plate edges to the centre in the early stages of discharge. In a cell with plane parallel electrodes the primary current distribution will be high at the plate edges since the current lines can pass outside the space between the electrodes. In early cycles more zinc is deposited at the edges than is deplated in the subsequent oxidation, the zincate concentration at plate edges rapidly decreases, and the electrode polarizes. After reduction the edge positions were found to have a more negative potential than the centre. The concentration gradient could be diminished by zincate diffusion from the centre, but McBreen

postulated that the equilization took place by dissolution of zinc at the electrode edges and deposition at the centre, since diffusion could not account for the rapid potential relaxation observed.

Choi, Bennion and Newman[84] proposed an alternative mechanism for shape change based on a mathematical model with a 1-dimensional convective flow parallel to the separator membrane, and went on to test their theory in a paper with Hamby[85]. The analysis postulates that zinc is redistributed by the coupling of zincate concentration changes with convective flow driven primarily by membrane pumping. The electrolyte, flowing upward toward the reservoir within a vertical porous zinc electrode during charging (reduction) is depleted of zincate; during oxidation the downward flowing electrolyte is supersaturated with zincate. The process is pumped by the osmotic and electro-osmotic effects of the membrane with a net result that zinc relocates from the upper to the lower portions of the electrode. The model suggests that shape change could be eliminated if this tidal convective flow could be suppressed.

Modified zinc-silver oxide cells were used for the experiments; one in which the rates of electrolyte flow could be measured, and a second designed to suppress convective flow along the longtitudinal axis of the electrode by sealing, making sure all components filled the available spaces, and operating with no head space. Constant current oxidation/reduction cycles were applied and the cell potential recorded. Measurements of flow rates and ZnO distribution were in agreement with those predicted by the model. Limitations on convective flow virtually suppressed zinc electrode shape change. However, the authors noted that this was not a practical solution to the shape change problem. Convective flow is an important factor determining the cell capacity

and high rate capability. Furthermore, steps to suppress convective flow may have detrimental side effects on the control of gas evolution.

Hamby and Wirkkala[86] carried out further experimental tests to verify the convective flow theory. A cell was built with an array of Hg/HgO reference electrodes to measure the potential distribution over the zinc electrode. In order not to disturb the flow regime in the cell, a flooded, non-vented reference electrode without head space was designed, and secured in the test cell in stainless steel holders. A pre-charged zinc counter electrode was used. This avoided confusion with phenomena associated with the silver counter electrode used in the previous work. Results indicated that the anodic performance of porous zinc flooded, non-vented electrodes with restricted convection was limiting. Oxidising to approximately 15% of theoretical capacity gave an average anodic overpotential that increased with the number of cycles. In contrast to McBreen's[83] observations for a cell with normal convection, Hamby and Wirkkala found no corresponding change in average cathodic overpotential. Passivation, lateral rather than longtitudinal shape change, and separation of metallic zinc from the current collector were considered as possible limiting factors in the anodic performance, but the data was insufficient to identify the failure mode for these electrodes. It was concluded that it was difficult to correlate the individual overpotentials with material redistribution.

In a second paper Hamby and co-workers[87] continued their investigations of concentration changes in porous zinc electrodes during cycling. A silver oxide counter electrode was used and the cells were cycled at constant current. An array of Hg/HgO reference electrodes was used as before[86]. Small volumes of electrolyte were withdrawn from various places inside the porous electrodes during cycling. The concentration

changes predicted by the convective flow theory were not observed, and potential measurements taken during cell operation did not correlate with values of the concentration overpotential calculated on the basis of the observed concentration changes. A movement of material from the electrode sides to the centre was found which again is not predicted by the theory. The reaction distribution on the zinc electrode, it was suggested, was dependent on the reaction distribution on the silver counter electrode. Current is produced at reaction locations near the centre of the silver initially, and they move out towards the electrode edges for complete formation of the monoxide, before divalent oxide formation begins at the electrode centre again. The results do not therefore give general information about the reaction distribution on cycled porous zinc electrodes.

Sunu and Bennion[88] proposed a third model for zinc electrode shape change based on concentrated ternary electrolyte theory. A highly non-uniform reaction profile was predicted with a very thin reaction zone near the electrode surface, which would accentuate the failure due to electrolyte depletion in the pores of the electrode, and result in a low discharge capacity. On repeated cycling the difference in anodic and cathodic reaction distributions causes the redistribution of solid zinc and zinc oxide. In a cell with no membrane separator 55% of the oxidised product would precipitate as ZnO, while the remaining half diffuses into the counter electrode compartment. This will lead to dendrite formation on charging. If a separator is used 95% of the zincate is retained in the zinc electrode compartment on oxidation. A number of failure mechanisms were postulated depending on electrode use. During oxidation 'genuine' passivation may occur due to surface films (at high rates), or failure may be the result of pore-plugging or KOH depletion. During reduction depletion of zincate or dendrite

formation may be limiting. On cycling, failure may be caused by zinc dendrite formation and short circuiting, shape change in the y-direction parallel to the electrode surface, redistribution of zinc in the direction perpendicular to the electrode surface, or by the accumulation of evolved gases. The authors note that a combination of factors may operate.

Experimental results[89] were in reasonable agreement with theory. A porous electrode of 1 mm thickness and 1 cm^2 cross-sectional area was used, and cut into sections for examination after cycling. A very thin reaction zone typically 0.2 mm was identified near the electrode surface. The mathematical model as stated considered passivation by precipitation of a type I film only. This model predicts potential-time curves similar in shape to those obtained by Elsdale et al[71] and Coates et al[61]. The abrupt increase in overpotential observed near the end of anodic oxidation in the present case was believed to be due to the formation of a type II passivating film. The type II film would be expected to form when the zinc surface becomes severely depleted of $(OH)^-$ ions.

Poa and Wu[90,91] have adopted a more pragmatic approach. Initial measurements were made on zinc-silver oxide secondary cells of an industrial type. The electrode arrangement in these cells was different from that reported by previous workers (reviewed above), in that a porous zinc plaque was sandwiched between two silver oxide counter electrodes. Cycled electrodes were sectioned and examined using S.E.M. The results indicated that the extent of shape change was directly affected by the rate of discharge and charge, and ZnO content of the electrolyte. Shape change was mitigated by adding a layer of non-woven fabric treated with $Fe(OH)_2$ to the edge sections of the electrode. The

iron complex lowers the hydrogen overpotential reducing the zinc plating efficiency at the electrode edge. It can also effect deposit morphology. Applying McBreen's[83] theory this would improve the uniformity of zinc materials on the electrode surface in the early stages of cycling, delaying the formation of concentration cells which lead to shape change. The extent of shape change was also reduced by increasing the thickness of separator at the electrode periphery. Orientation of the zinc electrode with respect to the Earth's gravitational field, and the method of electrode preparation have no apparent effect on shape change.

Later work[91] used a segmented silver oxide electrode with series resistors for current measurement, and an array of Hg/HgO reference electrodes. Fe_2O_3 was added to the edges of the separator of some cells. Shape change was explained as resulting from secondary currents arising from differences in polarization over the surface of the zinc electode, and the beneficial effects of an iron complex were demonstrated.

4.6. Amalgamation

Elsdale et al[71] noted that the potential for the Zn(II)/Zn electrode reaction was 400 mv more cathodic than the reversible hydrogen electrode. Brodd and Leger[92] have calculated that there is only a weak hydrogen-zinc interaction and zinc is essentially free from a chemisorbed layer of atomic hydrogen, and has a high hydrogen evolution overpotential. Even so, when zinc is left standing in alkali, appreciable amounts of hydrogen may be evolved, which will stop parts of the electrode reacting, when it comes to be anodically oxidised. Mercury is commonly added to raise the hydrogen evolution overpotential. It also breaks down the crystal structure of the zinc presenting an equi-potential surface to the electrolyte. Unfortunately amalgamation makes the electrodes more

toxic, and increases costs and fabrication time. Research continues to find a more suitable additive.

Gregory et al[93] investigated the rate of hydrogen evolution from porous zinc electrodes. The rate was found to decrease with the addition of lead or mercury to the zinc. Wagner and Himey[94] surveyed possible mercury substitutes, and found that PbO, Tl_2O_3 and CdO could be valuable. Keily and Sinclair[95] have been among workers to show that hydrogen evolution can be inhibited by the addition of tetraalkylammonium compounds to the electrolyte. Adsorption of the alkyl cation increases the hydrogen overpotential due to changes in the structure of the double layer. Conversely when anions are specifically adsorbed the hydrogen overpotential is decreased. McBreen and Gannon[96] have investigated the incorporation of various oxides of high hydrogen overpotential metals (HgO, Tl_2O_3, PbO, CdO, In_2O_3, In and Ga_2O_3) in pasted zinc electrodes. Some additives (e.g. $In(OH)_3$ and PbO) were thought to increase electrode polarizability, and decrease rates of shape change.

CHAPTER 5

EXPERIMENTAL TECHNIQUES

5.1. Electrolytic Systems

5.1.1. Electrolytic Cells

All cells were made from borosilicate glass fitted with P.T.F.E.-sleeved ground glass joints. The cells together with all glassware were cleaned by steeping in a 50:50 mixture of nitric and sulphuric acid for at least 48 hours, followed by thorough washing with tri-distilled water. Rubber bungs and tubing were boiled in tri-distilled water to remove any volatile substances.

A conventional 3-limbed cell (Fig. 5.1) was used for the rotating disc, linear sweep, and impedance experiments. The design enabled the passage of nitrogen through the cell in order to deoxygenate the electrolyte, and to pass nitrogen over the top of the electrolyte for long term experiments. White spot nitrogen was used which had been deoxygenated itself by passing through copper turnings at 400°C. The reference electrode was connected to the working electrode compartment via a Luggin capillary and a ground glass joint. The counter electrode compartment was separated from the cell by a coarse frit.

A cylindrical cell (Fig. 5.2) with a separate reference electrode arm and tap junction was used for the galvanostatic experiments. This was modified for later experiments to include a water-jacket connected via polythene tubing to a thermostat bath, so that the temperature could be regulated. The working electrodes were mounted at the bottom of the cell to form an upward-facing horizontal electrode with containing walls

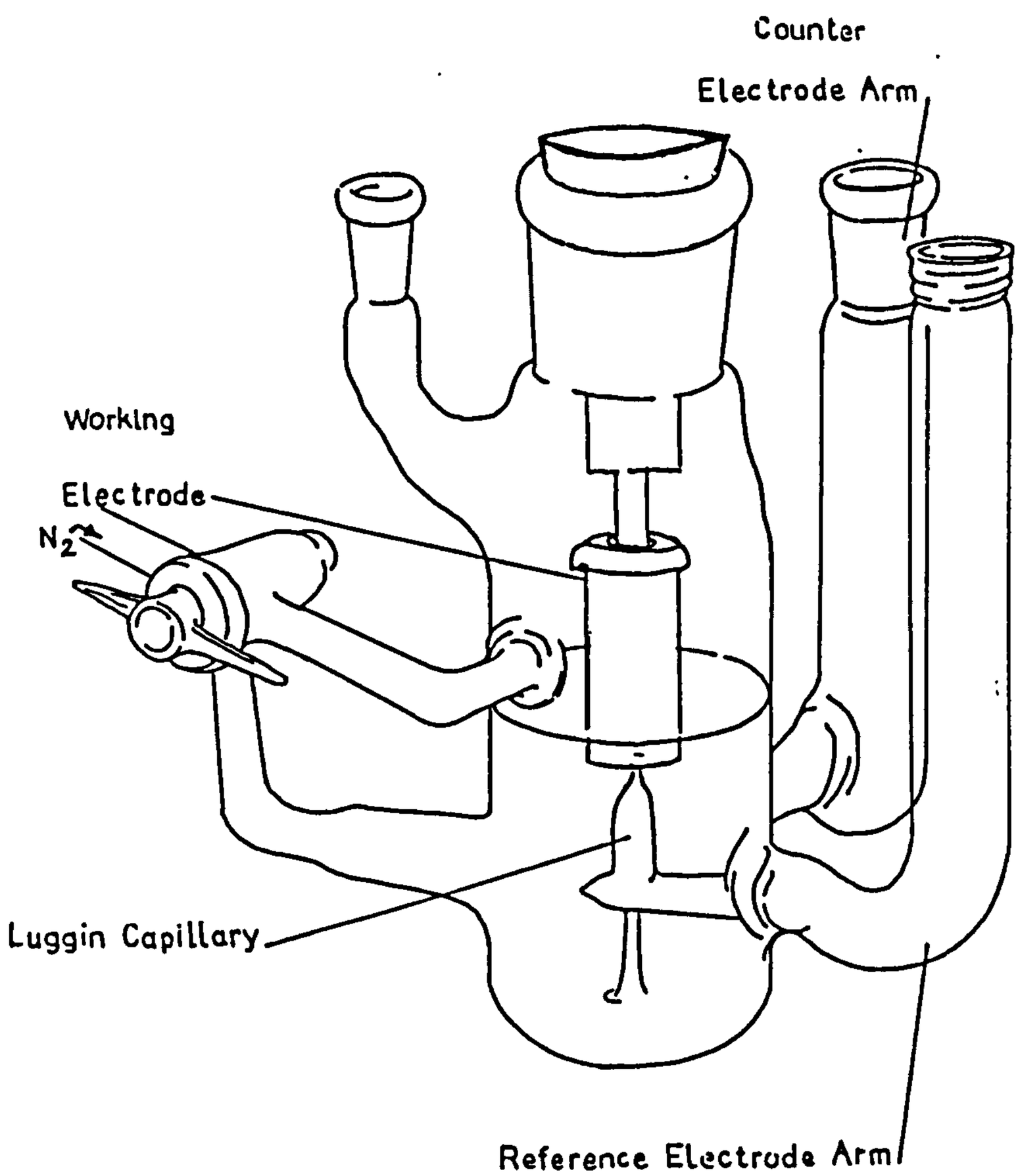

Fig 5.1 3-limbed Cell Used For Rotating Disc, Linear Sweep, and A.C. Impedance Experiments

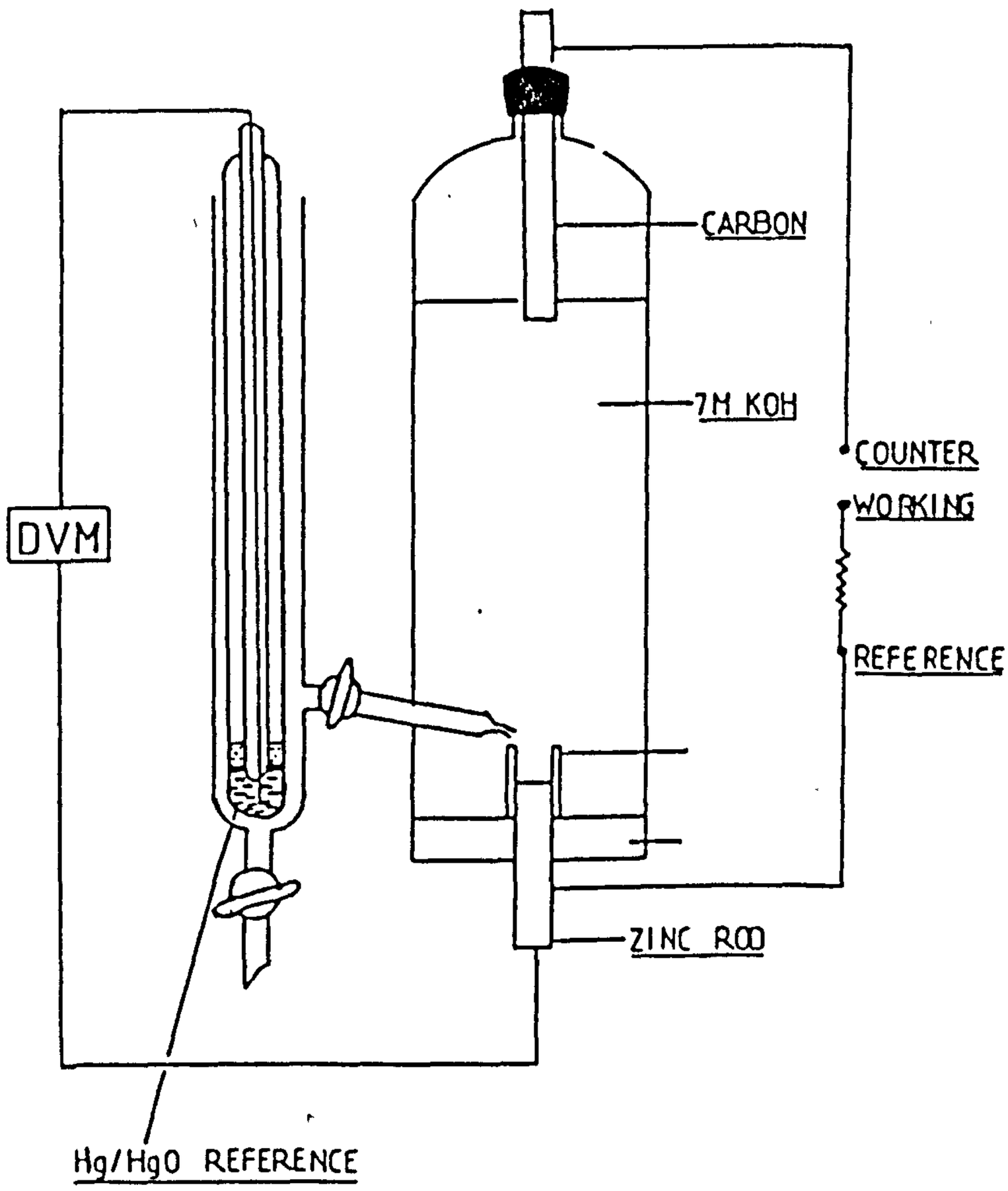

Fig 5.2 Cell Used For Galvanostatic Experiments

projecting vertically up into the bulk electrolyte. The counter electrode was mounted 15 cm vertically above the working electrode, while the Luggin capillary projected to just above the edge of the working electrode's containing wall.

The cells used to contain the cycling experiments (Fig. 5.3) were cylindrical with a flat bottom, and an arm to allow constant nitrogen purging. Nitrogen was passed through the copper turnings at 400°C then through a Dreschel bottle containing tri-distilled water, and a second containing 7M KOH. Exhaust gases were led through a further Dreschel bottle containing 7M KOH, and in this way the carbon dioxide levels in the electrolytes was kept to a minimum for several months. The cell lids were made from machined perspex with a rubber 'O'-ring to seal the cell. Five holes had been drilled in the top, two for reference electrodes, two for electrical connections and a fifth for the gas outlet. When a test cell had been assembled, it was finally sealed under vacuum with silicone rubber, and left for 24 hours before nitrogen purging commenced.

5.1.2. Working Electrodes

The planar working electrodes used throughout this work were made from zinc rods, (99.999% supplied by Koch-Light). They were machined and cut orthogonally to the long axis to expose a face of 0.3 cm diameter, (cross-sectional area = 0.071 cm^2), and set firmly in a P.T.F.E., shroud (Fig. 5.4). A stout spring was soldered to the back of the electrode, and the shroud screwed into a P.T.F.E., holder with a liquid-tight seal. The holder could be attached to a shrouded stainless steel shaft of a rotating disc assembly. Electrical contact was maintained via a mercury pool at the top of the shaft. The electrical resistance

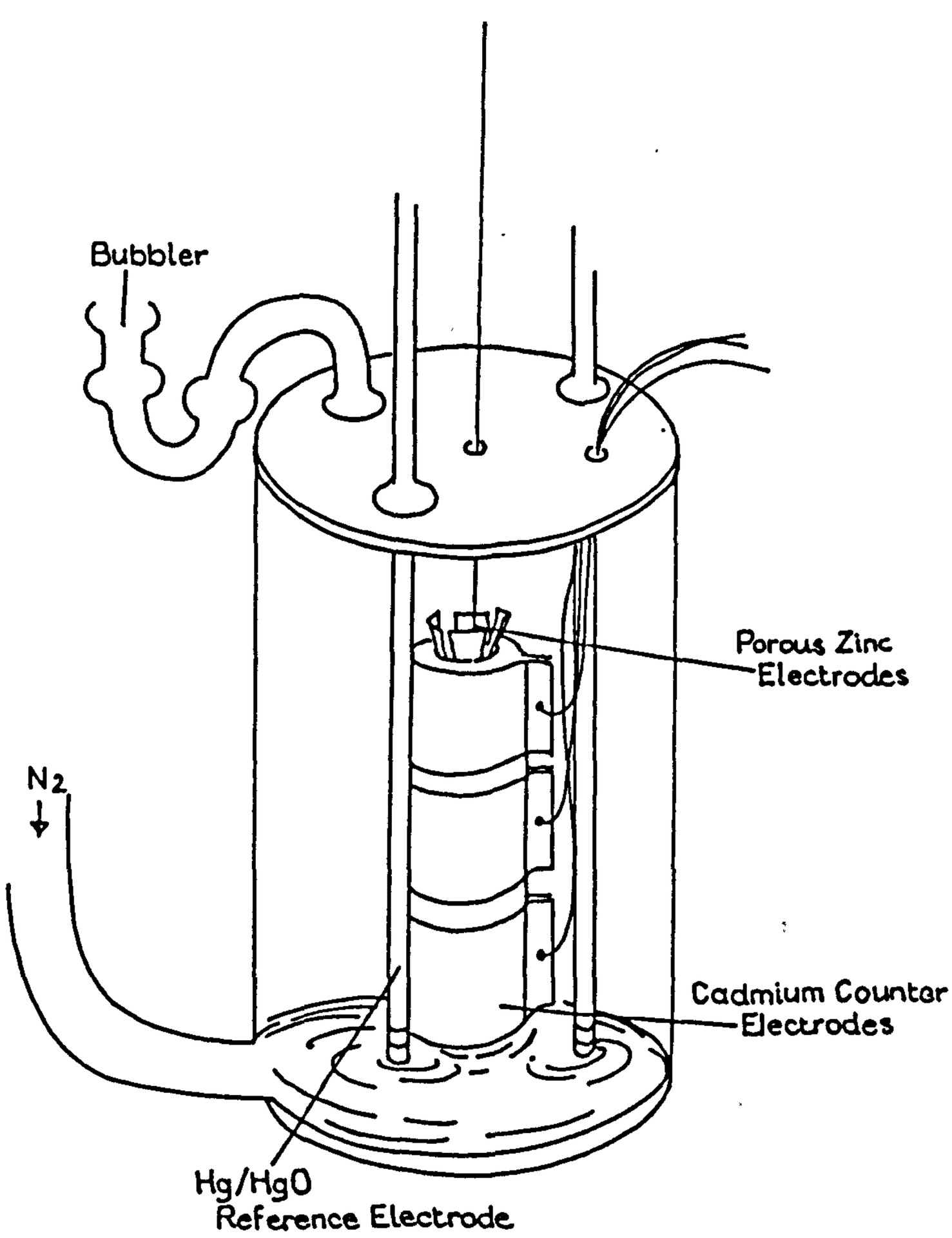

Fig 5.3 Cell Used For Electrode Cycling

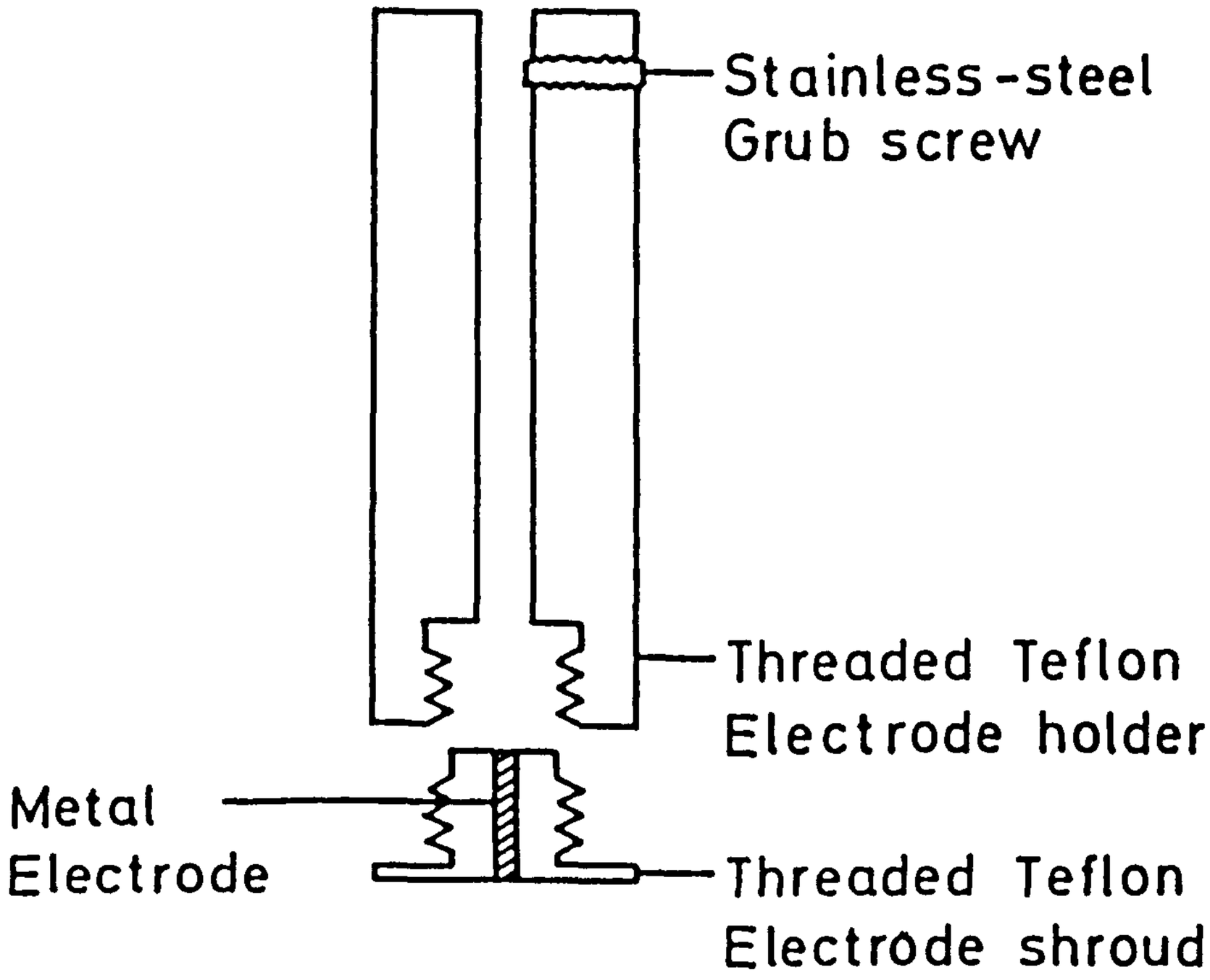

Fig 5.4 P.T.F.E. Rotating Disc Electrode Sheath

of this arrangement was less than 1Ω when rotating.

The set up was used for rotating disc, linear potential sweep, and impedance measurements. Generally a routine method of polishing and etching was used, but a more detailed study of the surface preparation was made using impedance techniques and is discussed in Chapter 6. The electrode was polished on various grades of SiC paper down to 1200 grade, then thoroughly washed in a jet stream of tri-distilled water, followed by acetone, then carbon tetrachloride, and was free from any traces of embedded SiC when examined with an optical microscope. It was etched in 50% HCl for 60 s at 600 r.p.m. and washed in tri-distilled water for 5 minutes whilst continuing the rotation. The electrode was put into the cell wet.

The electrodes used in the galvanostatic experiments were made from the same rod machined to 0.8 cm diameter (cross-sectional area = 0.503 cm^2). They were coated with epoxy resin and polished on SiC paper down to 600 grade, and finally on roughened glass, and were free from any traces of debris when examined with an optical microscope. The electrodes were then encased in polythene pipe (0.8 cm I.D., 0.1 cm wall thickness), so that the sides of the polythene projected about 0.5 cm above the front plane of the electrode. Replicate experiments could be made without removing the electrode from the cell by vigorous stirring on open circuit. The potential relaxation was followed, and depassivation was judged by a rest potential that was stable for at least 1 minute. A further 10 minutes was allowed before any experiments were resumed. Replicate experiments did not differ by more than 1% for the time of active dissolution.

Porous zinc electrodes were used in galvanostatic, impedance and cycling experiments. The materials were supplied by the Advanced Projects

Laboratory, Berec Group Ltd., (now Venture Technology), and included zinc amalgam (92% Zn : 8% Hg), carbopol (a modified carboxymethlycellulose), and "nickel-silver" wire, (an alloy of nickel and copper), as well as some commercial porous zinc gel electrode paste. A section of the nickel-silver wire was recast, and then machined to the dimensions of the zinc rod used in the galvanostatic experiments, and was similarly prepared. A 2 cm projection of polythene pipe was used for this electrode and the similar zinc rod electrode, and the cavity was partially fitted with commercial zinc gel, to form an electrode of constant cross-sectional area with a depth dependent on the amount of gel used.

A modified electrode holder as used with the rotating disc experiments but with a recessed planar zinc electrode was pasted with porous zinc gel. The impedance of the resulting porous electrode was measured in order to determine the surface area. The current distribution was measured along some other porous zinc electrodes during oxidative and reductive cycling. These electrodes are described fully later in this chapter.

5.1.3. Counter and Reference Electrodes

The counter electrode in the galvanostatic experiments was a pure carbon rod. In all the other experiments except the current distribution measurements a platinum gauze was used. For the current distribution measurements a sectioned cadmium/cadmium oxide electrode was used (see 5.3.2.).

Three types of reference electrode were utilised. In the acid and neutral solutions a wick-type calomel electrode (Beckman Instruments) with the electrolyte changed to saturated NaCl, (+ 0.236V vs. H_2 electrode), was used. In alkali a mercury/mercury (II) oxide electrode, (+ 0.97V vs.

H_2 electrode), was employed in the same electrolyte as the working electrode, except where stated. A more robust design of mercury/mercury (II) oxide electrode (Fig. 5.5) was used in the current distribution experiments. Figure 5.6 shows the potentials of some reference electrodes on the hydrogen scale. Potentials reported in this thesis are quoted against the appropriate reference electrode.

5.1.4. Electrolyte systems

Electrolyte solutions were prepared from AnalaR grade reagents where available, and tri-distilled water. Technical grade potassium silicate (B.D.H.), polymaleic acid (50% solution, molecular weight 800 - 1500, Ciba-Geigy), and carbopol (Berec Group Ltd.) were used where indicated.

5.2. Electrical Circuits

5.2.1. Galvanostatic Oxidation

The electrical circuit along with the experimental cell is illustrated in Fig. 5.2. A potentiostat (Kemitron PS-40) with a resistor between the reference and working electrode terminals was used as a constant current supply, with a separate circuit containing a y/t recorder (Bryans 27000) to monitor the potential of the working electrode.

5.2.2. Rotating Disc Studies

Potentiostatic control was obtained using a potentiostat (Kemitron PS-40) with a conventional 3-electrode system. The disc assembly was rotated by a G.E.C. motor generator controlled by an "in-house" control box with feed-back loop and L.E.D. display. The current was determined by measuring the potential drop across a 1kΩ counting resistor using a

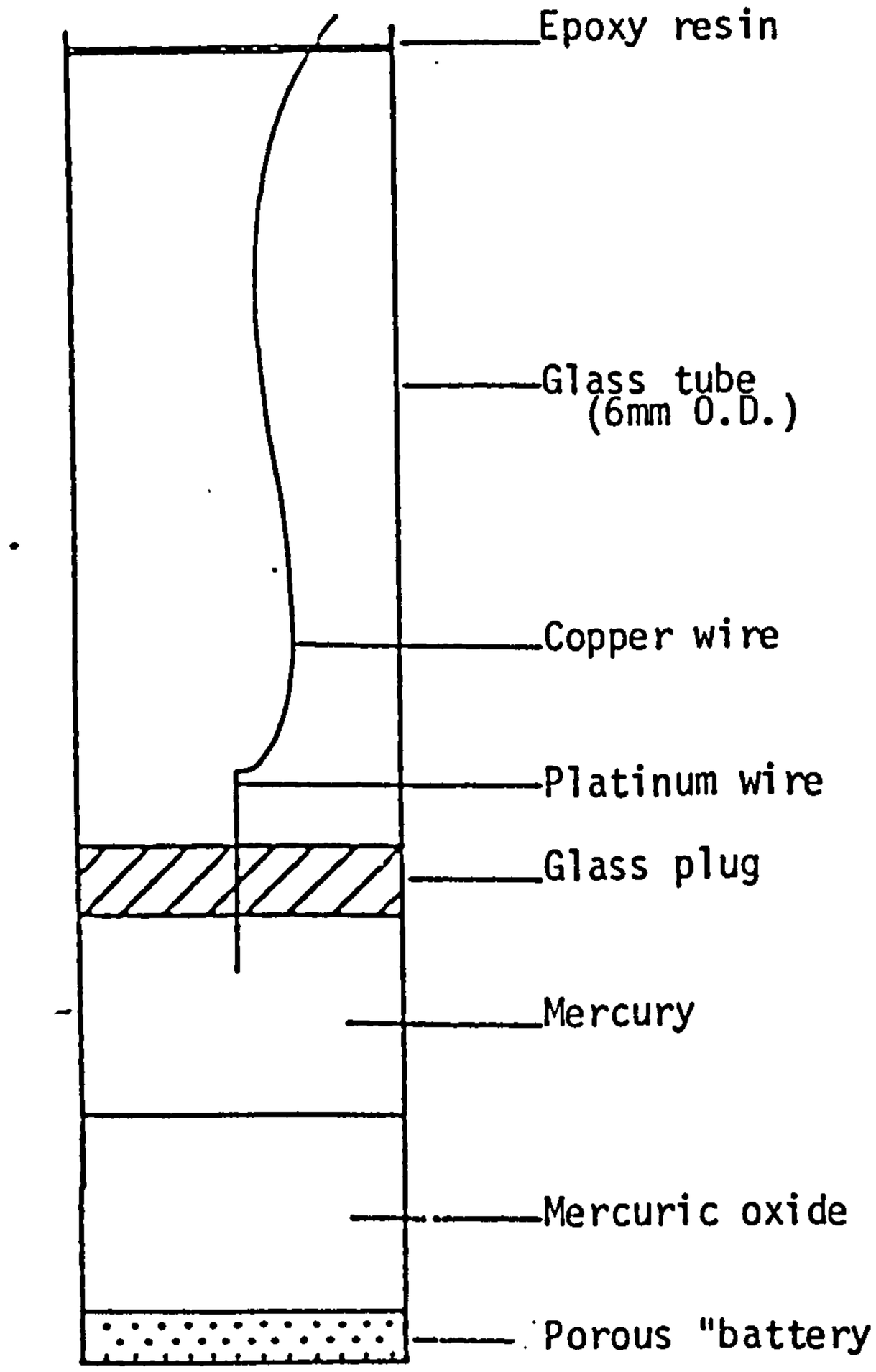

Fig 5.5 Hg/HgO Reference Electrode

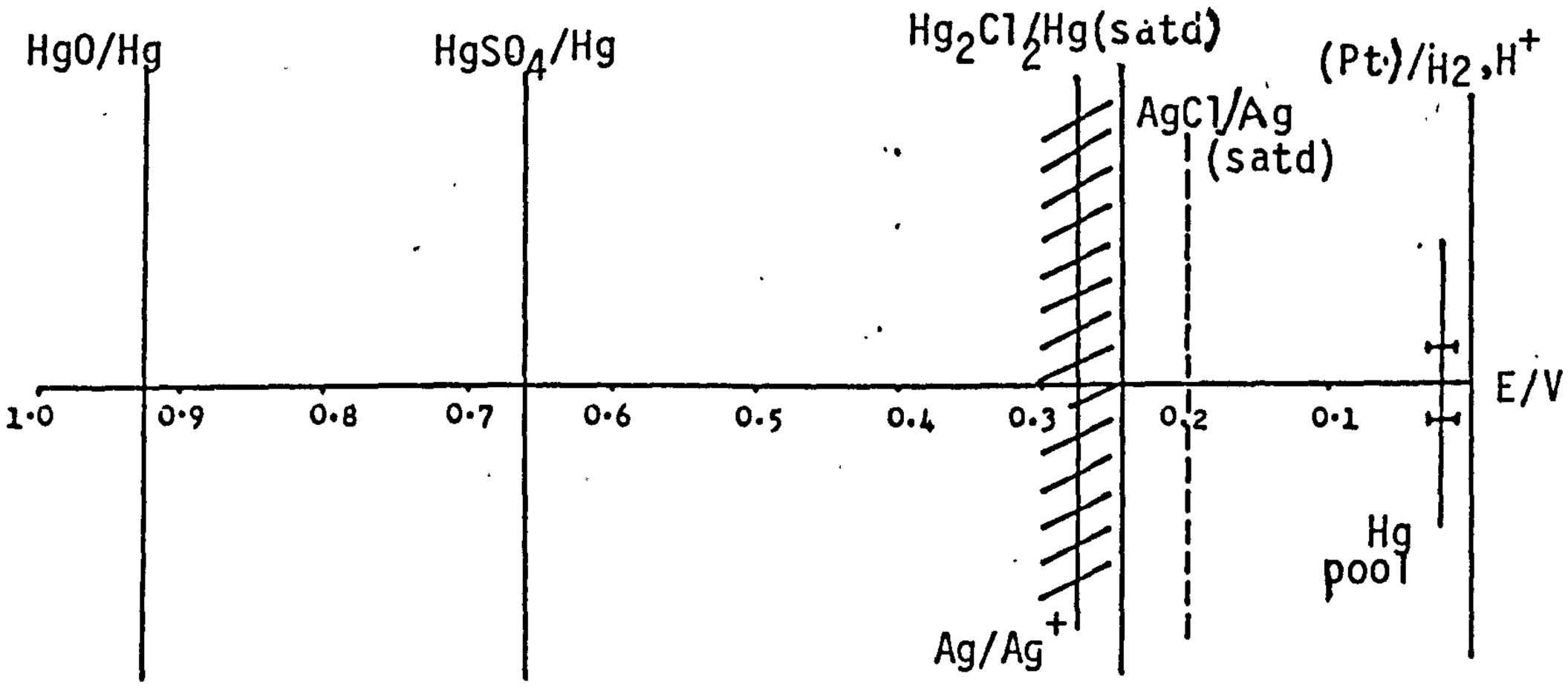

Fig 5.6 Reference Electrode Potentials On The Hydrogen Scale

digital multimeter, (Gould Advance DMM 7A) (Fig. 5.7).

5.2.3. Linear Sweep and Cyclic Voltammetry

Potentiostatic control was maintained using a potentiostat (Kemitron PS-40), and a function generator (Kemitron), in conjunction with an x/y/t recorder (Bryans 26000 A4) (Fig. 5.8).

5.2.4. Faradaic Impedance Measurements

A semi-automatic method was employed based on the Solartron 1170 Frequency Response Analyser (F.R.A.) with an 1182 Solartron Electrochemical Interphase to control the potential. The F.R.A. consists of a programmable generator which provides the perturbing signal, measures the response of the system, analyses the result with the aid of a correlator, and displays it.

The F.R.A. has the advantage of rejecting all harmonics present in the output of the system, and minimises the effect of random noise. The generator can be programmed to select a frequency and measure the response at that frequency, or more usually to scan through a range of frequencies from up to 10 kHz to 1 mHz. The instrument sequentially scans in either direction. The response at each frequency is averaged over a number of cycles, and then displayed in one of three possible notations : amplitude (A) and phase angle (ϕ) relative to the output signal, log (A) and (ϕ), or the real and imaginary parts of the impedance. The results are stored in a Solartron Data Transfer Unit, and may be printed out on a teletype printer or paper punch tape, and simultaneously plotted via a Solartron 1180 Plotter Interface and x/y recorder (Bryans 26000, A3). A schematic diagram of the experimental circuit is shown

Fig 5.7 Rotating Disc Electrode Circuit .

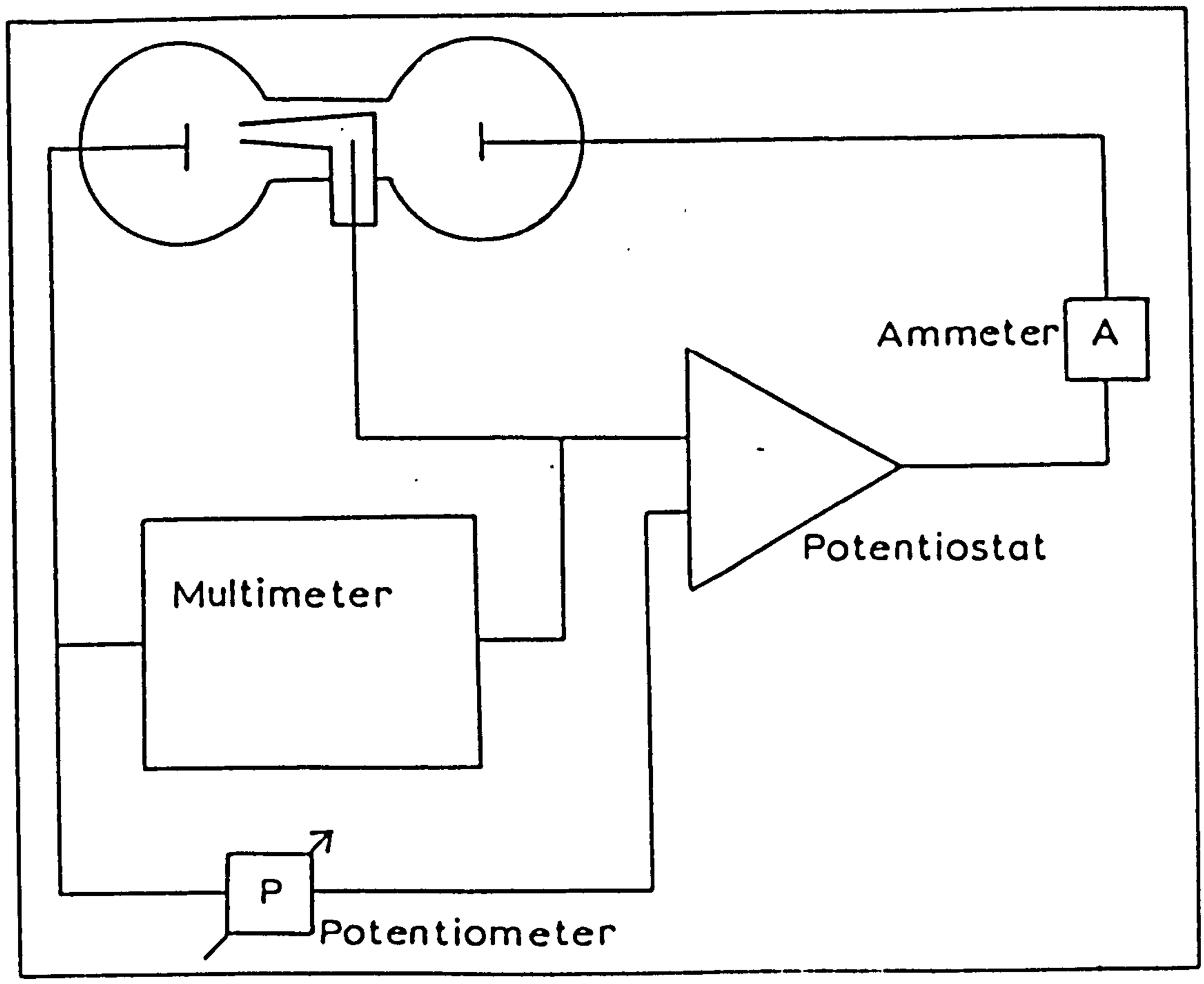

Fig 5.8 Linear Sweep Voltammetry Circuit

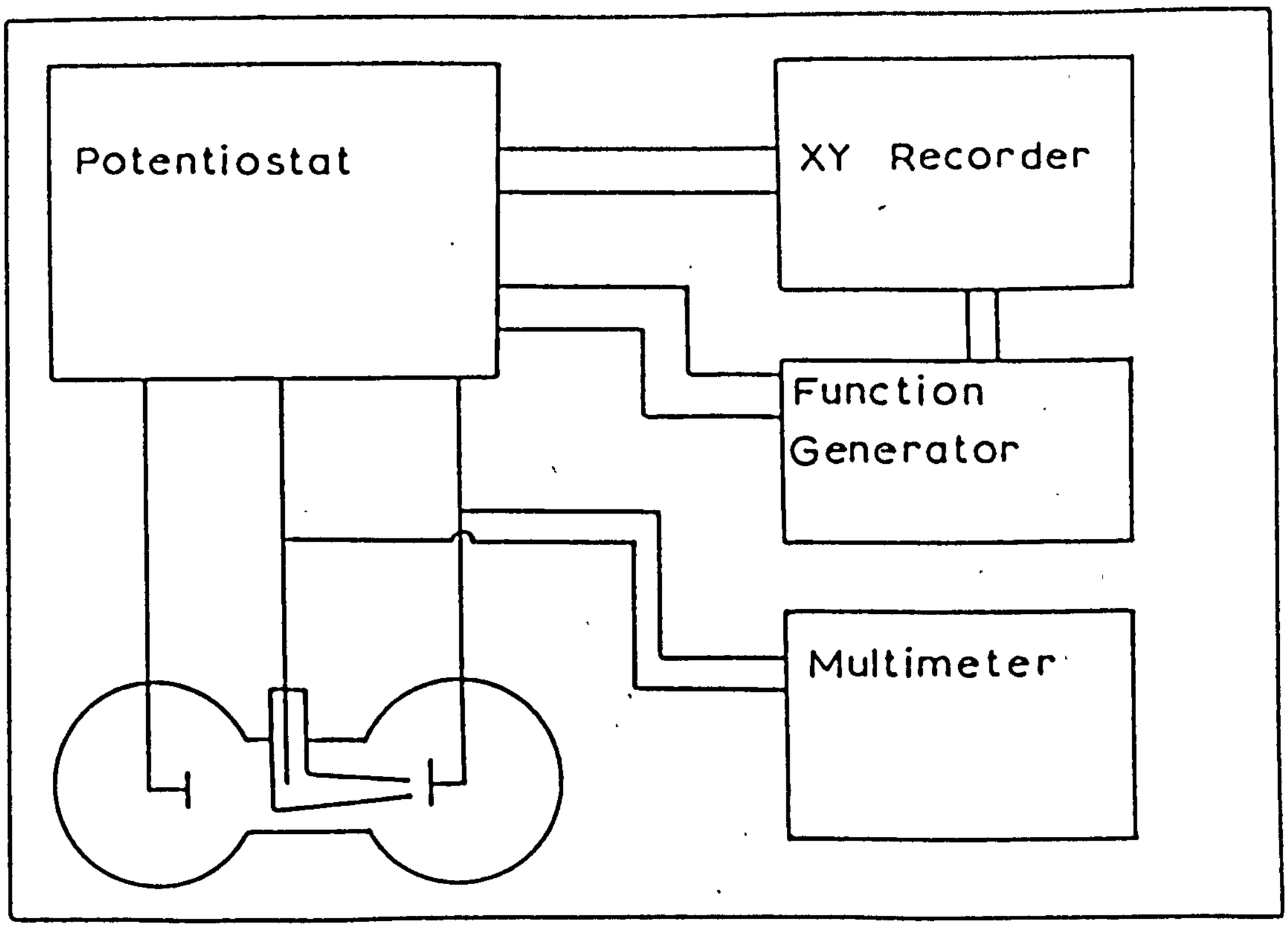

in Fig. 5.9.

The punch tape facility allowed the results to be fed into the PRIME 400 University computer. An interactive graphics terminal (TEKTRONIX) was then used to obtain the complex plane (Sluyters Plot) and Randles plots. Some of these plots were analysed to obtain a theoretical model.

5.3. The Development of an Electrochemical Cell to Investigate Characteristics of a Cycling Porous Zinc Electrode

5.3.1. Introduction

A zinc electrode will be an important component in all of the cheap, reliable, secondary power sources at present under consideration by the major companies. This section of the thesis describes a system which has been developed to investigate the cycling characteristics of a porous zinc electrode in situ.

Nagy and Bockris[79] had suggested three ways of approaching this problem:-

i) measuring the potential distribution along the electrode.

ii) sectioning the electrode and analysing the products of the reaction.

iii) measuring the current distribution directly using a sectioned counter electrode.

The first method has been criticized by the battery industry[97] since in the confines of a commercial cell the luggin probes can shield the working electrode. The second method is destructive allowing only one examination of the system. The third method allows in situ measurements to be made, and the system can be continuously monitored over any number of oxidation and reduction cycles. McBreen[83] has used this method to

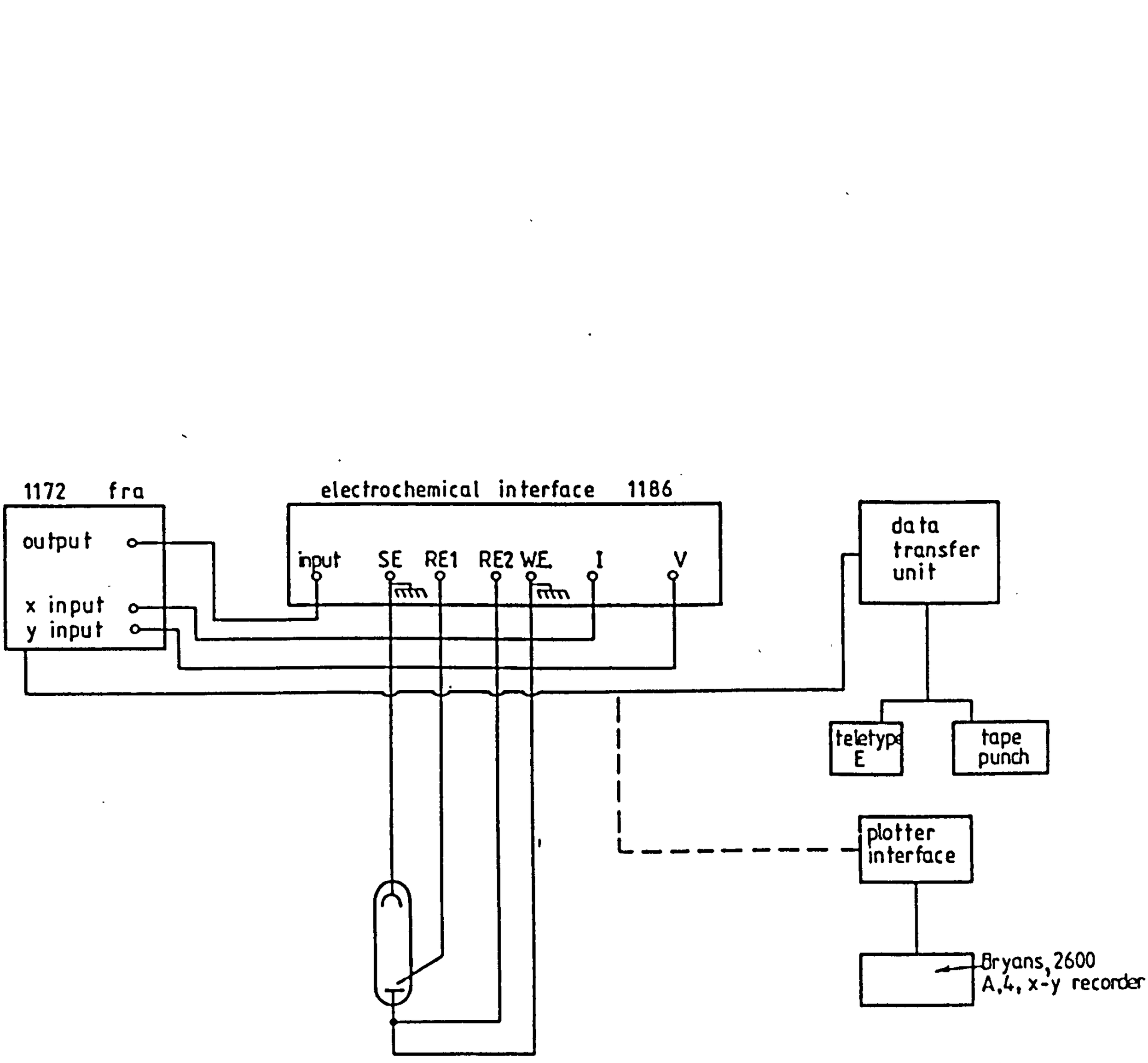

Fig 5.9 Cell Impedance Measurement System

detect shape change occurring on cycling a zinc electrode, and the technique has been developed by Poa and Wu[90,91].

The electrochemical cell used in the present study was a model of the R6 cylindrical cell and was itself the result of a long development programme. It was operated under the electrolyte starved conditions of the commercial cell, and required the construction of a segmented counter electrode consisting of a number of rings isolated from each other, so that each could act as an independent electrode to the zinc gel electrode that was to be injected into its centre. The shape and size of the rings was based on the LR6 size MnO_2/graphite ring. A suitable mix of materials had to be found that gave the rings good mechanical and electrical stability, and this needed to be encapsulated in such a way as to provide a good electrical contact to all parts of the ring.

5.3.2. Counter Electrode

Composition

A mix consisting of 95 parts CdO (B.D.H., 99.5%), 5 parts nickel powder (Inco 225) and 2 parts P.T.F.E. (L169 powder) was used. The CdO was sieved through a 220 mesh to remove the fine material, as this was found to flow during pressing and also produced a gradation in the pressed ring noticeable in appearance and strength. The mix was blended prior to pressing in a rotarory mixer, and 2.5 g was pressed at 12 tons (per square inch) pressure. The amount of P.T.F.E. was critical; too little producing a ring of low strength, while too much caused the mixture to "ball-up" into large particles.

Encapsulation

Nickel foil (Inco 100 μm) was cut to the same height as the ring, and shaped to give a close fit all the way around the ring and leave projecting tabs. The tabs enabled the foils to be clamped around the rings, and provided a point where electrical contact could be made with the test circuit. Electrical contact was improved using silver paint (Radio Spares) on the inner surface of the foil and the outer surface of the ring.

5.3.3. Cycling Tests

During the development of the rings the outer surface of the nickel foil was insulated using Fortolac (W. Canning). A test cell was assembled (Fig. 5.10), with a nickel screen positioned in the centre of the ring as a counter electrode. This was enclosed in a polythene mesh to stop evolved gases damaging the cadmium electrode. The mesh itself was enclosed by two layers of felted polypropylene separator with a grafted cellulose backing, so that the cellulose layers were adjacent. From the counter electrode therefore there was polythene mesh, felted polypropylene, cellulose, cellulose, cellulose, felted polypropylene, and CdO. The assembly was placed in a cell flooded with electrolyte. After allowing 48 hours for the electrolyte to permeate the pores of the CdO electrode, it was reduced galvanostatically for 5 hours, then oxidised for 5 hours using two power supplies (Coutant). The power supplies were connected through a pair of mechanical timers (Crouzet) allowing the oxidation and reduction cycle to be repeated automatically (Fig. 5.11).

The first rings to be cycled in this manner highlighted two problems with the proposed system:-

i) Loss of capacity on cycling. This was probably due to loss of

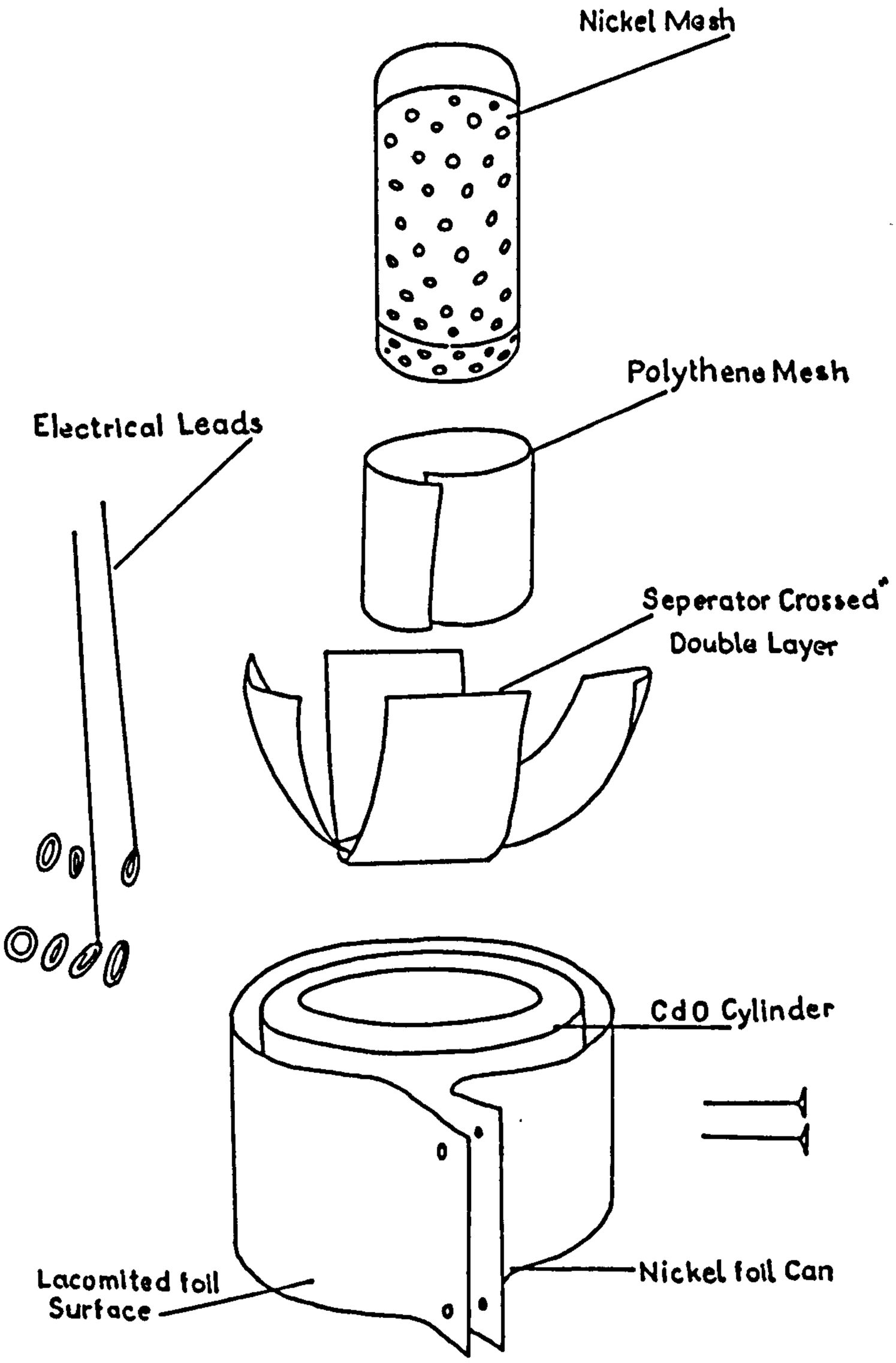

Fig 5.10 Cadmium Ring Counter Electrode Construction

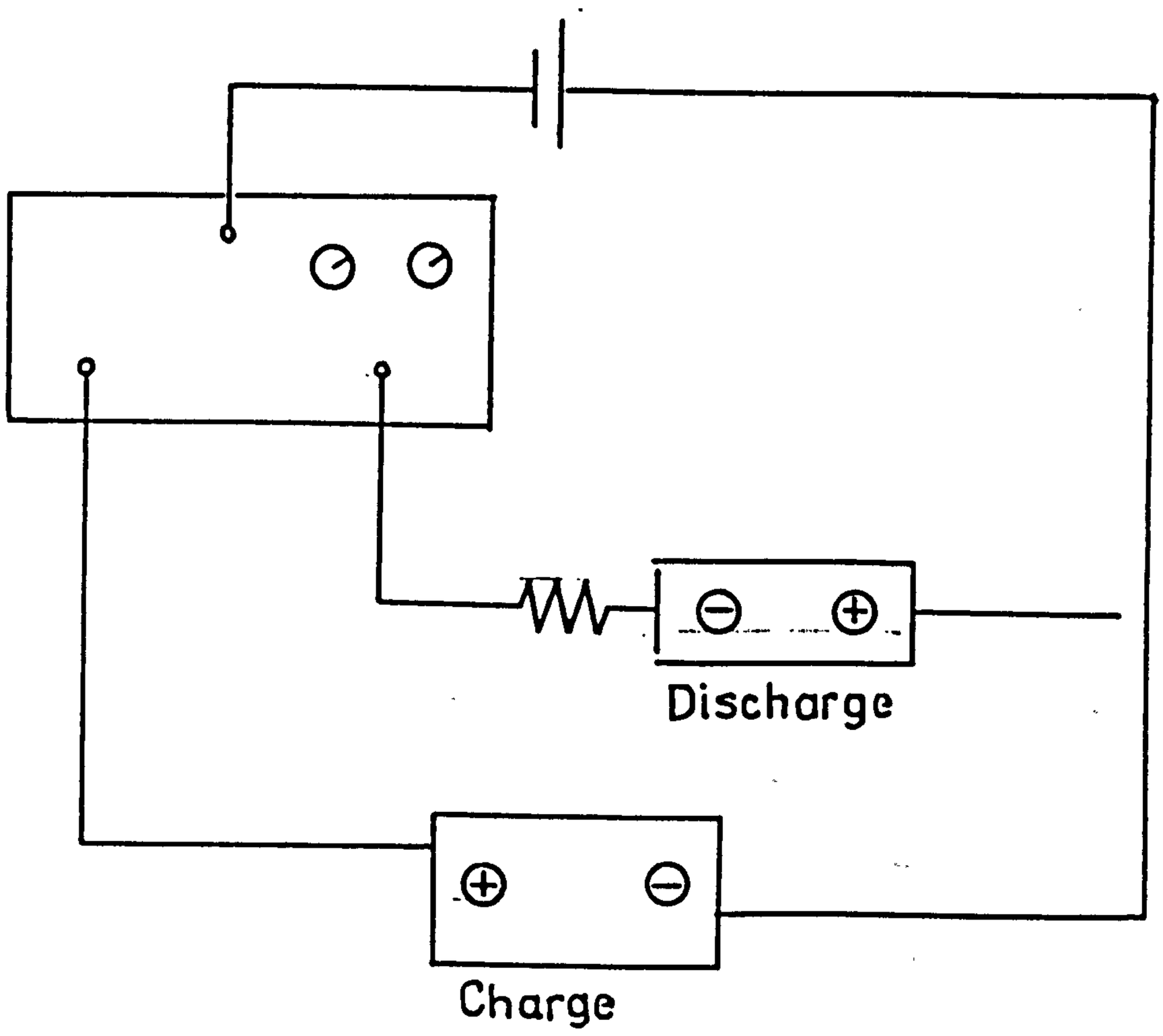

Fig 5.11 Cycling Circuit

material. Nickel hydroxide (B.D.H. G.P.R.) was added to the mix in the proportion 0.17 g nickel hydroxide to 1 g cadmium oxide to improve the mechanical integrity of the rings.

ii) Dendrite growth of cadmium extended from the ring edges resulting in short-circuiting. This was countered using polythene washers (0.5 mm thickness) cut from 9 mm bore tubing, and araldited at the top and bottom of each ring.

Stacked Electrode Systems

Rings incorporating all the necessary modifications were constructed. A perspex tube (14 mm internal diameter) was cut into 6 cm lengths, with a longtitudinal slot 1 mm wide cut along one side. This enabled the rings to be accurately stacked on top of each other. The polythene washers formed an isolating junction between two electrodes. A 3-electrode stack was used throughout (Fig. 5.12). The individual electrodes were sealed into the tube using epoxy resin and the entire assembly was allowed to set for 48 hours. The crossed separator, polythene mesh and counter electrode were added as before, and the assembly placed in a cell flooded with electrolyte for a further 48 hours. Hg/HgO reference electrodes were added.

Each electrode was individually reduced galvanostatically at 100 mA for 5 hours. A number of oxidation/reduction cycles were necessary before the individual cadmium electrodes were connected up as a single counter electrode. The 3-electrode stack was cycled at 300 mA for a 10 hour complete cycle, and one electrode ring would often carry nearly all of the current if the individual cycling had been omitted. A test 3-electrode stack completed 90 cycles without failure.

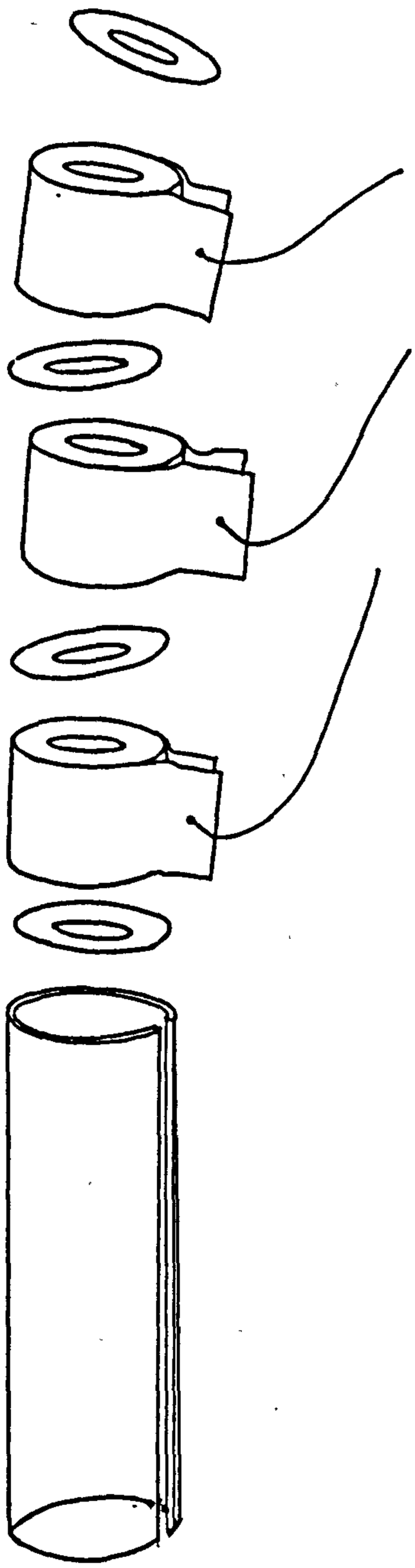

Fig 5.12 Counter Electrode Stack Assembly

After several test cycles the central counter electrode and separator was replaced by fresh separator containing porous zinc electrode. A nickel-silver wire was positioned along the longtitudinal axis of the zinc as a current collector. All of the electrolyte except a few cm^3 was emptied from the cell. The bottom of the perspex tube was sealed using a plastic battery cap with battery separator acting as a wick. Another 48 hours was allowed before the zinc electrode was oxidised. The automatic cycling circuit was again employed.

Each ring was connected to a small shunt resistor, (constantan wire 20 s.w.g.), and the current was determined by measuring the potential drop across each resistor using the Solartron Compact 2 data logging system. The voltage inputs were connected to the cam-block terminals of a 50-channel head unit (LU 1976). A digital clock unit (LU 1963) measured the real time, while a scanning control unit (LU 1975) was set up to receive a pulse from the clock at 10 minute intervals to initiate a scan. The scanning unit then threw relays in the head unit to present the digital voltmeter (LM 1426) with the first selected channel. The potential difference was determined and relayed to the printer drive unit (LU 1966) that sent a coded pulse to the Addo-X printer. The printer returns a pulse that enables the scanning unit to proceed, and give a sequential scan of the desired channels. Scale selection is via a diode plug-board, and patch-board on the front of the head unit. Channel selection is via the scanning unit, or patch-board, or plug-board, and the scan rate can be selected on the scanning unit. The results were processed on the University computer.

CHAPTER 6

THE OXIDATION AND PASSIVATION OF PLANAR ZINC ELECTRODES IN KOH

6.1. Introduction

Commercial cells use complex electrolytes with porous electrodes, and expanders. In order to build up an understanding of commercial zinc electrodes the contribution of each of these factors has been examined, and is reported in the following chapters. This chapter deals with the simplest case, with a planar zinc electrode in a KOH solution. The interaction between zinc and the hydroxide ions is of primary importance in zinc-alkali systems, and linear sweep voltammetry, rotating disc, and a-c impedance techniques have been employed to examine the kinetics and mechanism of the oxidation reaction. Linear sweep voltammetry was combined with rotating disc experiments to investigate the cathodic peak observed on the return sweep in the cathodic direction, following electrode oxidation. The relationship between anodic current density, hydroxide ion concentration and time to passivation was investigated using the galvonostatic method.

6.2. Experimental

Electrodes were made from zinc rod, (Koch Ligh, 99.999%). Their preparation, and pretreatment has been described in Chapter 5. Electrolyte solutions were made up by dissolving KOH pellets (Fisons A.R.) in tri-distilled water. Linear sweep voltammograms were recorded in 7M KOH between -1.7V and -0.7V versus the Hg/HgO reference electrode, with the initial sweep in the anodic direction. Sweep rates were in

the range 1 - 300 mV s^{-1}. Rotating disc experiments used 7M KOH also, in the potential range -1.375V to -1.260V against Hg/HgO electrode. The impedance measurements were made in 7.44M KOH over a frequency range from 10 kHz sweeping down a logarithmic scale to 6 mHz.

6.3. Results and Discussion

6.3.1. Galvanostatic Oxidation and Zinc Passivation

The constant current oxidation of a planar zinc electrode resulted in a characteristic anodic transition time dependant on the applied current density. The anodic transition was indicative of electrode passivation. The time t, taken for passivation was measured from the start of polarization to the abrupt change when the potential rose to that for oxygen evolution. The determination of the true transition time used the method of measuring from the start of the experiment, to the time indicated by the intersection of lines drawn as extensions of the active dissolution curve, and the process transition curve[98]. Figure 6.1 shows the passivation times t, for solutions of KOH and mixtures with KF, correlated with current density i, in the form

$$i = k\, t^{-\frac{1}{2}} + i_L \qquad (6.1)$$

k is a constant

i_L is the limiting current density below which the electrode will not passivate.

The results in KOH solutions are in good agreement with established data[64,69]. The linear relationship of current density with $t^{-\frac{1}{2}}$ is indicative of a diffusion controlled process. Hampson et al[70] have shown that a similar expression to (6.1) holds for vertical electrodes,

FIG. 6.1 Passivation time-current density relationship plotted as i versus $t^{-\frac{1}{2}}$. Zn electrode in KOH. 23°C.
△ 7M KOH; ▲ 13M KOH; O 13M w.r.t. K^+, 7M w.r.t. OH^-, 6M w.r.t. F^-.

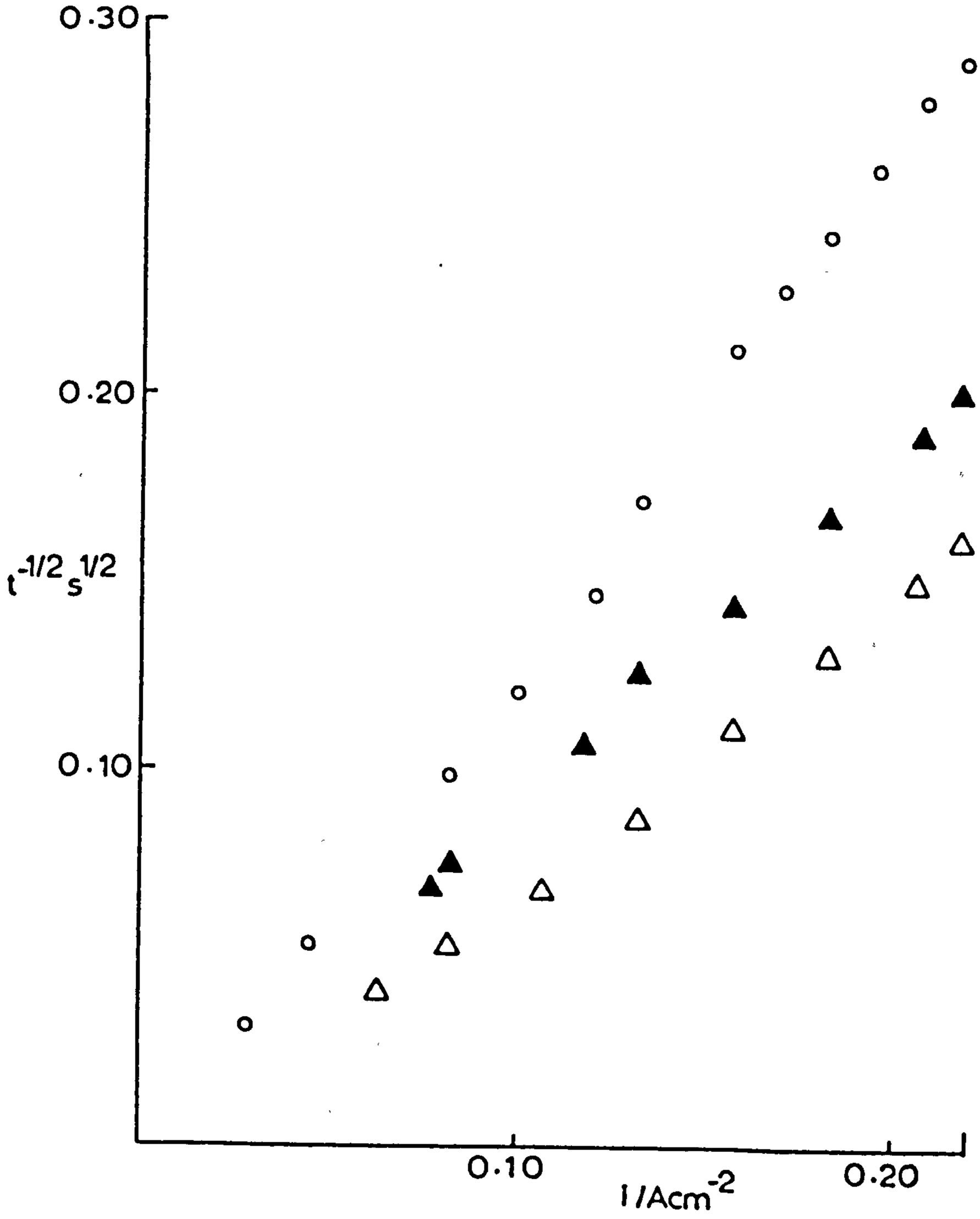

where there is a considerable contribution to mass transport from convection. The value of the limiting current i_L, can be determined by extrapolating to infinite time, and is greatly increased under convective conditions. In these experiments the small values of the limiting current indicated that convection had been suppressed (Table 6.1).

Hampson et al[99] have shown that the value of k is given by

$$k = \tfrac{1}{2}\, nFA(\pi/D)^{\frac{1}{2}}\, \Delta C_i \qquad (6.2)$$

where ΔC_i is the critical concentration gradient (measured in moles cm^{-3}) leading to passivation. The term k is a measure of the rate of dissolution, and the reaction is controlled by the electrolyte solution conditions alone. Figure 6.2 compares the results of the present study with those of an earlier investigation[69]. A maximum in the region 8.5 - 9M KOH is confirmed.

Calculation shows that most of the water molecules are used in ionic co-ordination spheres in 7 molar solution. At higher concentrations there is competition for solvating water. According to Falk and Salkind[100], the electrolyte conductance goes through a maximum about 7M KOH, and the activity coefficient increases rapidly at concentrations above this value. At concentrations below 7 molar, the reactivity of the Zn-KOH system increases with increasing hydroxide ion concentration. Above 7 molar solution the reactivity passes through a broad maximum then tails off. If water is required to hydrate the zinc dissolution reaction product, then the tailing off of the reactivity at high solute concentrations can be explained.

Dirkse and Hampson[101,102] have proposed a mechanism for zinc dissolution that requires hydrating water molecules.

TABLE 6.1

[KOH]	i_L*(mA cm^{-2})	i_L**(mA cm^{-2})	i_L***(mA cm^{-2})
1	0.52	8.8	-
2	0.21	49.0	-
3.5	1.49	74.0	-
5	0.19	84.0	-
6.5	0.12	-	-
7	-	-	15.5
8	0.60	-	-
9	-0.69	-	7.7
10	-0.08	-	-
11	-	-	6.2
12	-0.92	-	-
13	-	-	0.8
13.8	0.21	-	-

* Ref 69

** Ref 70

*** The present study

$$Zn_{kink} + OH^- \longrightarrow Zn_{ad}\,OH^- \qquad \text{(v. slow and atom diffusion with } OH^-\text{)}$$

$$ZnOH^-_{ad} \xrightarrow{\text{slow}} Zn(OH)_{ad} + e$$

$$Zn(OH)_{ad} + OH^- \longrightarrow Zn(OH)_2 + e$$

$$Zn(OH)_2 + 2OH^- + 2H_2O \xrightarrow{\text{fast}} [Zn(OH)_4.2H_2O]^{2-}$$

Bockris et al[103], on the other hand, found no evidence of pseudocapacitance indicative of an absorbed species, and suggested the alternative mechanism:-

$$Zn + OH^- \longrightarrow Zn\,OH + e$$

$$ZnOH + OH^- \rightleftharpoons Zn\,(OH)^-_2$$

$$Zn(OH)^-_2 + OH^- \longrightarrow Zn(OH)^-_3 + e$$

$$Zn(OH)^-_3 + OH^- \rightleftharpoons Zn(OH)^{2-}_4$$

which would show no water dependance. Dirkse[104] in a recent paper supports the Hampson/Dirkse mechanism but concedes that his results only apply to the equilibrium situation.

The fluoride ion is isoelectronic with the hydroxide ion, and might be expected to have a similar ion atmosphere. Dirkse and Hampson[105] showed that the fluoride ion required the same amount of water as the hydroxide ion for solution. It is the logical replacement therefore, in order to study the effects of water in the zinc dissolution reaction. The present study compared the dissolution rates at constant ionic concentration. Figure 6.1 shows that the reactivity is greatest for 7M KOH, 13M KOH is less reactive, and when 6 moles of KOH are replaced by 6 moles of KF then reactivity is

further reduced. Figure 6.2 and Table 6.2 show this comparison with the mixed electrolyte system over a range of concentrations.

TABLE 6.2

Zinc passivation data correlated in the form $i = kt^{-\frac{1}{2}} + i_L$

Solution	k (A $s^{-\frac{1}{2}}$ cm^{-2})	i_L (A cm^{-2})	Correlation coefficient
7 M KOH	1.2827	0.0155	0.9990
9 M KOH	1.3222	0.0077	1.0000
11 M KOH	1.2406	0.0062	1.0000
13 M KOH	1.0869	0.0008	0.9990
9 M K^+, 7 M OH^-, 2 M F^-	1.0712	0.0085	0.9990
11 M K^+, 7 M OH^-, 4 M F^-	0.0877	0.0112	0.9999
13 M K^+, 7 M OH^-, 2 M F^-	0.0789	0.0081	0.9982

Thornton and Carlson[106] have investigated similar mixed electrolyte systems, and have found that the conductivity is lower in the solutions containing KF. This is not surprising as the presence of F^- would tie up free water in its ion atmospheres, and drastically reduce the transport number of the hydroxide ion. From the present study it can be concluded that the amount of free water and hydroxide ion concentration are both important in the active dissolution of zinc.

6.3.2. Linear Sweep Voltammetry

(a) On a Stationary Electrode

Figure 6.3 (a & b) show the anodic and cathodic potential sweeps on a stationary zinc electrode in 7M KOH at a sweep rate of 1 mVs^{-1}.

FIG. 6.2 k from $(i - i_L)t^{\cdot\frac{1}{2}}$ = plotted against concentration for various systems.

O KOH solutions reported by Hampson and Tarbox.

▲ KOH; △ solutions 7M w.r.t. KOH with KF additions.

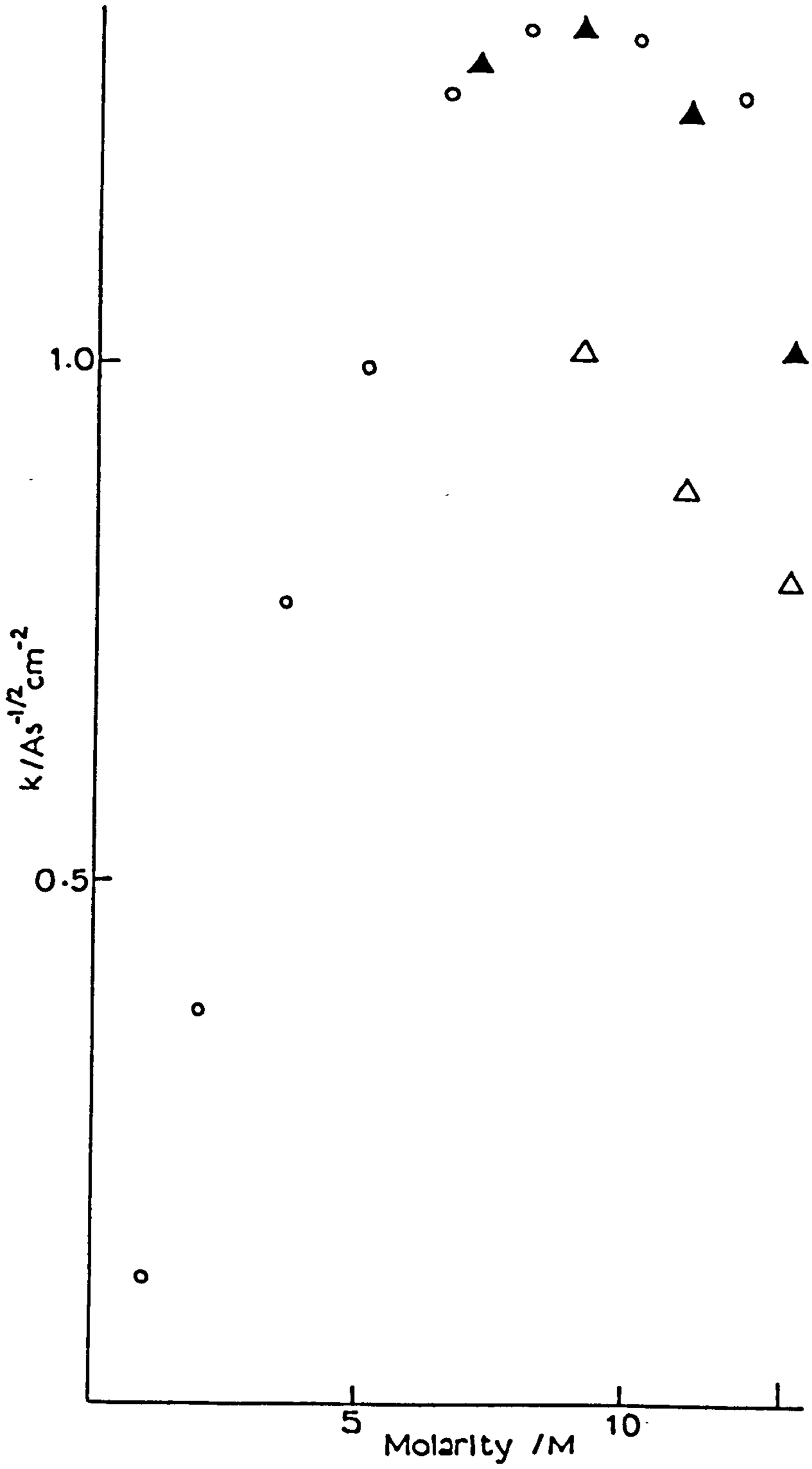

FIG. 6.3 Linear sweep voltammogram - planar zinc in 7M KOH. Sweep rate 1 mVs^{-1}, (a) anodic, (b) cathodic.

(a)

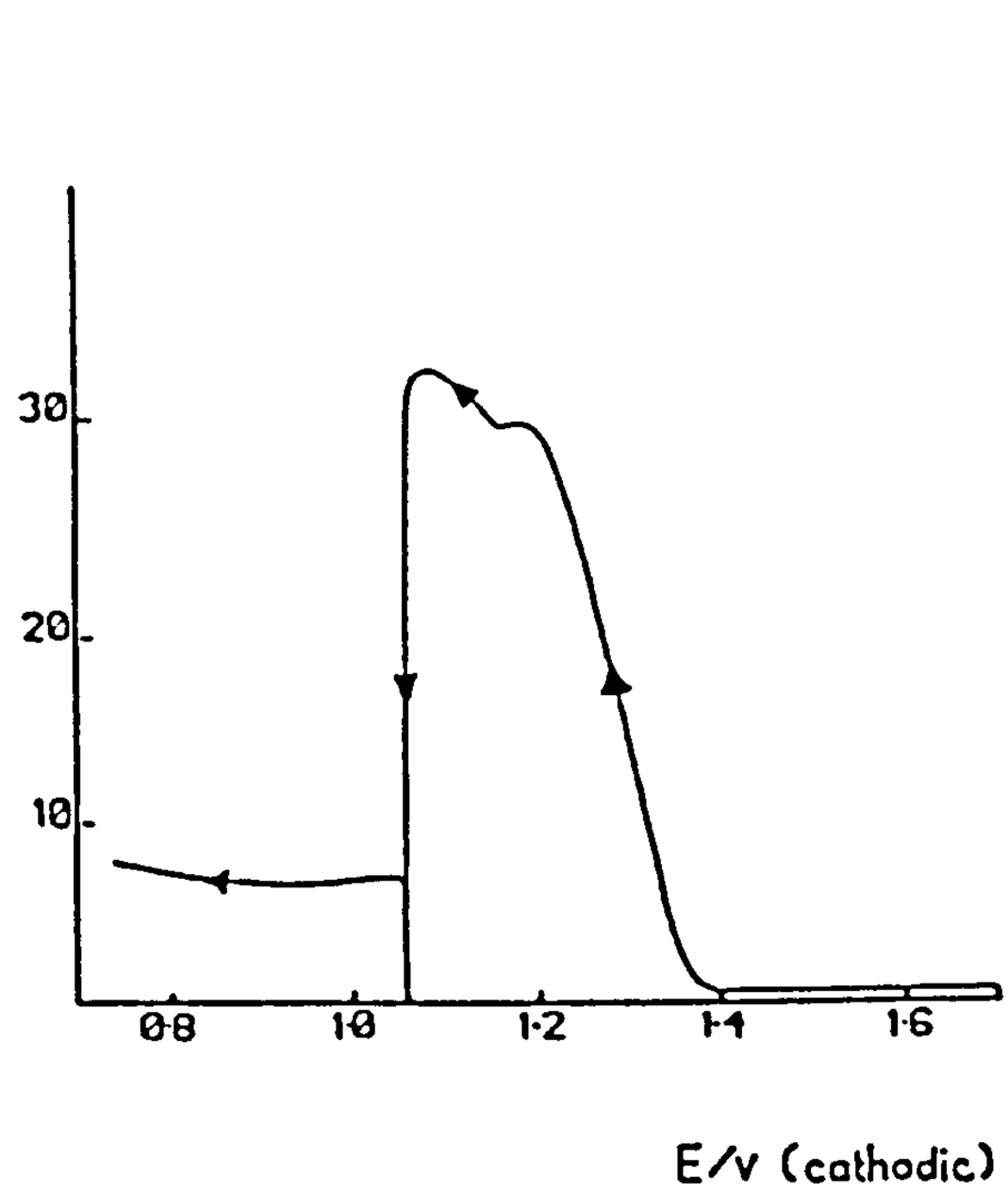

(b)

In the anodic sweep (Fig. 6.3a) an anodic current was seen at all potentials above -1.380V, and a double peak was observed with peak potentials at -1.190V and -1.080V, and peak currents of 32.0 mA and 34.5 mA respectively. The current between -1.380V and -1.190V was due to the active dissolution of zinc. The electrode passivates at a potential of -1.060V, but a substantial current (∿ 7 mA) continues to flow at potentials more anodic than this.

On the cathodic sweep a 7 mA current is maintained until a potential of -1.060V, when the electrode is re-activated. A large current spike was observed, then the current went through a broad maximum of 37.5 mA at a potential of -1.120V. As the cathodic potential excursion continued the current returned to the transient previously described as "active-dissolution".

The first anodic peak is smaller than the second at the lowest sweep rate, but this situation is reversed at higher sweep rates. Figure 6.4a shows an anodic sweep at a rate of 10 mVs^{-1}. On the cathodic sweep (Fig. 6.4b) a smaller cathodic peak appears with a peak potential at -1.415V. The size of this cathodic peak increases with sweep rate. The peak potentials and currents are shown in Table 6.3 for the two anodic peaks (A & B) and the cathodic peak, (C).

A plot of the peak current for (A) against the square root of the sweep rate (Fig. 6.5) is linear at the higher sweep rates, while the lower sweep rates ($\leqslant$ 10 mVs^{-1}) exhibit a limiting current. Figure 6.5 indicates that the reaction is a solution (diffusion) controlled process, but at low-sweep rates the concentration gradient is not significantly different from one sweep rate to another to produce a change in the rate of dissolution. What effectively is

FIG. 6.4 Linear sweep voltammogram - planar zinc in 7M KOH. Sweep rate 10 mVs^{-1}, (a) anodic, (b) cathodic.

(a)

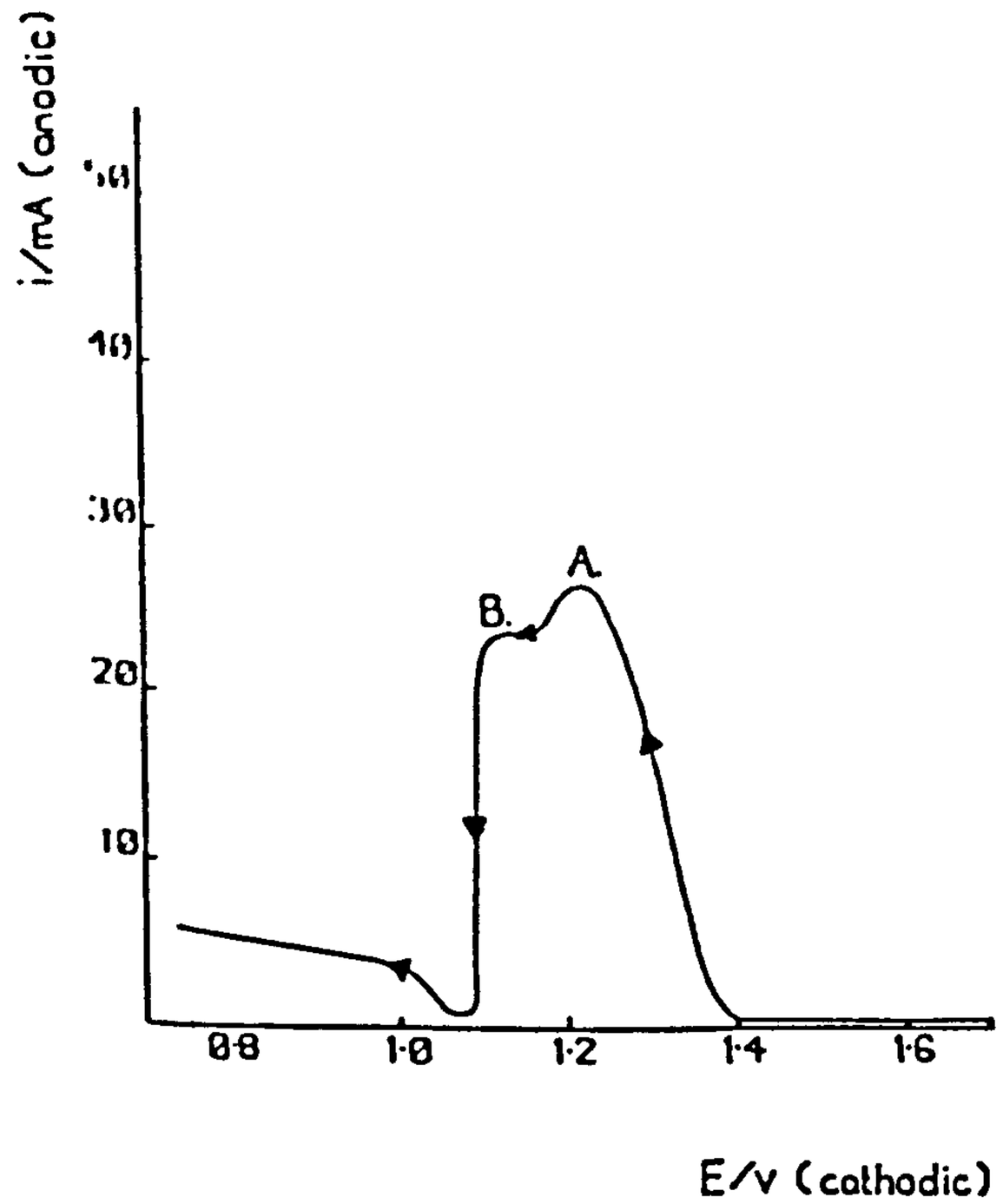

(b)

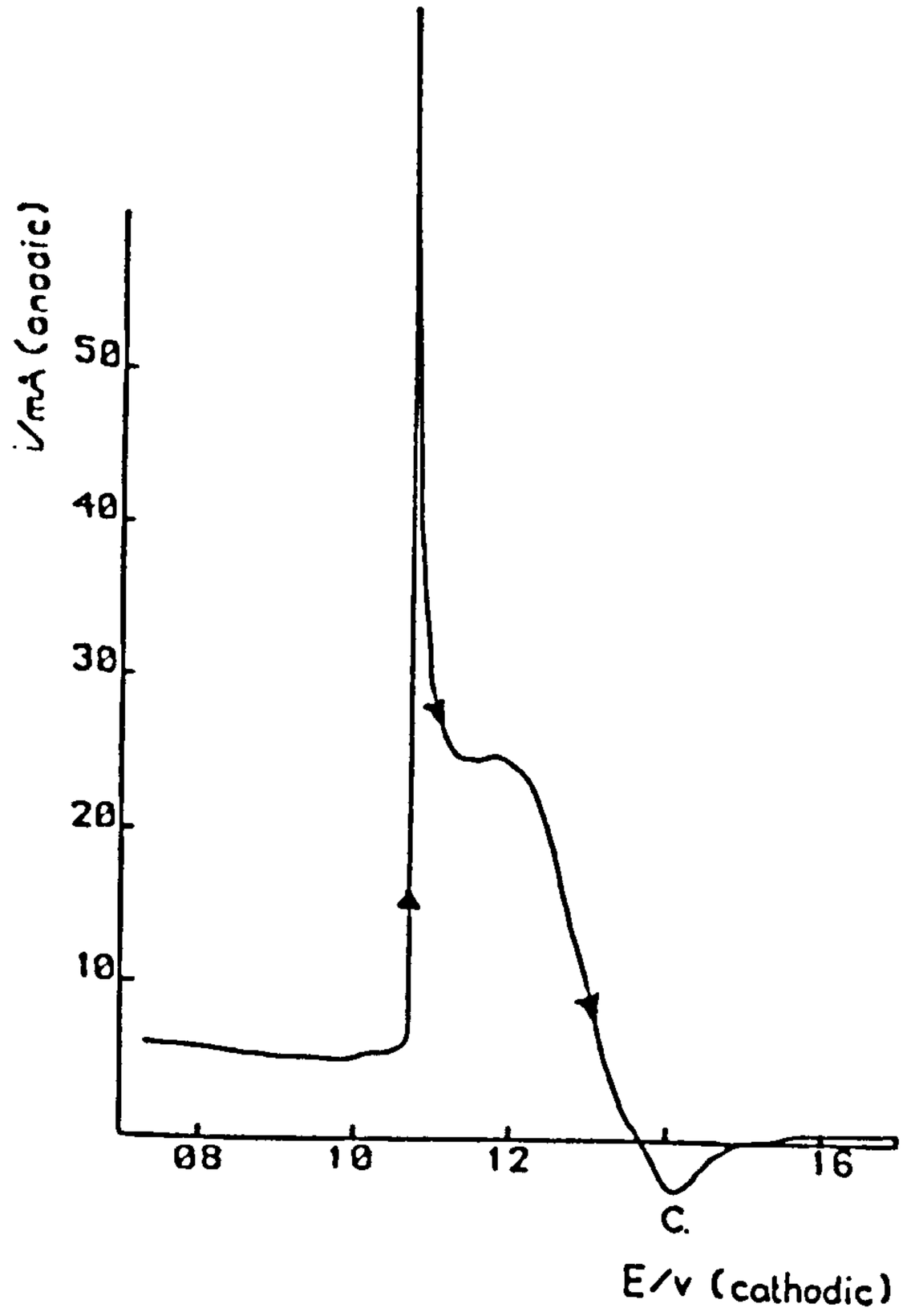

TABLE 6.3

First Anodic Peak (A)

Sweep Rate (mVs^{-1})	Peak Potential (V)	Peak Current (mA)
1	-1.190	32.0
3	-1.200	26.4
10	-1.220	26.7
30	-1.095	51.8
100	-1.130	64.8
300	-0.985	93.0

Second Anodic Peak

Sweep Rate (mVs^{-1})	Peak Potential (V)	Peak Current (mA)
1	-1.080	34.5
3	-1.100	30.6
10	-1.140	26.7
30	-1.040	42.0
100	*	-
300	*	-

* Two separate anodic peaks were no longer descernable.

Sweep Rate (mVs^{-1})	Peak Potential (V)	Peak Current (mA)
1	**	-
3	**	-
10	-1.415	3.5
30	-1.445	10.0
100	-1.470	27.5
300	-1.540	41.0

** Peak not discernable.

FIG. 6.5 Peak current plotted against the square root of sweep rate for Zinc in 7M KOH.

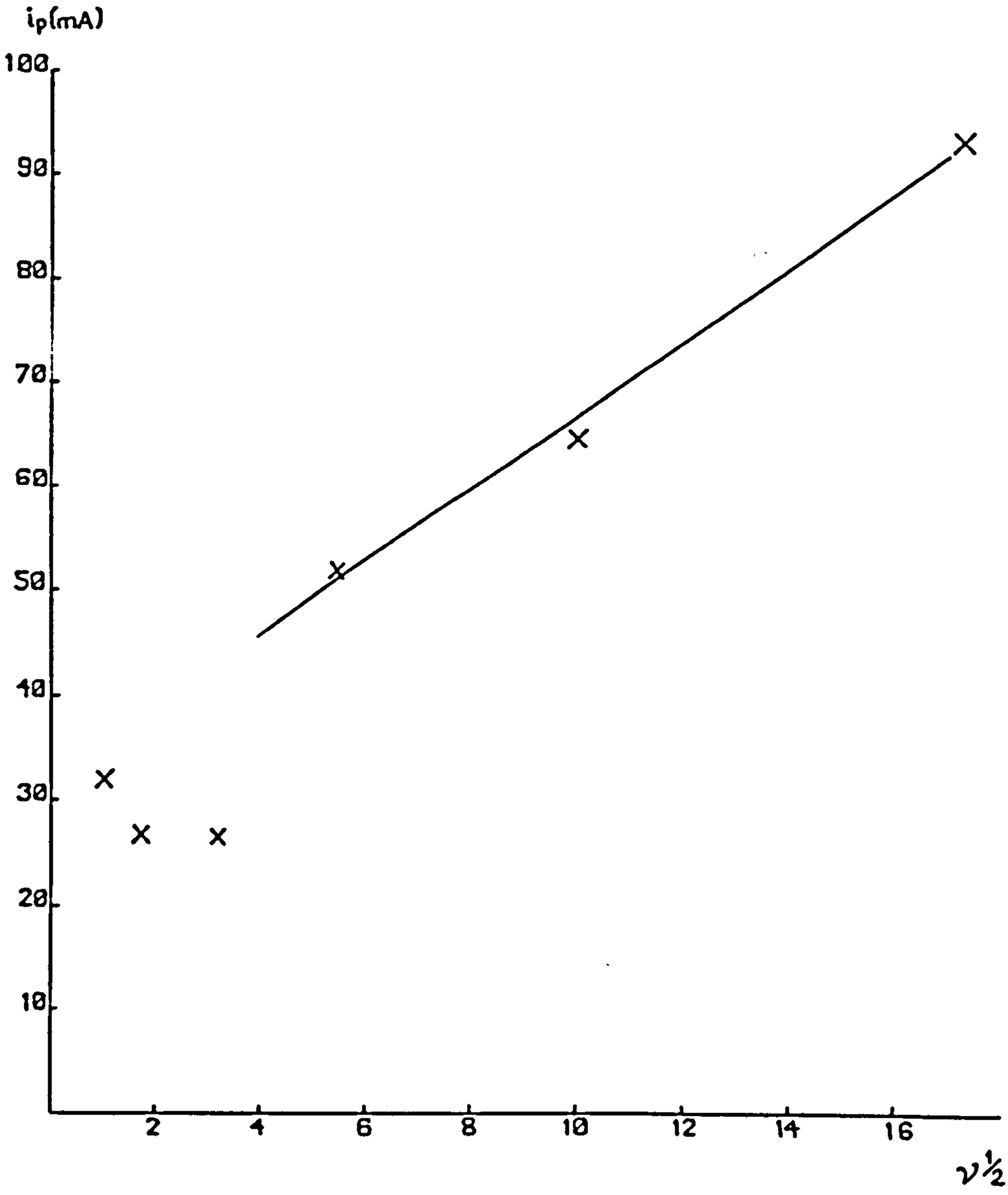

observed is the polarization curve under psuedo-steady state conditions at low sweep rate. At higher sweep rates an i_p versus $\nu^{\frac{1}{2}}$ relationship is obeyed. Undoubtedly the overlap with the second anodic peak, (attributed to the solid state oxidation of zinc by some workers), is a complicating factor in the determination of peak potentials and currents.

The electrode passivated at a potential of -1.060V during the anodic sweep at 1 mVs^{-1}, and was re-activated at the same potential on the cathodic sweep. The sharp anodic current spike on the cathodic excursion indicated film breakdown. At 3 mVs^{-1} the electrode passivated at -1.080V and re-activated at -1.065V. This led to a number of violent current oscillations on the cathodic sweep (Fig. 6.6) until a potential of -1.080V was reached, when final re-activation and current decay occurred. This behaviour has been observed by other workers[64,65,67,107], and is generally associated with film breakdown and repair. The phenomenon is usually associated with the anodic branch of a linear sweep voltammogram, and the peaks in Fig. 6.3a, do exhibit a fine structure, which the scale is too small to show in any detail.

The passivation/re-activation potentials at various sweep rates are shown in Table 6.4.

TABLE 6.4

Sweep Rate (mVs^{-1})	Passivation Potential (V)	Reactivation Potential (V)
1	-1.060	-1.060
3	-1.080	-1.065 & -1.080
10	-1.090	-1.070
30	-1.015	-1.055
100	-1.050	-1.090
300	-1.042 spread	-1.100 spread

FIG. 6.6 Cathodic linear potential sweep - Zinc in 7M KOH.
Sweep rate 3 mVs^{-1}.

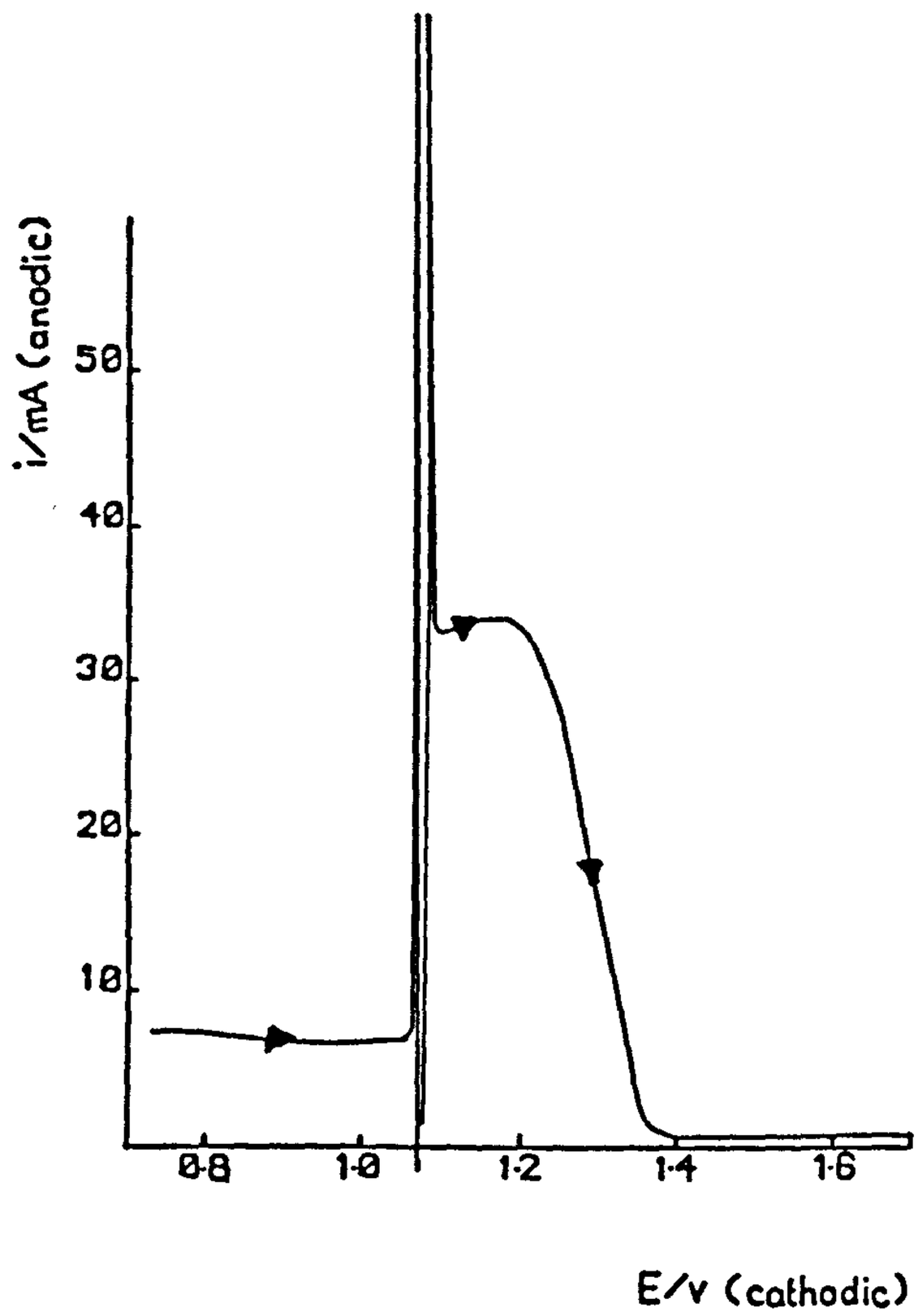

At low sweep rates the potentials were similar for the cathodic and anodic sweeps. At higher sweep rates the values diverge, resulting partly from the sweep "catching" a higher concentration of dissolved zincate at the electrode surface on the return excursion, and partly from a potential induced strain in the film due to a slow reduction reaction.

The total charge resulting under the anodic peak on the cathodic sweep is generally greater than the charge observed on the anodic sweep. This is because of pitting and surface roughening of the electrode during the initial anodic scan, and the actual surface area is increased for the return cathodic excursion. At high sweep rates this charge relationship is inverted. The sweep "catches" higher concentrations of zincate at the electrode surface, and a net current is observed made up of components due to zinc oxidation and reduction.

A cathodic peak was observed at higher sweep rates at more negative potentials. This is due to the reduction of the anodic products. Higher concentrations of products are encountered at the highest sweep rates, and a larger cathodic current was observed. A plot of peak current versus square root of sweep rate is linear (Fig. 6.7) indicating a diffusion controlled process. As there is no bulk zincate concentration this relationship can only be treated as an approximation. The nature of the cathodic reaction was investigated more thoroughly in the second part of this section.

FIG. 6.7 Plot of peak current against the square root of sweep rate for the small cathodic peak (c).

(x) L.S.V. results

(⊹) L.S.V. on R.D.E.

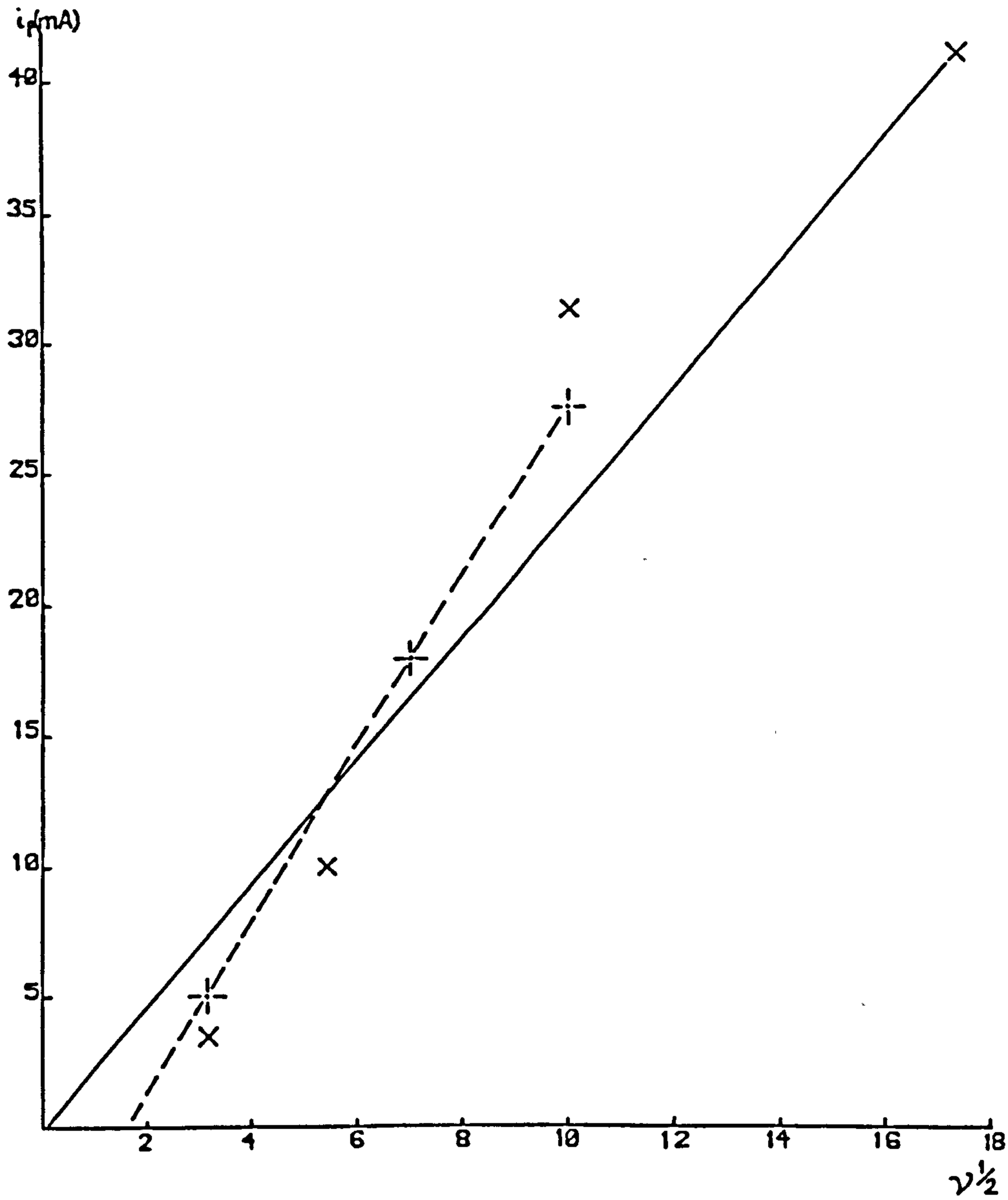

(b) Linear Sweep Voltammetry on a Rotating Disc Electrode

Dirkse[108] has questioned the mechanism of the reduction process leading to the cathodic peak on the cathodic potential excursion. The process could be the activation controlled reduction of a type II solid film, or the reduction of soluble zincate species in the electrolyte solution. The type II film continues to dissolve in KOH once formed, and re-activation has been observed by McKubre and MacDonald[67]. The effect of sweep speed on the cathodic sweep is therefore either to detect the amount of undissolved, oxidised zinc remaining in the solid film at different times, or to reduce the soluble zincate species as a function of concentration. If the electrode is rotated the diffusion layer thickness is defined, and should not affect the rate of the solid state reaction, whereas soluble species will have diffused into the bulk of solution, and the rate of reduction will depend on the pseudo-bulk concentration of soluble species around the electrode.

Figure 6.8 shows a current-potential plot on a stationary zinc electrode. The anodic sweep rate was kept constant at 100 mVs^{-1}, but the cathodic sweep rate was changed. The peak heights are included in Fig. 6.7 where they are plotted against the square root of the cathodic sweep rate. This second set of points undoubtedly fall on a straight line confirming diffusion control, and give an intercept on the x-axis suggesting a limiting sweep rate (2.65 mvs^{-1}) below which the peak will not be observed.

Figure 6.9 shows current potential curves at the same cathodic sweep rates on a rotating electrode. The reduction in size of the cathodic peak, and its eventual disappearance as the rotation speed is increased (Fig. 6.9b) provided further corroboration that the

FIG. 6.8 Cathodic linear sweep voltammogram for a stationary zinc electrode in 7M KOH.

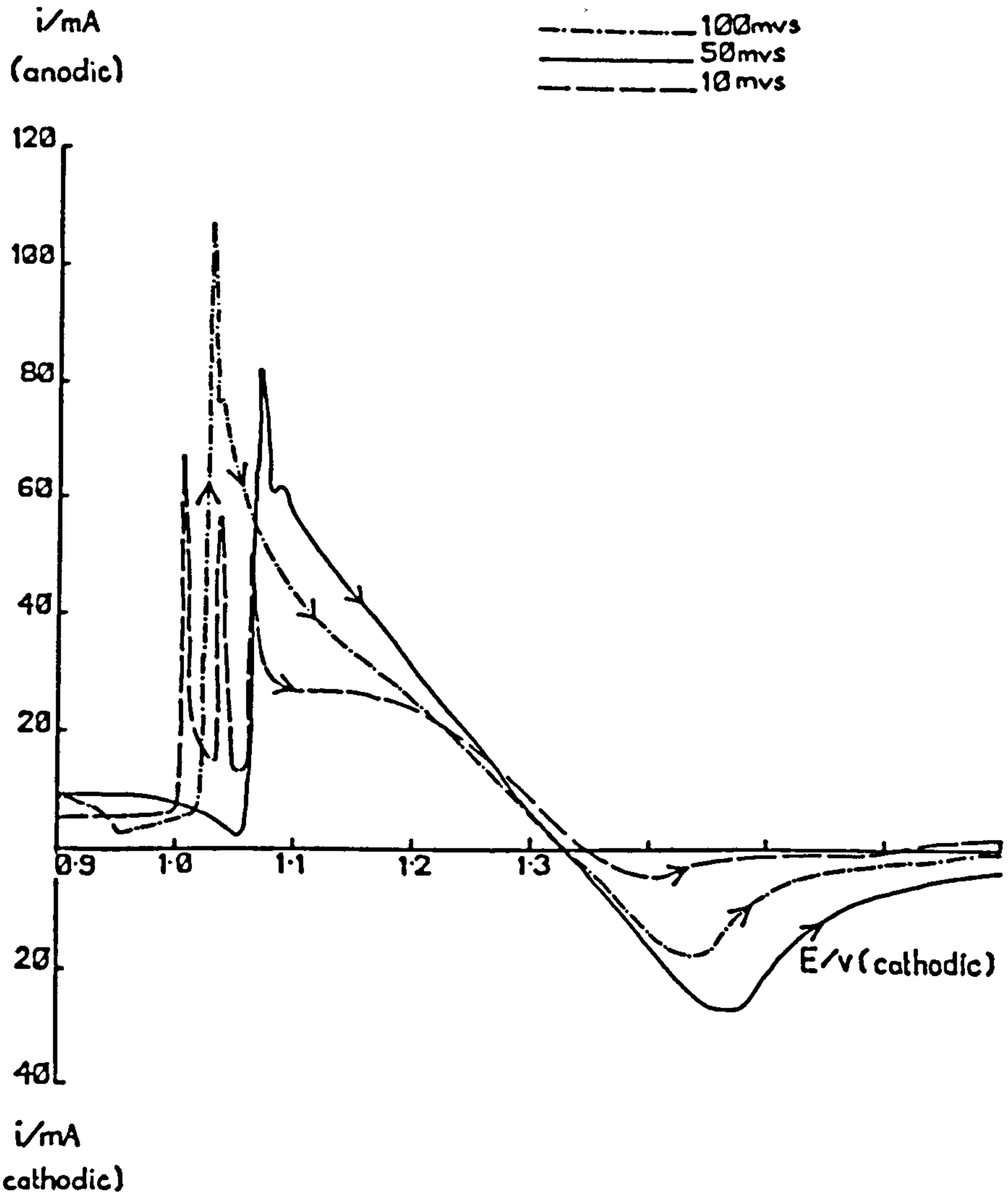

FIG. 6.9(a) Cathodic linear sweep voltammogram on a rotating Zinc electrode.
Rotation speed 225 r.p.m.

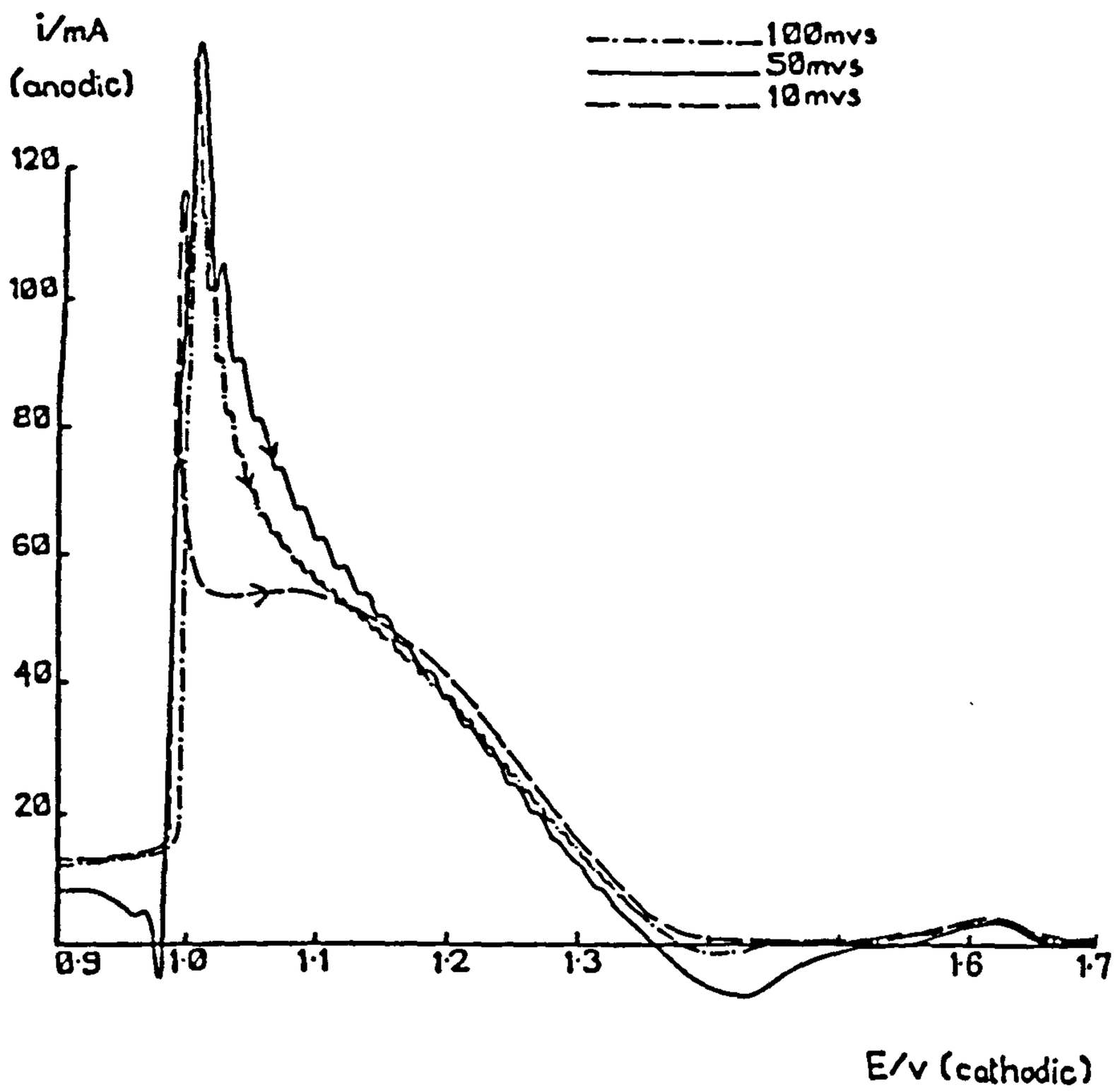

FIG. 6.9(b) Cathodic linear sweep voltammogram on a rotating Zinc electrode.
Rotation speed 612 r.p.m.

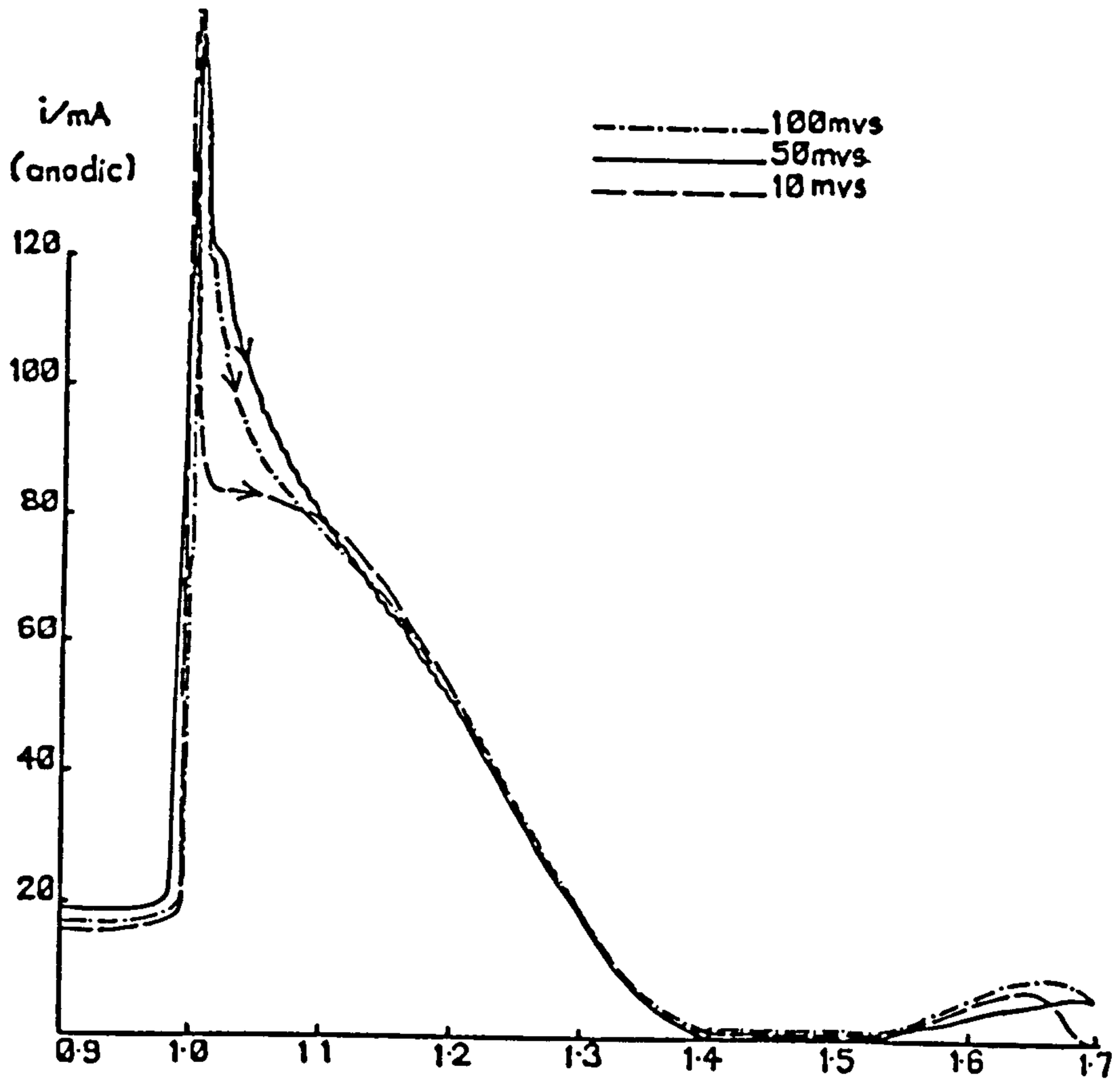

process is controlled by the diffusion of zincate ions.

6.3.3. Rotating Disc Electrode Experiments

Figure 6.10 shows some plots of $^1/i$ against $^1/\omega^{\frac{1}{2}}$ for the zinc electrode in 7M KOH at anodic potentials with respect to the zero current potential. Linear plots were observed in the potential range investigated (-1.375V to -1.260V w.r.t. Hg/HgO). The values of the intercepts at infinite rotation speed provide evidence that the oxidation process is irreversible. Figure 6.11 is a plot of potential versus $\log_{10}$ (^{1}/intercept). In the low potential region (-1.375V to -1.300V) a linear Tafel portion was found with a slope of 58 mV decade^{-1} increase in current density. Gerischer[109] has reported a Tafel slope of 58 mV decade^{-1} for zinc amalgams in KOH. This was interpreted as a two-step mechanism with the first step being rate-determining.

$$Zn(Hg) + 2OH^- \xrightarrow{r.d.s.} Zn(OH)_2 + 2e^-$$

$$Zn(OH)_2 + 2OH^- \longrightarrow Zn(OH)_4^{2-}$$

Armstrong and Bulman[110] investigated the oxidation reaction at solid zinc electrodes, and found a Tafel slope of 42 ± 5 mV decade^{-1}. This they attributed to a contribution from the back reaction resulting in the simultaneous deposition of zinc.

Figure 6.12 shows a plot of potential versus $\frac{\partial i^{-1}}{\partial \omega^{-\frac{1}{2}}}$. A theoretical 30 mV decade^{-1} line is included for a two electron transfer reaction, and it is clear that the experimental curve diverges from this value at high overpotential. This is consistent with the formation of a film at these high overpotentials. The Tafel plot (Fig. 6.11) shows a limiting current at this potential which can again be explained by

FIG. 6.10 Plot of the reciprocal of the current against $1/w^{1/2}$ for a rotating zinc electrode in 7M KOH.

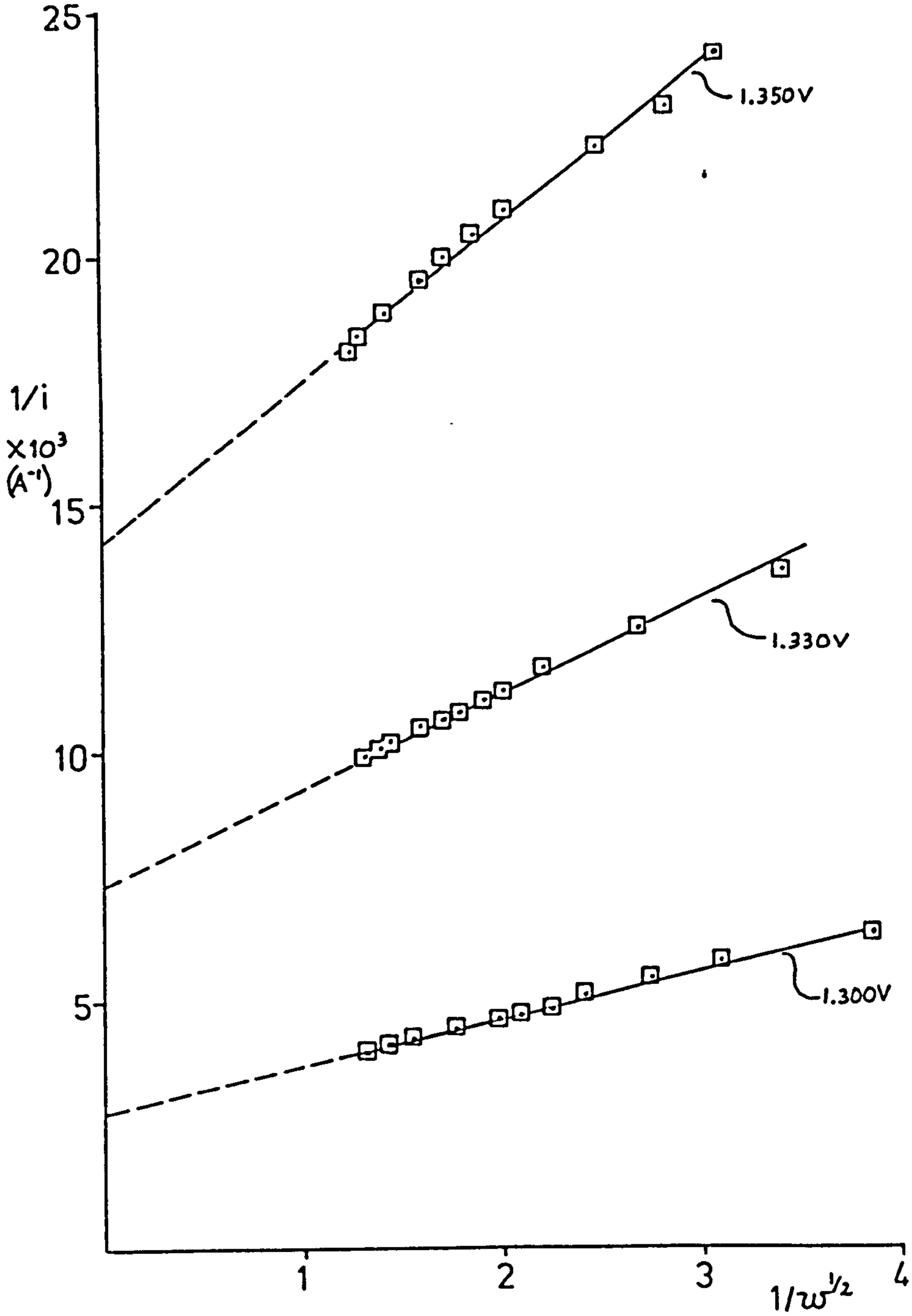

FIG. 6.11 Tafel plot for a rotating zinc electrode in 7M ZOH.
—— ——60 mV decade^{-1} line.

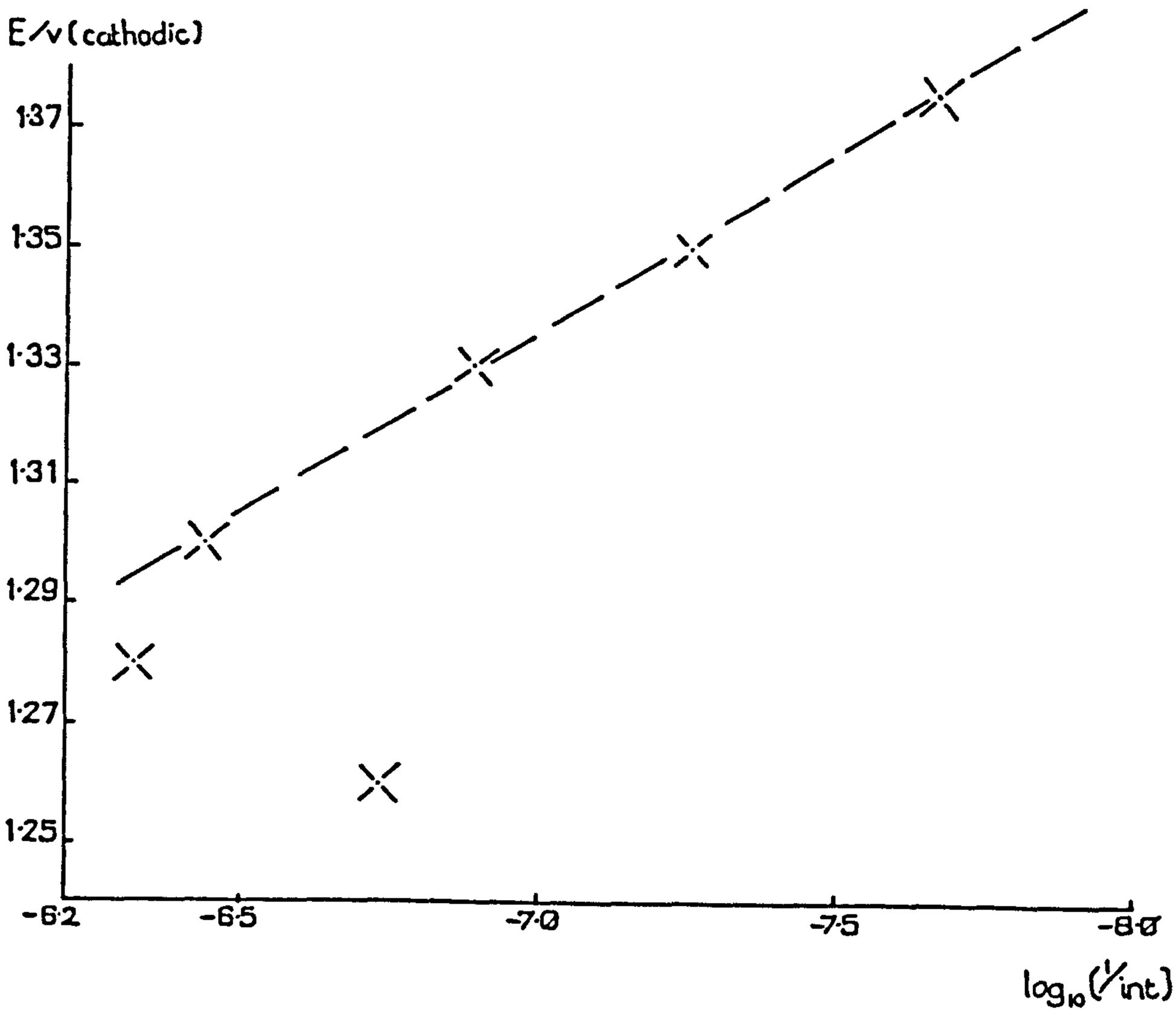

FIG. 6.12 Plot of the slope from the rotating experiments against potential.

— — — 30 mV decade^{-1} line.

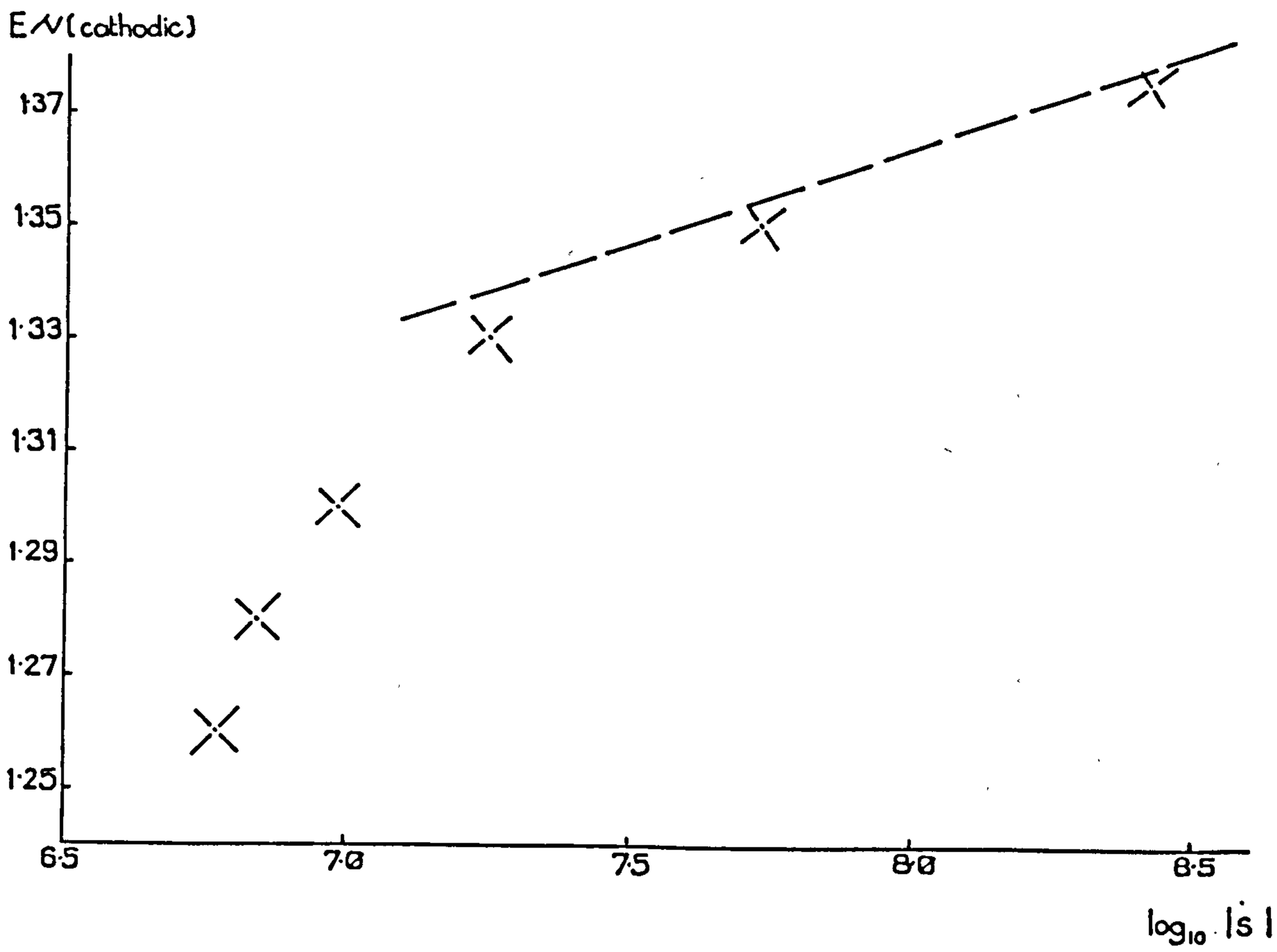

the formation of a resistive film. Armstrong and Bulman[110] noted a strong dependence on hydroxide ion concentration for the dissolution rate, and only made measurements up to a concentration of 2M NaOH. It appears that at the concentration used in the present study, the rate of active dissolution is sufficiently fast to allow the rate of the reduction reaction to be neglected.

6.3.4. A.C. Impedance Measurements

The impedance locus for a planar zinc electrode in 7.44M KOH at the stabilized zero-current potential (-1.432V) is shown in Fig. 6.13. It consists of a semicircular region which can be fitted to a simple Randles type circuit in the frequency range 10 kHz to 20 Hz. The double layer capacitance was obtained by measuring the frequency at the top of the high frequency semicircle and substituting this value into equation 3.34. A value of 82 μF cm^{-2} was calculated, which seems of the correct magnitude for a zinc electrode in 7M electrolyte. At lower frequencies the impedance locus increases in dihedral above 45°, and eventually appears to be random (Fig. 6.14). Figure 6.15 is the impedance plot at a potential 10 mV anodic of the zero current potential. The form of the locus is unaffected in shape at higher frequencies but the size of the semicircle decreases with increasing polarization. At low frequencies there is evidence of a loop in the capacitive-resistive plane, but at 10 mV anodic displacement from the zero-current potential this loop is not well defined. By increasing the polarization the loop becomes better defined (Fig. 6.16), shifting partially to the inductive-resistive plane at high polarizations, (e.g. +90 mV - Fig. 6.17).

FIG. 6.13 Sluyters Plot:- Stationary zinc electrode in 7.44M KOH.
-1.432V, Open circuit potential
10,000 - 10 Hz.

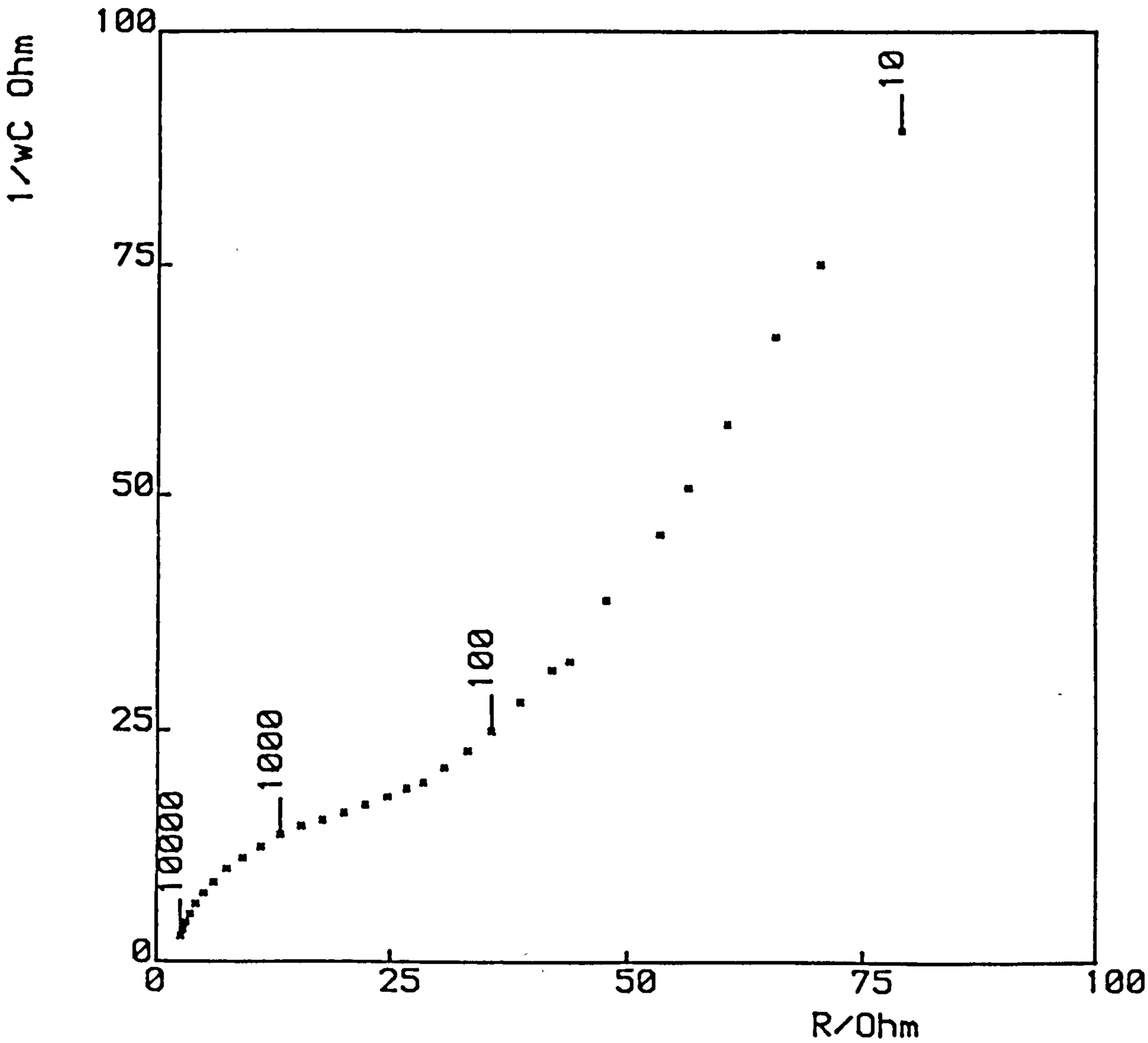

FIG. 6.14 Sluyters Plot:- Stationary zinc electrode in 7.44M KOH.
-1.432V, Open circuit potential
Full scale.

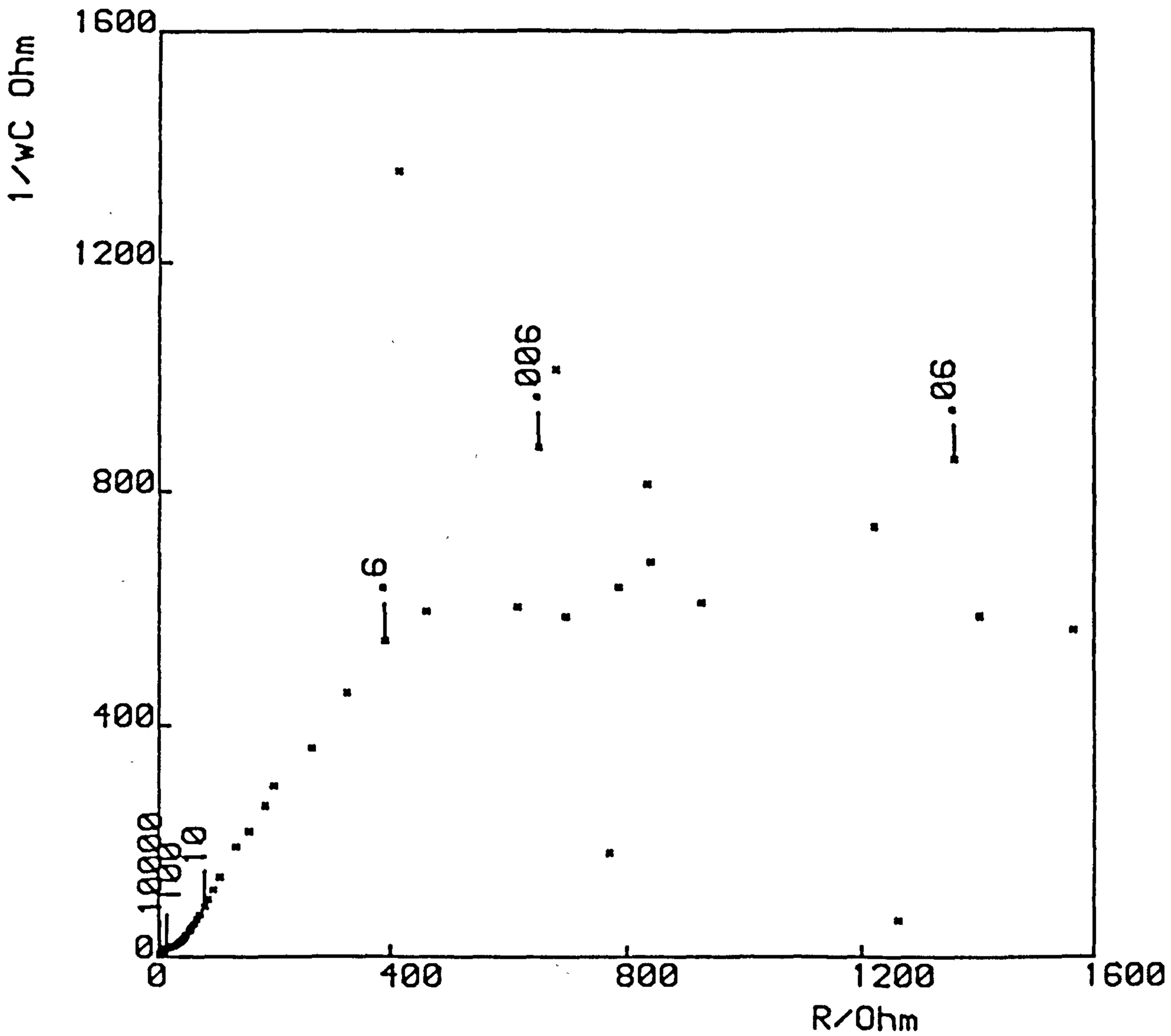

FIG. 6.15 Sluyters Plot:- Stationary zinc electrode in 7.44M KOH.
1.422V, O.C.V. + 10 mV

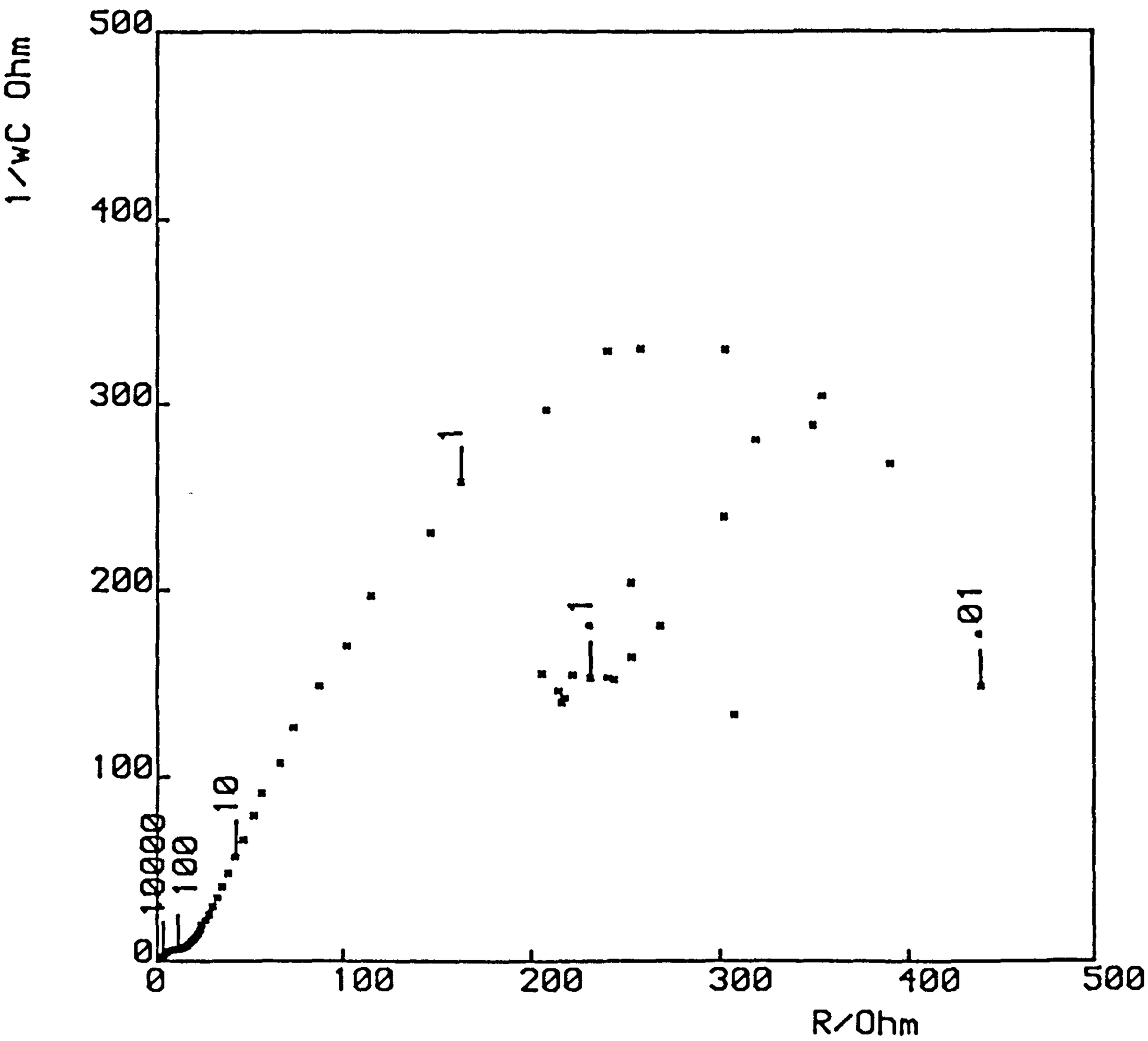

FIG. 6.16 Sluyters Plot:- Stationary zinc electrode in 7.44M KOH.
-1.392V, O.C.V. + 40 mV

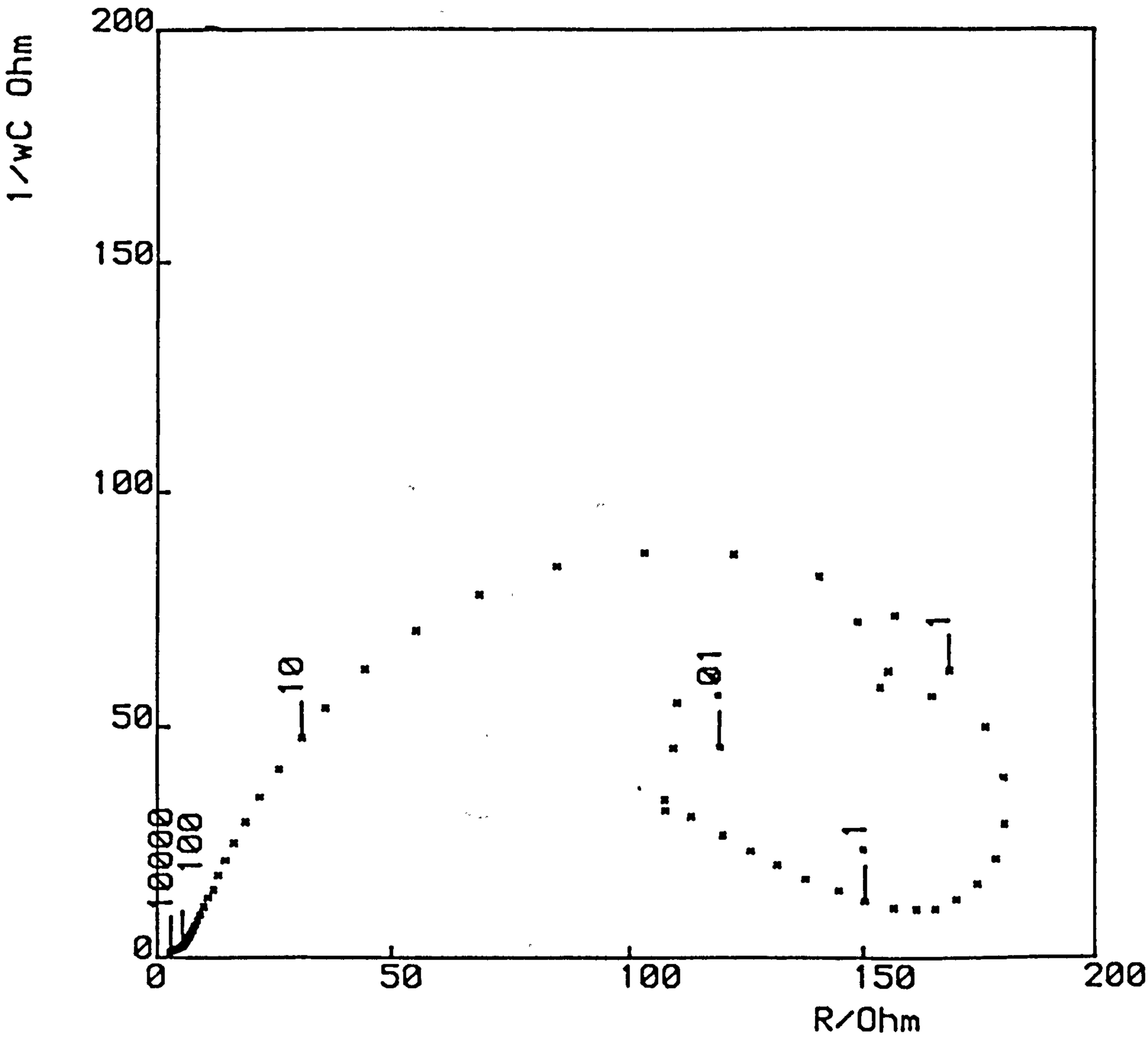

FIG. 6.17 Sluyters Plot:- Stationary zinc electrode in 7.44M KOH.
-1.342V, O.C.V. + 90 mV

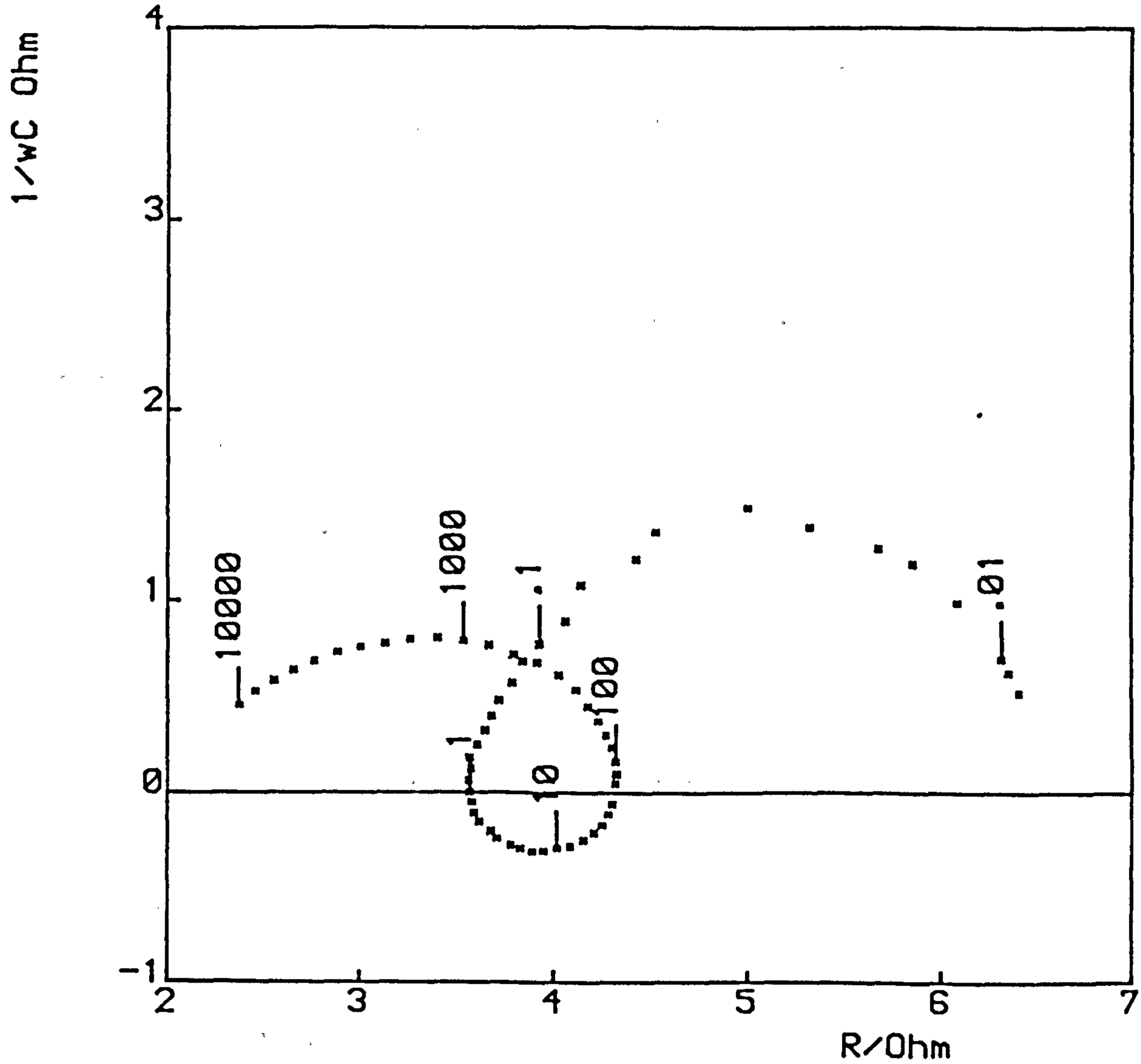

These results are predicted by Armstrong and Bell's[49] analysis of the system. At low polarizations the loop in the capacitive-resistive plane is indicative of a solution reaction involving soluble intermediates. At higher polarizations there is a change in the kinetic constants, shifting the reaction to a state where the reaction intermediates are increasingly adsorbed at the electrode, giving rise to the inductive loop in the impedance plot. It this argument is justified the semicircular shape at high frequencies is the charge transfer resistance for the two electron, two-step exchange reaction. Accordingly a Tafel relationship results from plotting log R against potential, (Fig. 6.18). The Tafel slope is 44 mV decade^{-1} which is in excellent agreement with the previously published work[49], but not at all in agreement with the results obtained on the rotating disc presented in the previous section. Both sets of results need re-examining.

The lowest potential at which measurements were made on the rotating disc was -1.375V, and current readings were less than 1 μA. From the current/potential curve (Fig. 6.3a) it can be seen that this potential is at the foot of the rising active dissolution transient, and it was at the lower limit of detection for the rotating disc apparatus used here. At this potential; 57 mV anodic of the zero-current potential, the impedance locus has a well developed inductive loop, and the reaction is proceeding via an adsorbed intermediate. The simple Randles circuit (charge transfer and diffusion) could only be applied to the impedance results up to 40 mV anodic of the zero-current potential, and there was no evidence of adsorption from the loop developing at low frequencies. Armstrong and Bell's results were collected in 1M KOH, and show a zero-current potential at -1.380V. At +40 mV they confirmed a solution soluble intermediate, while at +70 mV the change in kinetic constants resulted in an adsorbed inter-

FIG. 6.18 Plot of $\log_{10}$ Charge Transfer Resistance Against Overpotential.

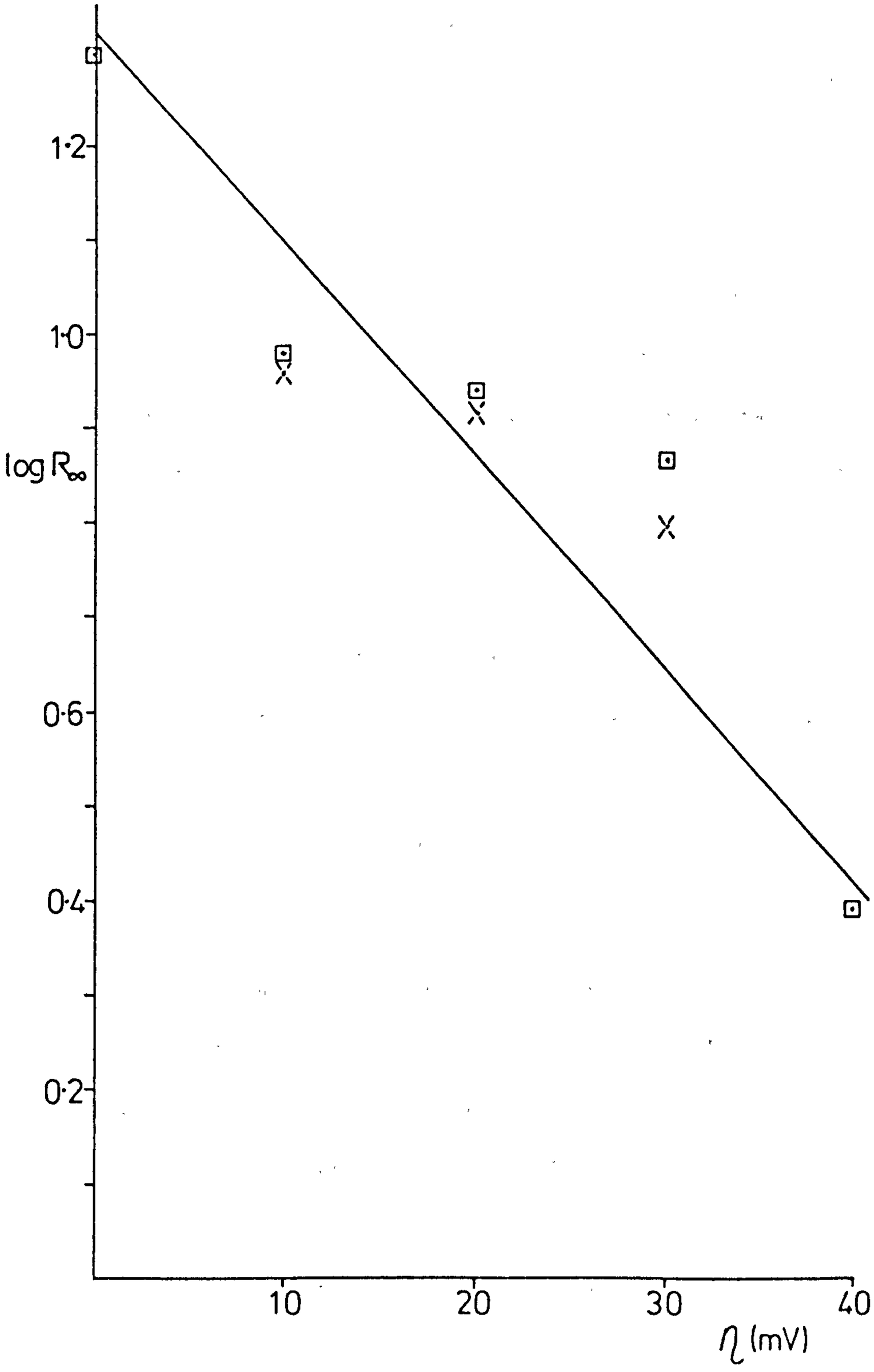

mediate. The higher concentration of hydroxide ion in the present study would favour the adsorbtion mechanism. It appears that at the high polarizations used for the rotating disc experiments, the reaction proceeds via an adsorbed intermediate and a single step two-electron irreversible process, while at lower polarizations a two step process occurs with a considerable contribution from the back reaction. There is no evidence of film formation in the Tafel plots until very high polarizations (+130 mV, -1.302V, Fig. 6.11), where the Tafel slope begins to increase exponentially.

In the zinc/KOH system at low frequencies the Warburg slope was greater than 45°, and became unstable at approximately 0.5 Hz. This is due to the absence of a steady state for that part of the a.c. perturbation when the electrode potential was driven negative of the zero-current potential, since there was sufficient charge in the half-cycle to remove all the Zn(II) species from solution. Under these condition the electrode is reasonably polarisable and the Warburg slope increases in excess of 45°. The unstable part of the impedance loci at very low frequency is due to the intrusion of the hydrogen evolution reaction, when sufficient Zn(II) has been removed from solution.

The impedance locus with a potential-determining ion present is similar to that in the absence of Zn(II) except that the Warburg line is correct at the higher frequencies for a smooth electrode, and degenerates at very low frequencies to that for a rough electrode, as seen by a change in the dihedral from 45° to 22.5° (Fig. 6.19). This is expected by the work of Lorenz[111]; when the reaction layer is thin at high frequencies, the electrode is effectively planar with the geometric area equivalent to the true surface area; when the reaction

FIG. 6.19 Sluyters Plot:- Stationary zinc electrode in solution: 7.44M OH^-, 1M $Zn(OH)_4^{2-}$, 9.44M K^+. -1.363V, O.C.V.

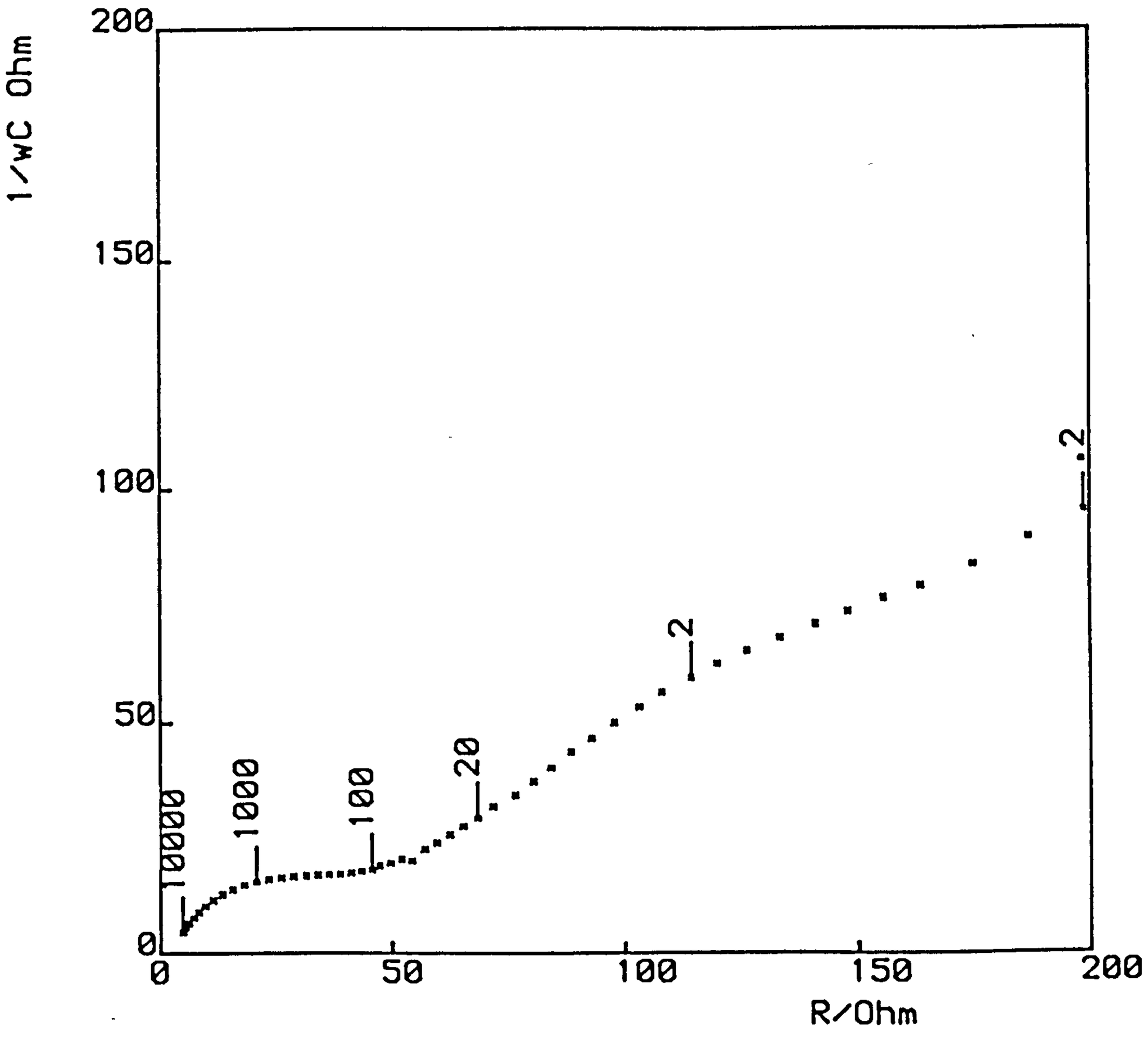

layer is thicker at low frequency, the effective area is the projected surface area with the electrode apparently rough, and giving a Warburg slope approaching 22.5° as predicted by DeLevie[18]. At higher polarizations the loci fall into the expected pattern. A well defined circular, partly inductive region is clearly apparent at a +40 mV polarization (Fig. 6.20), which ultimately tends to a Warburg line with a dihedral of 22.5° characteristic of a roughened electrode. Reduction in the concentration of zincate resulted in the expected changes in magnitudes of the impedance locus (Fig. 6.21) at the equilibrium potential, and the development of a loop (Fig. 6.22) at low positive polarization levels, which becomes inductive at higher polarizations (Fig. 6.23).

When the electrode was pre-polarized at +15 mV for 8 hours in the electrolyte the impedance locus was changed (Fig. 6.24). This is due to metallurgical changes which occur as a result of the exchange reaction. The more stable faces of the polycrystalline surfaces develop at the expense of the less stable (high energy) surfaces. In the present case the diameter of the high frequency semi-circle is ostensibly unaffected, but the loop is materially affected. This can be interpreted as the adsorbtion of reaction intermediates on the different faces available on the polycrystalline electrode.

The typical Randles plot corresponding to the impedance data for the electrolyte containing 1M ZnO at the reversible potential (-1.363V) is shown in Fig. 6.25. It comprises two parallel lines, the capacitive one passing through the origin at infinite frequency. The pattern is similar to the results of Farr and Hampson[112] which indicated that over a limited frequency range a pseudo-Randles type circuit behaviour occurred. This same behaviour is shown by the present data (Fig. 6.25). At the higher frequency range at a lower Zn(II) concentration the charge

FIG. 6.20 Sluyters Plot:- Stationary zinc electrode in solution:
7.44M OH^-, 1M $Zn(OH)_4^{2-}$, 9.44M K^+.
-1.323V, O.C.V. + 40 mV

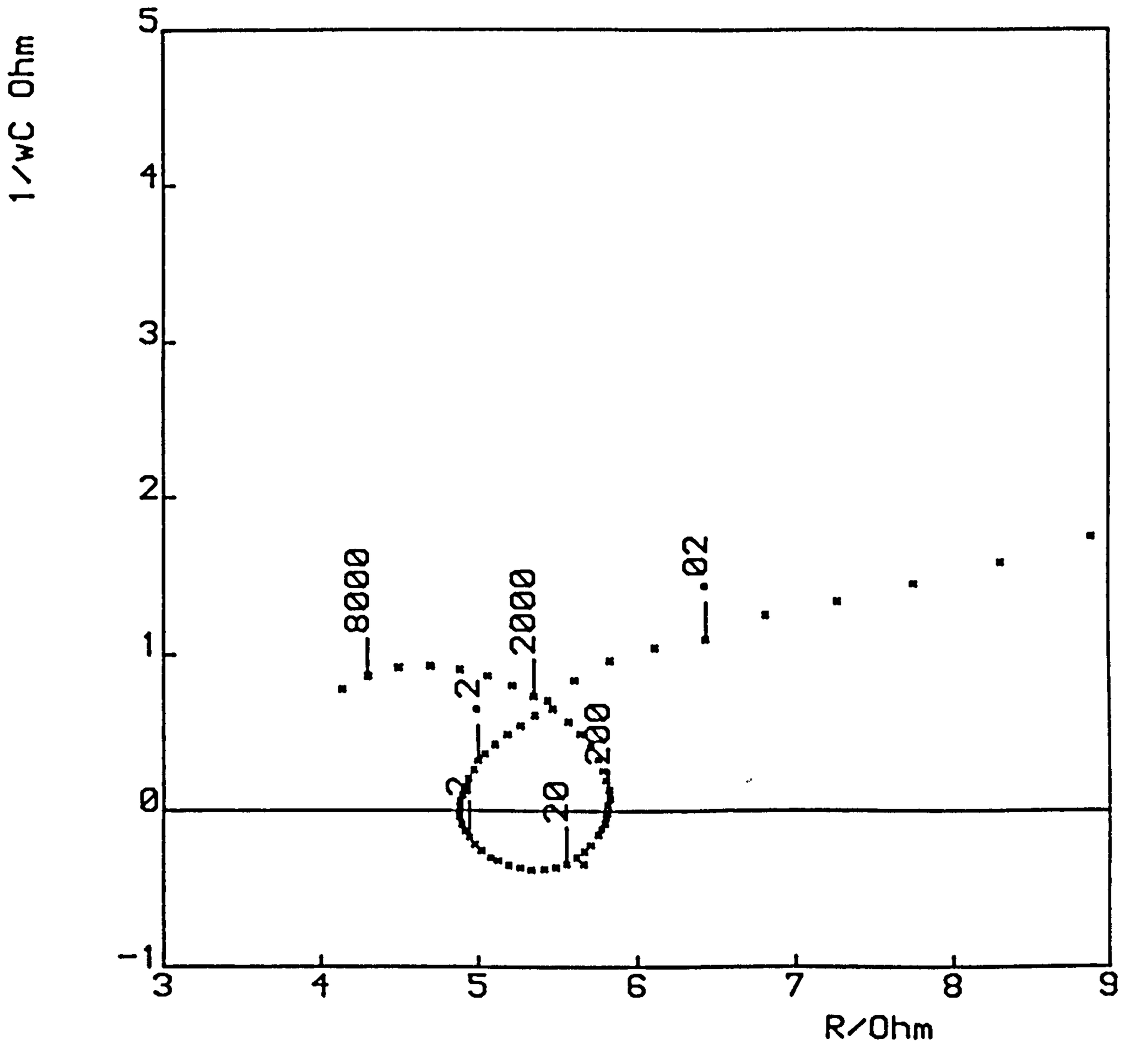

FIG. 6.21 Sluyters Plot:- Stationary zinc electrode in solution: 7.44M OH^-, 0.1M $Zn(OH)_4^{2-}$, 7.64M K^+. -1.383V, open circuit voltage.

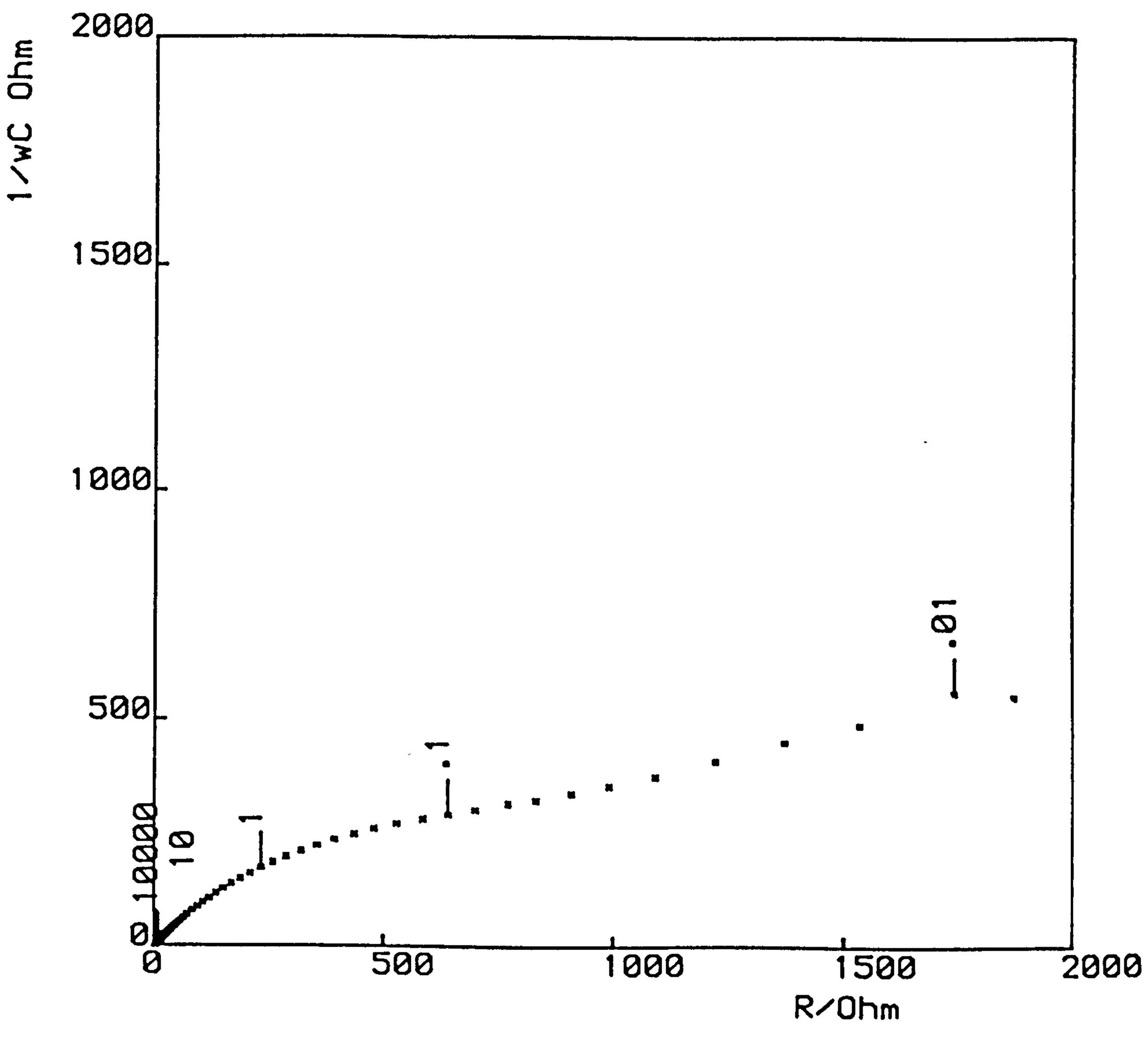

FIG. 6.22 Sluyters Plot:- Stationary zinc electrode in solution:
7.44M OH^-, 0.1M $Zn(OH)_4^{2-}$, 7.64M K^+
-1.372V, O.C.V. + 10 mV.

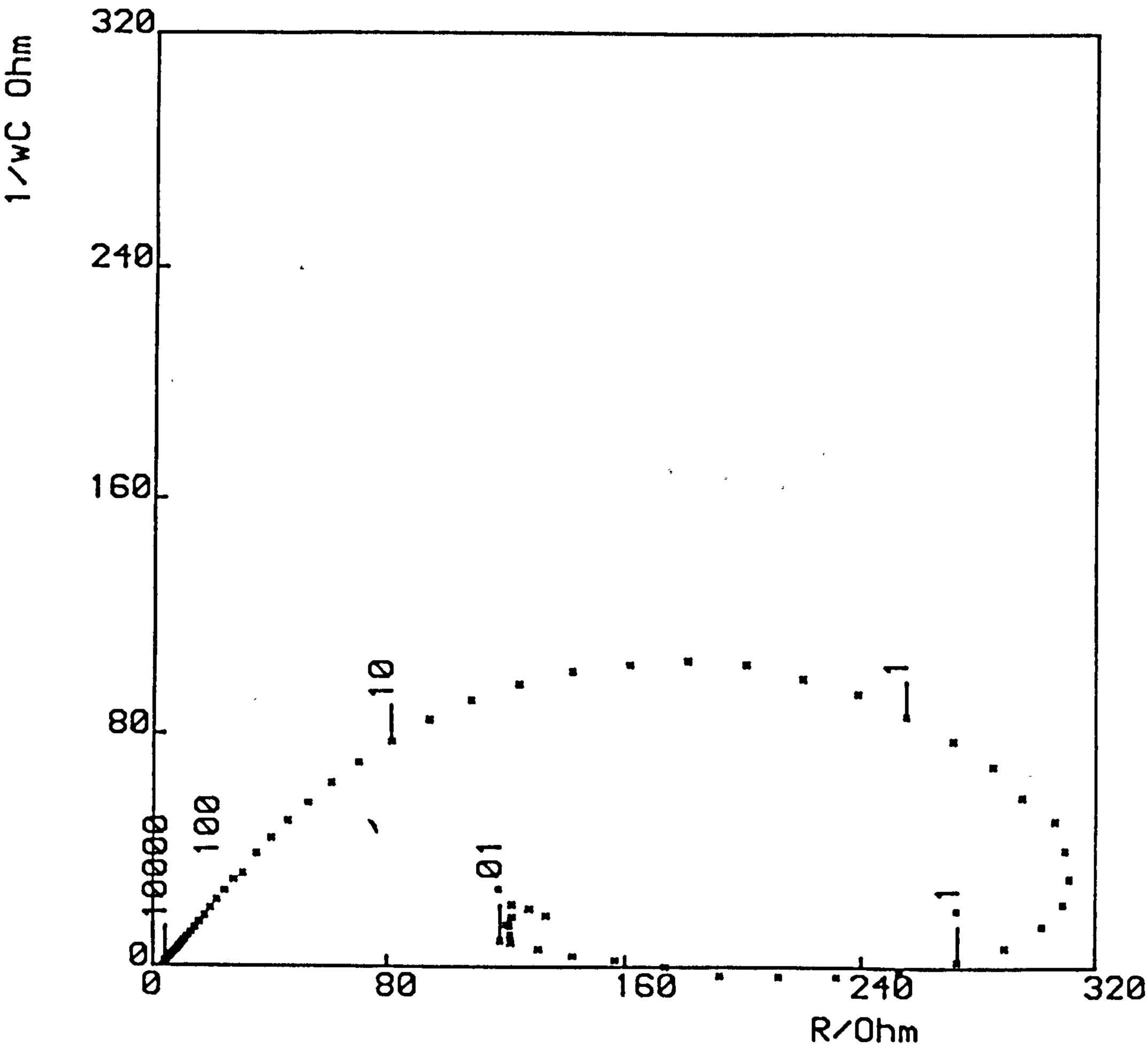

FIG. 6.23 Sluyters Plot:- Stationary zinc electrode in solution:
7.44M $(OH)^-$, 1M $Zn(OH)_4^{2-}$, 9.44M K^+
-1.367V, O.C.V. + 15 mV.

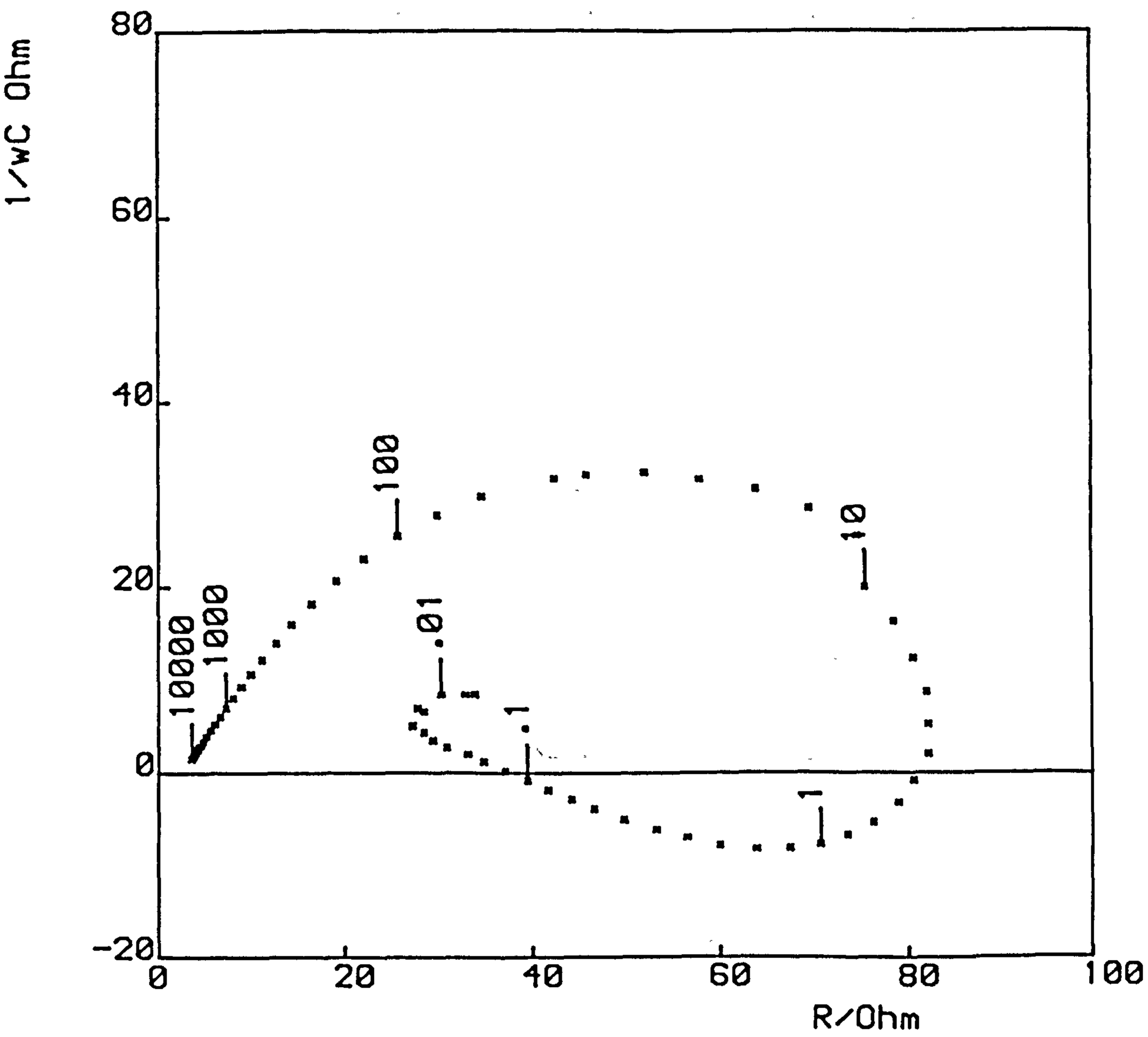

FIG. 6.24 Sluyters Plot:- Stationary zinc electrode in solution: 7.44M OH^-, 1M $Zn(OH)_4^{2-}$, 9.44M K^+. Prepolarize at -1.348V. Run at -1.348V, O.C.V. + 15 mV.

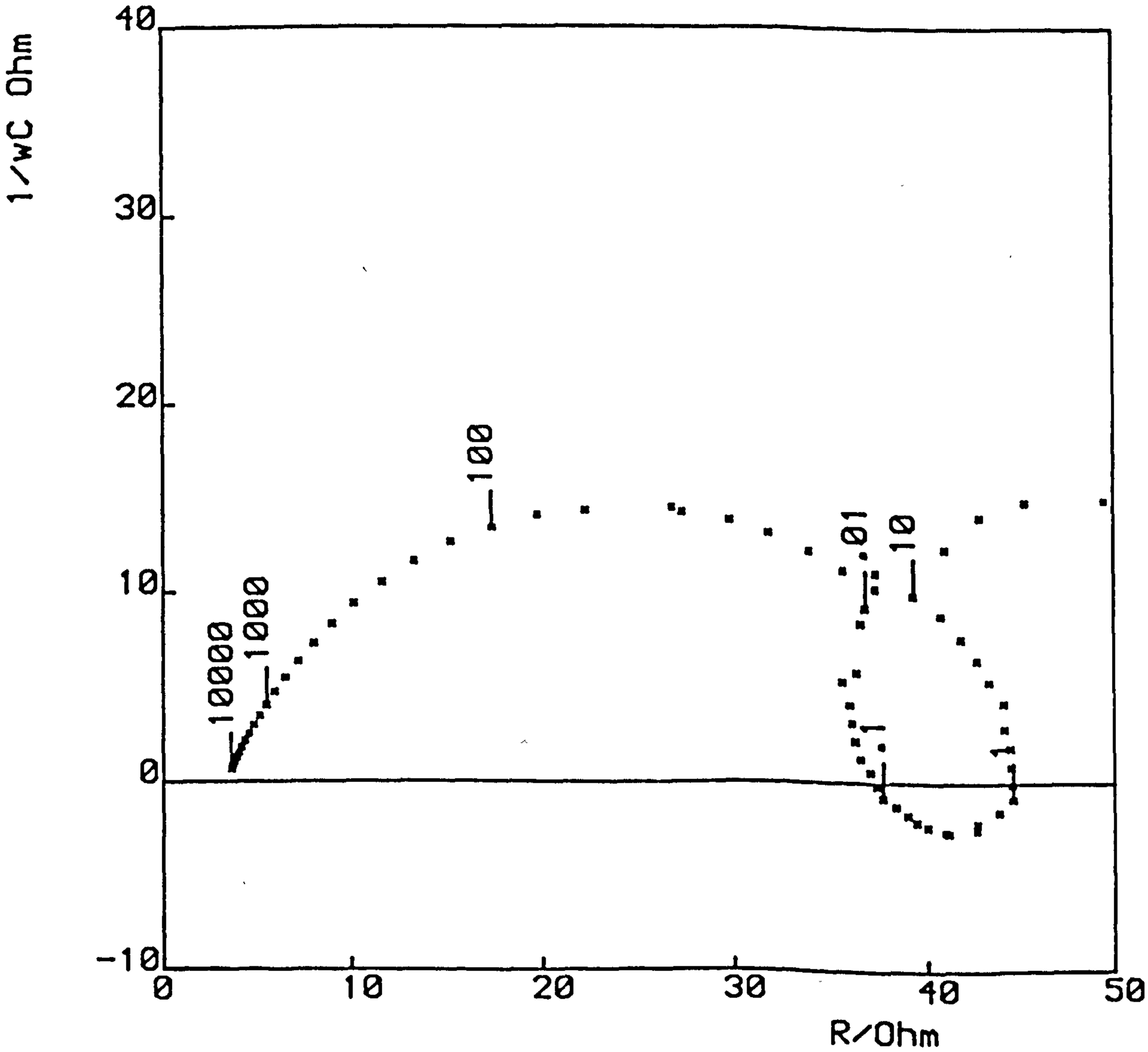

FIG. 6.25 Randles Plot:- Stationary zinc electrode in solution: 7.44M $(OH)^-$, 1M $Zn(OH)_4^{2-}$, 9.44M K^+. -1.363V, open circuit voltage.

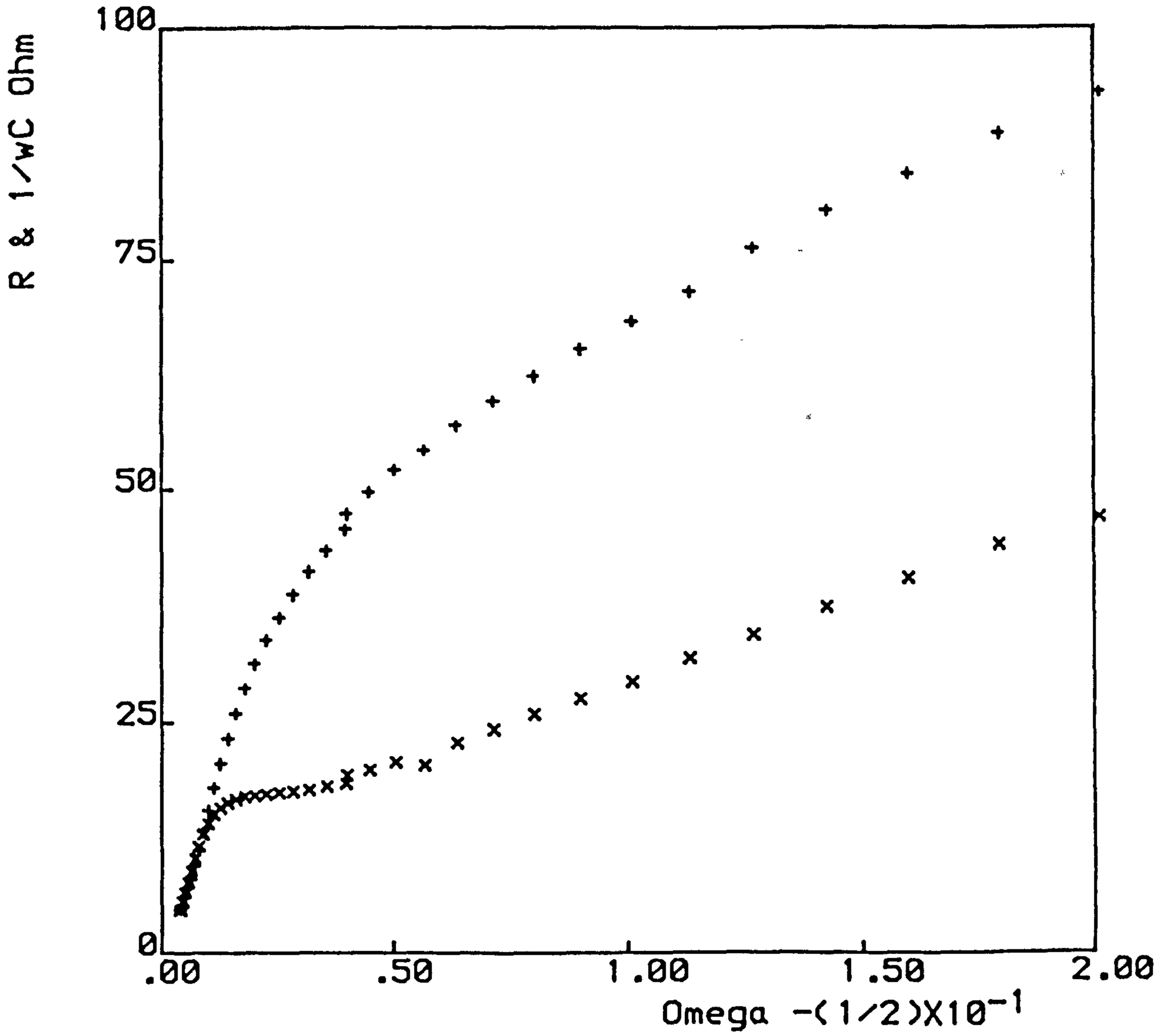

FIG. 6.26 Randles Plot:- Stationary zinc electrode in solution: 7.44M $(OH)^-$, 0.1M $Zn(OH)_4^{2-}$, 7.65M K^+. -1.382V, open circuit voltage.

<u>High Frequency Spectrum</u>

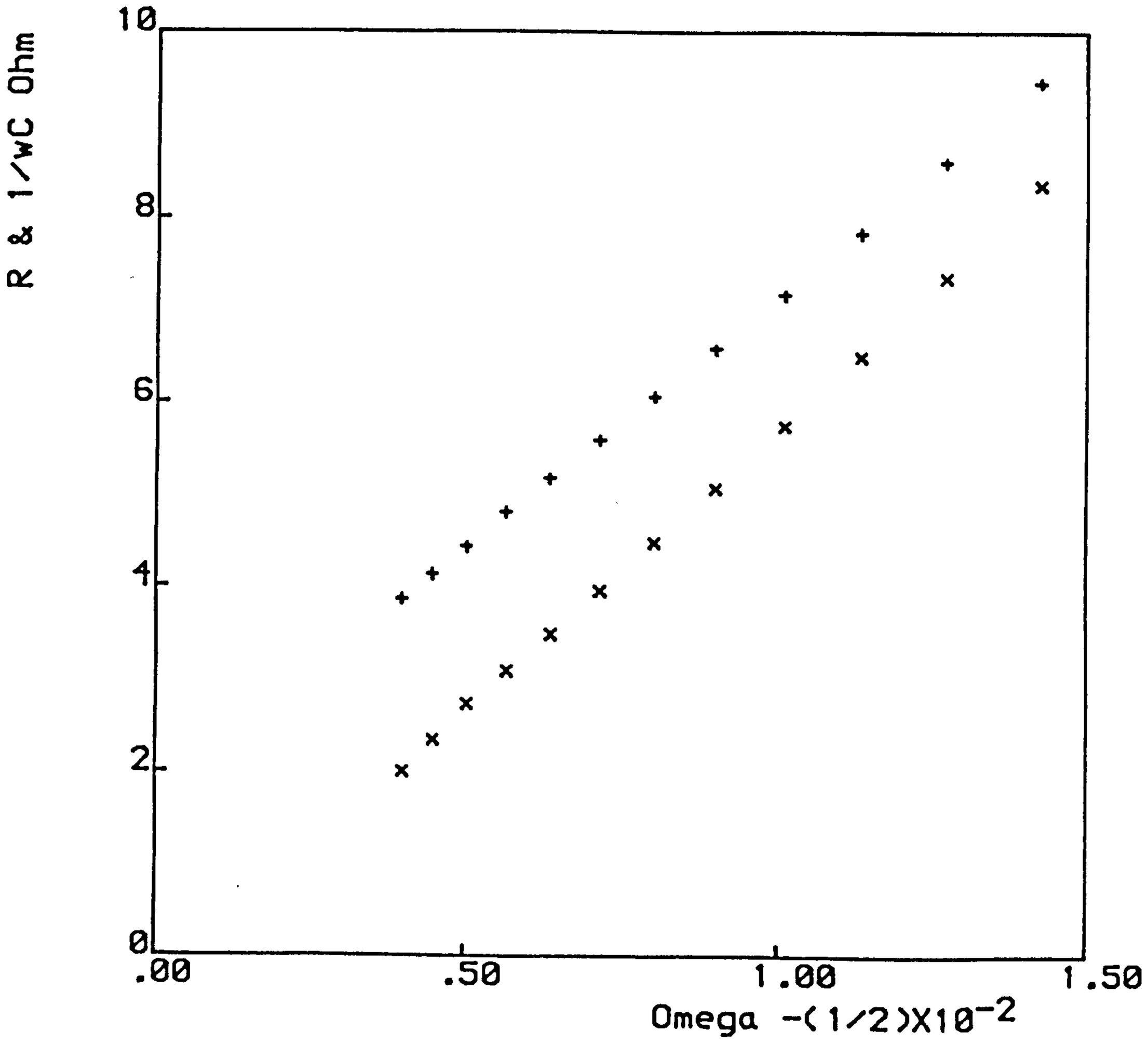

FIG. 6.27(a) Randles Plot:- Stationary zinc electrode in 7.44M KOH -1.432V. Open circuit voltage.

<u>High Frequency Spectrum</u>

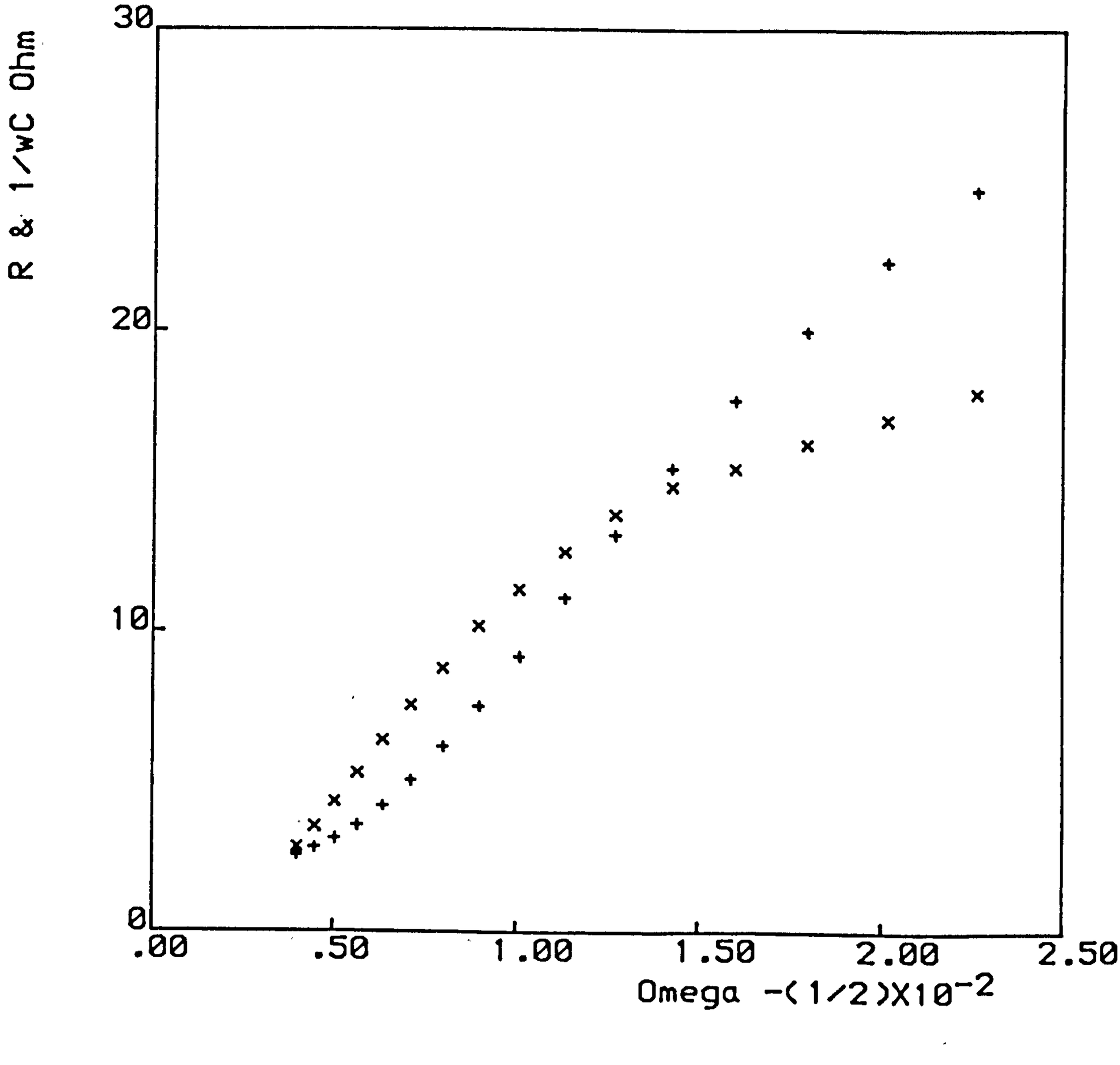

FIG. 6.27(b) Randles Plot:- Stationary zinc electrode in 7.44M KOH -1.432V. Open circuit voltage.

<u>Intermediate Frequency Spectrum</u>

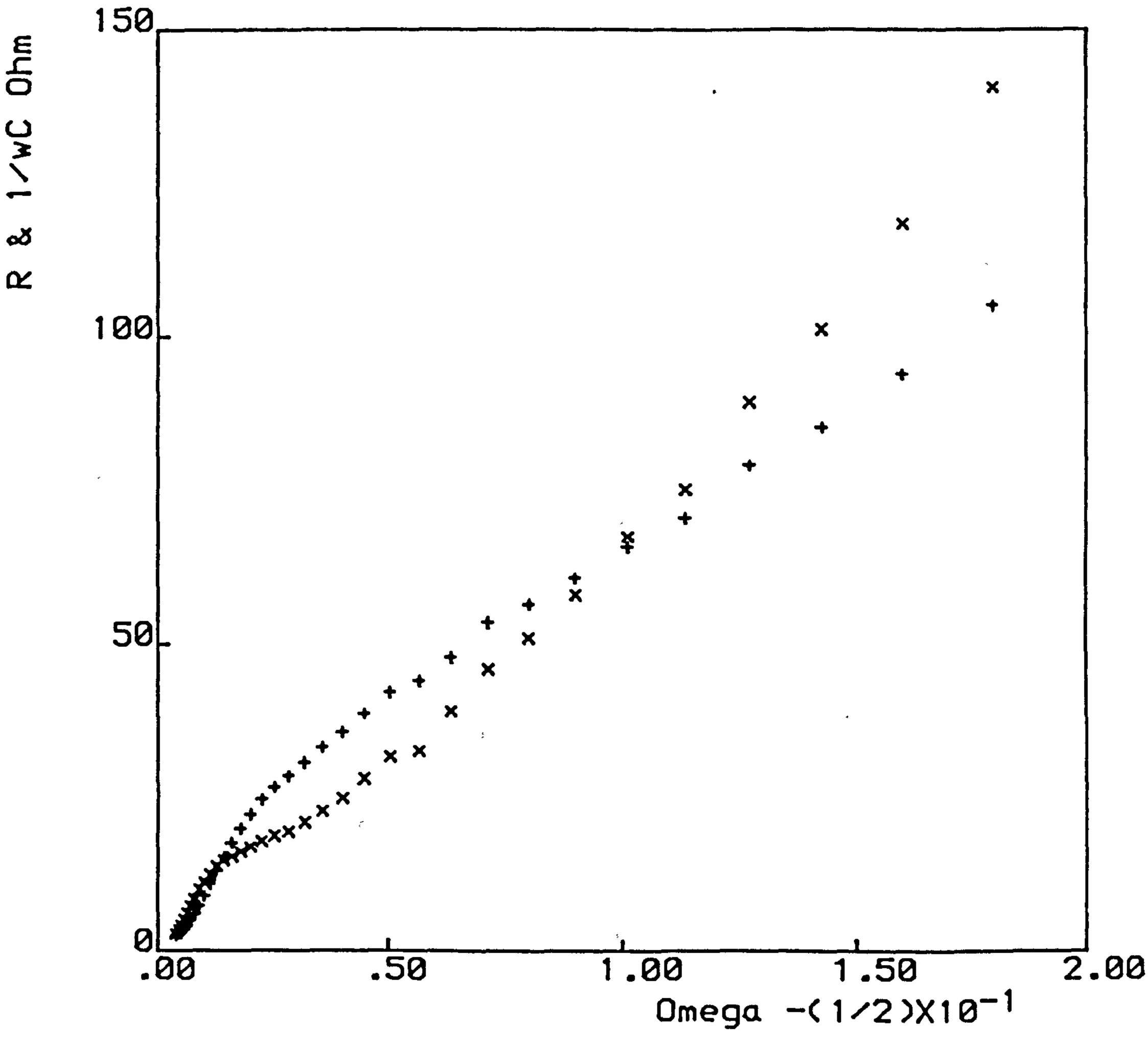

FIG. 6.27(c) Randles Plot:- Stationary zinc electrode in 7.44M KOH -1.432V. Open circuit voltage.

Complete Spectrum

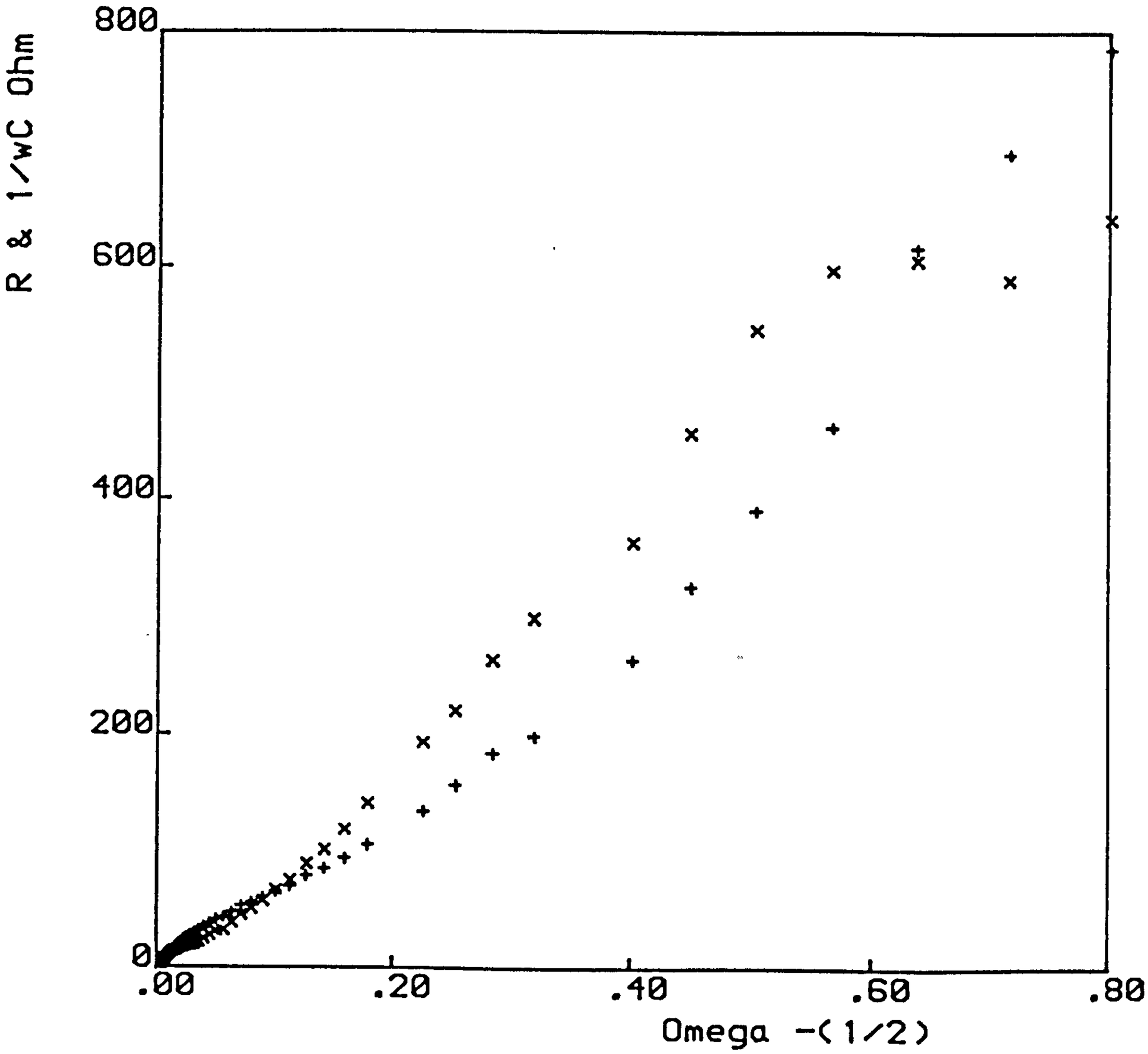

FIG. 6.28 Sluyters Plot:- Rotating zinc electrode, solution: 7.44M $(OH)^-$, 0.1M $Zn(OH)_4^{2-}$, 7.64M K^+
-1.382V, open circuit voltage

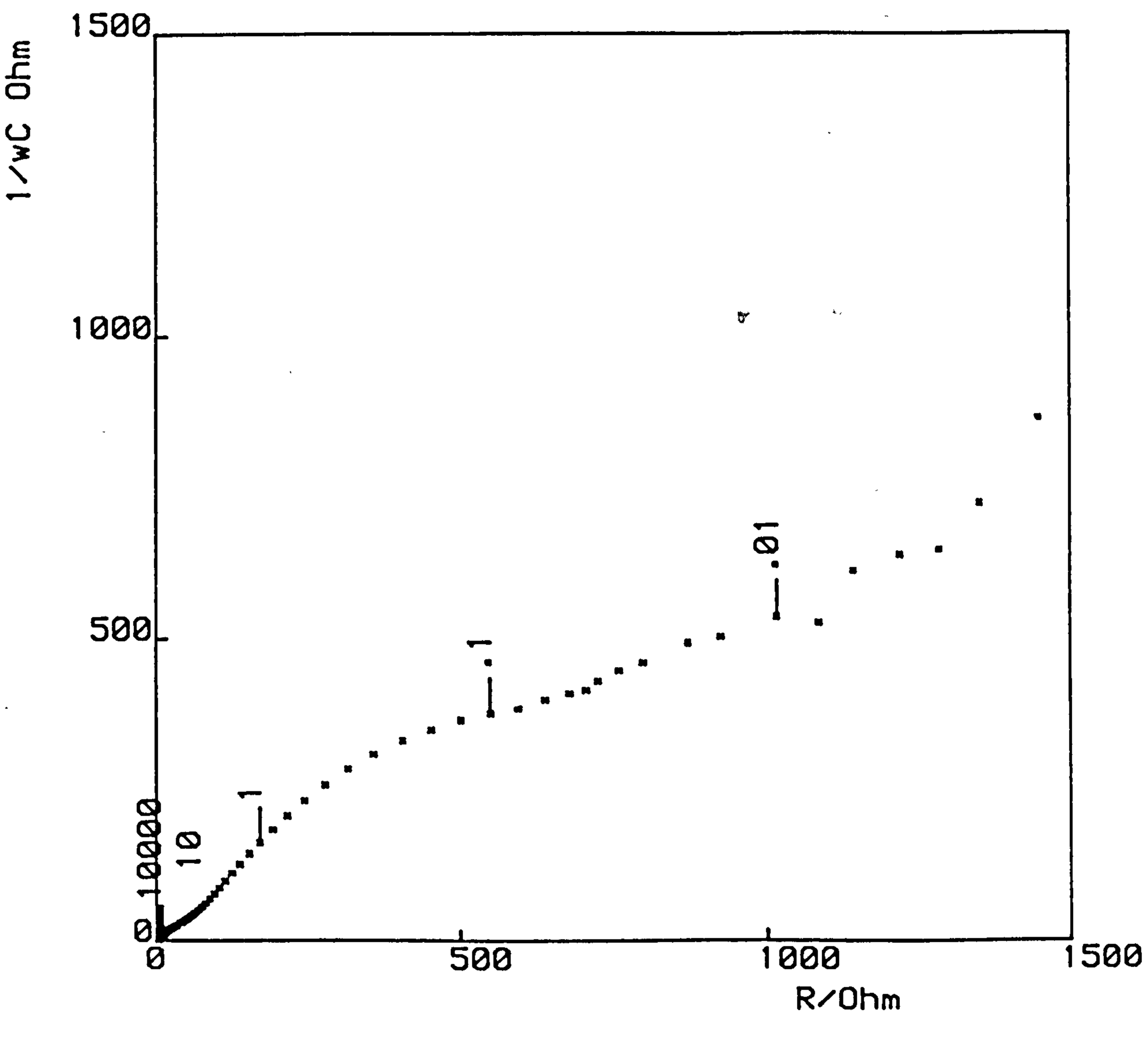

transfer effects are clearly observed (Fig. 6.26).

In KOH solutions without ZnO additions the capacitive component exceeds the resistive component at high frequencies (Fig. 6.27a), a phenomenon generally associated with adsorption. Detailed analysis shows that the capacitive and resistive components cross over at three frequencies, (Fig. 6.27a, b, c). The high frequency intersection (5434 Hz) can be seen from the corresponding Sluyters plot (Fig. 6.13) to occur in the charge transfer region and the adsorption may be attributed to the reactive intermediate. At lower frequencies the second intersection occurs at 107 Hz and the capacitive component once again exceeds the resistive component suggesting adsorption. The third intersection (2.5 Hz) appears on the Sluyters plot at slightly higher frequency than when the impedance was random. This second adsorption process appears to be the adsorption of hydrogen prior to gas evolution at the lower frequencies. Myers and Marchello[62] postulated a slow hydrogen adsorption step followed by discharge, following the mechanism:-

$$Zn^{\circ} + H^{+} + e^{-} \rightleftharpoons Zn(H)_{chem}$$

$$2Zn(H)_{chem} \rightleftharpoons 2Zn^{\circ} + H_2$$

The low frequency adsorption detected here can be explained by this mechanism.

A generally complicating factor in the experiments was the presence of the Warburg due to the diffusional processes at the electrode. Epelboin[113], and Armstrong and Bell[49] have made measurements on an electrode rotating fast enough for all the reaction products to immediately leave the reaction zone. Figure 6.28 shows the result of such an experiment at the equilibrium potential with the

electrode rotating (700 r.p.m.). At low anodic polarization the locus is elliptical in form with the low frequency points lying along the real axis (Fig. 6.29). At somewhat higher polarizations (Fig. 6.30) a familiar loop appears in the positive region of the capacitive-resistive plane, and at even higher polarizations (Fig. 6.31) the loop is shifted into the inductive part of the plane. In this locus the low frequency points were clearly returning to the real axis confirming that the Warburg contribution has been reasonably well removed by rotation.

The interesting shape emerging from the impedance loci on rotating electrodes is the inclined elliptical loop formed at low polarizations. Its shape and size result from a combination of kinetic and diffusional constants, and its form was extremely sensitive to the method of electrode pretreatment, (Fig. 6.32a, b, c). It is clear from the magnitudes of the impedance components that the effects of electrode films are clearly evident as a result of mechanical polishing and non-aqueous treatment. At this potential the exposure of a true unimpeded electrode surface is extremely difficult. The occurrence of the elliptical shape can be explained quantitatively only. At high frequencies the potential excursion does not sufficiently perturb the system to remove the film. At low frequency during the anodic cycle there is sufficient charge to remove the film and reveal the true electrode surface. At lower frequencies still this effect is intensified and the impedance moves towards lower resistances.

The results show that the uncontrolled surface effects can be considerable, increasing the impedance many times. The variability of electrode impedance was intensified as the concentration of Zn(II) in solution was decreased. The initial surface condition was maintained

FIG. 6.29 Sluyters Plot:- Rotating zinc electrode, solution: 7.44M $(OH)^-$, 0.1M $Zn(OH)_4^{2-}$, 7.64M K^+ -1.372V, O.C.V. + 10 mV.

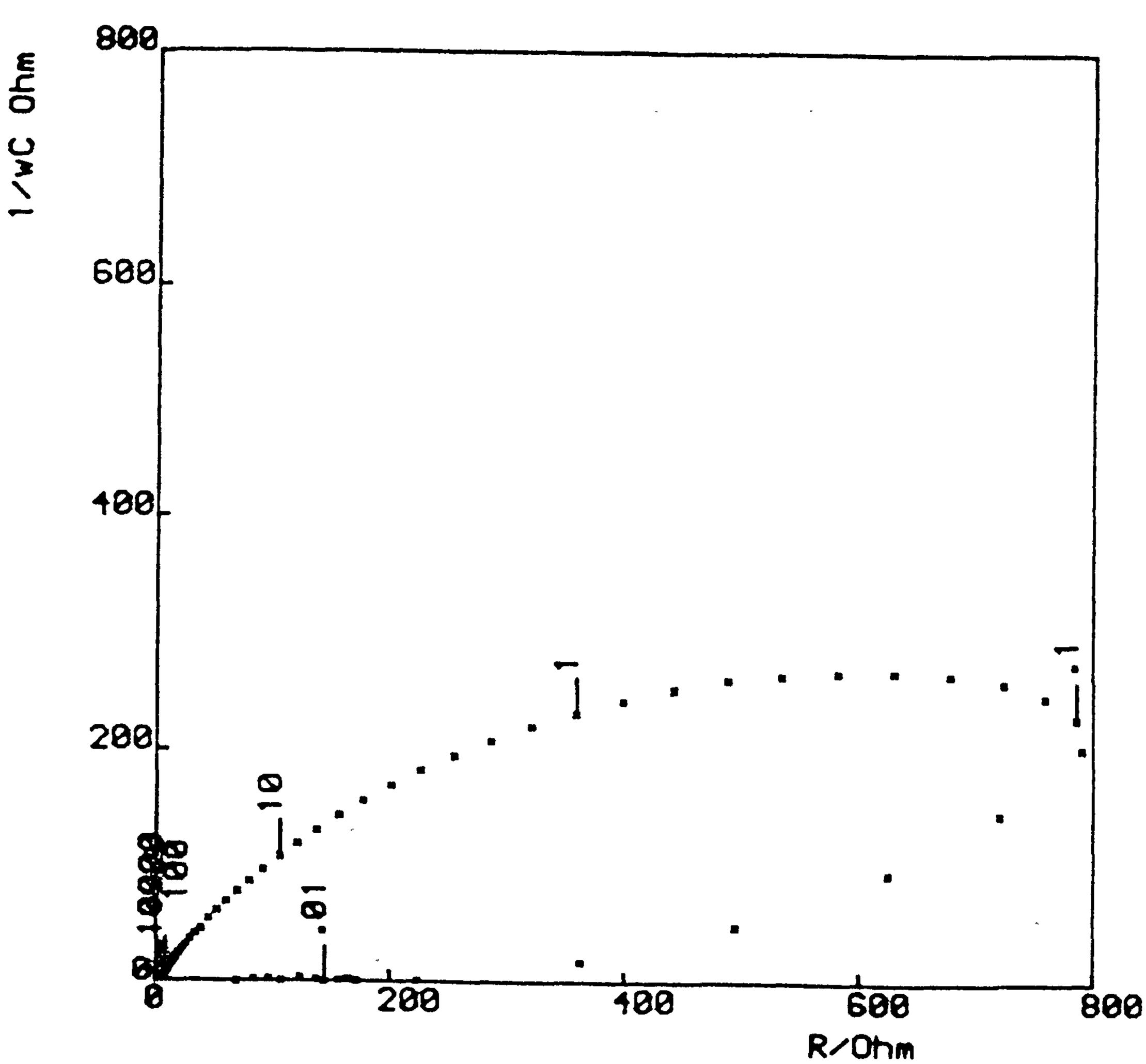

FIG. 6.30 Sluyters Plot:- Rotating zinc electrode, solution: 7.44M $(OH)^-$, 0.1M $Zn(OH)_4^{2-}$, 7.64M K^+ -1.362V, O.C.V. + 20 mV.

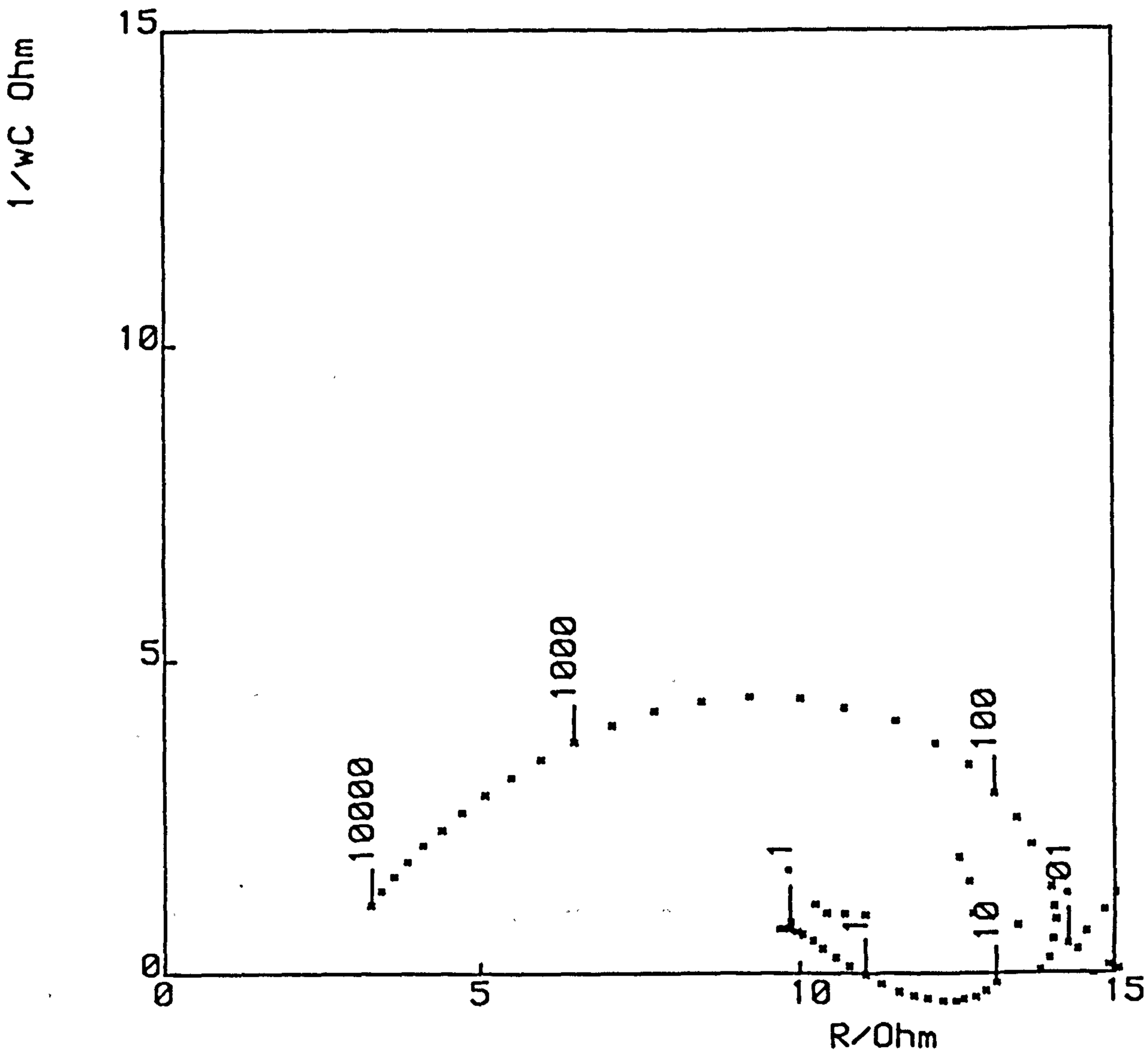

FIG. 6.31 Sluyters Plot:- Rotating zinc electrode, solution: 7.44M $(OH)^-$, 0.1M $Zn(OH)_4^{2-}$, 7.64M K^+ -1.357V, O.C.V. + 25 mV.

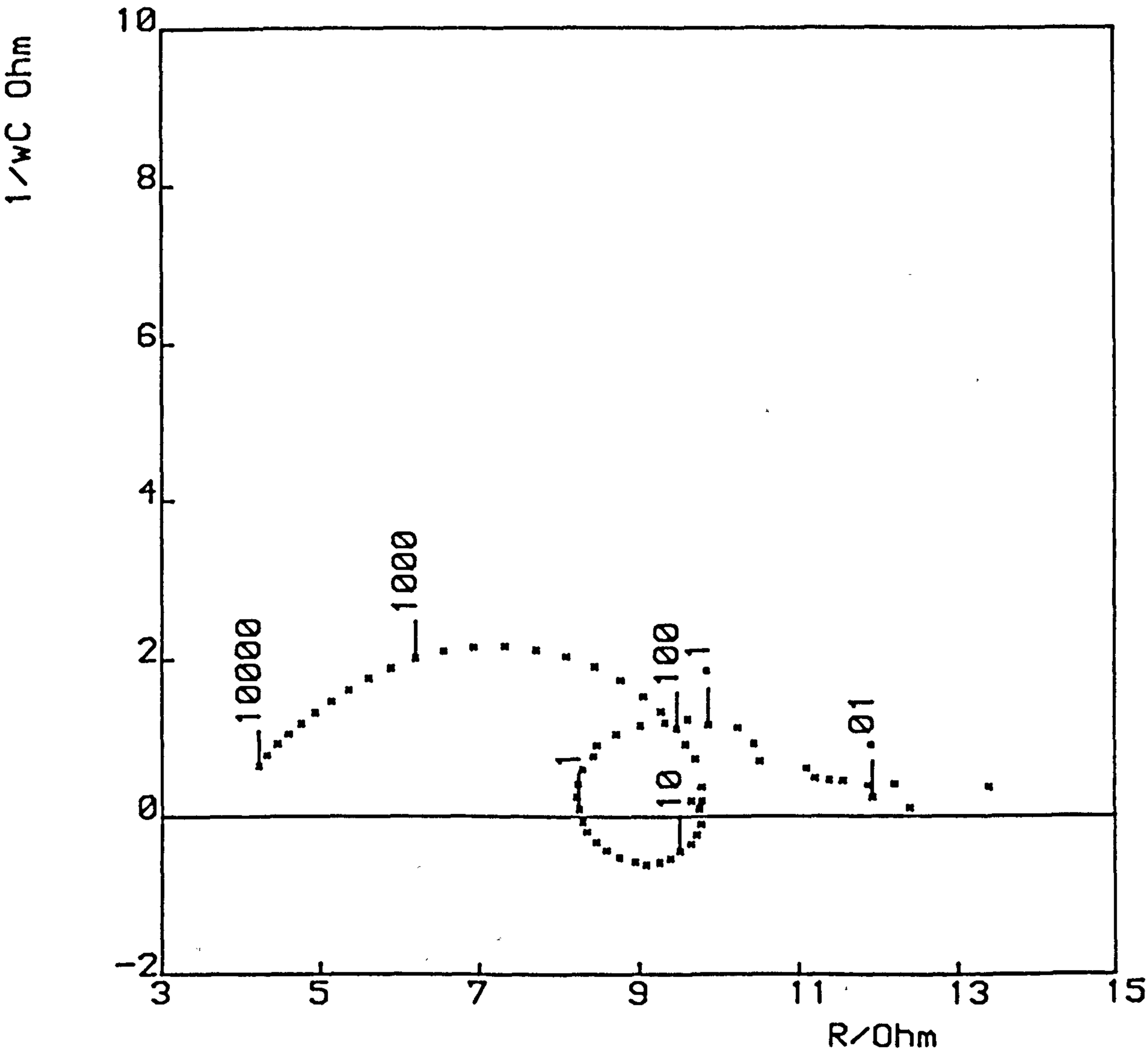

FIG. 6.32(a) Sluyters Plot:- Rotating zinc electrode, solution:
7.44M $(OH)^-$, 0.1M $Zn(OH)_4^{2-}$, 7.44M K^+
Mirror polish, no acetone wash
-1.372V, O.C.V. + 10 mV.

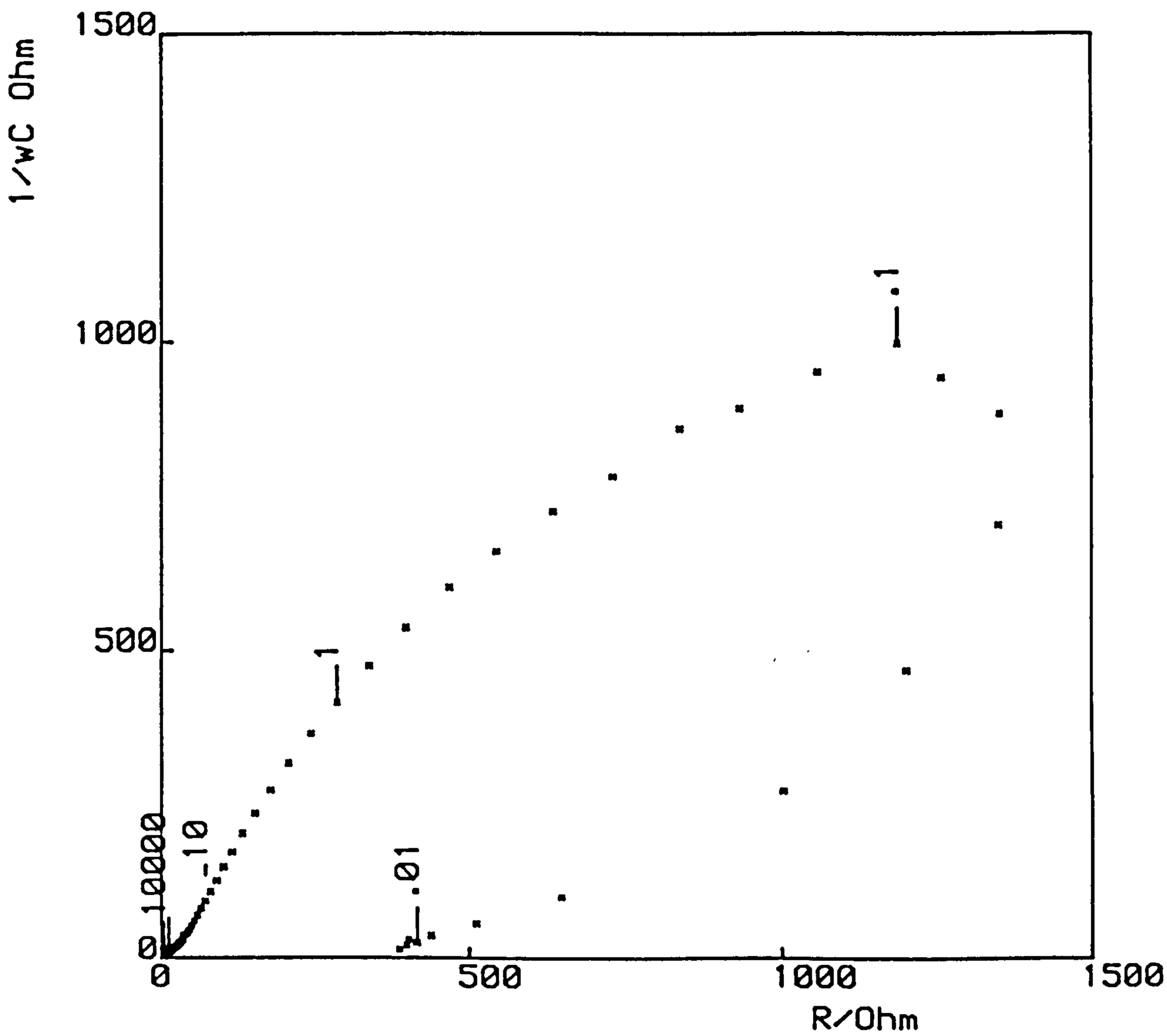

FIG. 6.32(b) Sluyters Plot:- Rotating zinc electrode solution:
7.44M $(OH)^-$, 0.1M $Zn(OH)_4^{2-}$, 7.64M K^+
$HClO_4$ Etch
-1.372V, O.C.V. + 10 mV.

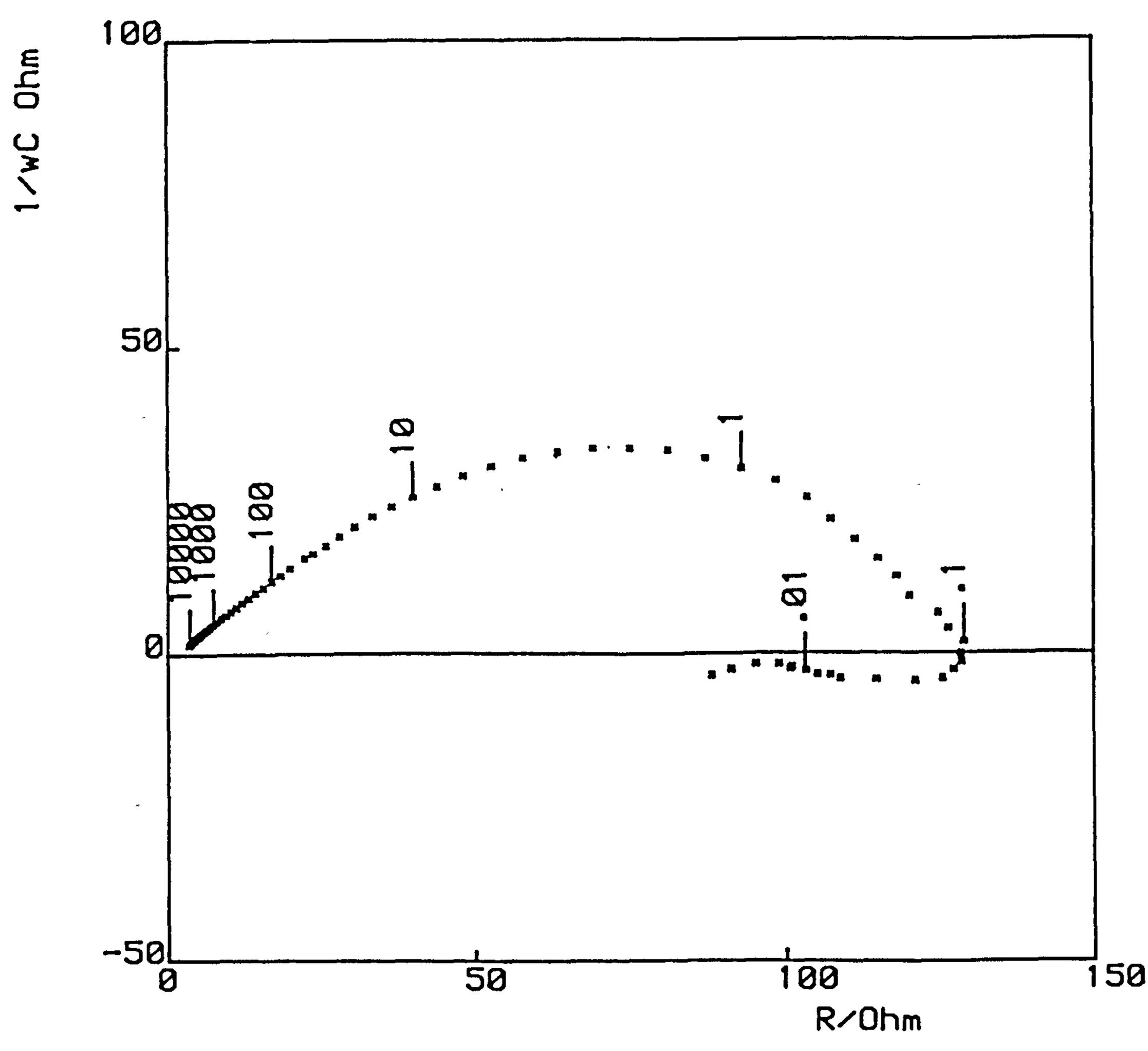

FIG. 6.32(c) Sluyters Plot:- Rotating zinc electrode solution:
7.44M $(OH)^-$, 0.1M $Zn(OH)_4^{2-}$, 7.64M K^+
HCl etch, prepol at -1.372V
Run -1.372V, O.C.V. + 10 mV.

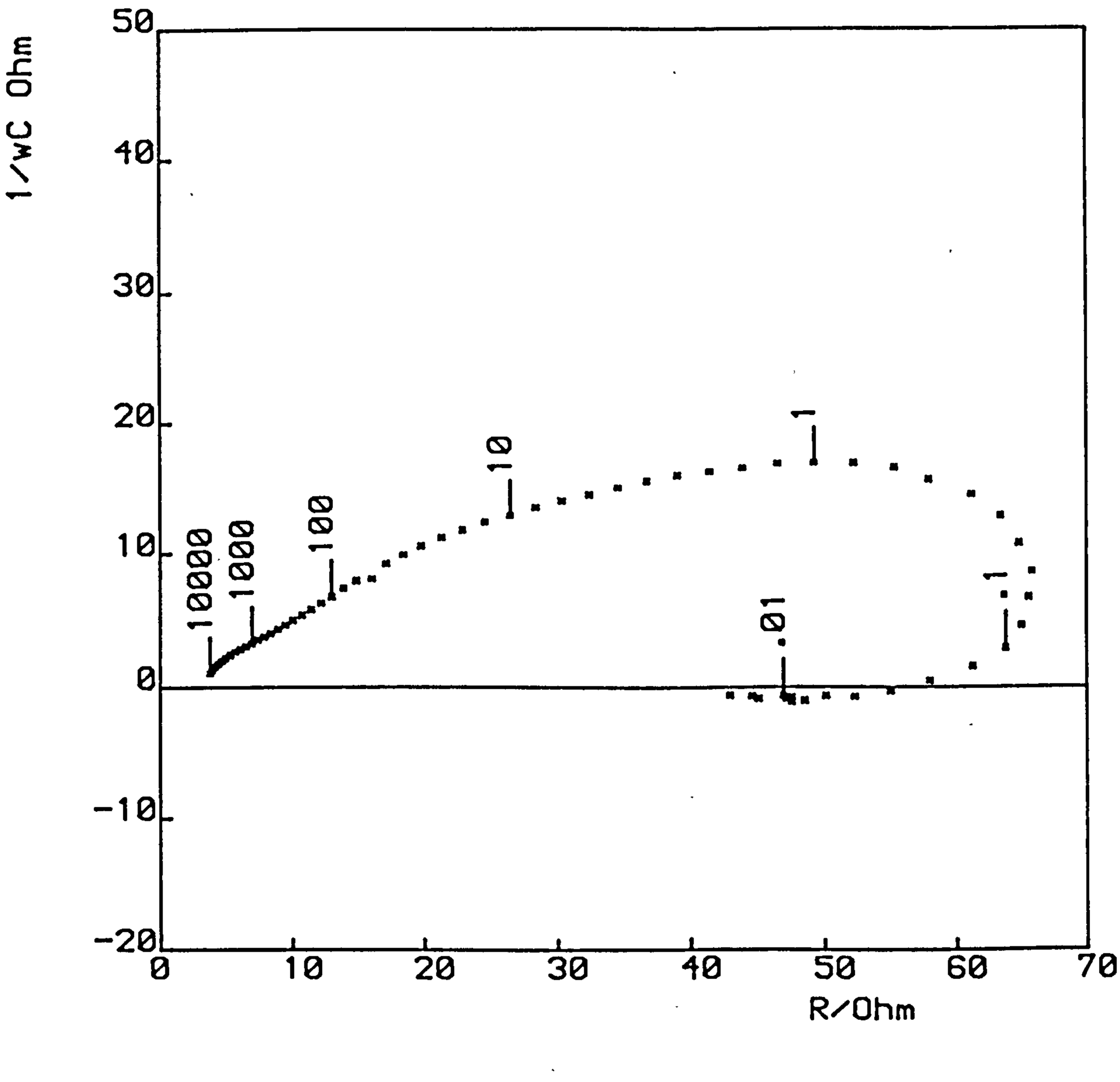

in the absence of a significant exchange reaction due to low Zn(II) concentration or low polarization. In the presence of an exchange reaction the surface structure of the electrode rapidly equilibrates, and a steady-state corresponding to the true interfacial state of the system results. A careful choice of electrode pre-treatment and reproducibility is required.

When the electrode is polarized the Sluyters plots and Randles plots indicate the presence of intermediates which may be adsorbed at the electrode surface if polarization is intense enough. These behaviours have been previously noted by Armstrong and Bell[49] for zinc in relatively dilute KOH. For Armstrong's experiments a frequency range down to mHz was sufficient to observe the whole of the electrochemistry. In the present experiments, the same range is not extensive enough, and often only fragments of the shapes noted by Armstrong are observed, (e.g. Fig. 6.20). Nevertheless, similar characteristics are evident; for small positive polarizations a loop in the positive region of the capacitive-resistive plane gives way to one partially in the inductive region at higher polarizations. Under the experimental conditions in the present study this latter feature is particularly well developed (Fig. 6.20).

The dependence of the rate of charge transfer on potential can be obtained by measuring the diameter of the high frequency semicircle (R_∞). This is approximately 33 mv decade^{-1} (Fig. 6.33), although there is a definite tendency for an increase in slope at the higher positive potentials. A plot of R_o (as defined by Armstrong) was found to have a 74 - 120 mv slope variation. The slope $\frac{\partial \ln R_o^{-1}}{\partial E}$ (Fig. 6.34) at an electrode rotating at a rate to suppress the Warburg is a function of potential, and gives a mean value of 70 mv decade^{-1}.

FIG. 6.33 Plot of $\text{Log}_{10} R_{,<}$ against the anodic overpotential of a stationary zinc electrode in solution containing 7.44M $(OH)^-$, 1M $Zn(OH)_4^{2-}$, 9.44M K^+.
Slope 33.5 mV decade^{-1}.

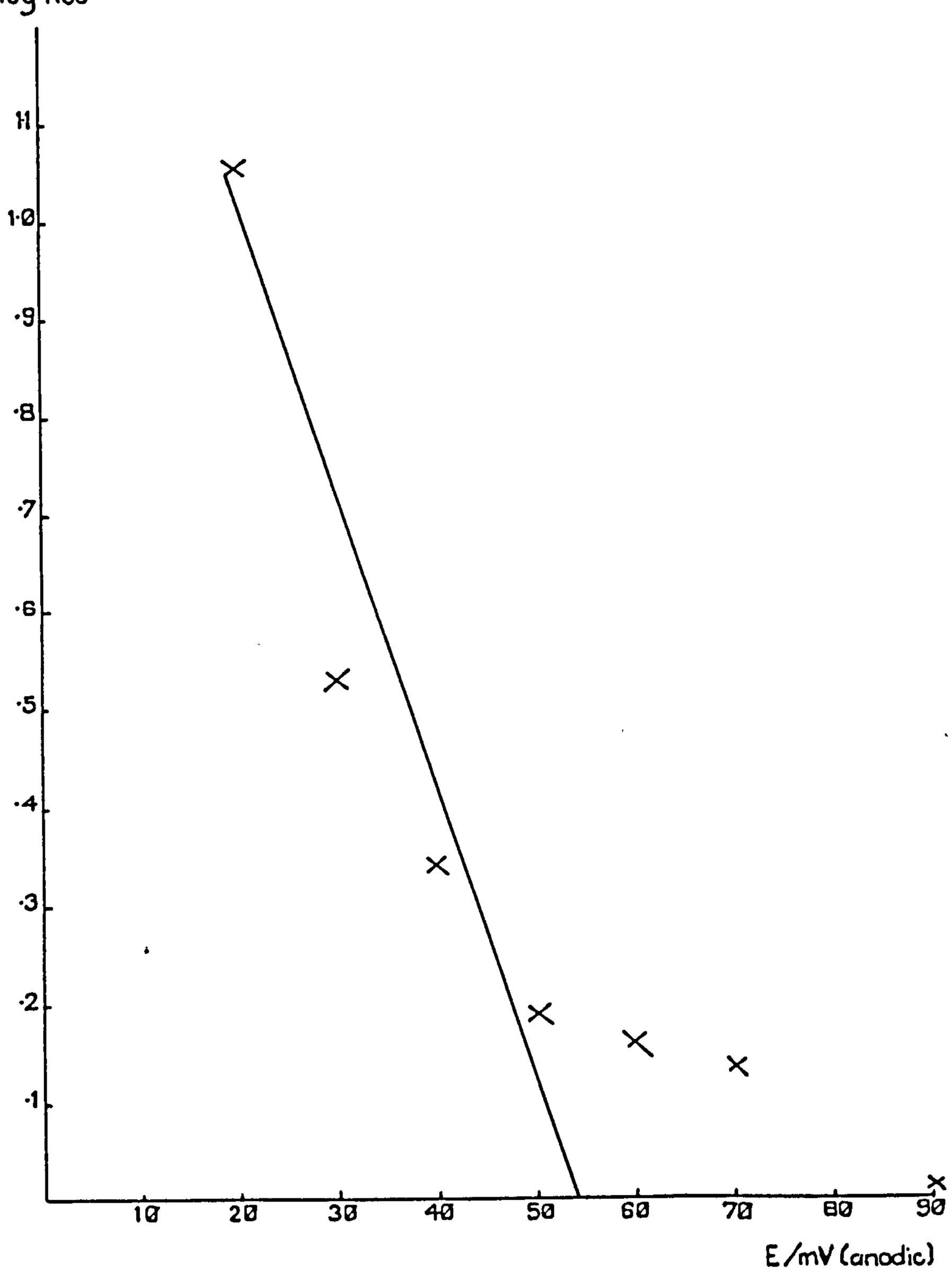

FIG. 6.34 Plot of Log ($^{1}/R_{o}$) against anodic overpotential for a stationary zinc electrode in 7.44M $(OH)_4^{2-}$, 1M $Zn(OH)_4^{2-}$, 9.44M K^+.
Slope 70 mV decade^{-1}.

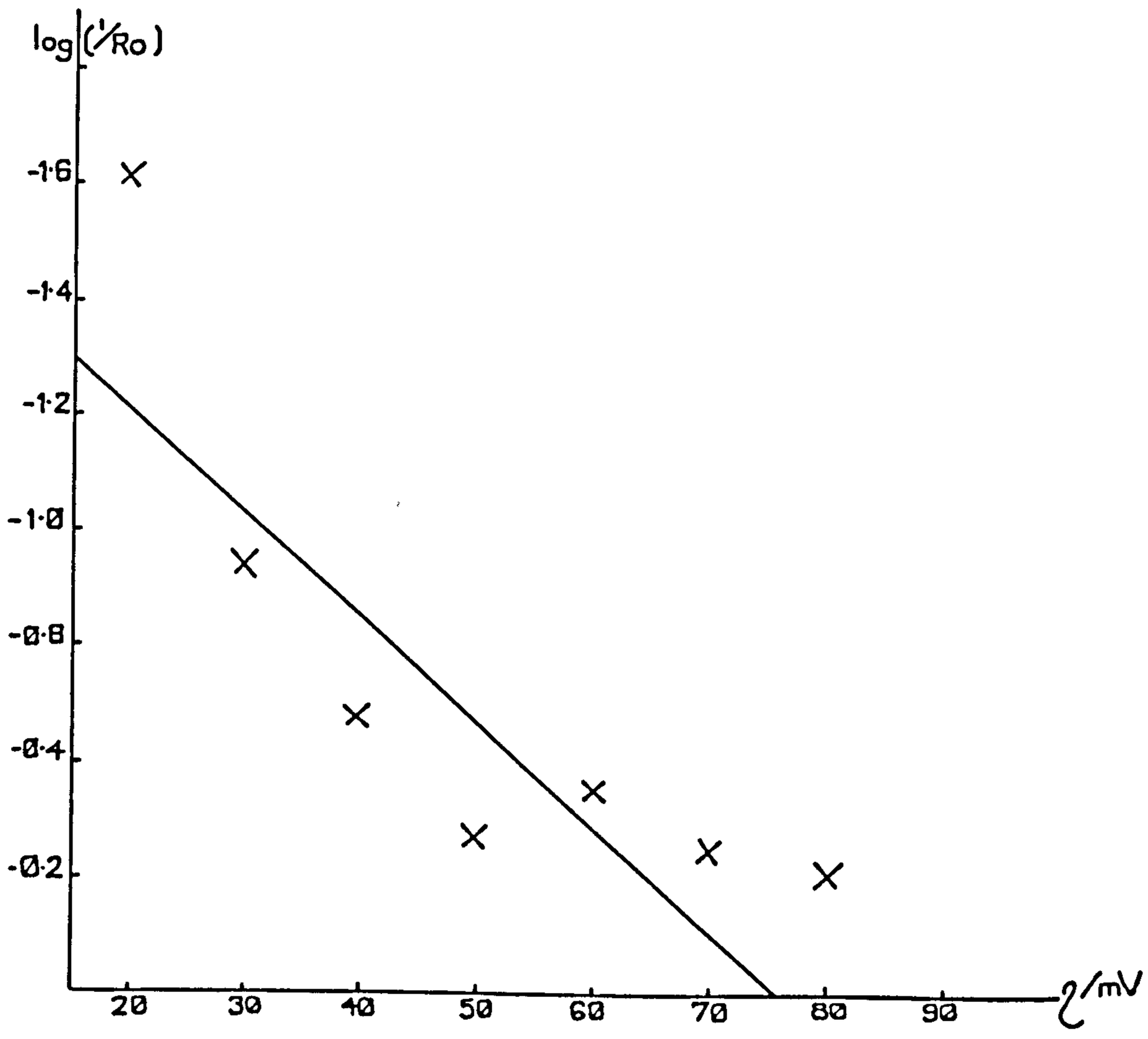

Clearly there is no potential independent Tafel slope to be found throughout the whole of the experimental range.

Armstrong and Henderson[44] have shown that for the case of an adsorbed intermediate

$$\frac{1}{R_\infty} = \left[n_1 F\left(\frac{\partial \nu_1}{\partial E}\right)_\Gamma + n_2 F\left(\frac{\partial \nu_2}{\partial E}\right)_\Gamma \right] \tag{6.3}$$

$$\frac{1}{R_o} = \tau \left[n_1 F\left(\frac{\partial \nu_1}{\partial \Gamma}\right)_E + n_2 F\left(\frac{\partial \nu_2}{\partial \Gamma}\right)_E \right] \left[\left(\frac{\partial \nu_1}{\partial E}\right)_\Gamma - \left(\frac{\partial \nu_2}{\partial E}\right)_\Gamma \right] \tag{6.4}$$

$$\tau = \left[\left(\frac{\partial \nu_2}{\partial \Gamma}\right)_E - \left(\frac{\partial \nu_1}{\partial \Gamma}\right)_E \right] \tag{6.5}$$

where if the reaction can be written as

$$A - ne \underset{k_1^1}{\overset{k_1}{\rightleftharpoons}} B - ne \underset{k_2^1}{\overset{k_2}{\rightleftharpoons}} C$$

the rates of reaction ν_1 and ν_2 can be expressed as

$$\nu_1 = k_1\left(1 - {}^{\Gamma}/_{\Gamma_s}\right) \exp f_1 E - k_1^1 \Gamma \exp - f_1^1 E \tag{6.6}$$

$$\nu_2 = k_2 \Gamma \exp f_2 E - k_2^1 c^\circ \left(1 - {}^{\Gamma}/_{\Gamma_s}\right) \exp - f_2 E \tag{6.7}$$

These equations assume that the adsorption of intermediate obeys a Langmuir isotherm where Γ_s represents the maximum surface coverage of intermediate. If $n_1 = n_2 = 1$ and we assume that $f_1 \sim f_1^1 \sim f_2 \sim f_2^1$ equations (6.3) - (6.5) can be rewritten as

$$\frac{1}{R_\infty} = Ff\left[k_1\left(1 - {}^{\Gamma}/_{\Gamma_s}\right) + k_1^1\Gamma + k_2\Gamma + k_2^1 c^\circ\left(1 - {}^{\Gamma}/_{\Gamma_s}\right)\right] \tag{6.8}$$

$$\frac{1}{R_o} = Ff\tau\left[k_2 + \frac{k_2^1 c^\circ}{\Gamma_s} - \frac{k_1}{\Gamma_s} - k_1^1\right] \left[k_1\left(1 - {}^{\Gamma}/_{\Gamma_s}\right) + k_1^1\Gamma - k_2\Gamma - k_2^1\left(1 - {}^{\Gamma}/_{\Gamma_s}\right)\right] \tag{6.9}$$

$$\tau = \left[{}^{k}/_{\Gamma_s} + k_1{}^{1} + k_2 + k_2{}^{1}\, C^{o}/_{\Gamma_s} \right] \qquad (6.10)$$

Equations 6.8 and 6.9 can be simplified if we introduce the steady state condition:

$$k_1 \left\{ 1 - {}^{\Gamma}/_{\Gamma_s} \right\} - k_1{}^{1}\Gamma = k_2\Gamma - k_2{}^{1}\, C^{o} \left\{ 1 - {}^{\Gamma}/_{\Gamma_s} \right\} \qquad (6.11)$$

$$\frac{1}{R_\infty} = \frac{2Ff(k_2{}^{1}C^{o} + k_1)(k_1{}^{1} + k_2)}{k_1{}^{1} + k_2 + {}^{k_1}/_{\Gamma_s} + {}^{k_2{}^{1}C^{o}}/_{\Gamma_s}} \qquad (6.12)$$

$$\frac{1}{R_o} = 2Ff\left[k_2 + \frac{k_2C^{o}}{\Gamma_s} + \frac{k_1}{\Gamma_s} + k_1{}^{1}\right]\left[k_1k_1{}^{1} - k_2k_2{}^{1}\, C^{o}\right] \qquad (6.13)$$

The low frequency semicircle will be inductive (i.e. R_o will be positive), when two conditions are fulfilled:

$$k_2 + \frac{k_2{}^{1}C^{o}}{\Gamma_s} > \frac{k_1}{\Gamma_s} + k_1{}^{1} \qquad (6.14)$$

$$k_1k_1{}^{1} > k_2k_2{}^{1}C^{o}$$

These equations can be expected to hold as long as the adsorption of the intermediate obeys a Langmuir isotherm, and that Γ is independent of the potential. What is observed in the present work is that at low overpotential there is a very high potential sensitivity of R_o which is reduced as the potential is made more positive. This can be understood if at the equilibrium the surface coverage with adsorbed intermediate is low, but increases with increasing potential to a maximum at about 100 mV positive of the equilibrium. This has the effect of making the second term in (6.9)

$$\Gamma_s\ (k_1{}^{1} - k_2)$$

and the whole of the equation is potential independent, if $k_2 \sim k_1/\Gamma_s$ assuming that at polarizations >100 mV the reverse constants are quite small.

The return of the Warburg to the real axis at low frequency was not observed in the present work irrespective of frequency. This would appear to be due to the highly reactive nature of the system. If there was a very high concentration of intermediate this may give rise to a capacitance component even at the lowest experimental frequency. Presumably the return of the Warburg to the real axis would have been observed at lower frequencies, if these had been available.

CHAPTER 7

PLANAR ZINC IN KOH WITH ADDITIVES

7.1. Introduction

The interest in additives that can modify the electrode reaction or the reaction layers in solution is intense, particularly when these can be applied to electrochemical energy conversion systems. A number of additives were used in the galvanostatic oxidation experiments to see whether any extended the time taken to passivation. Linear sweep voltammetry was used to examine the action of polymaleic acid. A.C. impedance measurements were made on solutions containing polymaleic acid and carbopol additives, and on amalgamated electrodes. Both carbopol and mercury are used at the present time in commercial cells.

7.2. Experimental

The electrodes were as described in section 6.2. Analar grade reagents were used where available, (Section 5.1.4.). A downward-facing zinc electrode was amalgamated by etching a rotating zinc disc (700 r.p.m.), in 10% HNO_3 (A.R. Fisons), adding triply distilled mercury (Alexander Pickering & Co.), to the solution after 30 seconds, and continuing to rotate for 5 minutes. A sample of the commercial electrolyte including carbopol was prepared, and the resulting gel pressed onto a recessed, planar electrode for some of the experiments.

The electrochemical techniques have been described in previous sections.

7.3. Results & Discussion

7.3.1. Galvanostatic Oxidation & Zinc Passivation

The zinc passivation data for the KOH electrolytes with various additives, are shown in Table 7.1.

TABLE 7.1

Zinc passivation data correlated in the form $i = kt^{\frac{1}{2}} + i_L$

Solution	$k(As^{-\frac{1}{2}}\ cm^{-2})$	$i_L(Acm^{-2})$	Correlation coefficient
7 M KOH	1.2827	0.0155	0.990
9 M KOH	1.3222	0.0077	1.000
7.07 M K^+, 7 M OH^-, 0.07 M Cl^-	1.2538	0.0178	0.9985
7.7 M K^+, 7 M OH^-, 0.7 M Cl^-	1.1696	0.0186	0.9989
7 M KOH + potassium silicate	1.3266	0.0080	0.9974
(specific gravity, 1.33)(25:1)	1.1890	0.0139	0.9965
	1.0217	0.0311	0.9628
7.3 M K^+, 7 M OH^-, 0.1 M PO_4^{3-}	1.2372	0.0146	0.9978
7.6 M K^+, 7 M OH^-, 0.2 M PO_4^{3-}	1.1856	0.0163	0.9988
7 M KOH + PMA (25:1)[a]	1.2197	0.0114	0.9993
7 M KOH + PMA (250:1)	1.3092	0.0173	0.9983

[a]PMA, polymaleic acid.

The addition of chloride ion is reported to leave the passivation times unaffected[92]. Table 7.1 shows that this is not so.

The addition of potassium silicate undoubtedly enhances the extent of active dissolution for a zinc electrode in alkali in a convection-dominated system[113,114]. It has been suggested previously[115] that the beneficial effects of the silicate must be sought in the solution phase characteristics. Table 7.1 shows that potassium silicate

additions to the electrolyte phase do not extend the active dissolution time for a zinc electrode under pure diffusion control. The data shows that very variable results are observed which depend to a large extent on the history of the electrolyte-electrode interaction. The effect of this was that a gelatinous cloud of zinc silicate formed around the electrode on prolonged contact. Occasionally the zinc electrode was observed to evolve a fine stream of hydrogen on open circuit. Attempts to trace this effect to the presence of impurities of low hydrogen overvoltage in the silicate solution were fruitless; however, these still cannot be ruled out. The disturbing feature of this effect was its unpredictability. However, the active dissolution was quite normal for systems not subjected to unduly long open-circuit stands. Table 7.1 shows that silicate had no beneficial effect on the time of the diffucion-controlled active dissolution.

We can conclude from this that the effect of silicate is vested in its effect on the convection equivalent current. An example of this would be if the flow of electrolyte over the face of the electrode was able to remove the particles of zinc oxide which block the electrochemistry and cause passivation.

The passivation time-current density data for KOH solutions with PO_4^{3-} additions is shown in Figure 7.1. From the values of the slopes it can be seen that the rate of dissolution, k, is largest in the straight-forward KOH solution, and decreases with increasing PO_4^{3-} concentration. It is recognised that there is a contribution due to the change in ionic strengths of the solutions, but in the concentration range considered, an increase in OH^- concentration would lead to an increase in k.

FIG. 7.1 Passivation time-current density data for KOH electrolytes containing $K_3PO_4.H_2O$: △ 7M w.r.t. OH^- ; □ 7M w.r.t. OH^-, 0.1M w.r.t. PO_4^{3-} ; ○ 7M w.r.t. OH^- , 0.2M w.r.t. PO_4^{3-}

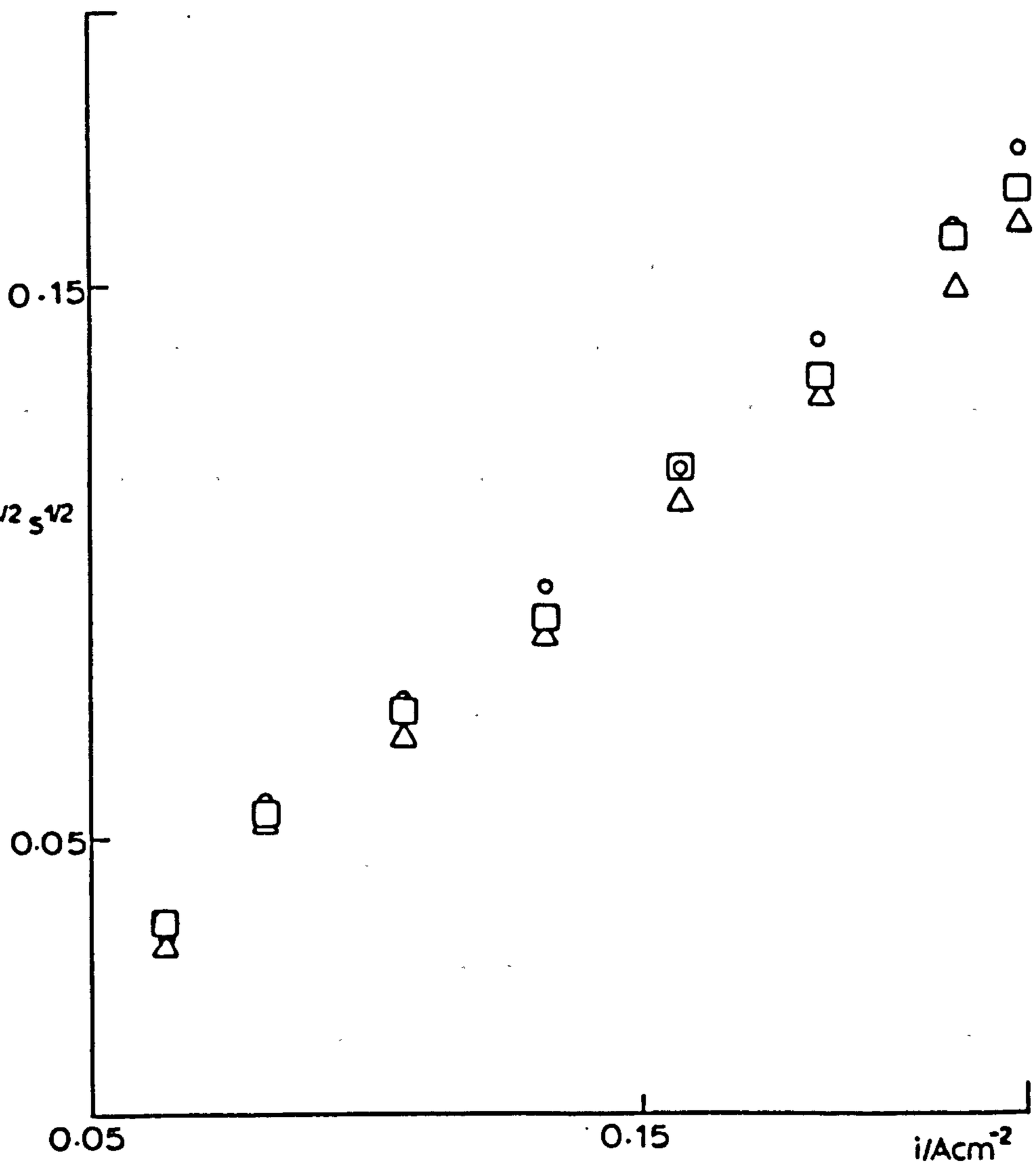

A compound of interest as a possible extender is polymaleic acid. This compound has been shown to modify the shape of $CaSO_4$ crystals to produce a spherical morphology, and there are also reports that it has the same effect on the morphology of oxidized iron, the particles being readily lost from the surface[116]. It is possible that the mechanism acts to change the shape of the zinc oxide particles to approximately spherical. Under such a modification the particles do not adhere to the substrate but are lost into the bulk. This is an effect very like the one observed in the "slurry region" of the zinc-silicate-KOH system in which a cloud of fine zinc oxide continually left the electrode. A number of experiments were made with KOH solutions containing polymaleic acid and Fig. 7.2 shows the passivation results in the completely diffusion-controlled system. Table 7.1 shows that the k value is largely unaffected. At low current density, when a certain degree of convection transport was present, there was, however, some evidence of enhancement.

From these experiments it was concluded that these additives were not suitable to increase the passivation time of zinc in alkali dissolving under completely diffusion controlled conditions.

7.3.2. Linear Sweep Voltammetry

The oxidation of zinc was examined on a downward-facing electrode in a KOH solution with polymaleic acid additive, to see whether any evidence of extender properties could be detected. The form of the transients on both anodic and cathodic excursion were very similar to those observed in 7M KOH solution, but generally the current was less at all potentials. Some current spikes were observed on anodic transients (Fig. 7.3) after the electrode had initially passivated

FIG. 7.2 Passivation time-current density data for KOH electrolytes containing polymaleic acid (PMA).

□ 7M KOH; o 7M KOH + PMA (25:1 $^{v}/_{v}$),

△ 7M KOH + PMA (250:1 $^{v}/_{v}$)

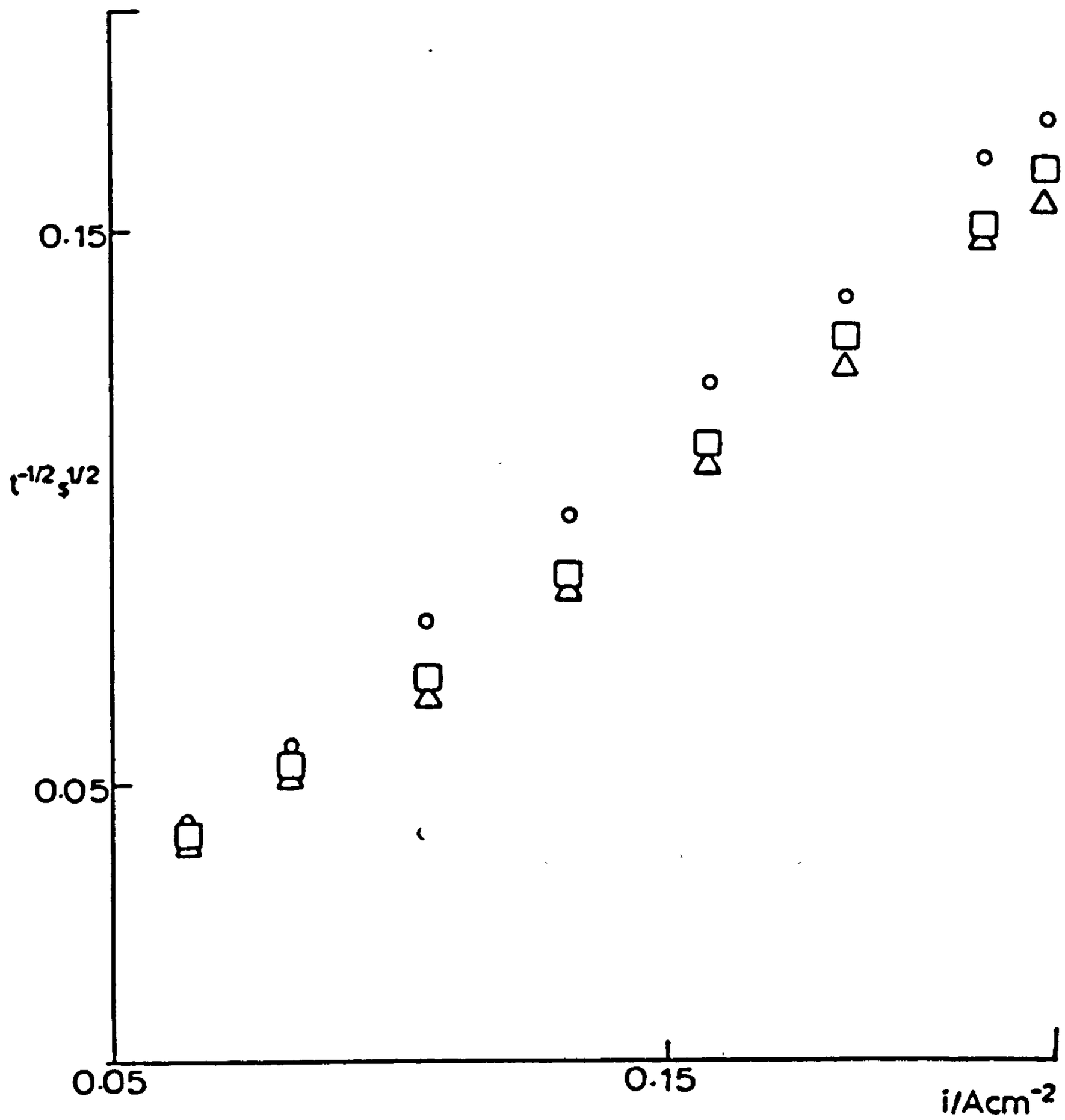

FIG. 7.3 Linear sweep voltammogram for zinc in 7M KOH with polymaleic acid additive.
Sweep rate 3 mVs^{-1}

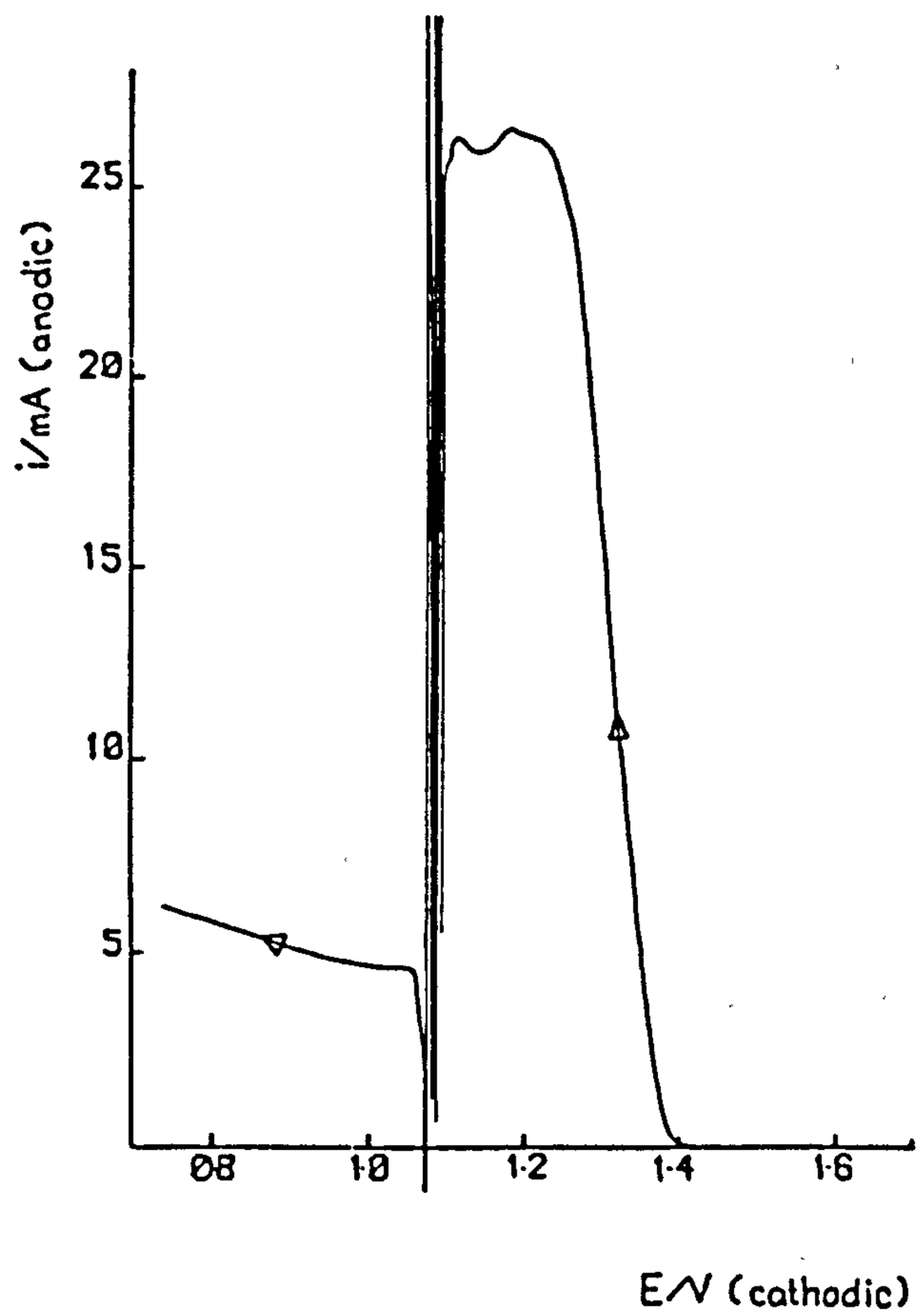

as well as on cathodic transients (cf on KOH alone, Section 6.3.2.). This indicates that with polymaleic acid the system is more active. The potential at which passivation occurred was similar between the two solutions, (KOH and KOH + P.M.A.), at the various sweep rates used.

The decrease in total current can be explained if the polymaleic acid is adsorbed at the electrode leaving a smaller area of exposed zinc for reaction. Current oscillations have been observed in KOH solutions, and are normally assigned to film breakdown and repair. The oscillations are increased in magnitude and frequency in the presence of polymaleic acid. If the 'extender' mechanism proceeded as suggested earlier (7.3.1.) by producing a layer of non-adherent particles, then the process of film breakdown would be exacerbated by polymaleic acid, and violent oscillations might be expected to occur. This process must rely on convection to transport loose particles from the electrode to the bulk of solution.

7.3.3. A.C. Impedance Measurements

A.C. measurements were made on 3 electrode/electrolyte systems:

i) planar zinc/7.44M OH^-, polymaleic acid, 1M $Zn(OH)_4^{2-}$

ii) planar zinc/7.44M OH^-, carbopol, 1M $Zn(OH)_4^{2-}$

iii) Zinc amalgam/7.44M OH^-, 1M $Zn(OH)_4^{2-}$

Figure 7.4 shows the impedance locus at the electrode rest potential with polymaleic acid additive. At low frequency the Warburg line is returning to the real axis indicating the increased establishment of convective diffusion (cf. Fig. 6.7). The pattern of an apparent smooth electrode giving rise to an apparently rough one at lower frequencies is again clearly demonstrated, with portions of the locus

FIG. 7.4 Sluyters Plot:- Stationary zinc electrode in solution: 7.44M$(OH)_4^{2-}$ 1M $Zn(OH)_4^{2-}$, 9.44 K^+, polymaleic acid.

-1.360V, open circuit voltage.

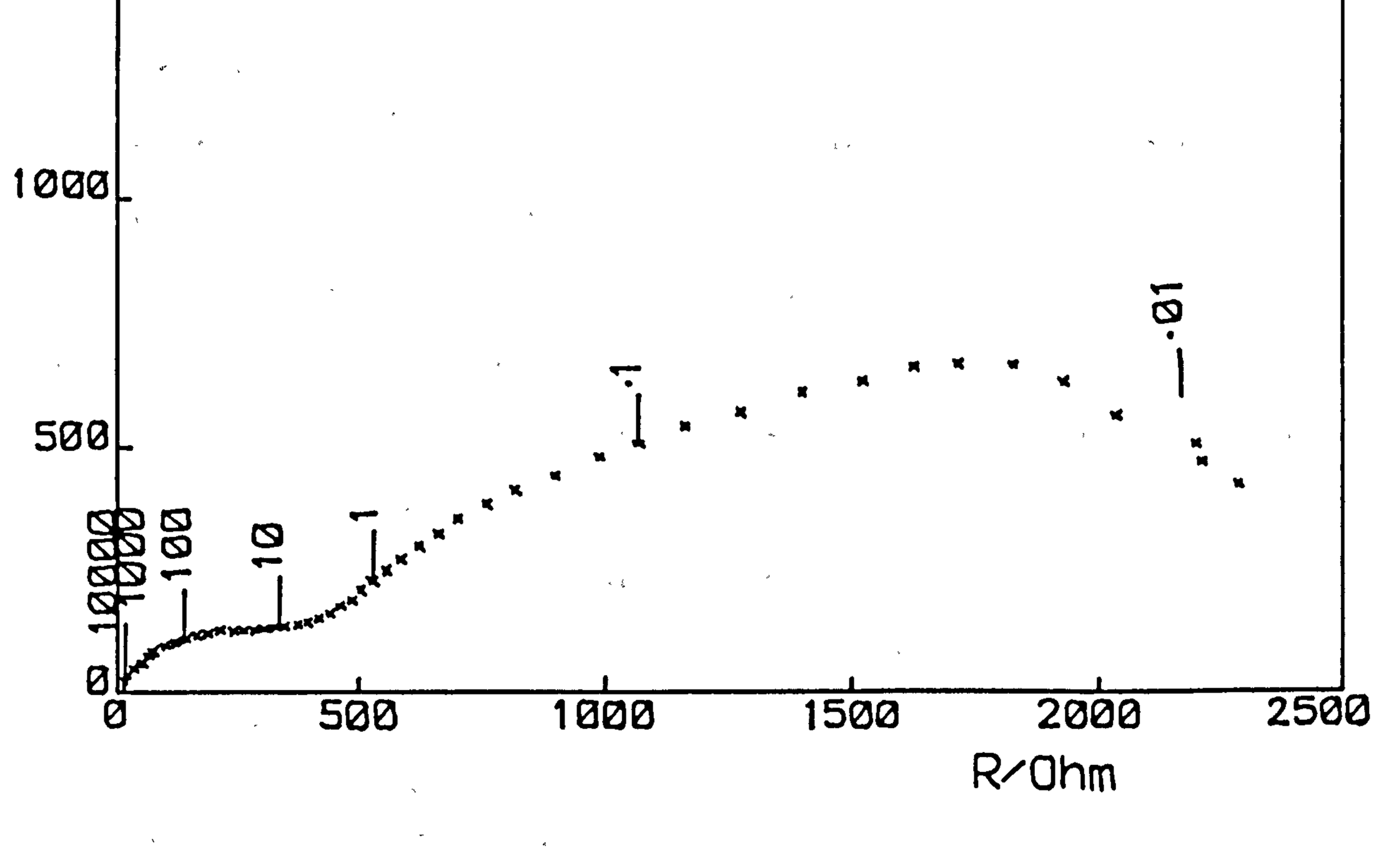

with dihedrals at 45° and 22.5° evident. It is also of considerable interest to note that polymaleic acid enhances the diameter of the high frequency semicircle suggesting that the presence of the organic additive is retarding the rate of reaction. On polarizing (Fig. 7.5a & b) the loci resemble those obtained in solutions without additive. It appears therefore that the polymaleic acid molecules, and hydroxide ions are both adsorbed on the electrode. At the rest potential polymaleic acid adsorption is in competition with hydroxide ion adsorption and the impedance locus shows an enhanced double layer capacitance. On polarization, hydroxide ion is more strongly adsorbed, and the contribution from polymaleic acid adsorption becomes negligable.

A Sluyters plot for a planar zinc electrode in contact with the electrolyte containing carbopol additive (commercial gel concentrations) is shown in Fig. 7.6. At intermediate frequencies a Warburg line with a 45° dihedral is observed, which reduces to 22½° at lower frequencies. This would be expected to return to the real axis at even lower frequencies, and it is clear that at the a.c. frequencies available only part of a locus similar to Fig. 7.4 is obtained. The different response at the same a.c. frequencies, between the two additives, indicates the way in which each has affected the hydrodynamics at the electrode.

The detailed plot of the high frequency end of the Sluyters plot (Fig. 7.7) reveals a high frequency semicircle. From the diameter of the semicircle the charge transfer resistance R_∞ was determined as 0.121Ω, an order of magnitude less than in KOH-ZnO solution, and two orders of magnitude less than with polymaleic acid. Clearly the carbopol is removing any resistive films from the zinc surface.

FIG. 7.5(a) Sluyters Plot:- Stationary zinc electrode in solution: 7.44M$(OH)_4^{2-}$, 1M $Zn(OH)_4^{2-}$, 9.44 K^+, polymaleic acid.
-1.340V, O.C.V. + 20 mV.

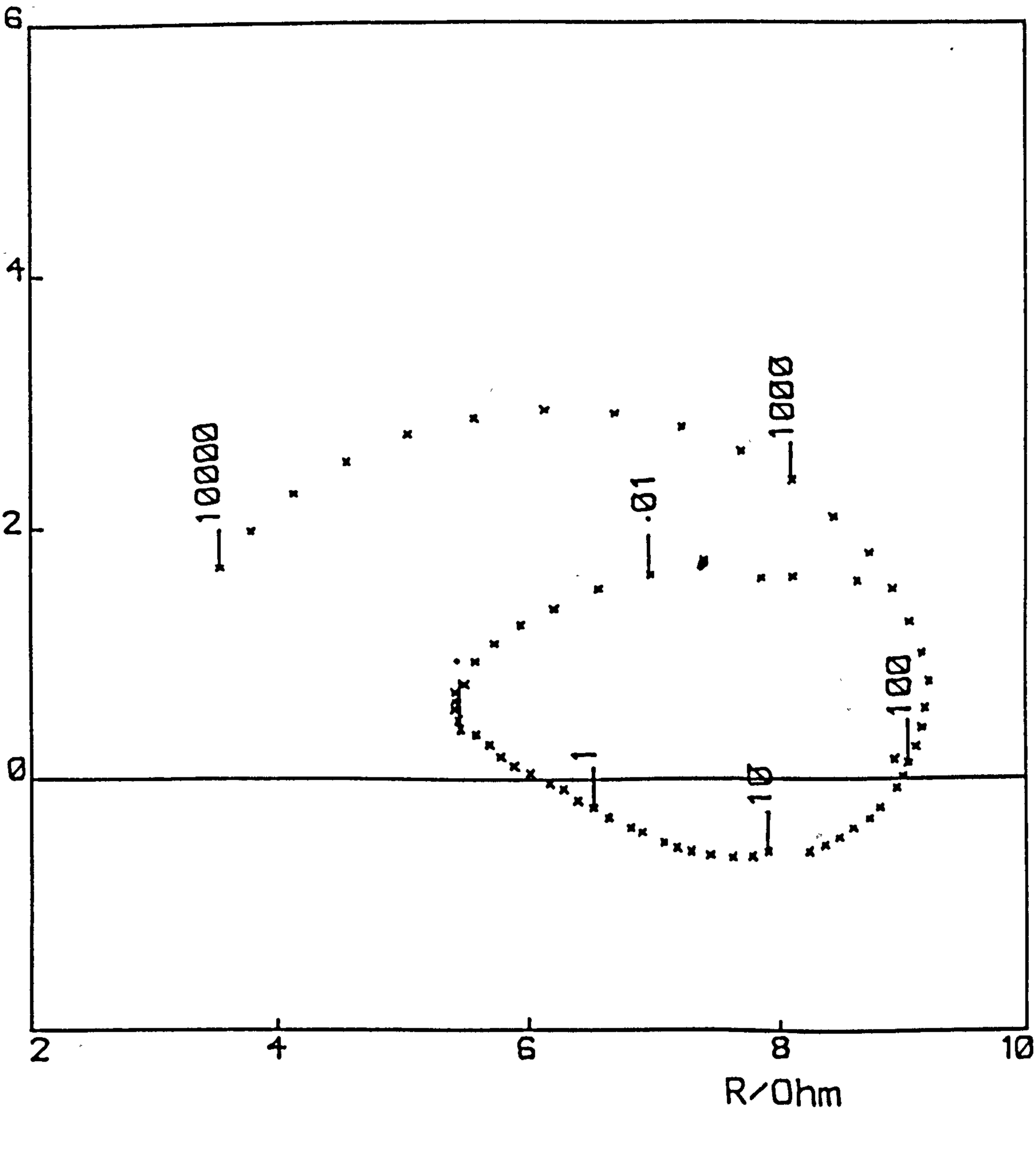

FIG. 7.5(b) Sluyters Plot:- Stationary zinc electrode in solution: 7.44M$(OH)_4^{2-}$, 1M $Zn(OH)_4^{2-}$, 9.44 K^+, polymaleic acid.
-1.320V, O.C.V. + 40 mV.

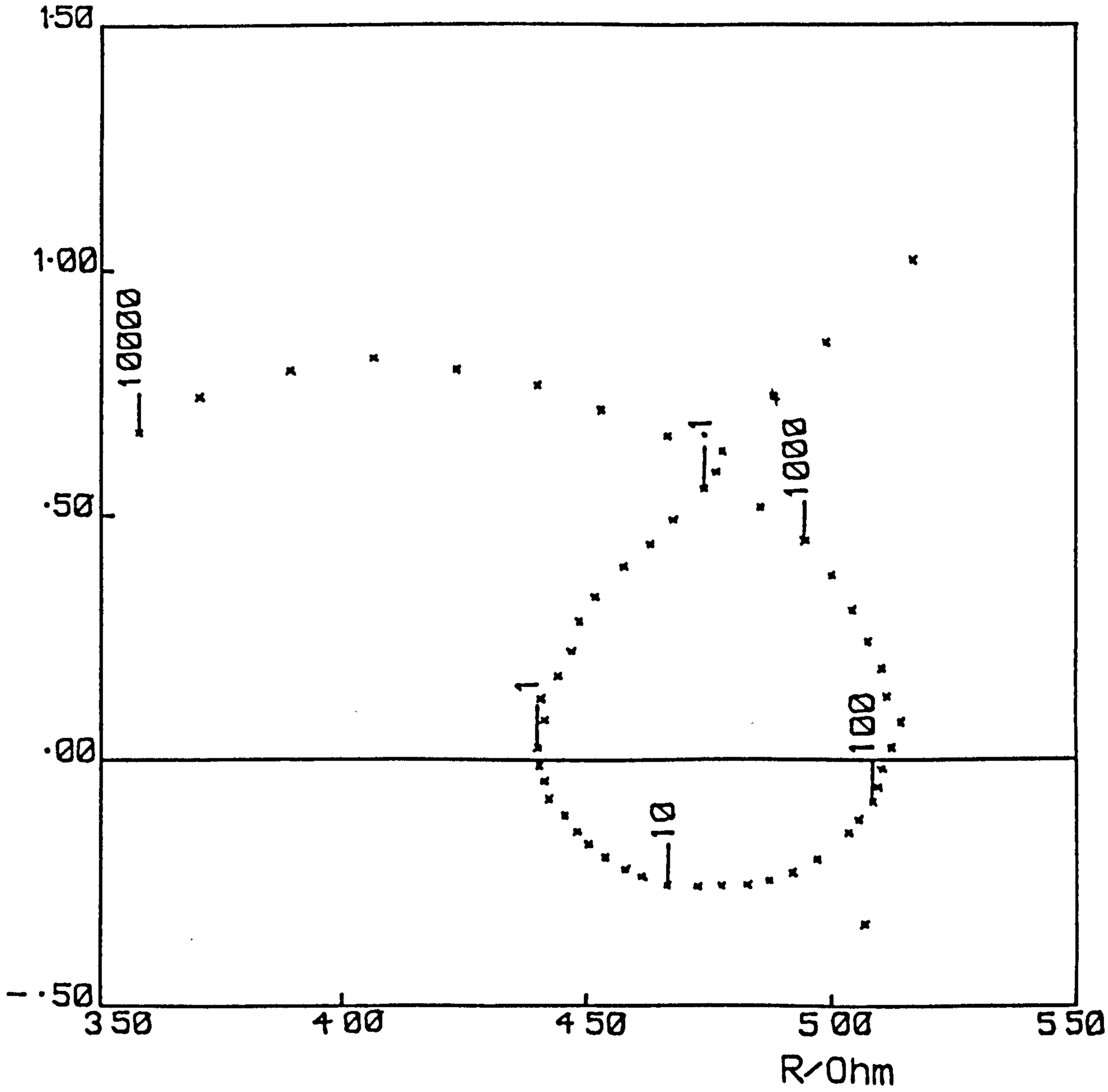

FIG. 7.6 Sluyters Plot:- Stationary zinc electrode, solution: 7.44M$(OH)_4$, 1M $Zn(OH)_4^{2-}$, 9.44M K^+, carbopol.
-1.360V, open circuit voltage.

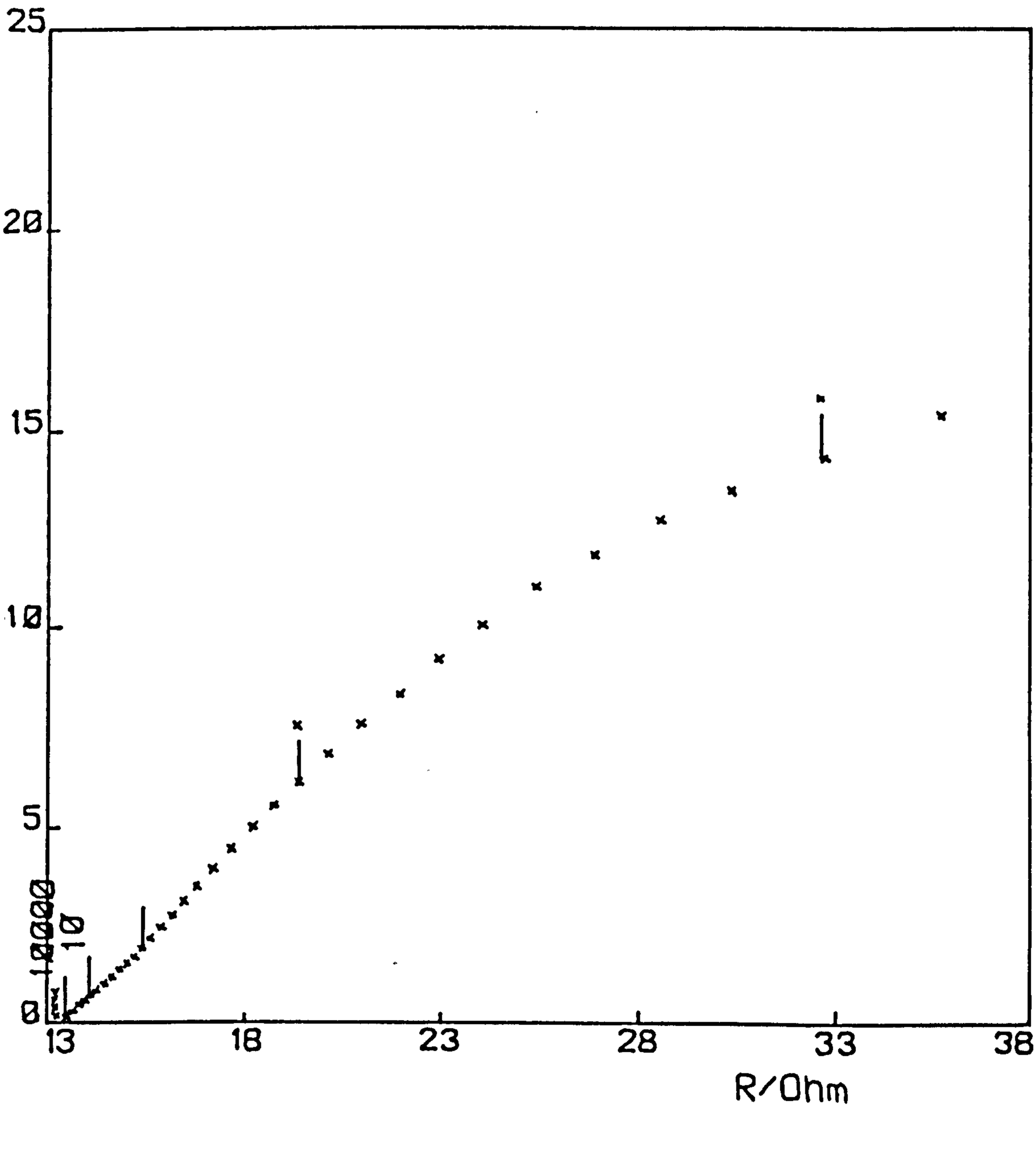

FIG. 7.7 Sluyters Plot:- Stationary zinc electrode, solution: 7.44M$(OH)_4$, 1M $Zn(OH)_4^{2-}$, 9.44M K^+, carbopol.
-1.360V, open circuit voltage. <u>High Frequency Spectrum</u>

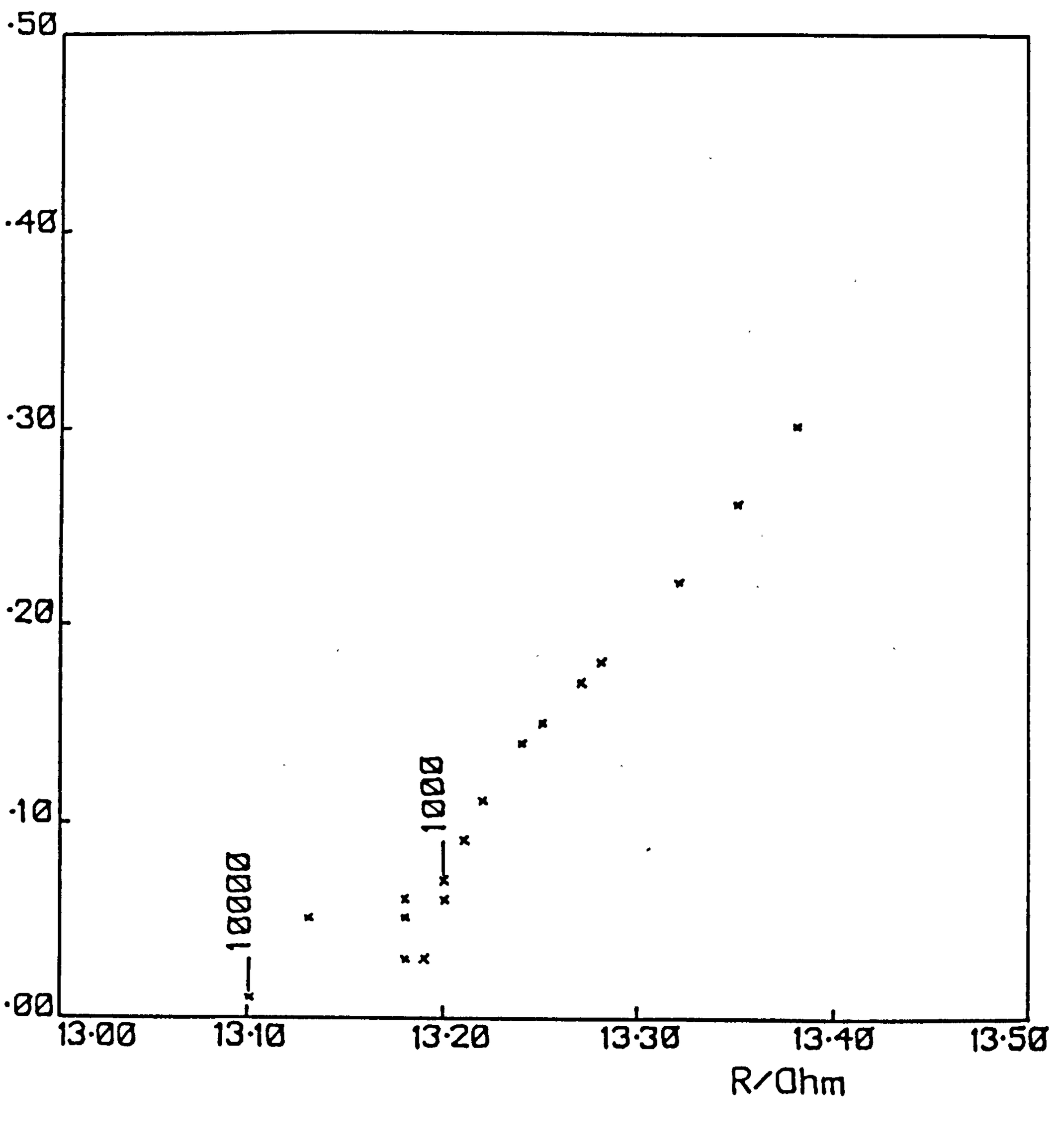

Figure 7.8 shows the Sluyters plot for the zinc/KOH-$Zn(OH)_4^{2-}$ system with mercury added to the zinc electrode. A 45° dihedral for the Warburg line is seen at intermediate frequencies tailing over towards the real axis at low frequencies. At high frequency only a small portion of the semicircle due to charge transfer is observed, indicating that the exchange reaction is very fast indeed. Only an estimate of the charge transfer resistance can be obtained, (approx. 0.8Ω). If the highest available experimental frequency is taken as the maximum of the semicircle, then from (3.34) the double layer capacitance is 271 μF cm^{-2}, which is of the expected magnitude for the system.

The Warburg coefficients were obtained from the Randles plots as the gradients of the capacitive lines for the KOH-$Zn(OH)_4^{2-}$ solution (Fig. 6.23), the KOH-$Zn(OH)_4^{2-}$ solution with carbopol additive (Fig. 7.9), and for the KOH-$Zn(OH)_4^{2-}$ solution with the amalgamated electrode (Fig. 7.10). From equation (6.2) if the geometric area is taken as the surface area of the electrode then the apparent diffusion coefficients shown in Table 7.2 are obtained.

TABLE 7.2

System	Warburg Coefficient, σ, (Ω)	Apparent Diffusion Coefficient ($cm^2\ s^{-1}$)	Apparent Area (%)
Zn/KOH-$Zn(OH)_4^{2-}$	238.89	7.78×10^{-12}	0.088
Zn/KOH-$Zn(OH)_4^{2-}$ - carbopol	4.88	1.86×10^{-8}	4.31
Zn(Hg)/KOH-$Zn(OH)_4^{2-}$	0.58	1.30×10^{-6}	36.15

The calculated values of the diffusion coefficient are well below those normally expected in aqueous solution, (approx. 10^{-5} $cm^2\ s^{-1}$). The zinc system without additives in particular gives an unexpected

FIG. 7.8 Sluyters Plot:- Stationary zinc amalgam electrode, solution: 7.44M $(OH)^-$, 1M $Zn(OH)_4^{2-}$, 9.44M K^+. -1.360V, open circuit voltage.

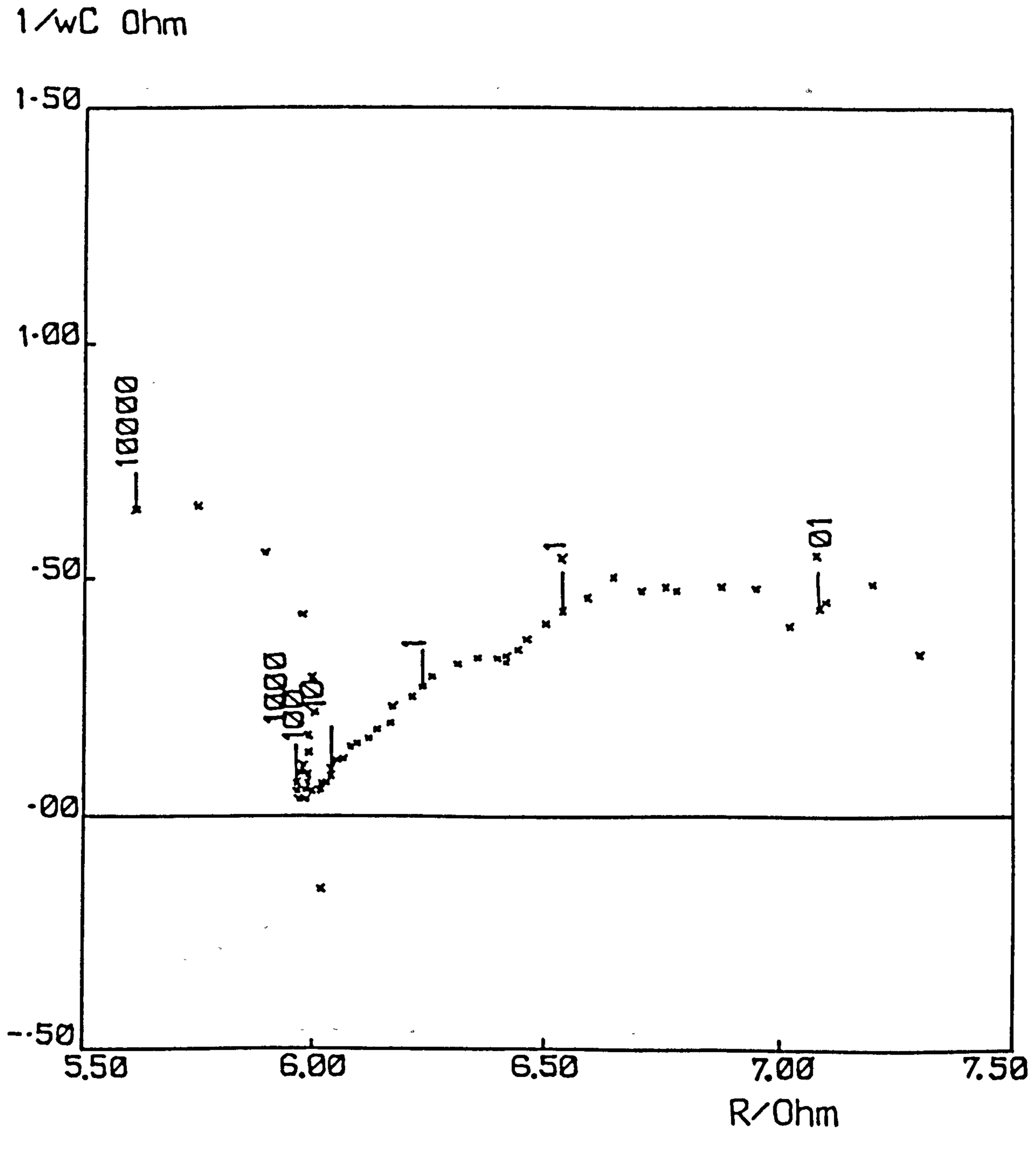

FIG. 7.9 Randles Plot:- Stationary zinc electrode, solution: 7.44M$(OH)^-$, 1M $Zn(OH)_4^{2-}$, 9.44 K^+, carbopol. -1.360V, open circuit voltage.

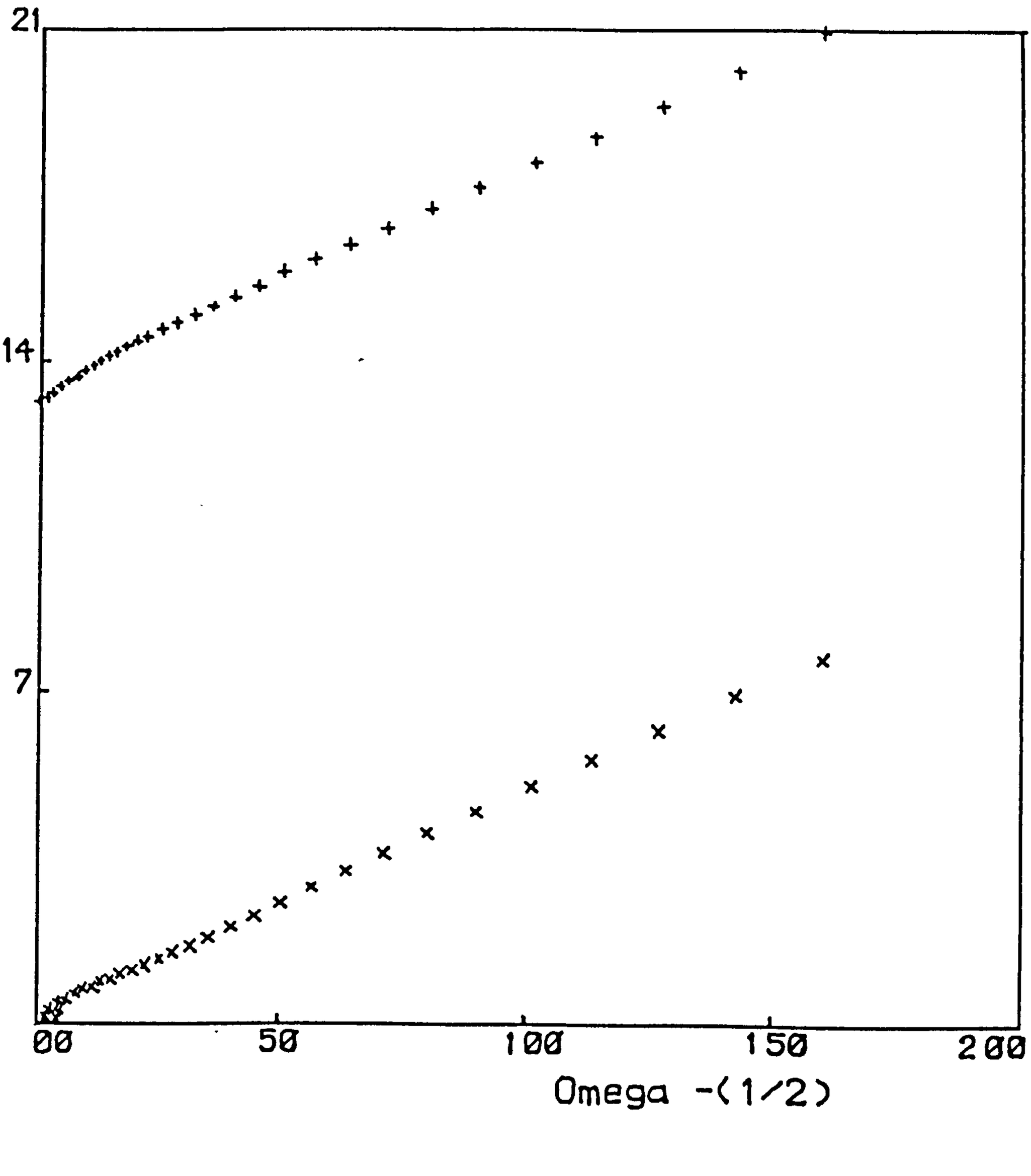

FIG. 7.10 Randles Plot:- Stationary amalgamated zinc, solution: 7.44M $(OH)^-$, 1M $Zn(OH)_4^{2-}$, 9.44M K^+. -1.360V, open circuit voltage.

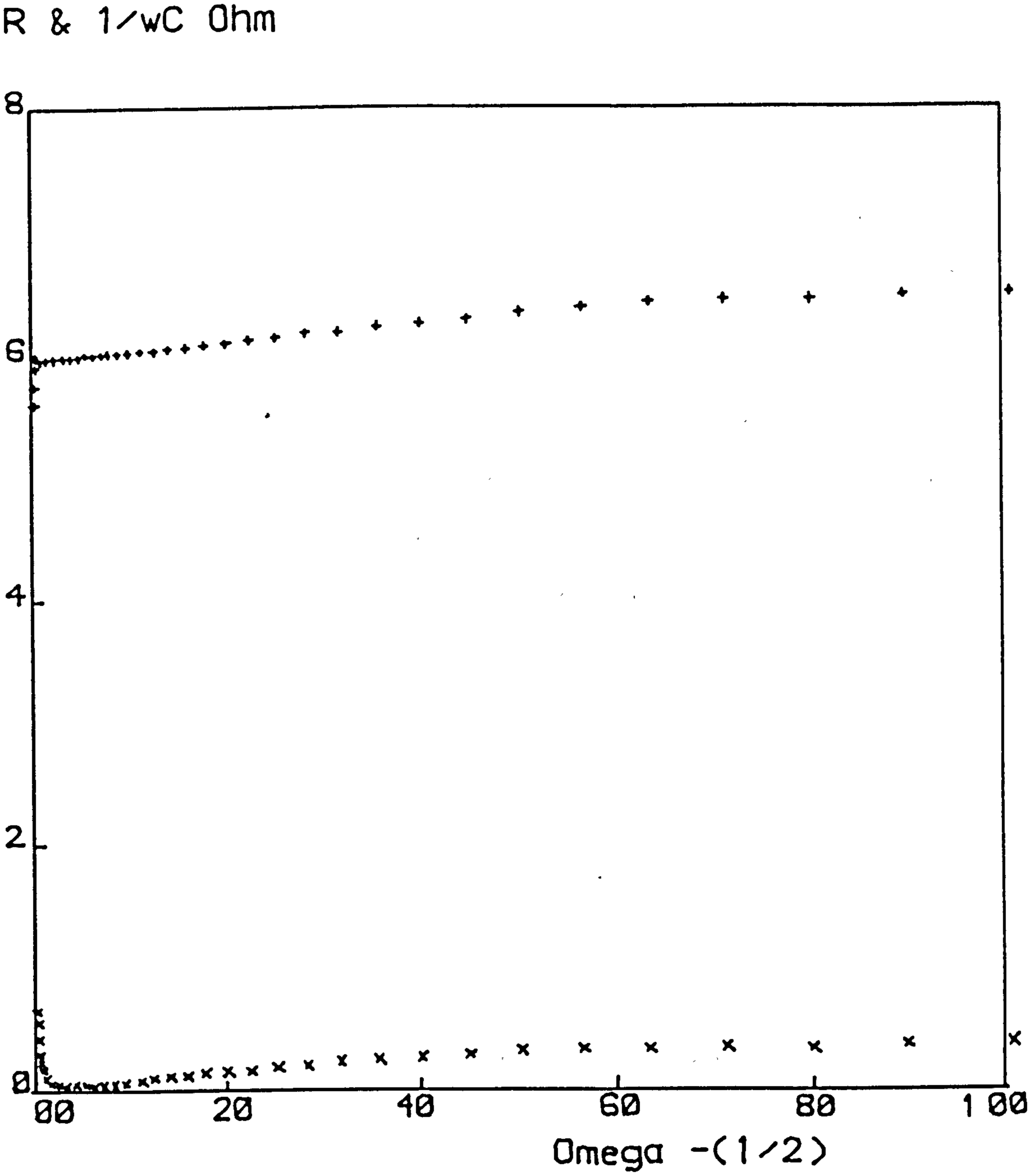

result. This could be due to the actual active electrode area being decreased by the formation of resistive films. The calculations were repeated assuming a diffusion coefficient of 10^{-5} cm^2 s^{-1}, in order to determine the active area of the electrode, and this is expressed as a percentage of the geometric area in Table 7.2. The $Zn/KOH\text{-}Zn(OH)_4^{2-}$ system would have less than 0.1% of active zinc area exposed. The magnitude of the apparent diffusion coefficient however, suggests that the system may be better represented by the diffusion of hydroxide ions through a solid film.

When the carbopol additive was used the apparent area from these calculations was 4.3%. The carbopol plug was pressed onto a recessed electrode. If the carbopol is thought of as forming a "solid" matrix with the electrolyte in the interstices, then some of electrode surface would be masked from the electrolyte by carbopol. Assuming the resistivity of the electrolyte is similar with or without the carbopol matrix, any change in solution resistance (R_{sol}) can be attributed to this masking effect, giving rise to a different cross-sectional electrode area. From these considerations only about 18% of the active area of the additive free system, (i.e. 0.02% of the geometric area) should be reacting. Since the apparent active area is 4.3% of the geometric area, it appears that the carbopol is playing a part in activating the electrode surface.

The amalgam electrode has 36% active area, which can be explained if the effect of amalgamation is to replace zinc atoms with mercury atoms at the electrode surface. A similar mechanism has been proposed by Karunathilaka et al[75] for observations on commercial cells containing amalgamated zinc electrodes. On ageing the surface concentration of mercury falls as the liquid metal diffuses into the centre of the zinc particles, and R_∞ decreases as the concentration of zinc increases.

CHAPTER 8

POROUS ZINC ELECTRODES IN KOH SOLUTIONS

8.1. Introduction

Galvanostatic operation is most similar to the situation in a discharging cell, of the electrochemical techniques. It was used therefore to study the oxidation and passivation of porous zinc gel electrodes. De Levie[18] predicts that the change from planar to porous electrodes should have a profound effect on the electrochemistry. In this investigation the oxidation was followed optically, and an attempt was made to measure the reacting area. This is compared with the surface area obtained from a.c. impedance measurements.

8.2. Experimental

The experimental technique has been described in Chapter 5. The polythene sheath surrounding the planar electrode was packed with the porous zinc gel. Zinc and nickel-silver electrodes were used as conductors. The porous zinc gel was discharged galvanostatically, and was followed using a travelling microscope.

A downward-facing, planar, recessed zinc electrode was packed with porous zinc gel for the a.c. impedance experiments.

8.3. Results and Discussion

Observations with the travelling microscope showed that the porous zinc gel electrode expanded during galvanostatic oxidation. The oxidation began with the rapid formation of a dark blue film at

the electrode/bulk electrolyte interface. A change in the gradient of the potential-time transient signified the total coverage of this interface. The blue film appeared to penetrate into the interior of the electrode in a plane parallel to the electrode/bulk electrolyte interphasial region. Figure 8.1 is a diagram showing the expansion and film penetration with time, for two electrodes of original height 6.23 mm, and 2.93 mm, oxidised at 36 mA and 18 mA respectively. At the higher rate, electrode expansion is linear with time, while film penetration was initially rapid, but tailed off at longer times. Figure 8.2(a) shows the electrode soon after polarization began. At the lower rate the gel electrode appeared to shrink slightly during the early stages of oxidation, but a rapid expansion was later observed. A white precipitate was formed in the electrode pores.

In both cases the potential-time transients shows a double passivation. The first of these passivations gave rise to a concentration polarization of approximately 200 mV, followed by the second passivation some minutes later which led to oxygen evolution. The electrode condition at the first and second passivations is illustrated in Fig. 8.2(b) and (c). After complete passivation the upper part of the electrode was coated with a blue film which could be removed easily, but the lower white layer was much more consolidated. This can be explained if the zinc undergoes a solid-state transformation to produce the blue oxide film, which itself dissolves and saturates the electrode pores with zincate. The white zinc oxide is precipitated from the solution in the electrode pores causing the matrix to swell.

The initial investigation assumed that the current distribution over the electrode was uniform. A number of electrodes of different heights were oxidized galvanostatically at a current equivalent to

FIG. 8.1 Plot showing the expansion of two porous zinc electrodes during oxidation.

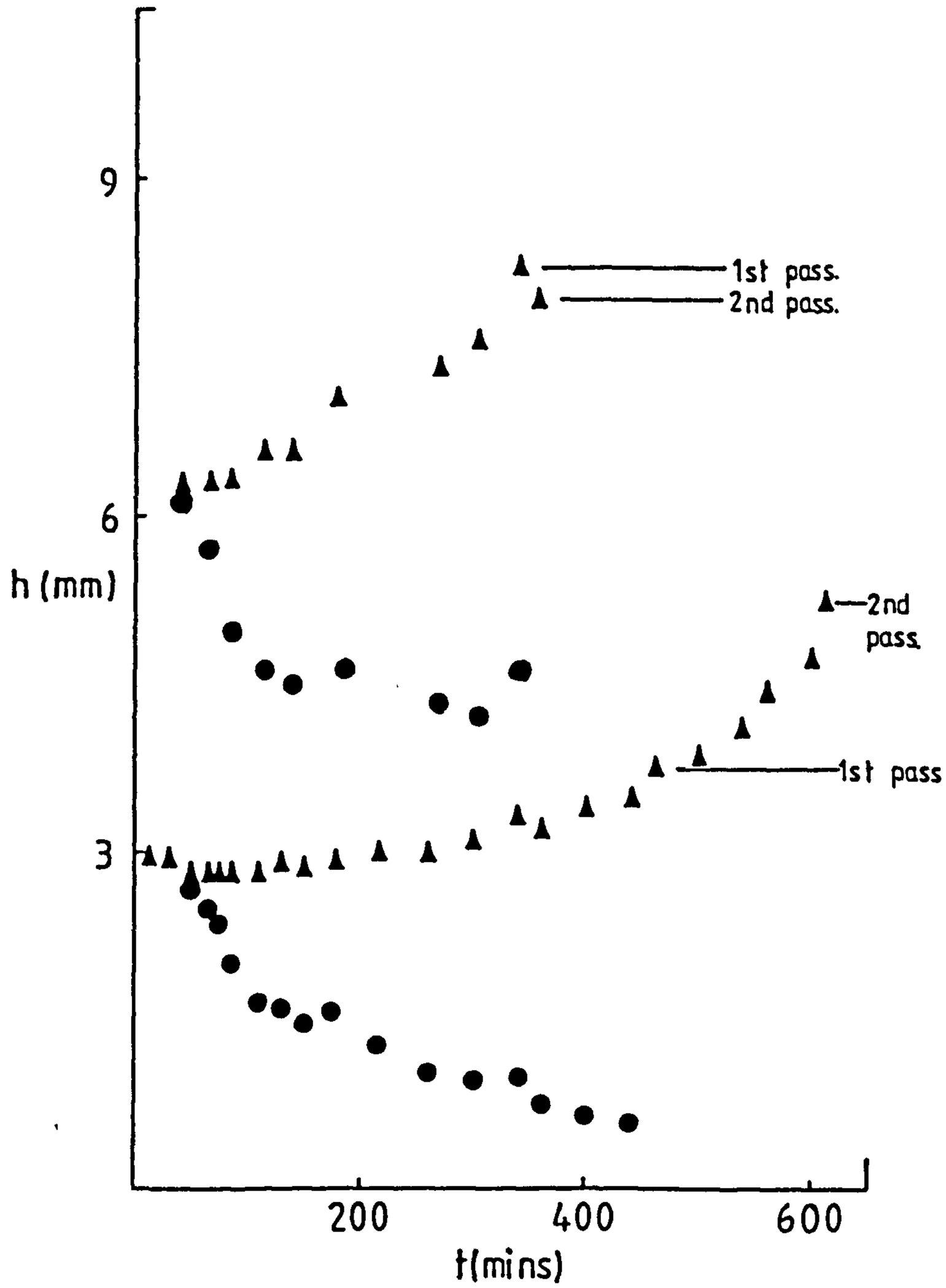

FIG. 8.2 Schematic of the zinc electrode at three times during the oxidation.

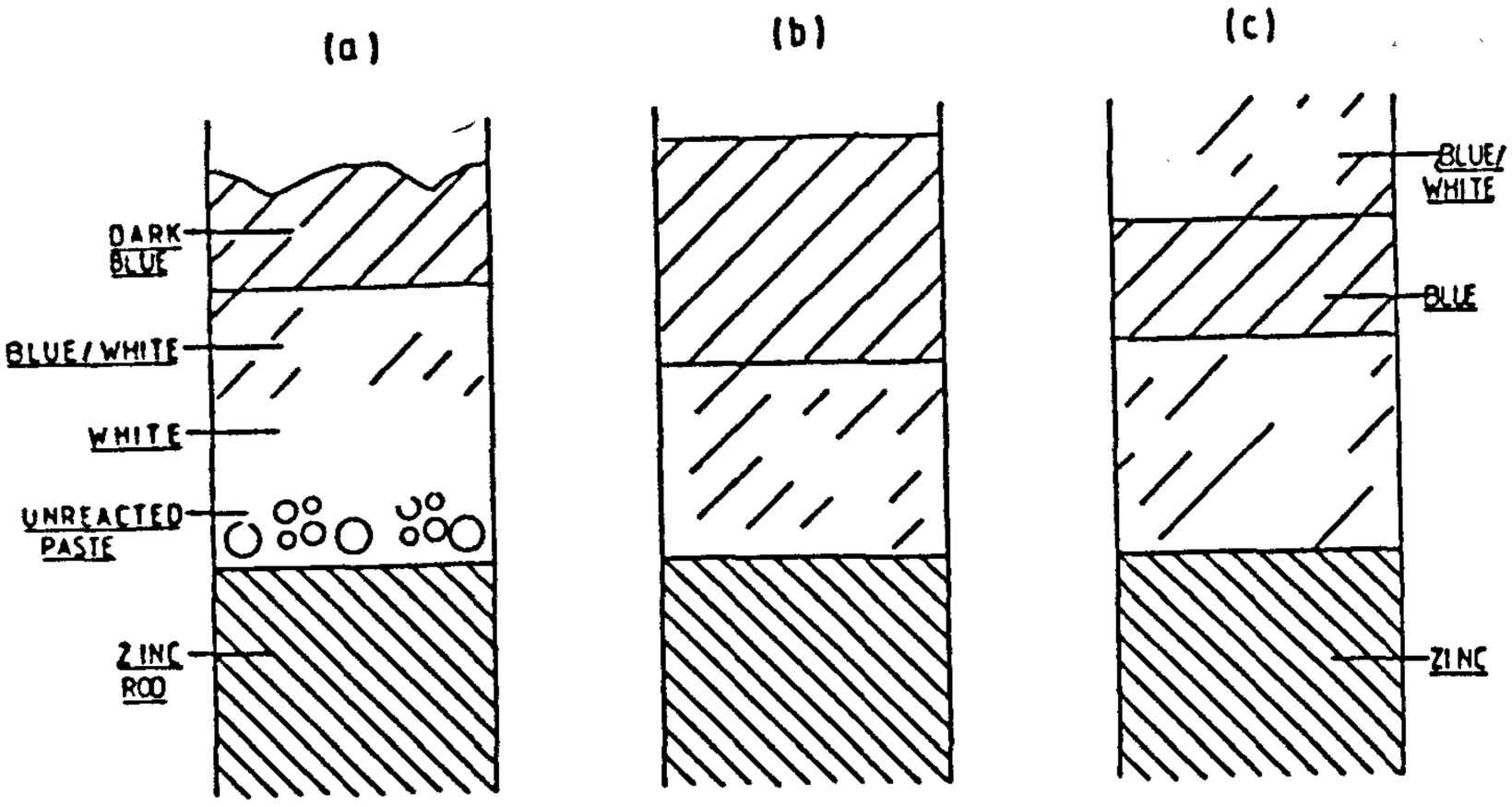

60 mA cm^{-1}, (cross-sectional area 0.503 cm^2). Double passivations were observed in most cases, and Fig. 8.3 is a plot of charge versus the original electrode heights showing the charge attributed to the individual passivations, and the total. The total charge can be fitted to a linear relationship, but on extrapolation will not pass through the origin, as required by the uniform current distribution theory.

The values of the component charges appear to be generally unpredictable, although the charge to the second passivation in all cases was a smaller proportion of the total. Tye[59] discusses the final passivation of zinc in terms of the completion of a type II film. Liu et al[78] have proposed a double passivation mechanism for planar electrodes at low current density based on an intermediate period of restricted diffusion. At the beginning of this time ZnO is precipitated from solution resulting in an initial passivation, and the final passivation is again explained in terms of the total coverage of the electrode by a type II film. The oxidation and passivation processes observed on the porous zinc gel electrode appear to follow a similar mechanism.

Figure 8.4 shows a plot of charge versus electrode height for a number of porous zinc gel electrodes of different height oxidised at a constant current of 40 mA. Clearly there is a linear relationship, and doubling the electrode height (and hence electrode surface area), doubles the amount of charge that can be recovered. This can be explained if a reaction plane is envisaged that is parallel to the electrode/bulk electrolyte interphasial region, and penetrates the electrode at a uniform rate. Some additional oxidations were carried out using a nickel-silver conductor instead of zinc and these are plotted in Fig. 8.4, where it can be seen that they follow the same

FIG. 8.3 Plot of the charge obtained from electrodes of varying height:

□ 1st passivation

O 2nd passivation

● Total

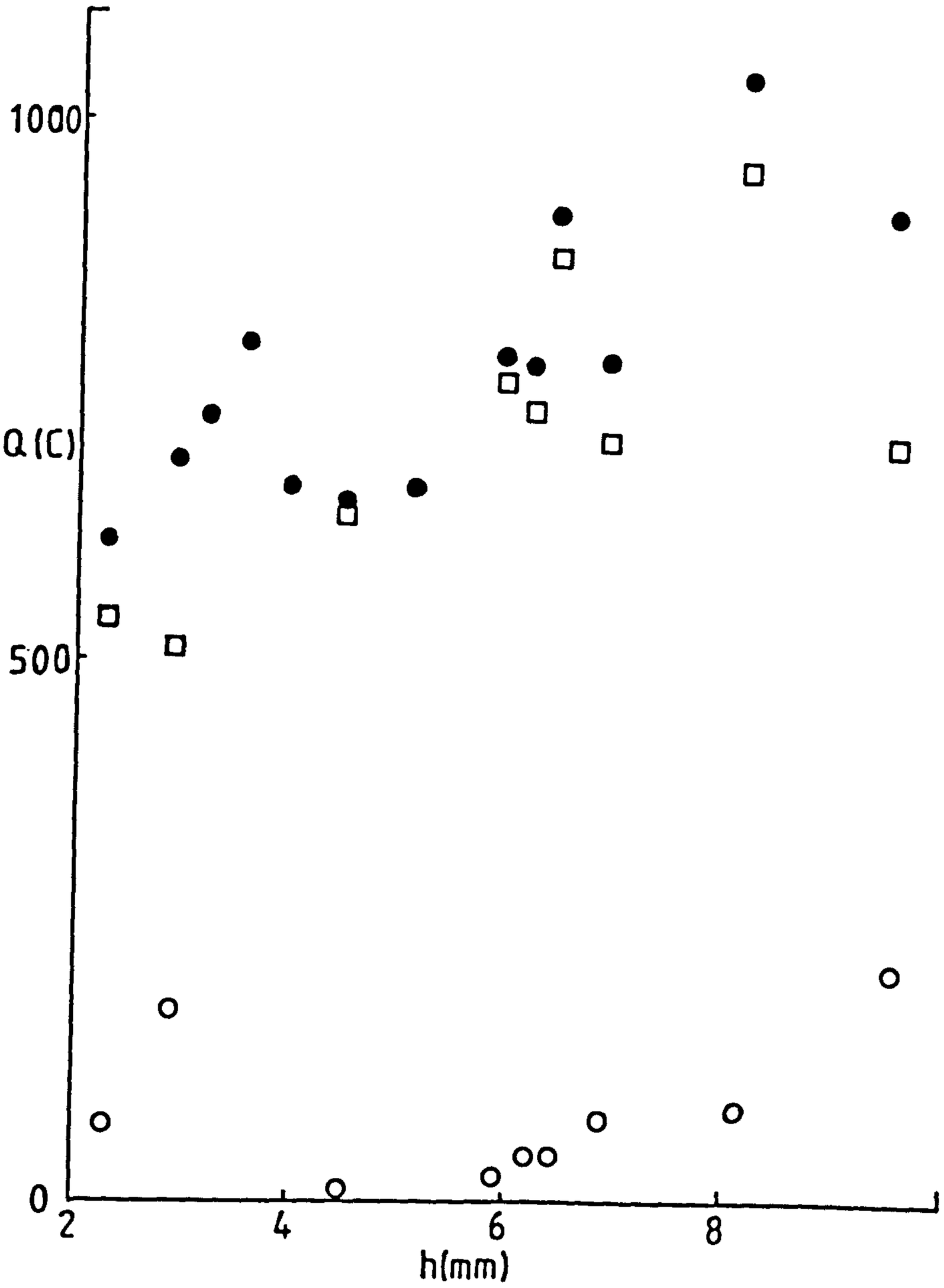

FIG. 8.4 Charge-Electrode Height Relationship for a Constant Current Discharge (40 mA).

● Zinc current collector

⊡ Nickel-silver current collector

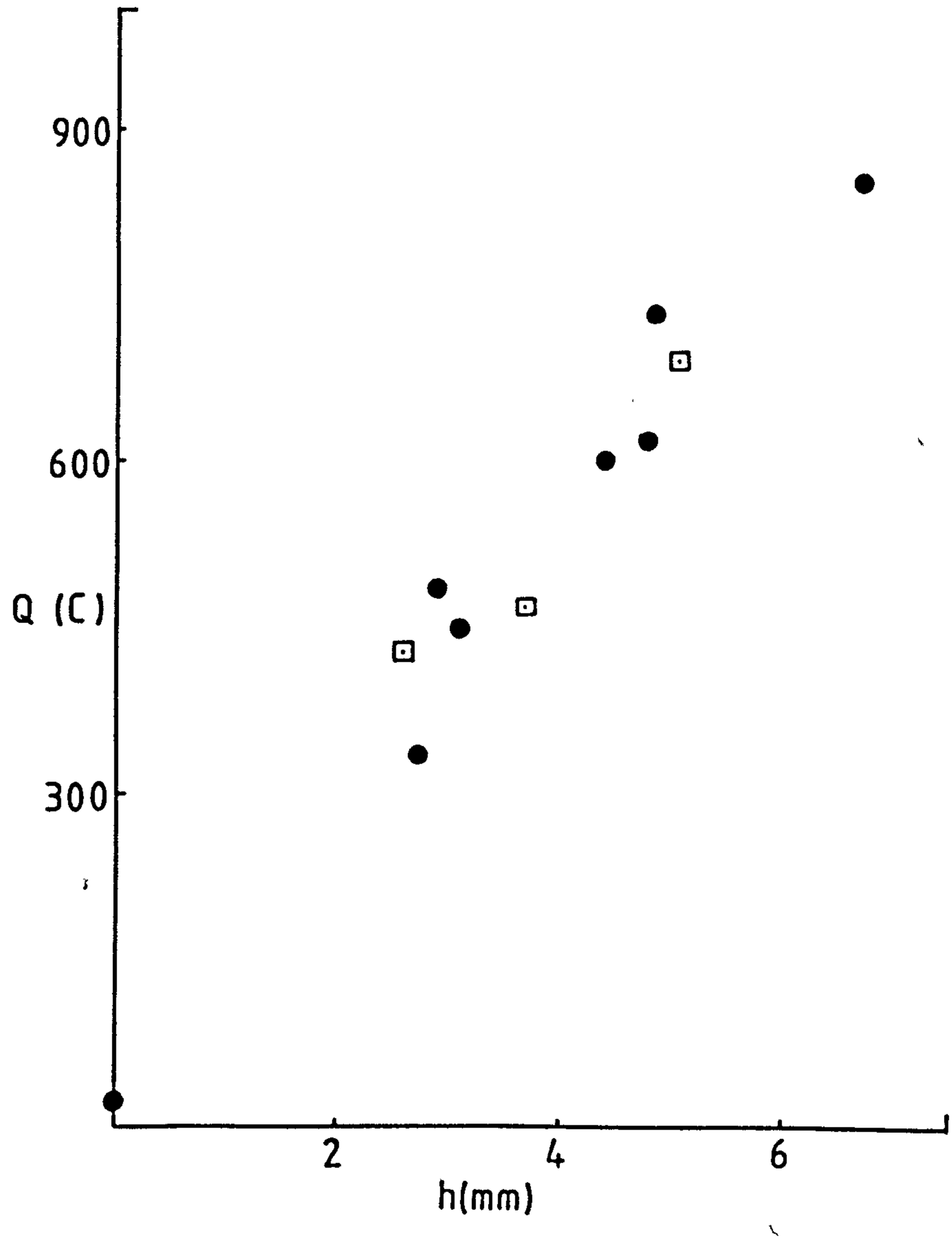

linear charge-height relationship. This means that the oxidation of the conductor is negligable, and is an important observation, since if part of the zinc conductor passivated it would have produced an uneven horizontal current distribution in the porous gel electrode. An electrode that was subsequently reduced following oxidation showed the formation of black zinc particles at the electrode/bulk electrolyte interphasial region initially, and this colour penetrated the electrode along a reaction plane similar to that found in the oxidation process.

If the charge/electrode height relationship is assumed to hold over the range of applied currents used in Table 8.1 (Fig. 8.3), then the charge for any electrode height may be extrapolated. The charge associated with a 1 cm high electrode was calculated for each value of current (Table 8.1), and a plot of $t^{-\frac{1}{2}}$ versus i was linear (Fig. 8.5). From the value of the slope the electrochemically active area was calculated assuming passivation followed the Sand's equation (6.1).

$$k = \frac{1}{\text{slope}} = \frac{1}{0.15} = 6.67$$

and $$k = \tfrac{1}{2} nFA\ (\pi D)^{\frac{1}{2}}\ \Delta C$$

$$A = \frac{2k}{nF\ (\pi D)^{\frac{1}{2}}\ \Delta C}$$

Let $D = 1 \times 10^{-5}$, $\Delta C = 3.5 \times 10^{-3}$

then $A = 3.5\ cm^2$

or $\underline{7.01\ cm^2\ cm^{-3}}$

The surface area can also be calculated from the particle size of the zinc amalgam in the gel, since the gel density is known.

TABLE 8.1

Electrode Height (cm)	Charge (C)	Extrapolation to 1cm high (C)	Current (mA)	Time (s)	$t^{-\frac{1}{2}}$
0.235	609.25	2592.55	14	1.85×10^{5}	2.32×10^{-3}
0.293	687.42	2346.14	18	1.30×10^{5}	2.77×10^{-3}
0.328	725.52	2210.36	20	1.10×10^{5}	3.01×10^{-3}
0.360	793.80	2205.00	21	1.05×10^{5}	3.09×10^{-3}
0.400	661.68	1654.20	24	6.89×10^{4}	$3.81\ 10^{-3}$
0.450	643.79	1430.64	27	5.30×10^{4}	4.30×10^{-3}
0.523	659.37	1260.74	31	4.07×10^{4}	4.90×10^{-3}
0.623	772.20	1239.49	36	3.44×10^{4}	5.40×10^{-3}
0.690	776.13	1124.83	41	2.74×10^{4}	6.04×10^{-3}
0.833	1034.50	1241.30	50	2.48×10^{4}	6.35×10^{-3}
0.956	912.28	954.27	57	1.67×10^{4}	7.73×10^{-3}

FIG. 8.5 Plot of $t^{-\frac{1}{2}}$ against current for a theoretical porous electrode 1 cm high.

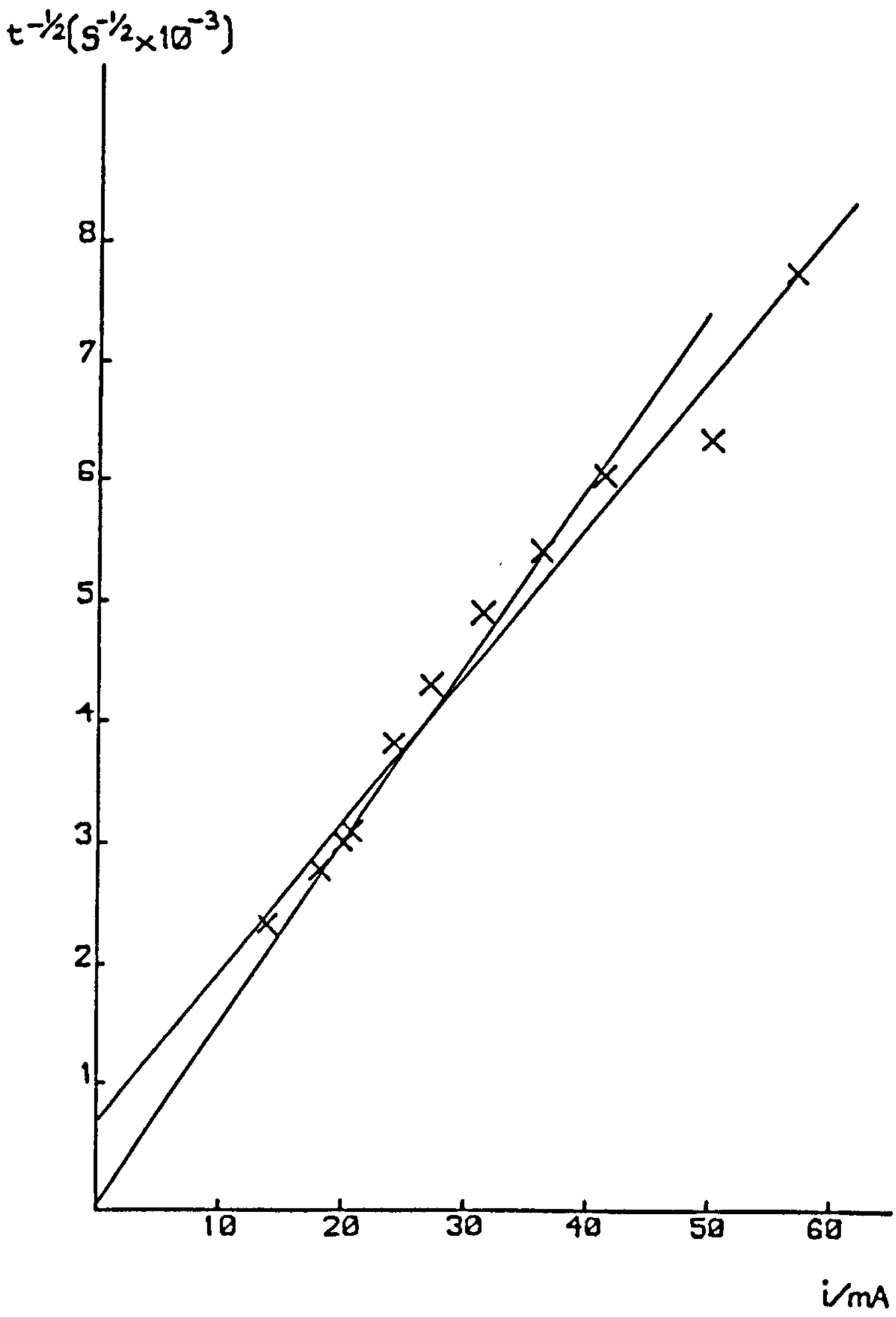

Electrode density (gel after evacuation) = 2.96 cm^{-3}

65.5% of gel by weight is Zn(Hg)

Total mass of Zn(Hg) = 1.94 g cm^{-3}

The density of zinc = 7.14 g cm^{-3}

The density of mercury = 13.59 g cm^{-3}

If the density of the Zn(Hg) is assumed to result from the densities of its components, it can be calculated statistically using weighted averages.

Hence 8% Hg : 92% Zn density 7.661 g cm^{-3}

The particle size corresponds to 20-72 mesh, which means a diameter from 210-814 μm, and gives sphere volumes in the range

Volume	4.8×10^{-6} cm^{-3}	- 311.4×10^{-6} cm^{-3}
Mass	37×10^{-6} g	- 2.38×10^{-3} g
No. of spheres in 1cm^3 of gel	52,224	- 813
Total surface Area	72.35 cm^2 cm^{-3}	- 18.07 cm^2 cm^{-3}

The diameters would be expected to be distributed normally with a mean of 525.5 μm, and since the surface area is a function of r, the total surface area would be expected to be nearer the value for the smaller particle size.

The surface area was also determined by measuring the double layer capacitance using the a.c. impedance technique. The Sluyters plot for the porous zinc gel electrode is shown in Fig. 8.6. A semicircle was fitted to the high frequency locus and by substituting the value of the frequency at the top of the semicircle into equation (3.34), the double layer capacitance was calculated as 31.9 μF.

FIG. 8.6 Porous zinc gel electrode, solution: 7.44M $(OH)^-$, 1M $Zn(OH)_4^{2-}$, 9.44 K^+.
-1.360V, open circuit voltage.

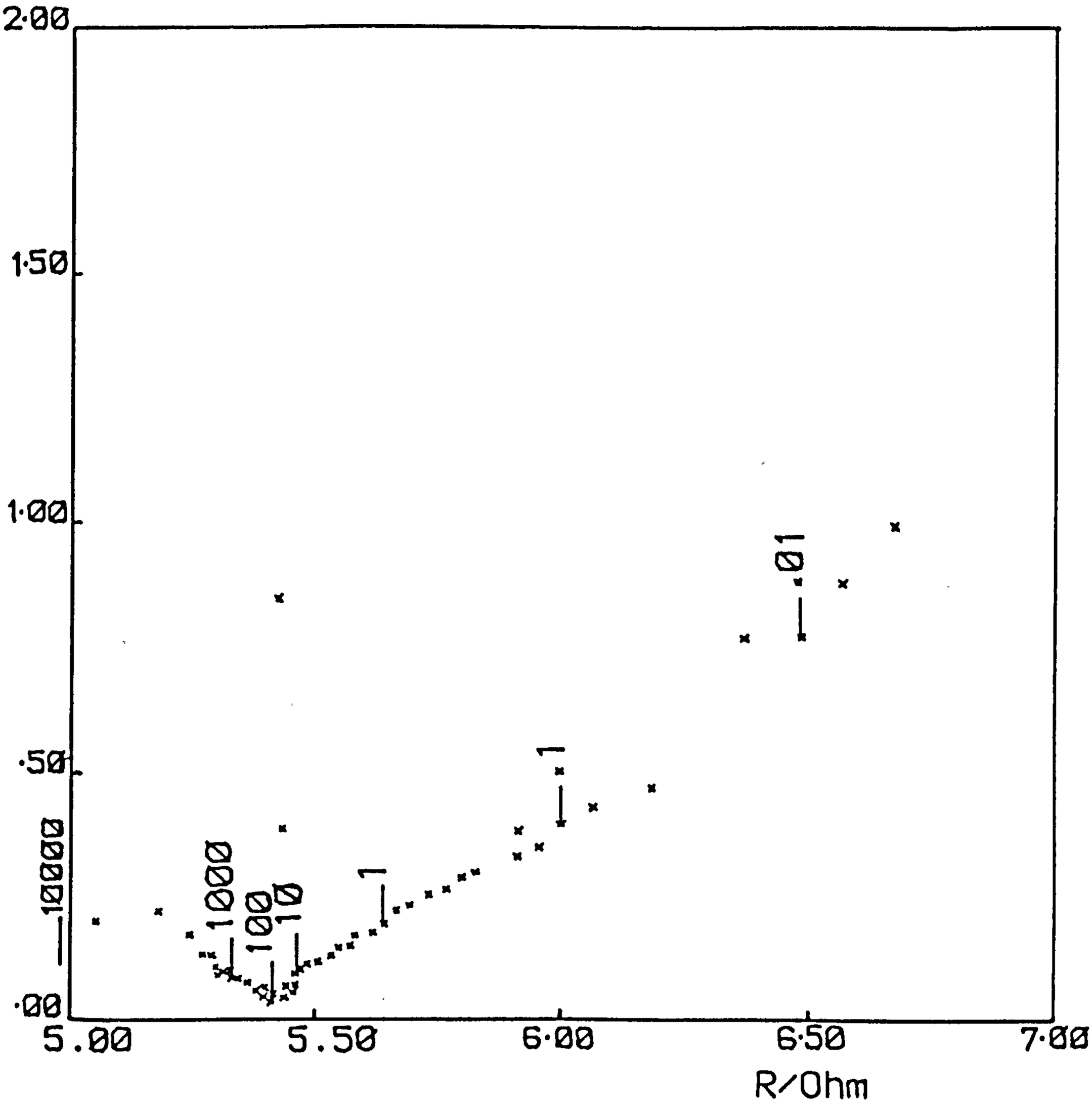

The volume of the test electrode is 0.013 cm^3. The double layer capacitance on a planar Zn(Hg) electrode has been determined as 271 $\mu F\ cm^{-2}$.

The area given by the impedance technique is

$$\frac{31.9}{271}\ cm^2 \quad = \quad 0.12\ cm^2$$

The cross sectional area of the electrode = 0.0706 cm^2.

The galvanostatic technique predicts a surface area = 0.0917 cm^2 and from particle size considerations the surface are a = 0.946 - 0.236 cm^2.

The calculated surface areas are of the order of the electrode cross-sectional area, and support the theory that the reaction occurs in a reaction plane. At the high frequencies used for the impedance experiments the electrochemically active layer would be expected to be at the electrode/bulk electrolyte interphasial region following the reasoning of De Levie[18], where high frequency perturbations do not penetrate into the electrode pores. In the galvanostatic oxidations the reaction region penetrates the electrode along a plane parallel with the electrode/electrolyte interphasial region. The area calculated here is the oxidising area of the electrode. This will remain more or less constant if passivation of the upper layers of the electrode activates zinc at lower levels and drives the reaction deeper into the electrode.

CHAPTER 9

RECHARGEABLE ZINC ELECTRODES

9.1 Introduction

The previous chapters have concentrated on the oxidation of zinc. This chapter considers the subsequent reduction and cycling of porous zinc gel electrodes, which is the basis for a rechargeable system. This has been accomplished in a configuration and under conditions similar to those found in commercial cells. The current distribution along the electrode and its potential have been measured.

9.2 Experimental

Cylindrical porous zinc gel electrodes were cycled against a segmented cadmium counter electrode, and the current passing through each segment was determined by measuring the potential drop across a resistor. The results were recorded periodically using a data logger (Solatron Compact 2), and transferred to the University computer for analysis. Current-time plots were integrated numerically using the trapezium rule to obtain charge-time plots. Charge versus number of cycles was plotted, and since the electrode charge and discharge reactions are dependant, the sum or "Residual Charge" was plotted against cycle number. This figure can be related to zinc relocation, providing there are no parasitic reactions. The cumulative total of these residual charges showed the progression of zinc relocation with cycle number. The potential of the zinc electrode was monitored throughout.

9.3 Results and Discussion

A complete listing of all the results and plots of data for this section is given in Apendix 3 (Vol. 2), and is summarized in Table 9.1. Stacks 3, 4, 5, 7 and 8 all had cylindrical porous zinc working electrodes. The other stacks were constructed to test the counter electrode design, and will not be discussed further here. Generally, zinc electrode polarization was greatest during the early cycles, and decreased with increasing cycle number. This is a common characteristic of rechargeable electrodes associated with an increase in surface area.

It was originally planned to oxidize the zinc electrodes at the C/20 rate to 25% of their original capacity, calculated by the weight of zinc. However, it soon became clear that stack 3 would not sustain these conditions, and this stack was cycled to 15% theoretical capacity at the C/33 rate. The zinc electrode in stack 3 had been made to a different design than the other stacks, and it was suspected that a lower density has given rise to the inferior cycling characteristics.

The results from stack 4 are of particular interest, since the zinc electrode in this stack only partially filled the available cavity. Such an arrangement should allow convective flow. The bulk of the electrode was placed in the centre of the electrode cavity. The potential-time plot (Appendix 3, p86), for the initial zinc oxidation, was a steep, smooth curve. The corresponding current-time plot (Appendix 3, p95), shows that the bottom part of the electrode takes most of the current initially, but rapidly tails off leaving the middle and top segments to dominate. The electrode was recharged (reduced), then on subsequent discharge a peak was observed at 3.7 hours on the potential-time plot, (Appendix 3, p87). The current-time plot (Appendix 3,

TABLE 9.1

SUMMARY OF THE SHAPE CHANGE EXPERIMENTS

Stack	Initial Preparation & Counter Electrode	Cycling Current (mA)	Electrolyte	Zinc Electrode Weight (g)	Zinc Wt (g)	No. of Zn Cycles	% Discharge	Comments
1	Stack charge/discharge vs. Ni/Cu wire of three cadmium ring electrodes for 5 hrs. a half cycle.	210	7M KOH	N/A	N/A	N/A	N/A	Rings soon developed large current imbalance and stack scrapped.
2	Individual ring charge/discharge at 70 mA then connect as stack, all against Ni/Cu wire.	210	7M KOH	N/A	N/A	90 Cd cycles	N/A	This stack ran continuously for over a month with no apparent degradation.
3	Flooded cell as before. Charge Cd rings individually for 5 hrs at 70 mA then cycle 10 times all against Ni/Cu wire. Cell then drained and separator changed. Zinc electrode placed in central compartment and 1.80 cm^3 of Berec electrolyte* added to this compartment.	Initial Discharge 198 Then 119	7M KOH (outer) *7.44M KOH + 1M zincate (inner)	5.3580 (dry)	4.8308	43	15	98% Zn(Hg) 2% carbopol dry blended then formed into a porous "biscuit" using acetone. Electrolyte added in situ to complete Berec recipe. Cycled vertically. Termination : Suspected break in initial porous plug. Insufficient current control by power packs and zincate location.
4	Increase in Cd ring wt to 3.5g CdO charge/ Discharge/Charge at 100 mA individual rings then discharge stack versus Ni/Cu curve at 300 mA, 10 cycles for 5 hrs each half cycle. Drain then add zinc electrode. Allow to stand for 48 hrs to thoroughly wet out.	100	7.44M KOH + 1M zincate	4.0758	2.4561	10	25	Only partially filled cavity of Berec zinc paste electrode. Vertical. Battery separator plug at bottom of stack to stop leaching of zincate. Termination : Oxygen evolution on the zinc or the Ni/Cu conductor during discharge.
5	As 4.	167	7.44M KOH + 1M zincate	6.7479	4.0663	24	25	Filled cavity, cycled vertically with battery separator plug at bottom. Termination: Oxygen evolution on the zinc or Ni/Cu conductor during discharge.
6	Charge individual rings then discharge (100 mA) in an attempt to produce three rings with equivalent resistances. Ni wire counter. Then use as stack.	300	7.44M KOH + 1M zincate	N/A	N/A	N/A	N/A	No appreciable difference from other stacks.
7	Individual ring charge/discharge/charge at 100 mA against Ni wire with $Ni(OH)_2$ added vertical cycling. Stack imbalance so zinc added immediately.	160	7.44M KOH + 1M zincate	6.4479	3.8855	50	25	Filled cavity Berec paste. Stack cycled at 30° to horizontal. Porous plug and capped bottom.
8	As 7.	160	7.44M KOH + 1M zincate	6.5051	3.9200	13	25	Filled cavity Berec paste. 60° to horizontal. Porous plug and capped bottom.

p 96), shows that the segment currents were similar during the early stages of discharge, but gradually diverge with time. The potential-time peak corresponded to a point where the bottom of the electrode had virtually stopped passing current altogether. The middle and upper segments compensated for this by carrying high currents.

In the second cycle during charging, the segment currents again diverge (Appendix 3, p71), but the bottom segment dominated carrying 80% of the total current for the final 1.5 hours. On discharge the currents were uniform, but a potential peak at 3 hours (Appendix 3, p88), was reflected in the current distribution (Appendix 3, p97), by an increase in the bottom segment current followed by a sharp fall, and after 3 hours the lower segment carried the least current.

As cycling comtinued the lower segment began to dominate both the charge and discharge behaviour. During charging in cycle 6 the lower segment carries nearly 80% of the current for 4 hours, (Appendix 3, p74). On discharge the lower segment carried 50% of the 5 hours, (Appendix 3, p100). Clearly more coulombs pass during the reduction (charging), than during oxidation. Conversely for the middle and upper electrodes each carried approximately 10% of the current on charging, and 20% on discharge, and there is a coulombic gain on discharge.

These residual coulombic changes have been plotted against cycle number (Appendix 3, p115), and it can be seen that the bottom electrode had coulombic gain during reduction (reduction taken as positive), for every cycle except 3 and 4. During these cycles the charging current for the lower segment started off at a high value, but diminished in the final 2 hours of charging, (Appendix 3, p72, p73). On discharge in cycle 3 the currents are similar with the lower segment taking more coulombic charge, whereas by cycle 4 the lower segment is

dominating (Appendix 3, p98, p99). On discharge in cycle 9 the potential-time plot shows the evolution of oxygen (Appendix 3, p93), and this is effectively the end of the useful life of the system. The accumulated charge is plotted against cycle number (Appendix 3, p116), and it appears as though the bottom of the electrode is continually gaining coulombic charge during each reduction at the expense of the other 2 segments.

These results can be explained by considering the discharge in terms of the production of soluble zincate species. The high current flowing through the bottom segment during the early stages of the initial discharge is soon diminished as the supply of zinc is diminished. The more dense zincate solutions formed at positions higher on the electrode flow through the gel, and gather in the lower portion. This is repeated in the next discharge. On charging the bottom segment is able to carry a larger proportion of the current as zincate is being reduced there, while the remaining zincate in upper segments rapidly becomes depleted. A mechanism involving deposition of zinc in the lower portion of the electrode, and simultaneous zinc dissolution in the upper segments as proposed by McBreen[83], may account for the rapid change in current distribution over only 9 cycles. In the later cycles it is clear that the lower segment is accepting more coulombic charge on reduction than it is losing on discharge, while the opposite is happening to the upper segments. This result was substantially different from those obtained on the other porous zinc gel electrodes.

The configuration of the remaining stacks (3, 5, 7 and 8), was essentially similar in that the central cavity was completely filled with electrode paste. The cumulative charge plots (Appendix 3, p61, p201, p283, p329), show that there is a migration of zinc to the upper portions of the electrodes.

The polarization decreases on both charge (cf. Appendix 3, p202, p210), and on discharge (cf. Appendix 3, p241, p243). The first charging cycle for stack 7 (Appendix 3, p215), shows a higher current for the lower portions of the electrode. This can be explained as before, as resulting from an accumulation of zincate during the initial oxidation. The first discharge cycle (Appendix 3, p254), shows that the top of the electrode is more active during the early stages, but is later succeeded by the lower segments. This results in the bottom of the electrode gaining zincate. However, since the electrode is packed, zinc can only deposit in the electrode pores, and a densification occurs. Further cycling causes electrode expansion.

On cycle 8 the segment charging currents are similar (Appendix 3, p218), until the final 30 minutes when the lower segment current falls with a corresponding rise in the top segment current. On discharge (Appendix 3, p257) the upper segment current is greatest for 4 hours then rapidly decreases to nearly zero. The lower segment compensates by carrying a higher current, and the potential-time curve (Appendix 3, p244) shows a marked polarization and recovery of the electrode potential. It appears that the upper segment has passivated.

By cycle 30 the electrode had expanded, and the upper segment dominates the charge (Appendix 3, p223). On discharge the potential-time plot shows an increased polarization at 2.5 hours and the current-time plot (Appendix 3, p267) shows that the upper segment passivates. The lower segments allow the increased current to flow while the passivating film re-dissolves on the upper segment. Towards the end of the discharge the upper segment is reactivated, and the current distribution changes as more current flows through this segment. This process of reactivation followed by continued dissolution suggests

that passivation results on this electrode on the completion of a type II film of ZnO formed by solid state oxidation of the zinc surface. This breaks down at low current density, and anodic dissolution recommences.

It was not possible to make any conclusions as to how orientation effected these stacks.

CHAPTER 10

CONCLUSIONS

The anodic oxidation of zinc electrodes in KOH solutions has been investigated. Diffusion control under galvanostatic conditions has been confirmed. Linear sweep voltammetry and rotating disc electrode experiments were used with only limited success. A.C. impedance experiments have shown the sensitivity of zinc surfaces to different methods of surface preparation. It is probable that even at low polarizations the electrode surface is covered with adsorbed OH^- ions. The impedance experiments have shown the presence of an oxidation intermediate which is adsorbed onto the electrode at moderate polarizations.

A number of electrolyte additives have been examined under conditions of diffusion control. None have been found to extend the time to passivation of the electrode. A.C. impedance has shown that at low polarization polymaleic acid is adsorbed on the electrode in preference to OH^-. Carbopol appears to be surface active also, with the beneficial effect of breaking down resistive surface films on the electrode. Film break down resulted with amalgamation of the electrode as well.

Porous zinc electrodes were observed to swell on constant current oxidation, and the reaction proceeded through the electrode along a plane parallel with the electrode/bulk electrolyte interphase. As the reaction proceeds the outer layer passivates and the reaction is driven into the electrode from the bulk electrolyte towards the current collector. A double passivation was observed. Liu et al[82]

have predicted such a process, and correlate the first passivation with the formation of a flocculant type I film, and the second passivation with the completion of an oxide film grown in the solid-state.

Rechargeable electrodes gave a current distribution that showed a relocation of zinc to the lower portion of the electrode where this did not completely fill the electrode cavity. This can be explained in terms of dense zincate electrolyte flowing through the electrode. McBreen[83] has suggested the presence of small concentration cells that would result in a rapid relocation of zinc. Where the electrode cavity is completely filled, zinc initially relocates to the lower section of the electrode, but on later cycles zinc accumulates in the upper section. This is due to densification in the lower section of the electrode, and an electrode expansion. All electrodes failed due to oxygen evolution on discharge.

Sections of the recharging electrodes passivated during discharge. The current distribution showed that the other sections then compensated. Later in the discharge the section would reactivate and carry the majority of the current. This suggests the mechanism is dependent on type II film breakdown and repair.

APPENDIX 1

PLANAR ZINC ELECTRODES IN NEUTRAL AND ACID SOLUTIONS

A.1.1 Introduction

Zinc electrodes in neutral and acid electrolyte solutions are of interest to the primary battery industry. Some exploratory experiments were made to examine the oxidation of zinc in solutions containing bromide ions.

A.1.2 Experimental

A wick-type calomel reference was used to reduce transport between the reference and cell electrolyte solutions. The reference electrolyte was substituted with saturated NaCl solution (+0.236V against the standard hydrogen electrode). All potentials quoted in this chapter are referred to the modified calomel electrode.

Linear sweep voltammograms were recorded for zinc in 1mM $ZnBr_2$ with $NaClO_4$ as support electrolyte. A Tafel plot for the oxidation reaction was drawn from the current response at low sweep rate.

Rotating disc electrode experiments were used to examine the hydrogen evolution reaction on zinc in $NaClO_4$ at a number of pH's.

A.1.3 Results and Discussion

The oxidation of zinc was examined using linear sweep voltammetry. Figure A.1.1 shows the results of oxidising the electrode at two different sweep rates. At the higher anodic sweep rate the transient rises exponentially after approximately -1.050V, and the current-

FIGURE A1.1 Linear sweep voltammogram for a zinc electrode in 2M $NaClO_4$, 1 mM $ZnBr_2$

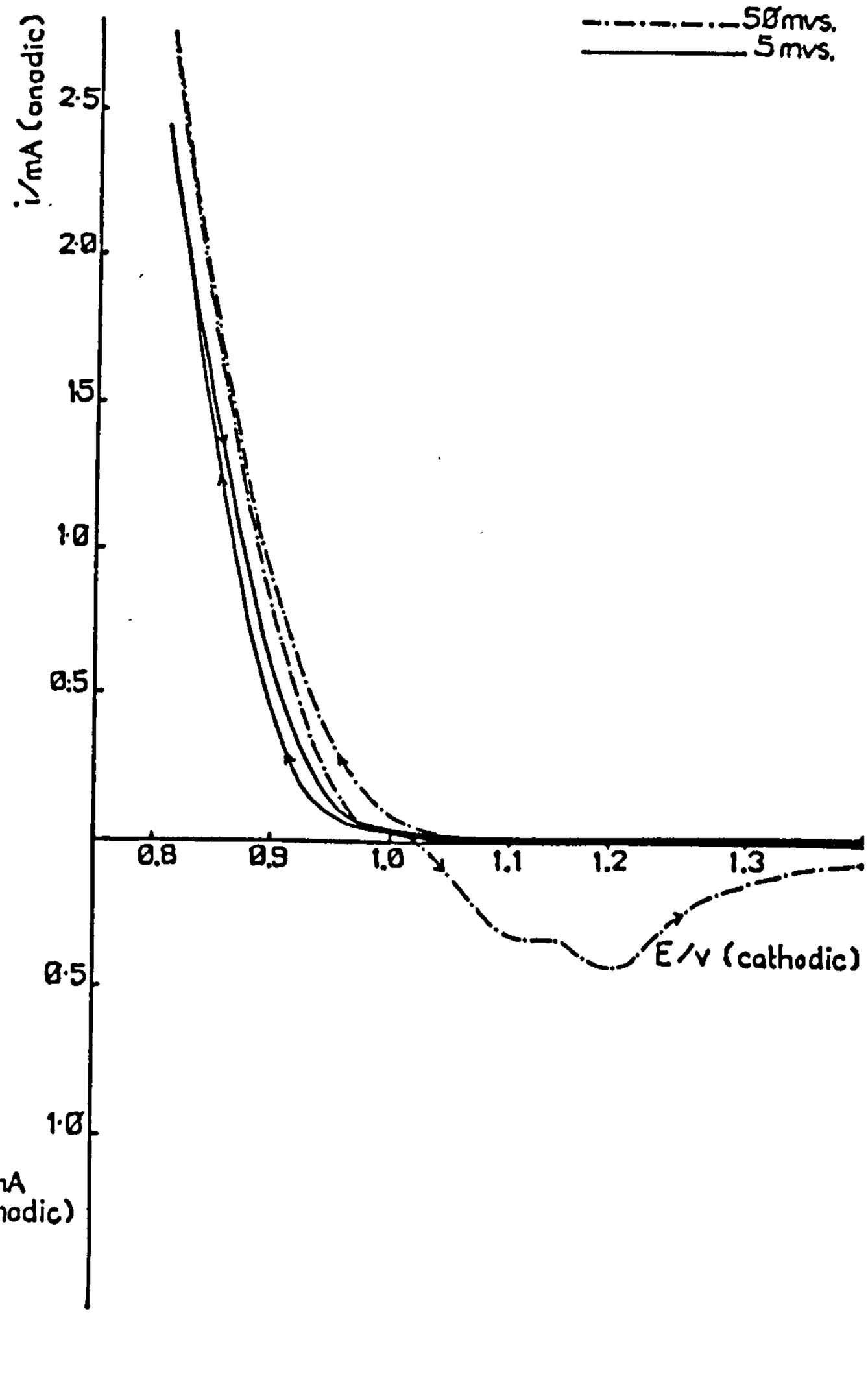

voltage curve rapidly becomes linear. A peak was not observed even at high anodic polarizations, and it appeared that oxygen evolution began without the electrode ever passivating. On the return sweep in the cathodic direction a double reduction peak was seen. At the low sweep rate a similar anodic transient was observed, but no cathodic current was seen on the return cathodic potential sweep.

A slow anodic sweep was made at 3 mVs^{-1}. A Tafel slope for the $\log_{10}$ (anodic current) is shown in Figure A.1.2 and gave a slope of 52 mv $decade^{-1}$ change in current.

The hydrogen evolution reaction on zinc in $NaClO_4$ was examined at two pH's, pH 4.0 and pH 2.5. Plots of $\omega^{\frac{1}{2}}$ versus $^1/i$ were generally linear, but the corresponding plots of the logarithm of the gradients versus potential (Figs. A.1.3a & b) gave exceptionally high slopes ($\sim$ 500 mV per decade) indicative of a highly resistive film covering the electrode surface. The electrochemistry is driven by a much smaller potential than is apparent from potential measurements, a large portion being dropped across the film. If the potential drop across the film is $\Delta\phi$ at a potential ΔE then $\Delta\phi$ must drive the ion current through the film at a rate equivalent to the overpotential for the electrochemistry. Thus

$$\Delta E = \eta + \Delta\phi$$

should be related to E by the Tafel equation and hence ϕ must be of the same form since ΔE has a log-relationship of current versus potential. This suggests that the current follows that required for a semiconductor. It seems reasonable to conclude that the electrode is complicated by a film through which the conduction follows a high field law similar to that of a semiconductor. The Tafel slopes of

FIG. A1.2 Tafel plot for a zinc electrode in 2 M $NaClO_4$, 1 mM $Zn\ Br_2$

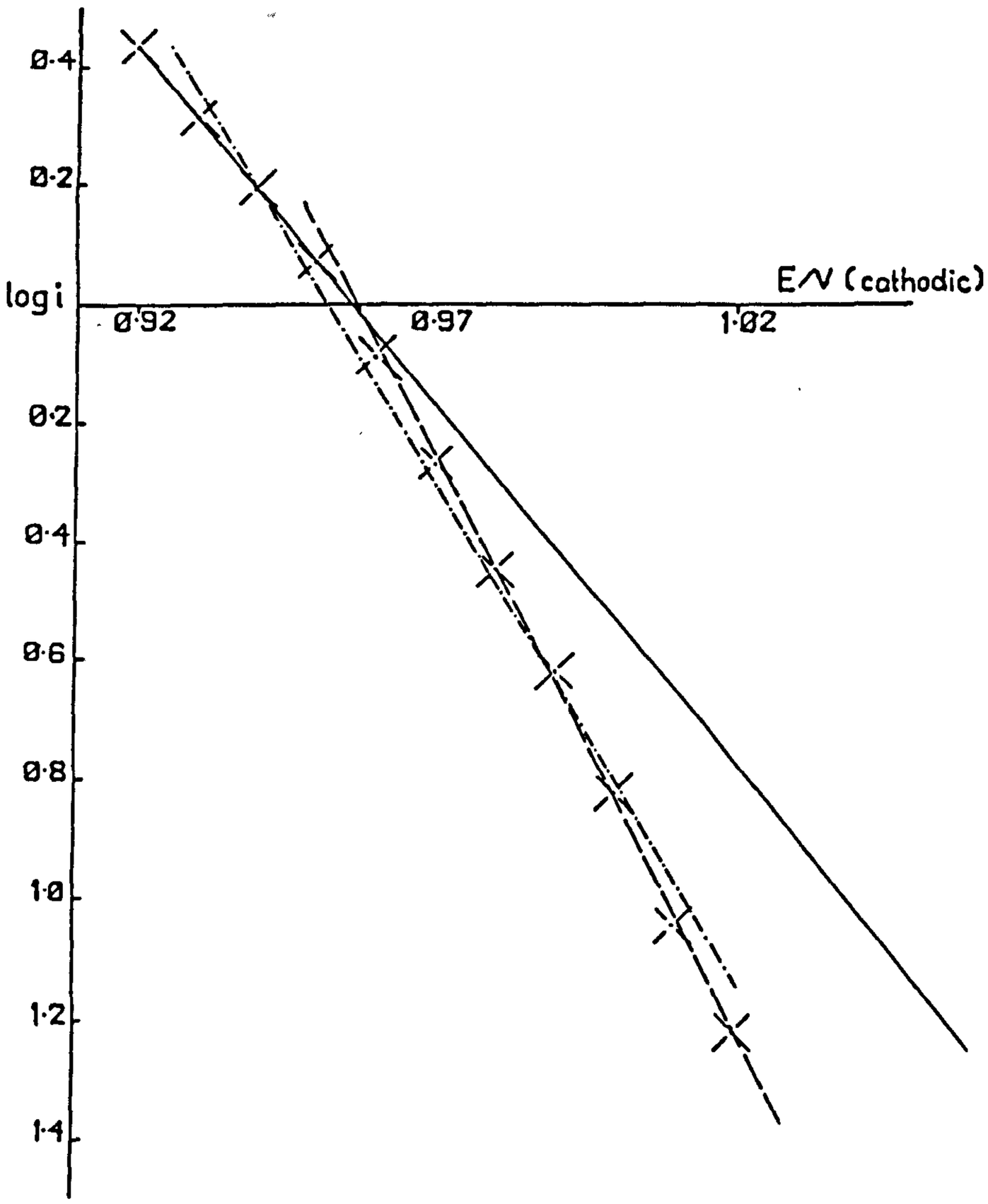

FIG. A1.3 Plots of the slopes $\frac{i^{-1}}{w^{-\frac{1}{2}}}$ against potential for a zinc electrode in 2 M $NaClO_4$ for the Hydrogen Evoluton Reaction. (a) pH 2.5 (b) pH 4.0

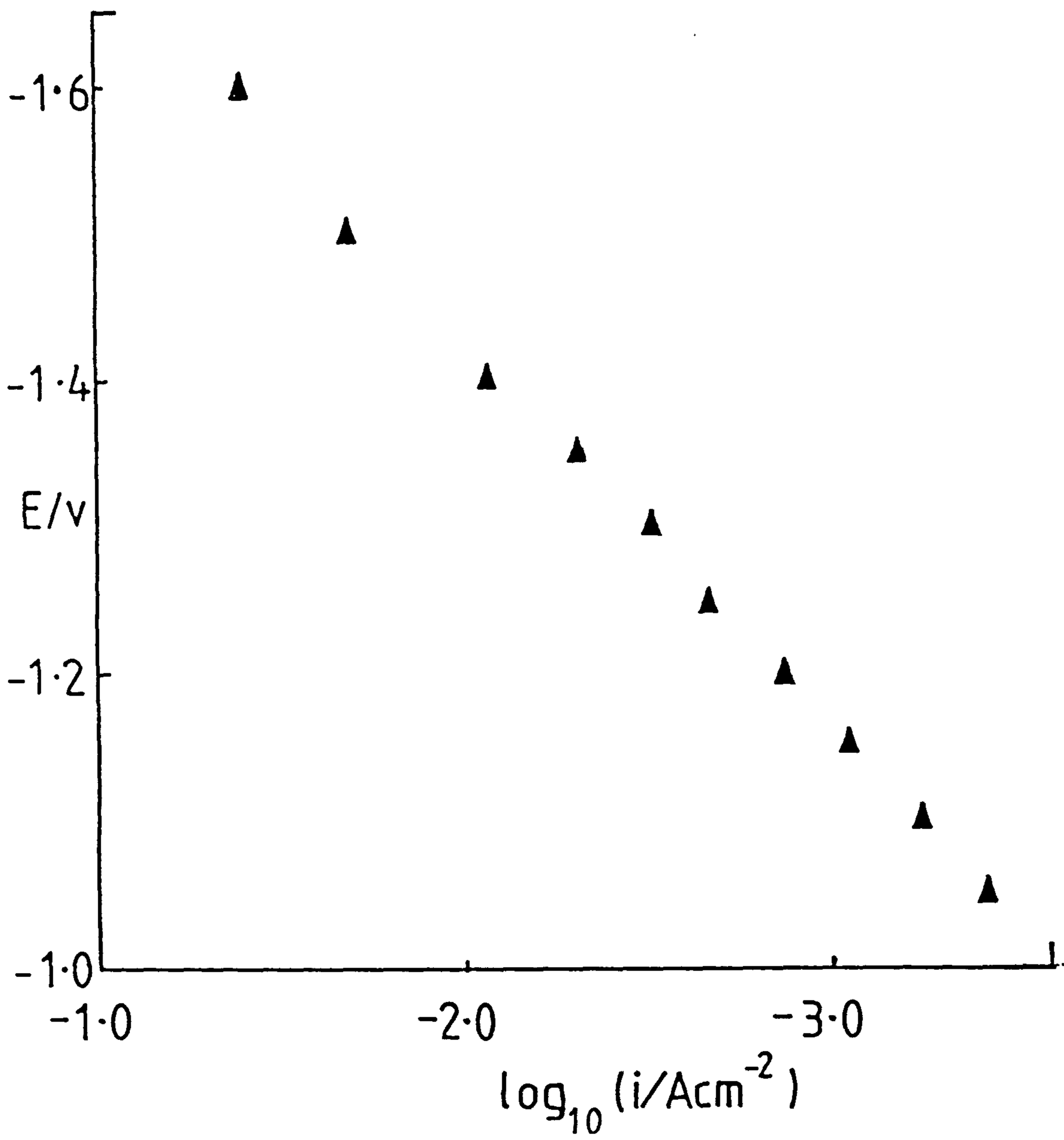

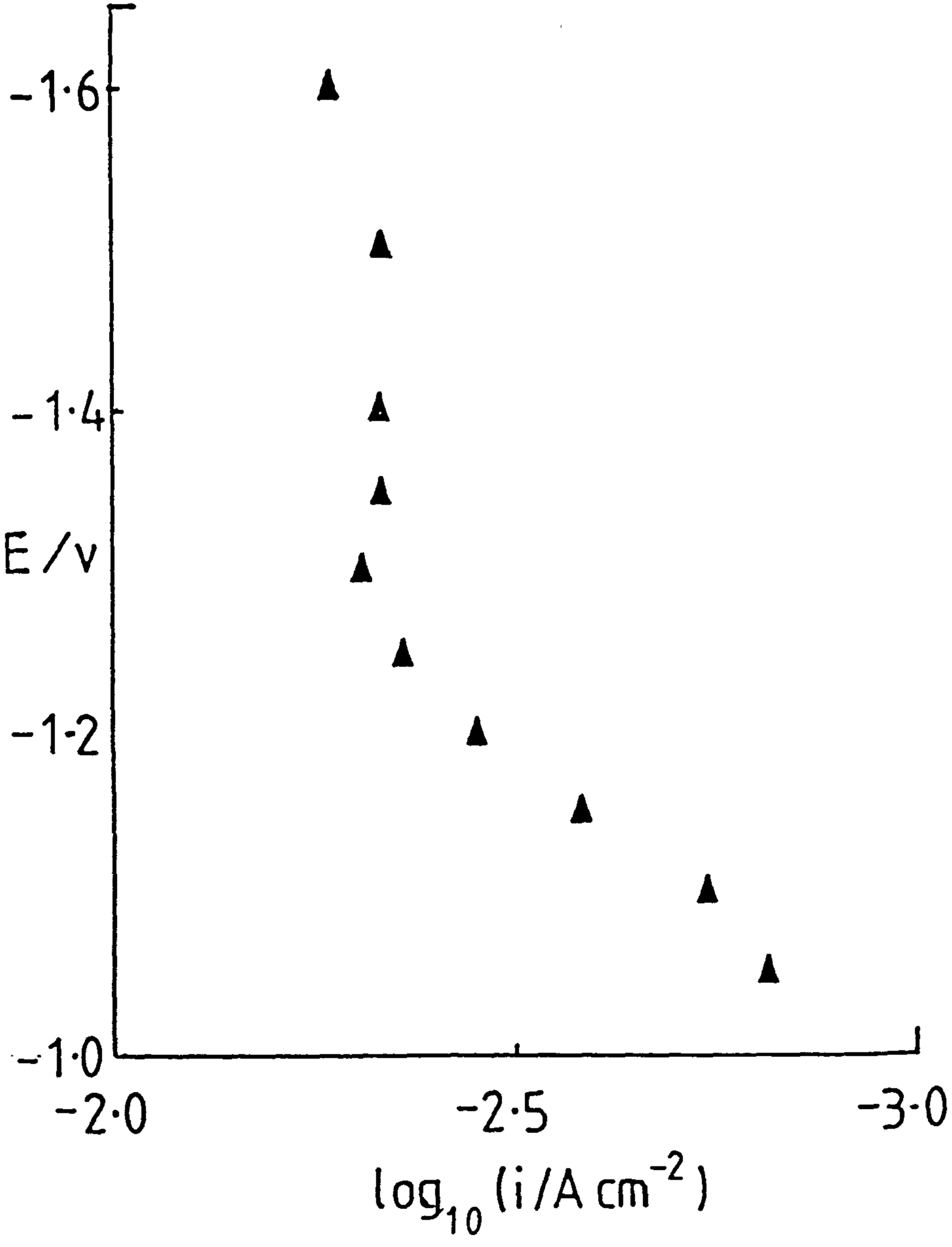

FIG. A1.3 Plots of the slopes $\frac{i^{-1}}{w^{-\frac{1}{2}}}$ against potential for a zinc electrode in 2 M $NaClO_4$ for the Hydrogen Evoluton Reaction. (a) pH 2.5 (b) pH 4.0

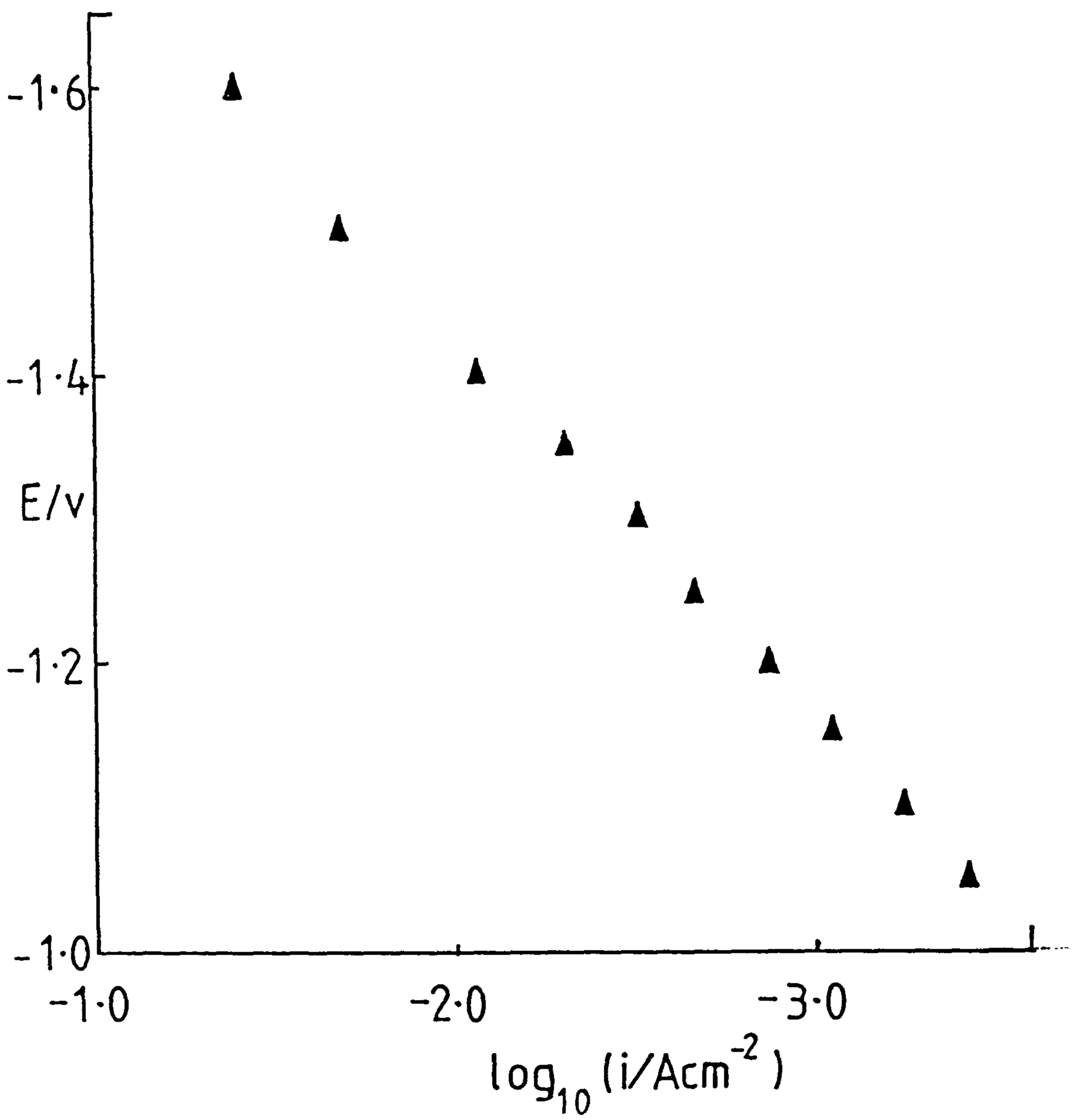

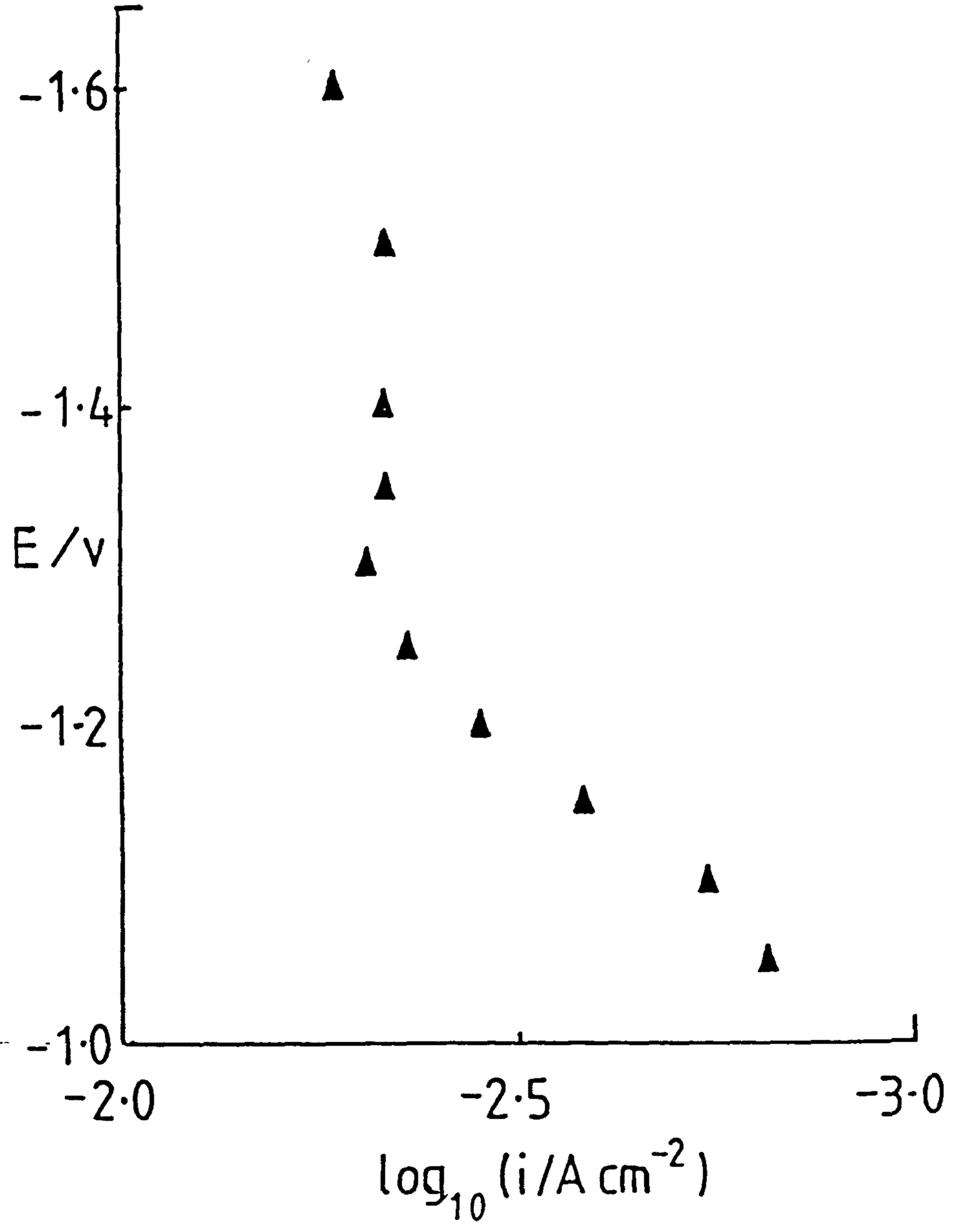

500 mV per decade are to be interpreted in this manner.

Baugh[117] suggests two mechanisms for hydrogen evolution on zinc.

$$2H_3O^+ + 2e \longrightarrow H_2 + 2H_2O \qquad \text{Proton Reduction}$$

$$2H_2O + 2e \longrightarrow 2OH^- + H_2 \qquad \text{Water Reduction}$$

The first reaction occurs at a potential more anodic than -1.30V (vs. N.C.E.), and is diffusion controlled, while the second occurs at potentials more cathodic than -1.40V and is activation controlled. The log ($^1/i_\infty$) versus E plot at pH 4.0 shows a limiting current in this region. At the lower pH a linear relationship is observed (Figs. A.1.4a & b).

FIG. A1.4 Plot of log $\left(i_\infty^{-1}\right)$ against potential for a zinc electrode in 2 M $NaClO_4$.

(a) pH 2.5

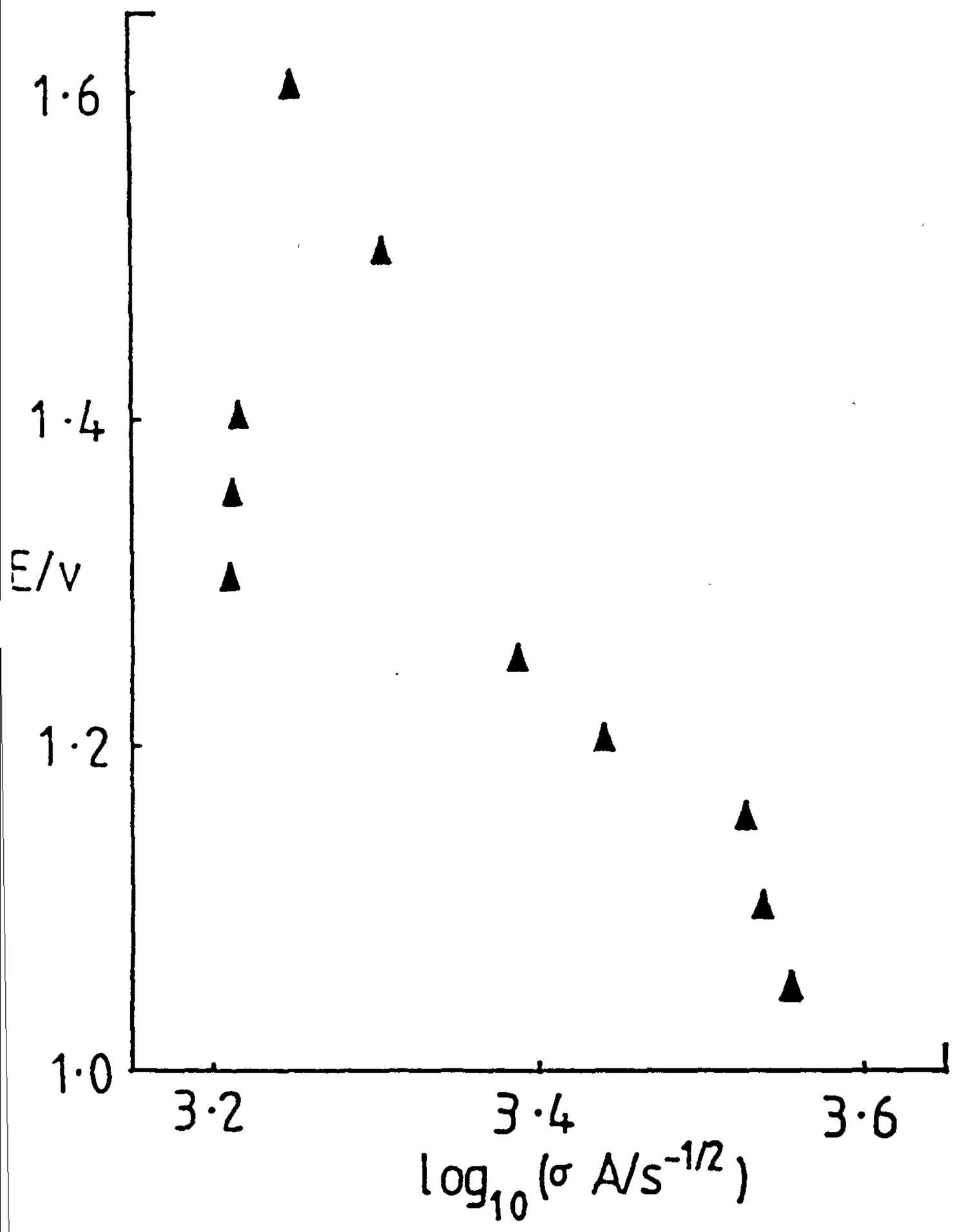

(b) pH 4.0

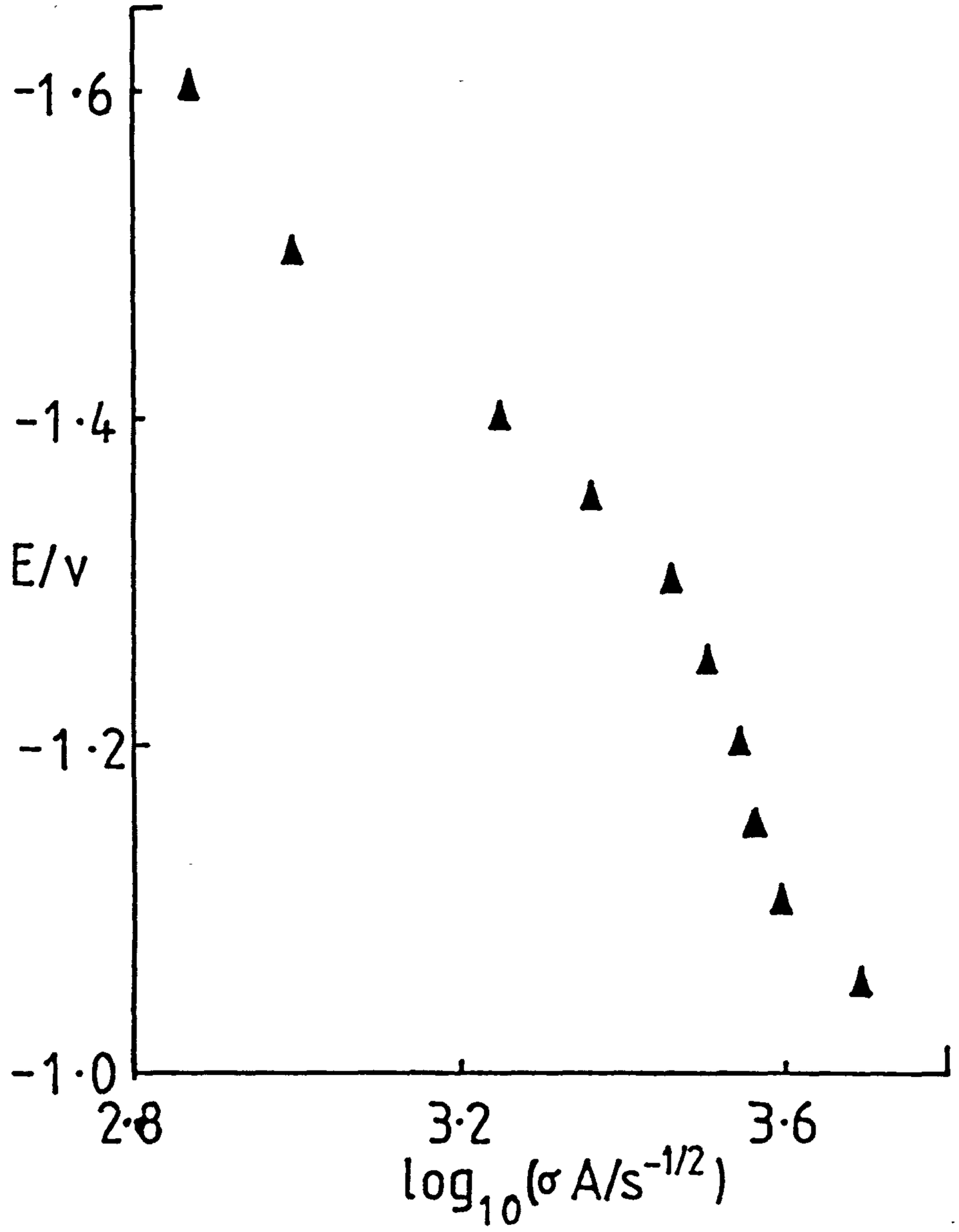

APPENDIX 2

THE FREQUENCY DISPERSION AT SOLID TIN ELECTRODES*

A.2.1 Introduction

The importance of this resistance-capacitance (R-C) frequency dispersion arises from the fact that many industrial systems contain areas with widely different (R-C) characteristics such as may be present in a partially filmed electrode. The situation is, of course, complicated by any porosity or roughness which may be present and indeed the isolation of the precise cause of dispersion in such industrial systems is almost impossible. Nevertheless one needs to know the magnitude of the double layer characteristics if a decomposition of electrode impedance is to be used for the isolation of the kinetic parameters. The question of the assignment of proper values for the double layer capacitance of an active electrode can be tackled by plotting data in the complex plane when the position of the maximum in the high frequency semicircle gives the effective capacitance and of course it is always possible to obtain the mean double layer capacitance by matching up the whole of the complex plane impedance locus on a computer and minimising the mean square deviations. It is nevertheless important to know how the double layer capacitance disperses with frequency and also to know what are the effects of various surface treatments on this dispersion. This appendix contains the results of an investigation into these effects for the case of polycrystalline tin electrodes in sodium perchlorate solutions at approximately pH 3.

---

* Footnote: This work was undertaken in collaboration with N.A. Hampson, S.A. Cotgreave, M. Welsh and R. Leek.

A.2.2 Experimental

The method used for finding the double layer capacitance was the classical bridge method. The method still produces the most precise data in the audio frequency range although it is extremely tedious.

Electrodes (99.999% tin supplied by Johnson Matthey) were mounted in polyethylene, polished on roughened glass, etched and then pretreated to produce the desired surface.

All measurements were made under nitrogen after the electrolyte solutions had been circulated for 7 days over purified charcoal.

A.2.3 Results and Discussion

The double layer capacitance - potential curves, an example of which is shown in Fig. A.2.1, are typical of others in the literature and consist of an undulating shape in which a minimum at -0.43 V develops at low concentration. The potential is apparently the potential of zero charge. When the frequency was changed the value of the measured capacitance also changed increasing as the frequency decreased. Fig. A.2.1 shows how for an electrolytically etched tin electrode in the experimentally polarisable region the capacity changes with frequency in the form of a plot of C_L/C_{Lo} against the square of the frequency, f. The shape is quite similar to that expected from both the capacitance surface heterogeniety and resistance heterogeniety. For roughness in the sense of DeLevie we would expect a change in (C_L/C_{Lo}) corresponding to a change in capacitive reactance of 50% as the frequency spectrum is scanned if the roughness was such that semi-infinite pores were present. The data shown in Fig. A.2.2 are for a surface which could not be rough to this extent and it must be concluded

FIG. A2.1 The capacitance-potential curve for tin electrodes polished and electrochemically etched in 0.008 M $NaClO_4$ at $22^{o}C$.

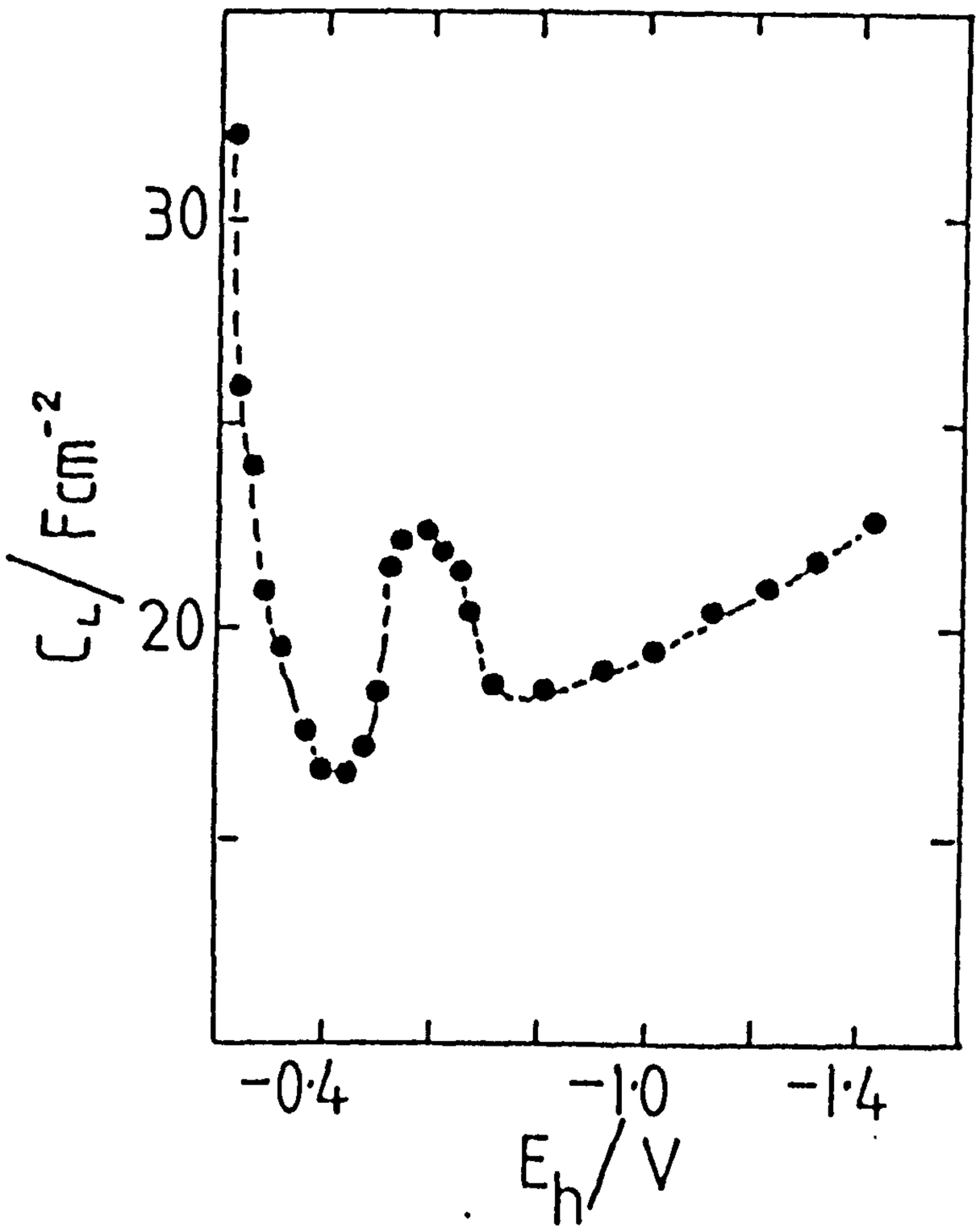

FIG. A2.2 Frequency dispersion for the electrodes of FIG. A2.1: curve A, 0.13 M $NaClO_4$ at -0.53 V; curve B, 0.036 M $NaClO_4$ at -0.46 V; curve C, 0.008 M $NaClO_4$ at -0.56 V.

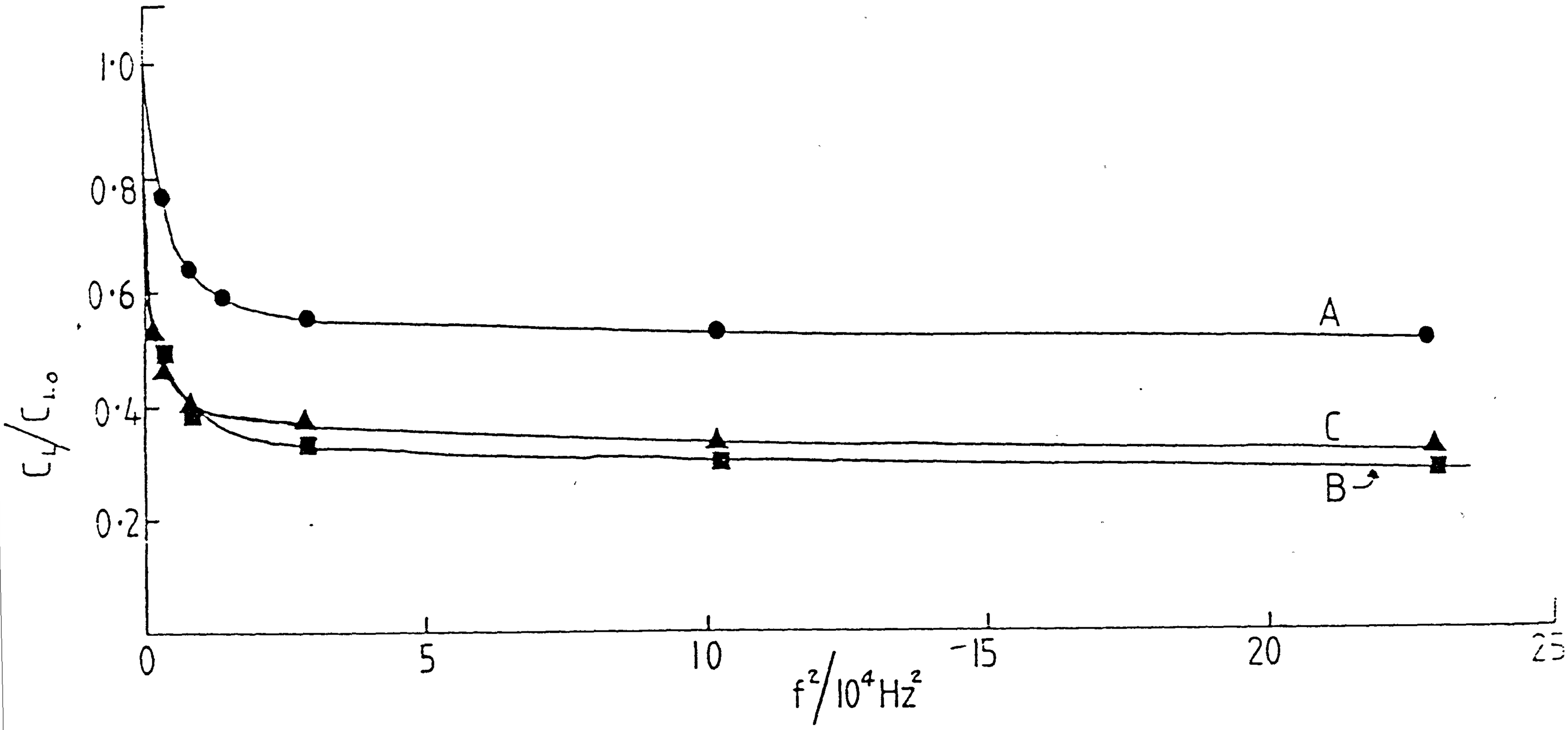

that other factors such as those of surface quality heterogeniety (as opposed to surface geometry heterogeniety) such as we have discussed must play a considerable part in frequency dispersion.

We have tried to force the surface roughness to play a more considerable part by arranging for scratches and microgrooves to be present at the electrode. The results of these experiments are shown in Figs. A.2.3-5 for a series of situations. The magnitude of the dispersion is not significantly greater than for the etched surface. This is an interesting point for it emphasises the relative importance of the surface effects, geometrical effects being relatively minor. When "fully" porous surfaces in the sense of spongy deposits are examined there is no doubt that there is a considerable effect. It must be concluded that roughness on the scale generally encountered in operational electrochemical systems is not the major source of the frequency dispersion of the double layer capacitance.

FIG. A2.3 Frequency dispersion for tin electrodes pretreated by mechanically abrading on roughened glass. Other data as for FIG. A2.2.

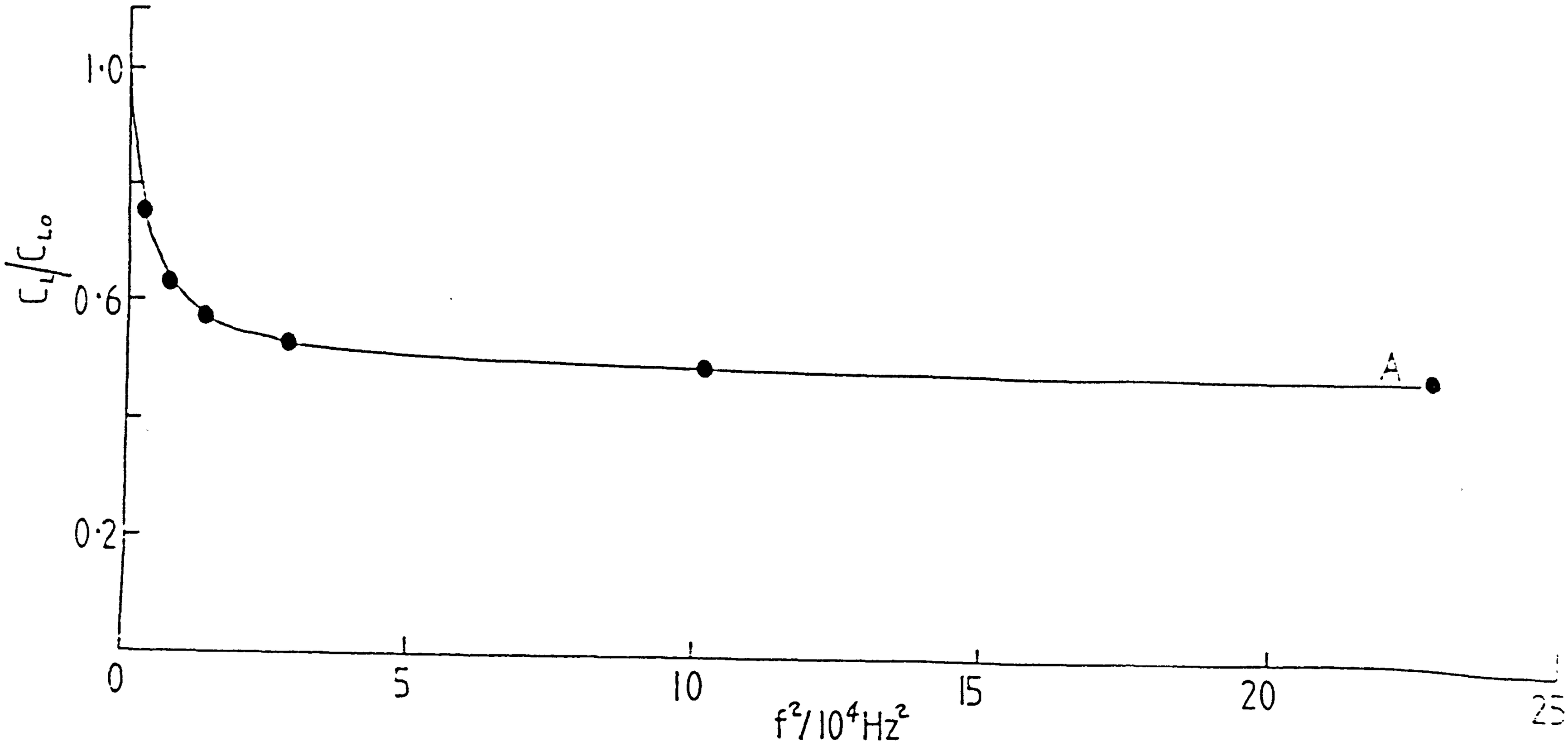

FIG. A2.4 Frequency dispersion for tin electrodes pretreated by scratching with emery paper and washing. Other data as for FIG. A2.2.

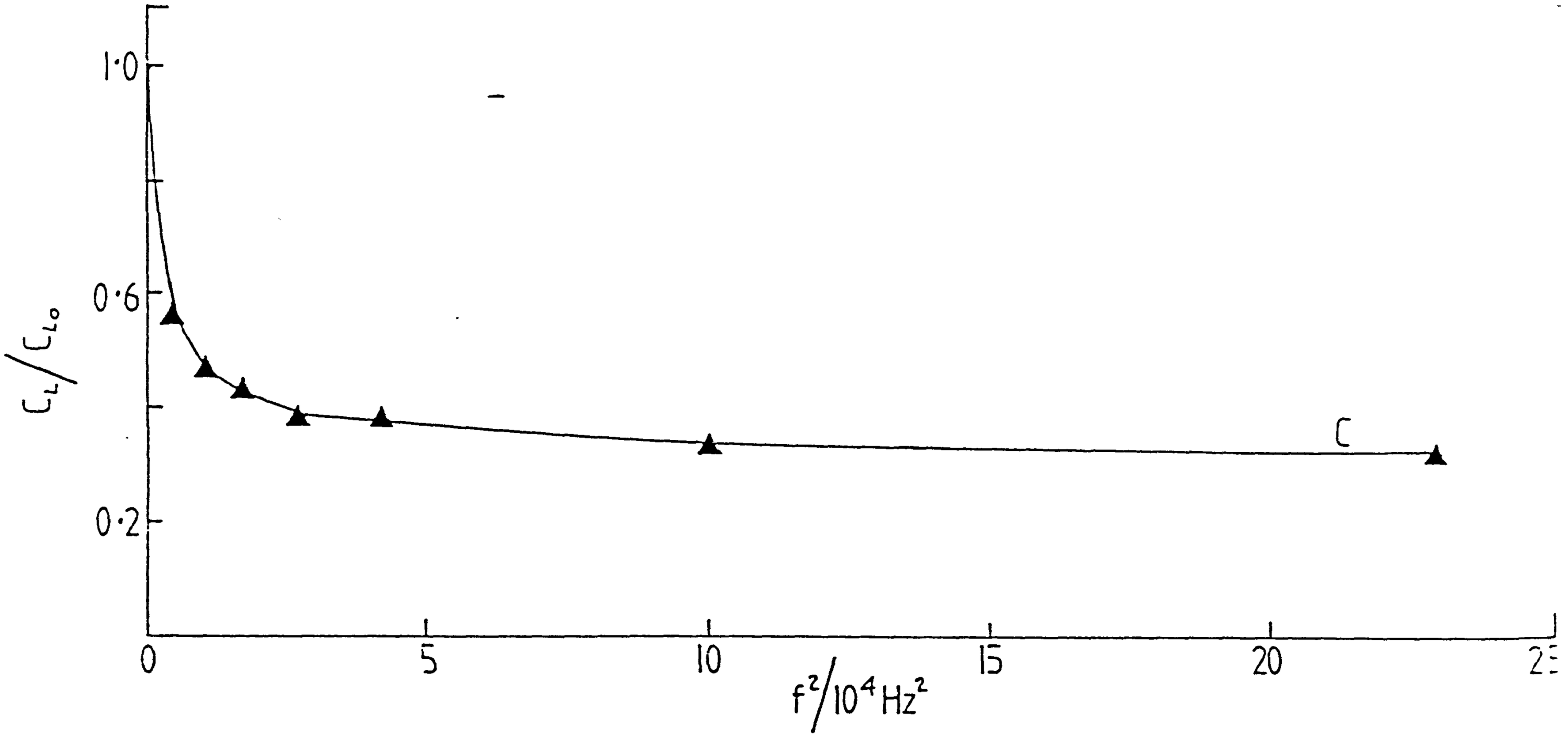

FIG. A2.5 Frequency dispersion for tin electrodes pretreated as for FIG. A2.3 and chemically etched in 10% $HClO_4$. Other data as for FIG. A2.2.

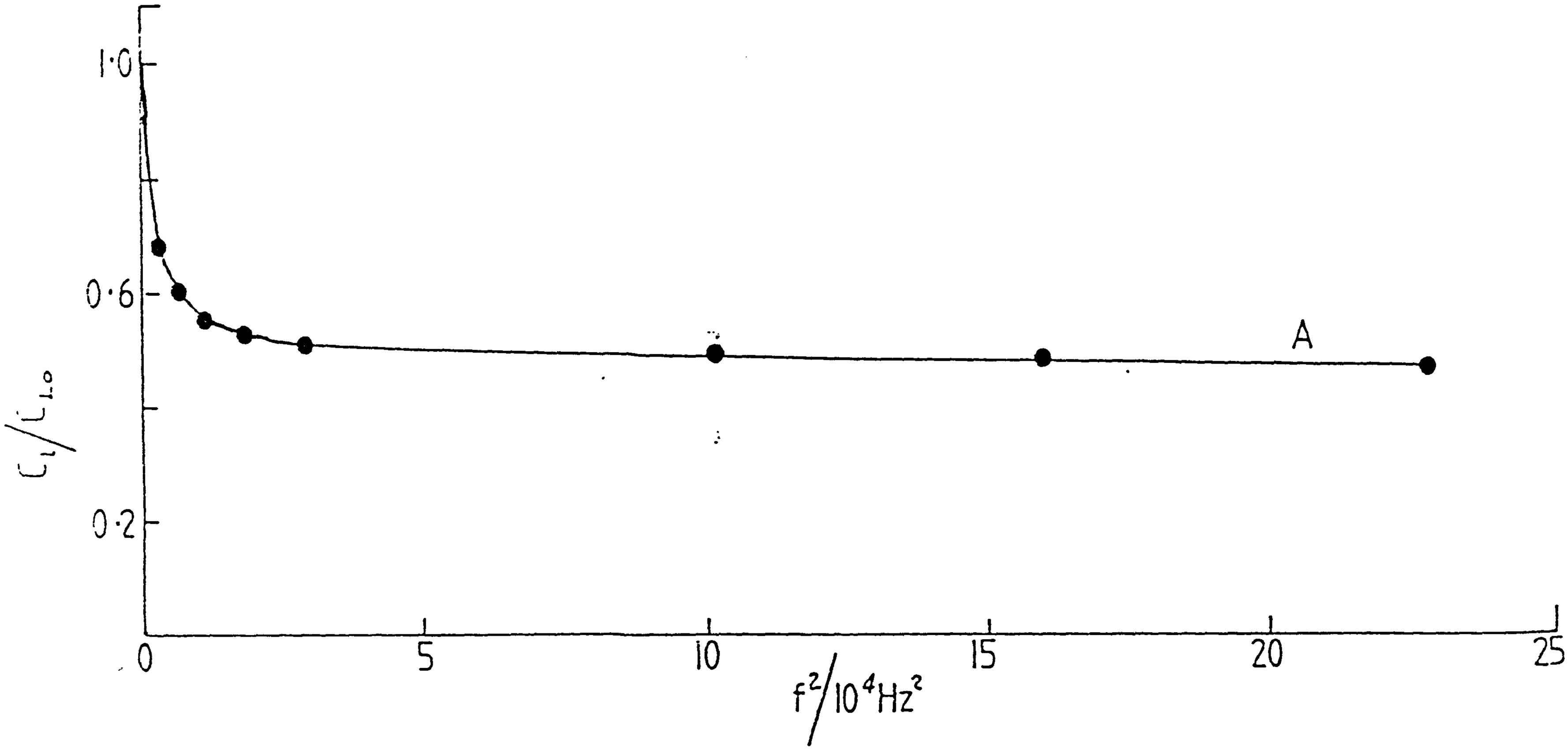

REFERENCES

1. A. Volta, Phil. Trans. Roy. Soc., 90 (1800) 403.

2. H. Helmholtz, Wied. Ann., 7 (1879) 377.

3. A. Gouy, J. Phys., 9 (1910) 457.

4. D.L. Chapman, Phil. Mag., 25 (1913) 475.

5. O. Stern, Ziet. Elektrochem., 30 (1924) 508.

6. D.C. Grahame, Chem. Rev., 41 (1947) 1441.

7. M.A.V. Devanathan, J.O'M. Bockris and K. Müller, Proc. Roy. Soc., London, A274 (1963) 55.

8. A.N. Frumkin, J. Electrochem. Soc., 107 (1960) 461.

9. Idem., Svensk Komisk Tischschoift, 77 (1965) 300.

10. S. Levine, G.M. Bell and A.L. Smith, J. Phys. Chem., 75 (1969) 3534.

11. B.B. Damaskin and A.M. Frumkin, Electrochim. Acta, 19 (1974) 173.

12. R. Parsons, J. Electroanal. Chem., 59 (1975) 229.

13. I.L. Cooper and J.A. Harrison, J. Electroanal. Chem., 66 (1975) 85.

14. Idem., Electrochim. Acta, 22 (1977) 519.

15. Idem, ibid., 22 (1977) 1361.

16. Idem, ibid., 22 (1977) 1365.

17. D.A. Brown, J.P.G. Farr, N.A. Hampson, D. Larkin and C. Lewis, J. Electroanal. Chem., 17 (1968) 421.

18. R. de Levie, in P. Delahay (ed.), Adv. Electrochem. Electrochem. Eng., Vol. 6, Interscience, New York, (1967) (a) p.380 (b) p.329.

19. R. Leek and N.A. Hampson, Surf. Technol., 7 (1978) 151.

20. Idem, ibid., 12 (1981) 383.

21. T. Erdy-Gruz and M. Volmer, Zeit. Physik. Chem., 105 (1930) 203.

22. P. Delahay, Double Layer and Electrode Kinetics, Interscience, New York (1965).

23. J. Tafel, Zeit. Physik. Chem., 50 (1905) 641.

24. K.J. Vetter, ibid., 194 (1956) 284.

25. V.V. Losev, "Modern Aspects of Electrochemistry", Vol. 7, Ed. B.E. Conway and J. O'M. Bockris, Bulterworths (1972) 314.

26. V.G. Levich, Advan. Electrochem. Eng., 4 (1966) 249.

27. R.A. Marcus, Electrochim. Acta, 13 (1968) 995.

28. R.R. Dogonadze, "Reactions of Molecules at Electrodes", Wiley (1971) 135.

29. V.G. Levich, "Physico-Chemical Hydrodynamics", Prentice Hall, Englewood Cliffs, (1962).

30. L.A. Matheson and N. Nichols, Trans. Electrochem., Soc., 73 (1938) 193.

31. J.E.B. Randles, Trans. Faraday Soc., 44 (1948) 327.

32. A. Sevcik, Coll. Chech. Chem. Commun., 13 (1948) 349.

33. R.S. Nicholson and I. Shain, Anal. Chem., 36 (1964) 706.

34. E. Warburg, Ann. Physik., 67 (1899) 493; 6 (1901) 125.

35. J.E.B. Randles, Discussion Faraday Soc., 1 (1947) 11.

36. H. Ershler, ibid., 1 (1947) 269.

37. H. Gerischer, Z. Phisik. Chem., 198 (1951) 286.

38. M. Sluyters-Rehbach, D.J. Kooÿam and J.H. Sluyters, "Polarography", Ed. G.J. Hills, Macmillan Press, (1964) 143.

39. J.H. Sluyters, Rec. Trad. Chim., 79 (1960) 1092.

40. M. Sluyters-Rehbach and J.H. Sluyters, "Electroanalytical Chemistry", Vol. 4, (ed. Bard), Dekker, New York, (1970) p.1.

41. D.C. Grahame, J. Electrochem. Soc., 99 (1952) 370C.

42. H.A. Laitinen and J.E.B. Randles, Trans. Faraday. Soc., 51 (1976) 5.

43. R.D. Armstrong, J. Electroanal. Chem., 34 (1972) 387.

44. R.D. Armstrong and M. Henderson, ibid., 39 (1972) 81.

45. R.D. Armstrong and R.E. Firman, ibid., 45 (1973) 3.

46. Idem, ibid., 45 (1973) 257.

47. R.D. Armstrong, R.E. Firman and H.R. Thirsk, Faraday Discuss. Chem. Soc., 56 (1973) 244.

48. Idem, J. Electroanal. Chem., 48 (1973) 150.

49. R.D. Armstrong and M.F. Bell, J. Electroanal. Chem., 58 (1975) 419.

50. R.D. Armstrong, M.F. Bell and A.A. Metcalfe, "Electrochemistry", Vol. 6, p.98, Specialist Periodical Reports, The Chemical Society, London, 1974.

51. M. Keddam, S. Stymar and H. Takenouti, J. Appl. Electrochem., 7 (1977) 539.

52. S.A.G.R. Karunathilaka, N.A. Hampson, R. Leek and T.J. Sinclair, J. Appl. Electrochem., 10 (1980) 799.

53. R. Darby, J. Electrochem. Soc., 113 (1966) 392, 496.

54. F. Gutman, J. Electrochem. Soc., 112 (1965) 94.

55. "Zinc-Silver Oxide Batteries", Edited by A. Fleischer and J.J. Lander, John Wiley & Sons Inc., New York, 1971.

56. R.V. Bobker, "Zinc in Alkali Batteries", The Society for Electrochemistry, University of Southampton, Great Britain, 1973.

57. R.D. Armstrong and M.F. Bell, "Electrochemistry", Vol. 4, p.1, Specialist Periodical Reports, The Chemical Society, London, 1974.

58. J. McBreen and E.J. Cairns, "Adv. Electrochem. Electrochem. Eng.", Vol. 11, Edited by H. Gerischer and C.W. Tobias, p.273, Wiley-Interscience, New York, 1978.

59. F.L. Tye, "Electrochemical Power Sources", Edited by M. Barak, The Institution of Electrical Engineers, London, 1980.

60. A. McNeil and N.A. Hampson, Specialist Periodical Reports 3, Vol. 8, in press.

61. G. Coates, N.A. Hampson, A. Marshall and D.F. Porter, J. Appl. Electrochem., 4 (1974) 75.

62. R.A. Myers and J.M. Marchello, J. Electrochem. Soc., 116 (1969) 790.

63. G. Duperay, G. Marcellin and B. Pichon, "Power Sources 8", Edited by J. Thompson, Academic Press, London, 1981, p.489.

64. R.W. Powers and M.W. Breiter, J. Electrochem. Soc., 116 (1969) 719.

65. R.W. Powers, ibid., 118 (1971) 685.

66. N.A. Hampson and A. Marshall, J. Appl. Electrochem., 7 (1977) 271.

67. M.C.H. McKubre and D.D. MacDonald, J. Electrochem. Soc., 128 (1981) 524.

68. T. Katan, J.R. Savory and J. Perkins, ibid., 126 (1979) 1825.

69. N.A. Hampson and M.J. Tarbox, ibid., 110 (1963) 95.

70. N.A. Hampson, M.J. Tarbox, J.T. Lilley and J.P.G. Farr, Electrochem. Tech., 2 (1964) 309.

71. R.N. Elsdale, N.A. Hampson, P.C. Jones and A.N. Strachan, J. Appl. Electrochem., 1 (1971) 213.

72. M.W. Breiter, Electrochimica Acta, 15 (1970) 1297.

73. S.A.G.R. Karunathilaka, N.A. Hampson, R. Leek and T.J. Sinclair, 10 (1980) 357.

74. Idem, ibid., 10 (1980) 603.

75. Idem, ibid., 11 (1981) 365.

76. Idem, ibid., 11 (1981) 573.

77. Idem, ibid., 11 (1981) 715.

78. M.B. Liu, G.M. Cook and N.P. Yao, J. Electrochem. Soc., 128 (1981) 1663.

79. Z. Nagy and J. O'M Bockris, ibid., 119 (1972) 1129.

80. S. Spzak and C.J. Gabriel, ibid., 126 (1979) 1914.

81. Y. Yamazaki and N.P. Yao, ibid., 128 (1981) 1655.

82. M.B. Liu, G.M. Cook and N.P. Yao, ibid., 129 (1982) 239.

83. J. McBreen, ibid., 119 (1972) 1620.

84. K.W. Choi, D.N. Bennion and J. Newman, ibid., 123 (1976) 1616.

85. K.W. Choi, D. Hamby, D.N. Bennion and J. Newman, ibid., 123 (1976) 1628.

86. D. Hamby and J. Wirkkala, ibid., 125 (1978) 1020.

87. D.C. Hamby, N.J. Hoover, J. Wirkkala and D. Zahnle, ibid., 126 (1979) 2110.

88. W.G. Sunu and D.N. Bennion, ibid., 127 (1980) 2007.

89. W.G. Sunu and D.N. Bennion, ibid., 127 (1980) 2017.

90. S.P. Poa and C.W. Wu, J. Appl. Electrochem., 8 (1978) 427.

91. Idem, ibid., 8 (1978) 491.

92. R.J. Brodd and V.E. Leger, "Encyclopedia of the Electrochemistry of the Elements", Vol. 5, Edited by A.J. Bard, 1976.

93. D.P. Gregory, P.C. Jones and D.P. Redfearn, J. Electrochem. Soc., 119 (1972) 1288.

94. O. Wagner and A. Himey, Proc. 28th U.S. Power Sources Symp., (1976) 135.

95. T. Keily and T.J. Sinclair, J. Power Sources, 6 (1981) 41.

96. J. McBreen and E. Gannon, Electrochim. Acta, 26 (1981) 1439.

97. D.J. Spiers, private communication.

98. T.P. Dirkse and N.A. Hampson, Electrochim. Acta, 16 (1971) 2049.

99. N.A. Hampson, P.C. Jones and R. Philips, Canadian Journal of Chemistry, 45 (1967) 2039.

100. S.U. Falk and A.J. Salkind, "Alkaline Storage Batteries", John Wiley, London, 1969.

101. T.P. Dirkse and N.A. Hampson, Electrochim. Acta, 17 (1972) 135.

102. T.P. Dirkse and N.A. Hampson, J. Electroanal. Chem., 35 (1972) 7.

103. J. O'M. Bockris, Z. Nagy and A. Damjanovic, J. Electrochem. Soc., 119 (1972) 285.

104. T.P. Dirkse, ibid., 126 (1979) 541.

105. T.P. Dirkse and N.A. Hampson, Electrochim. Acta, 17 (1972) 813.

106. R.F. Thornton and E.J. Carlson, J. Electrochem. Soc., 127 (1980) 1448.

107. R.C.V. Piatti, J.J. Podesta, A.J. Arvia, Electrochimica Acta, 25 (1980) 827.

108. T.P. Dirkse, private communication.

109. H. Gerischer, Z. Physik. Chem. Leipzig, 202 (1953) 302.

110. R.D. Armstrong and G.M. Bulman, J. Electroanal. Chem., 25 (1970) 121.

111. W. Lorenz, Z. Phys. Chem., NF19 (1959) 337.

112. J.P.G. Farr and N.A. Hampson, Trans. Farad. Soc., 62 (1966) 3493.

113. A. Marshall, N.A. Hampson, M.P. Saunders and J.S. Drury, J. Electroanal. Chem., 78 (1977) 307.

114. J.S. Drury, N.A. Hampson and A. Marshall, British Patents, 1, 411, 911, 1975; 1, 525, 383, 1978.

115. A. Marshall, N.A. Hampson, J.S. Drury and J.P.G. Farr, Surf. Technol., 5 (1977) 149.

116. A. Marshall, Ciba-Geigy Ltd., personal communication, January 1980.

117. L.M. Baugh, Electrochim. Acta, 24 (1979) 657.